Printing Conductive Traces to Enable High Frequency Wearable Electronics Applications

By

Ying Ying Lim

A Doctoral Thesis

Submitted in partial fulfillment of the requirements
for the award of
Doctor of Philosophy of Loughborough University
March 2015

Abstract

With the emergence of the Internet of Things (IoT), wireless body area networks (WBANs) are becoming increasingly pervasive in everyday life. Most WBANs are currently working at the IEEE 802.15.4 Zigbee standard. However there are growing interests to investigate the performance of BANs operating at higher frequencies (e.g. millimetre-wave band), due to the advantages offered compared to those operating at lower microwave frequencies. This thesis aims to realise printed conductive traces on flexible substrates, targeted for high frequency wearable electronics applications. Specifically, investigations were performed in the areas pertaining to the surface modification of substrates and the electrical performance of printed interconnects.

Firstly, a novel methodology was proposed to characterise the dielectric properties of a non-woven fabric (Tyvek) up to 20 GHz. This approach utilised electromagnetic (EM) simulation to improve the analytical equations based on transmission line structures, in order to improve the accuracy of the conductor loss values in the gigahertz range.

To reduce the substrate roughness, an UV-curable insulator was used to form a planarisation layer on a non-porous substrate via inkjet printing. The results obtained demonstrated the importance of matching the surface energy of the substrate to the ink to minimise the ink de-wetting phenomenon, which was possible within the parameters of heating the platen. Furthermore, the substrate surface roughness was observed to affect the printed line width significantly, and a surface roughness factor was introduced in the equation of Smith *et al.* [22] to predict the printed line width on a substrate with non-negligible surface roughness ($R_a \leq 1$ μm).

Silver ink de-wetting was observed when overprinting silver onto the UV-cured insulator, and studies were performed to investigate the conditions for achieving electrically conductive traces using commercial ink formulations, where the curing equipment may be non-optimal. In particular, different techniques were used to characterise the samples at different stages in order to evaluate the surface properties and printability, and to ascertain if measurable resistances could be predicted.

Following the results obtained, it was demonstrated that measurable resistance could be obtained for samples cured under an ambient atmosphere, which was verified on Tyvek samples.

Lastly, a methodology was proposed to model for the non-ideal characteristics of printed transmission lines to predict the high frequency electrical performance of those structures. The methodology was validated on transmission line structures of different lengths up to 30 GHz, where a good correlation was obtained between simulation and measurement results. Furthermore, the results obtained demonstrate the significance of the paste levelling effect on the extracted DC conductivity values, and the need for accurate DC conductivity values in the modelling of printed interconnects.

Keywords: Printing techniques, Surface modifications, Flexible substrates, De-wetting phenomenon, RF performance simulation, High frequency dielectric characterisation.

Acknowledgments

I am grateful to my supervisor, Dr Yee Mey Goh, for her kind guidance and constant support throughout the course of my PhD. I would also like to thank my co-supervisor, Prof. Changqing Liu, for giving me the opportunity to be seconded to AIST, Japan, for part of my PhD work. In addition, my appreciation goes to Dr David Hutt for the many helpful discussions along the course of my PhD work.

This PhD would not have been possible without the support of my many collaborators. Firstly, I would like to thank Dr Steve Jones and Dr Neil Chilton at Printed Electronics Ltd. for their interest and support in this project, and for giving me the freedom to pursue my research interests. I would also like to thank Mr Colin MacDonald from Rogers Corporation for the generous provision of the Rogers substrates in this project. My appreciation also goes out to Mr Mike Pickrell for the kind provision of the various Sun Chemical inks, and for the helpful technical support in the evaluation of the inks. In addition I am indebted to CST (US) and AET (Japan) for granting me a provisional software license to do part of this work. My heartfelt appreciation also goes to Prof. Ian Robertson for kindly allowing me access to the RF probe station facilities over at Leeds University for the high frequency characterisation work in this thesis.

Furthermore, I would also like to acknowledge AIST for providing me with the excellent research facilities to pursue the last stage of my PhD work. In particular I would like to thank Dr Masahiro Aoyagi, Dr Bui Thanh Tung, Dr Jun Akedo, Dr Manabu Yoshida and my colleagues at the 3D Integration group at AIST for their kind support and the friendships extended to me during my stay in Japan.

Finally, I would like to thank my close group of friends who have been greatly supportive during the course of my PhD work. In particular, I am grateful to Malcolm and Margaret King, whose kindness I am indebted to. In addition, my appreciation goes to Sooyoung Kim, Muthu, Jessica and Jasmine, for their encouragements and support all these while. Lastly I am grateful to my family for their kind understanding and unceasing support in my pursuit of a PhD. I am thankful for all of you.

List of Publications

The publications which arise from the work in this thesis are listed below.

Journals

1. Ying Ying Lim, Yee Mey Goh, Changqing Liu, "Surface Treatments for Inkjet Printing onto a PTFE-Based Substrate for High Frequency Applications", *Ind. Eng. Chem. Res*, Vol. 52, No. 33, pp. 11564-11574, 2013.

2. Ying Ying Lim, Yee Mey Goh, Changqing Liu, David Hutt, "Surface Modification of an Ambient UV-cured Dielectric to Realise Electrically Conducting Traces", *Surf. Coat. Technol.*, Vol. 266, pp. 93-104, 2015.

Conferences

1. Ying Ying Lim, Yee Mey Goh, Changqing Liu, "RF Performance of Inkjet and Stencil Printed Traces for Flexible Electronics Applications", Proc. *14th Electron. Packag. Technol. Conf. (EPTC)*, pp. 556-562, 2012.

2. Ying Ying Lim, Yee Mey Goh, Changqing Liu, "Fine Pitch Printing on a Non-Woven Fabric for High Frequency Applications", Proc. *M6 Conf.*, 1 pp., 2013.

3. Ying Ying Lim, Yee Mey Goh, Manabu Yoshida, Tung Thanh Bui, Tracey Vincent, Masahiro Aoyagi, Changqing Liu, "Silver Screen Printed Transmission Lines – Analyzing the Influence of Substrate Roughness on the RF Performance up to 30 GHz.", Proc. *16th Electron. Packag. Technol. Conf. (EPTC)*, pp. 22-26, 2014.

4. Ying Ying Lim, Yee Mey Goh, Hiroki Tsuda, Jun Akedo, Masahiro Aoyagi, Changqing Liu, "Adhesion of Aerosol Deposition Traces Targeted for Flexible Electronics Applications" Proc. *Third Int. Conf. Adv. Manuf. Multifunct. Miniaturised Devices (ICAM3D);* 1 pp., 2014. ***(Awarded Best Interactive Poster)***

List of Abbreviations

1D	One-dimensional
2D	Two-dimensional
3D	Three-dimensional
CNT	Carbon Nanotube
CPW	Coplanar Waveguide
CST	Computer Simulation Technology
CTE	Coefficient of Thermal Expansion
DC	Direct Current
DIC	Differential Interference Contrast
DUT	Device Under Test
FD	Frequency Domain
FEGSEM	Field Emission Gun Scanning Electron Microscope
FR4	Glass-reinforced Epoxy Laminate
GSG	Ground-Signal-Ground
IF	Intermediate Frequency
IoT	Internet of Things
ISM	Industrial, Scientific and Medical
ISO	International Standards Organisation
LED	Light-Emitting Diode
LRM	Line-Reflect-Match
PCB	Printed Circuit Board
PDMS	Polydimethylsiloxane
PET	Poly(Ethylene Terephthalate)
PI	Polyimide
RF	Radio Frequency
RFID	Radio Frequency Identification
SEM	Scanning Electron Microscope
SMA	Surface Mount Adaptor
TD	Time Domain
XPS	X-ray Photoelectron Spectroscopy
WBAN	Wireless Body Area Network

List of Symbols and Definitions

Macroscopic variables		**Usage(s)**
ε_r	Actual dielectric constant	Chapter 4
ε'_{eff}	Effective dielectric constant	Chapter 4
ε''_{eff}	Effective loss tangent	Chapter 4
β_0	Phase constant in free space	Chapter 4
b_0	Width of a drop on the substrate	Chapter 5
d	Diameter of droplet	Chapter 5
Δd	Length difference between 2 microstrip lines	Chapter 4
M_1 , M_2^{-1}	ABCD matrices	Chapter 4
T_r	Trace defined as the sum of the diagonal elements in the matrices	Chapter 4
k	Complete elliptic integral of the first kind	Chapter 4
k_r	Correction factor for the printed line width	Chapter 5
$\propto_{total}$	Total attenuation constant	Chapter 4
γ	Propagation constant	Chapter 4
γ_s	Solid surface tension	Chapter 3
γ_L	Liquid surface tension	Chapter 3
γ_{sL}	Solid and liquid boundary tension	Chapter 3
λ	Wavelength at the maximum frequency	Chapter 4
λ_0	Wavelength in free space	Chapter 4
$\propto_{cond}$	Conductor loss	Chapter 4
$\propto_{diel}$	Dielectric loss	Chapter 4
σ	DC conductivity	Chapter 4
ρ	DC resistivity	Chapter 4
δ	Skin depth	Chapter 4
g_1, g_2	Signal-ground spacing	Chapter 4, 7
θ_{1a}, θ_{1b}	Lower signal trace angles	Chapter 4, 7
θ_{2a}, θ_{2b}	Lower ground trace angles	Chapter 4, 7
θ_{3a}, θ_{3b}	Lower ground trace angles	Chapter 4, 7
θ	Contact angle	Chapter 5

θ_a	Advancing contact angle	Chapter 5
A	Cross-sectional area	Chapter 4
C	Capacitance	Chapter 4
I	Current	Chapter 7
l	Line or trace length	Chapter 4,7
L	Inductance	Chapter 4
Oh	Ohnesorge number	Chapter 5
p	Correction factor for surface roughness	Chapter 7
R	DC resistance	Chapter 4
R_a	Average surface roughness	Chapter 4, 5
S_{11}	*S*-parameter representing return loss	Chapter 4, 7
S_{21}	*S*-parameter representing insertion loss	Chapter 4, 7
t	Trace thickness	Chapter 4
t_{av}	Average trace thickness	Chapter 7
w	Signal width	Chapter 4
w_0	Printed width on a substrate (smooth)	Chapter 5
w_1	Printed width on a substrate with surface roughness	Chapter 5
w_{top}	Width of top surface of conductor	Chapter 7
w_{btm}	Width of bottom surface of conductor	Chapter 7
V	Voltage	Chapter 7
Z	Z number, used to describe drop formation	Chapter 5
Z_0	Characteristic impedance value	Chapter 4

Table of Contents

List of Figures

List of Tables

Chapter 1. Introduction

1.1 Research Background

It is anticipated that the Internet of Things (IoT) will become a reality in the future when sensors and internet connectivity enable individual devices to communicate, and thus becomes a feature of everyday living. To this end, wearable electronics offering ubiquitous connectivity are a promising development.

Wireless Body Area Networks (WBANs) comprise of wireless networks of wearable electronics devices. WBANs may be used for communications such as for monitoring the health and physiological conditions of its wearer (e.g. patients)[1, 2], in search and rescue operations [3] and in military operations [4, 5]. In particular, there has been a keen interest in the military domain in developing capability for body worn antennas [4, 5]. The key advantages of body worn electronics (i.e. wearable electronics on clothing) compared to traditional or mounted electronic devices include reduced weight, the possibility of covertness and user comfort.

Most WBANs are currently working at the IEEE 802.15.4 Zigbee standard [6]. There is a growing interest in investigating the performance of WBANs in the millimetre wave band (e.g. 60-GHz band), due to the advantages offered compared to when operating at lower frequencies. One advantage lies in the higher data rates that can be obtained (e.g. for audio and video sharing), which translates to reduced transmission times. This is aimed towards the high data rate requirements in 5G radio access. Another advantage lies in the increased security and lower interference with adjacent WBANs, due to the stronger attenuation of these signals in the atmosphere. This aspect is critical for medical sensor networks in hospitals operating in the Industrial, Scientific and Medical (ISM) band, which currently coexist with other equipment working in these bands. Operation in the current ISM band gives rise to security concerns [7, 8] of external systems interfering with current BANs (e.g. denial of use or data falsification), which poses a problem for the medical sensor networks. Furthermore, millimetre wave band WBANs are

crucial for enabling the secure transfer of sensitive data in military operations requiring covertness. Lastly the demand for highly miniaturised wearable devices motivates the use of higher frequencies [9]. If the size of the sensors and front-end electronics in a wearable device are large, the overall device may be bulky for use in long term monitoring applications (involving the collection of movement or psychological data), where users' comfort is key.

For high frequency applications such as those in the millimetre wave band, realising fine pitch interconnects is imperative since the wavelength (i.e. interconnect dimension) scales inversely with frequency [10]. From the electrical perspective, conductive traces with low resistance are crucial for good performance [11], which translates to low interconnect losses at higher frequencies. Furthermore, fine pitch interconnects enable a higher density of integration to be achieved, such as in multi-functional sensor systems.

Based on the above context, this research aims to realise fine pitch interconnects, targeted for high frequency wearable electronics applications. For such applications, fabrics are perceived as a promising substrate to integrate electronic circuitry, so as to obtain lighter modules along with improved user comfort.

1.2 Problem Statement and Research Motivation

To date, much of the work on wearable electronics uses conductive fibres and fabrics to form interconnects and antennas. These components are designed in the lower gigahertz frequency range below 3 GHz [12-15], due to the limitations of conductive fabrics. Challenges exist in using conductive fibres (and fabrics) to realise interconnects on fabrics. Firstly, issues arise in obtaining homogeneous line width and gaps [12, 13] using conductive fibres, which results in a reduced bandwidth of operation [12]. In addition, significant interconnect losses arising from the skin depth effect would result at higher frequencies, since the plated metal thickness of conductive fabrics is restricted to several hundred nanometres to maintain fabric properties [15].

Alternatives to the use of conductive fibres are printing technologies which offer fine pitch [16-18] and higher frequencies of operation [19, 20], through the deposition of traces onto the substrate of interest. These include inkjet printing and screen printing. However one challenge with realising interconnects on fabrics results from their being porous materials with inherent surface roughness, which has implications for the printing technique used for realising fine pitch interconnects. Among the printing technologies available, inkjet printing is currently the most viable technology used to realise fine pitch interconnects. However, using inkjet printing to deposit pico-litre ink volumes onto the fibrous surface of a non-woven fabric (shown in Figure 1.1) results in a penetration of the silver nanoparticles into the fibres [21]. This leads to discontinuous printed traces, and therefore necessitates surface modifications to alleviate the surface roughness and/or porosity of the substrate for inkjet printing. In order to achieve the research aim, the following four challenges related to the deposition of fine pitch interconnects and their electrical performances at high frequencies need to be overcome.

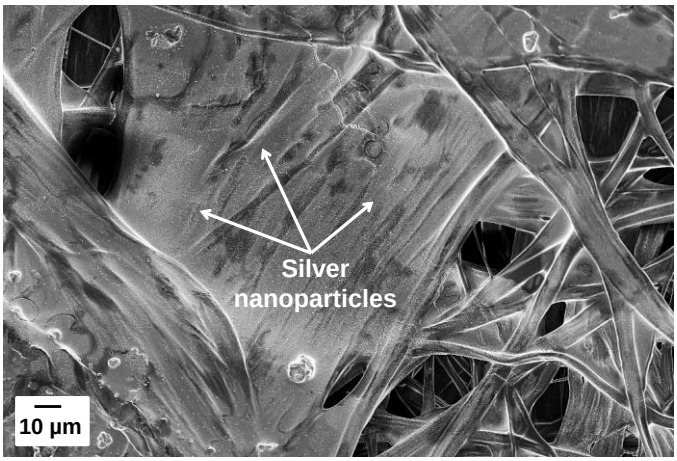

Figure 1.1 SEM image showing inkjet printed silver nanoparticles on the surface of Tyvek

(i) Overcoming the surface roughness of substrates

Most researchers consider substrates with relatively smooth surfaces for inkjet printing [18, 22, 23], where fine pitch interconnects are obtainable [16, 17]. The challenges of realising fine pitch on substrates with surface roughness (e.g. fabrics) arise from the ink spread on such surfaces [24, 25], which adversely affects the print resolution of the interconnects [25]. This necessitates a need for surface treatments to modify the substrate surface and alleviate the surface roughness.

(ii) Obtaining electrically conducting traces on the planarisation layers

UV-curable dielectric paste/inks [26, 27] have been used to form planarisation layers to alleviate the substrate surface roughness. From literature, the properties of the UV-curable dielectric paste/inks used were formulated to match the surface energies of the silver inks to be overprinted, such that no de-wetting would occur. Others [28] ensured that the UV-curable ink was properly cured using a high intensity UV source, prior to overprinting with a silver ink. In terms of material analysis, little work has been reported on the final cure status of such dielectrics [29, 30]. As such the assumption made by the author is that the dielectrics are fully cured. From what has been done so far, there exists a need to understand the parameters to be addressed to eliminate de-wetting when the surface energies of the ink and the planarisation layer are not matched, or when the UV source used for curing is non-optimal.

(iii) Determining the dielectric properties of fabric as a substrate for high frequency applications

The dielectric properties (dielectric constant, loss tangent) of fabrics are not readily available from manufacturers as they are not typically considered for high frequency applications. This is in contrast to conventional laminates used for such applications, where the dielectric properties are characterised to broadband frequencies [31, 32]. From literature researchers have characterised the dielectric properties of fabrics up to 10 GHz [33], but encountered issues in the repeatability of the results arising from the test structure used. Thus another research motivation is to characterise the dielectric properties of a fabric up to broadband frequencies ($\geq$ 20 GHz), with repeatable results.

(iv) Determining the RF performance of printed interconnects

From literature, work abounds on the electrical performance of printed interconnects in the DC and megahertz frequency range [18, 34-38]. Printed interconnects in this context refer to interconnects deposited by technologies other than printed circuit board (PCB) technology (e.g. inkjet printing, screen printing).

While the RF performance of printed interconnects have been reported up to 30 GHz [18], to the author's best knowledge, there is no simulation model at present which predicts the RF performance of fine pitch printed interconnects, because most of the applications considered are in the megahertz frequency range. Furthermore challenges arise in modelling for printed interconnects which have non-ideal characteristics (non-rectangular profile, surface roughness) and possibly small thicknesses (e.g. inkjet printed traces). Thus another research motivation lies in wanting to be able to accurately predict the high frequency performance of printed interconnects, so as to reduce the number of fabrication trials, with the aim of getting a right first time design. In addition there is a need to evaluate how variations in the test structures would influence the measured results and the simulation correlation.

1.3 Research Aims and Objectives

This thesis aims to address the knowledge gaps with regards to obtaining printed conductive traces of fine pitch (< 400 μm pitch) on flexible substrates, targeted for high frequency wearable electronics applications as explained in Section 1.2. The term "pitch" is defined as the centre-to-centre spacing between the printed traces, as shown in Figure 1.2. In this thesis, high frequency refers to the frequency range from 20-30 GHz. To pursue this aim, the following objectives were identified.

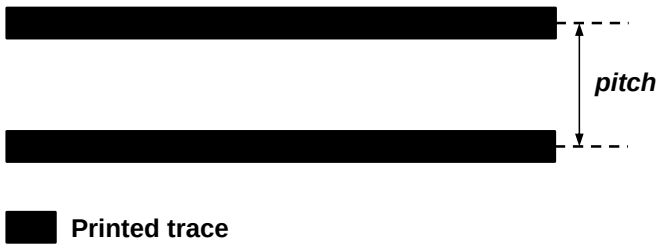

Figure 1.2 Definition of "pitch" in the context of this thesis

1. **To characterise the dielectric properties of a non-woven fabric up to 30 GHz.**

To develop a methodology to improve the current analytical approach for dielectric characterisation (based on transmission line structures). This is since the conductor loss formulas available according to the literature are not intended for calculating the transmission line characteristics beyond the higher gigahertz frequencies. From

the measurement aspect, a different measurement setup will be used for the electrical characterisation and the repeatability of the results will be evaluated.

2. To reduce the surface roughness of substrates for trace deposition using inkjet printing.

To select a suitable surface modification technique to planarise the surface roughness of substrates, and to investigate the effect of the substrate roughness on the printed trace widths.

3. To realise electrically conducting traces using inkjet printing.

To understand the parameters required to eliminate de-wetting when the surface energies of the planarisation layer and the silver ink are not matched. A sub-objective is to eliminate de-wetting and obtain measurable resistances for silver traces overprinted onto the planarisation layer, based on the hypothesis that the deposition of clear linear traces does not necessarily indicate that the traces are conductive.

4. To predict the high frequency performance of printed transmission lines.

To develop a methodology for accurate design which includes a consideration of variations in the test structures and non-ideal transmission line characteristics present in the fabricated transmission line structures. The results from the simulation model are correlated with experimental measurements. In addition, simulation guidelines for the modelling of printed transmission lines are developed.

To meet the research objectives set out in this thesis, two substrates are being considered for use. The first substrate considered is a non-woven fabric (Tyvek). This particular material is selected as it has previously been studied by other researchers [39, 40] using screen printing and inkjet printing techniques.

Nevertheless it is challenging to deposit traces onto Tyvek using inkjet printing, as shown from a pilot study the results of which are documented in Appendix A. The first challenge in inkjet printing onto untreated Tyvek arises from the fibrous surface (Figure 1.1) of the substrate, which results in a penetration of the silver nanoparticles into the fibres. Another challenge in printing onto Tyvek lies in the

inherent substrate roughness of the material. As described further in Appendix A, the deposition of dielectric layers (SU-8 coating, UV-curable dielectric) was not found to sufficiently planarise the substrate surface. The combination of substrate roughness and porosity present in Tyvek was found to increase the complexity of using inkjet printing to deposit conductive traces, and necessitates a simplification of one of the variables in order to achieve the objectives set out in this thesis.

Due to the challenges encountered in printing onto Tyvek, RO3006 [31] was considered as the other substrate in this thesis. RO3006 is similar to Tyvek in that it is a flexible substrate (due to its PTFE-based properties), and is designed for high frequency applications [31]. These properties make RO3006 a potential substrate for high frequency wearable electronics [41]. In the thesis, RO3006 is used as a reference substrate in the dielectric characterisation of Tyvek, due to its well-characterised broadband dielectric properties (up to 40 GHz). In particular, these known dielectric properties can be used to validate the extraction methodology for obtaining the dielectric properties of Tyvek (as described in Chapter 4 of this thesis). Furthermore, knowledge of the high frequency dielectric properties of RO3006 is imperative for investigating the RF performance of printed interconnects, such that uncertainties arising from the substrate properties do not arise in the modelling process. This pertains to the work detailed in Chapter 7 of this thesis.

Apart from being flexible substrates, a common challenge also exists in inkjet printing onto both RO3006 and Tyvek, due to the substrate roughness present on both surfaces. While Tyvek has an inherent surface roughness, the substrate roughness present on RO3006 is a trade-off for good adhesion of the cladded copper to the substrate. This is evident after etching away the top metal layer, where copper dendrite imprints are left on the etched substrate. Yet in contrast to Tyvek, RO3006 is a non-porous substrate. This property aids in simplifying the study of alleviating the surface roughness of a substrate based on the inkjet printing technique (as described in Chapter 5 of this thesis).

1.4 Thesis Structure

This thesis focuses on addressing the four objectives set out in Section 1.3 in order to obtain printed conductive traces on flexible substrates targeted for high frequency wearable electronics applications. The thesis presents the results of the research towards achieving the objectives in a systematic manner. Chapter 1 provides an overview of the research background and motivation needed to understand the research gaps, and the approaches to be undertaken to address them. Chapters 2 and 3 provide literature reviews of possible printing technologies for realising fine pitch interconnects, along with the material and electrical characterisation techniques which are relevant to this work. The research gaps pertaining to this thesis are identified from these two chapters.

Chapter 4 presents the dielectric characterisation of a non-woven fabric up to 20 GHz, where the results were validated with RO3006 as the reference substrate. In this case the upper frequency of 20 GHz was constrained by the equipment set-up. Research objective 1 is addressed in this chapter.

Chapters 5 and 6 focus on alleviating the substrate roughness and obtaining electrically conductive printed traces, based on inkjet printing. Chapter 5 discusses the experimental results from using a UV-curable dielectric to deposit a smooth planarisation layer on RO3006. In addition, the effect of the substrate roughness on the printed line width is investigated by reconsidering the empirical formula proposed by Smith *et al*. [22]. Chapter 6 goes on to investigate the processing parameters to be addressed to eliminate the de-wetting of the silver ink on the planarisation layer, such that clear linear traces are obtained. The study also demonstrates that measurable resistances can be obtained for silver traces overprinted onto the UV-curable dielectric, for the case where the curing equipment is non-optimal. Research objectives 2 and 3 are addressed in these chapters.

The work in Chapter 7 seeks to address research objective 4, where a methodology is proposed to accurately predict the high frequency performance of printed

interconnects on RO3006 substrate. This includes the consideration of non-ideal transmission line characteristics to emulate the actual printed structures.

Finally, Chapter 8 summarises the key contributions of this thesis and offers directions for future work. The overall thesis structure also is summarised in Figure 1.3.

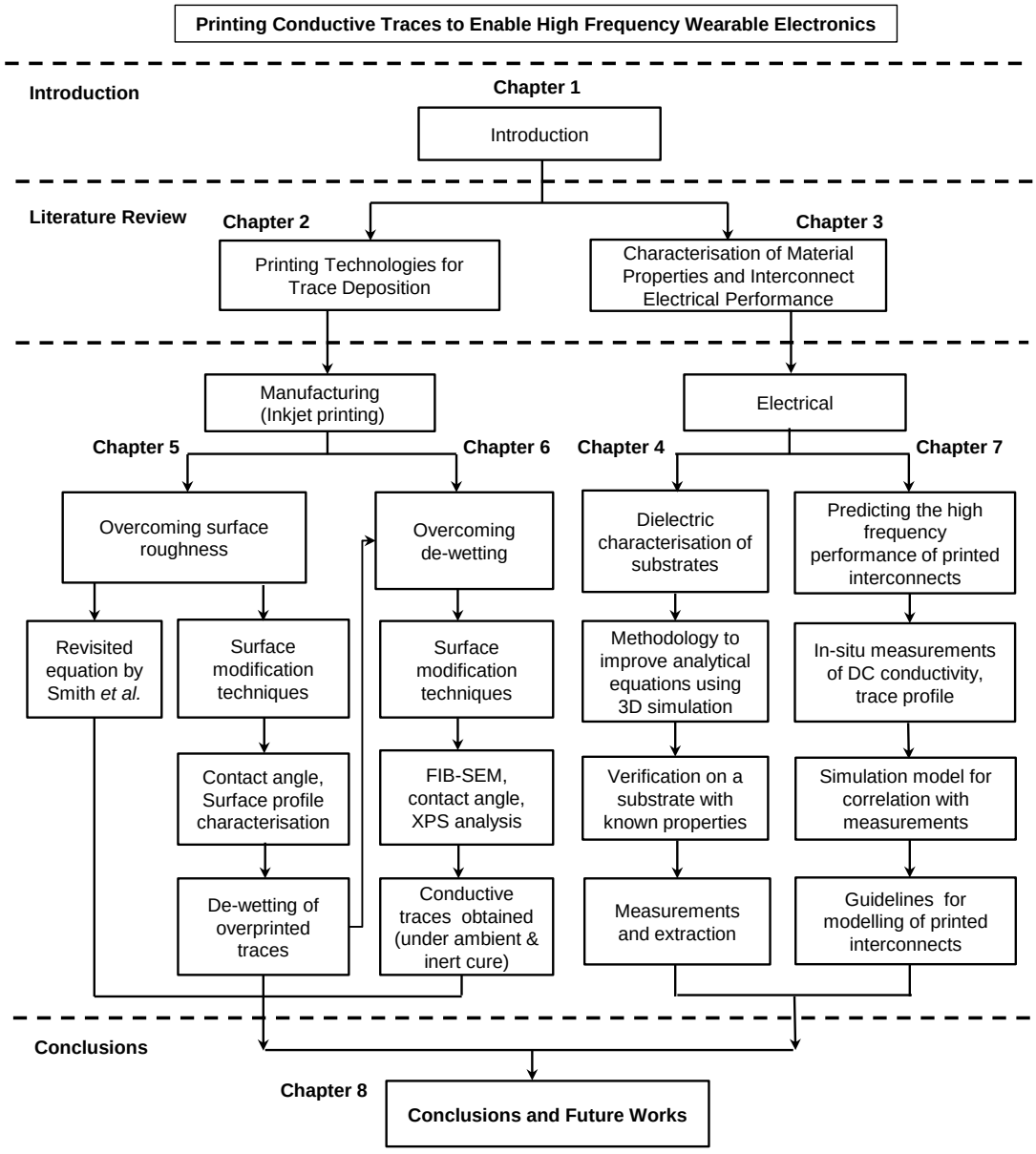

Figure 1.3 Schematic showing the overall thesis plan

Chapter 2. Printing Technologies for Trace Deposition

This chapter reviews the work done and identifies challenges towards realising conductive traces using printing technologies. Section 2.2 provides an overview of some of the key technologies, while Section 2.3 focuses on inkjet printing as a potential technique for obtaining fine line resolution and discusses the challenges involved.

2.1 Techniques for Realising Traces on Fabrics

Literature abounds in the use of copper tape, conductive threads and fabrics to realise traces. For higher frequency applications, fine pitch trace printing technologies are required as the dimensions scale inversely with frequency [10]. Muller *et al*. [42] recommended line width and space resolutions of within 50 µm for millimetre wave applications. For millimetre wave measurements, the pitch of the transmission lines has to be at or within 100 µm to match the RF probe tips [43]. Viable technologies for obtaining fine pitch trace printing include screen printing and aerosol deposition. These techniques are discussed in this section.

2.1.1 Copper Tape

Salonen *et al*. [44] employed copper tape to realise the conductive traces of patch antennas. While the antenna geometry is well-defined, a main drawback is the "rigidisation effect" [13] due to the use of the copper tape, where the tape can be bent only to a limited degree. This is in contrast to fabrics, which are drapable. Consequently, using stiffer copper tapes on textiles would result in a possible deformation of the conductive patterns, and/or delamination of the copper tapes when bent. This causes the antenna performance to be unpredictable.

To mitigate the effect of bending and the "rigidisation effect" on copper metal layers, Maleszka *et al*. [45] considered the use of meshed conductors. In their work [45], textile antennas and transmission lines were designed with meshed ground planes. The measured loss for a meshed transmission line was found comparable to

that of a solid line structure across a certain frequency band. For the textile antenna, it was noted that a copper film of 50 µm thickness (with adhesive on the underside) was used to form a patch antenna, with the ground plane being a meshed copper plane. Apart from improving the bending flexibility, the implementation of a meshed ground plane resulted in a reduction of the copper area by 35 % [45].

In terms of the electrical performance, the conventional copper foil or films are good options for forming the traces, since they are sufficiently thick (at 17.5 µm and above) for the skin depth at higher frequencies. The main drawback lies in that the fabrication process to obtain fine line resolution on fabric is tedious and subtractive. Laser processing can be an option to achieve the fine dimensions, but this can be an expensive process to obtain the required precision. Another drawback in using foils and films is that they are not as stretchable compared to fabrics, which could result in delamination when used on fabrics.

2.1.2 Conductive Fibres and Threads

To date, much of the work on electronic textiles (eg. textile antenna, textile electrodes) uses conductive fibres and threads to form conductive traces and patterns [12, 14, 46, 47].

Cottet *et al*. [12] used conductive fibres on a woven fabric to form transmission lines, and characterised them in terms of the attenuation constant, characteristic impedance (GS, GSG and GSSG configurations), up to 6 GHz. The dielectric permittivity of the fabric was extracted using parallel plate capacitor structures (2 different plate sizes and considering 1-8 textile layers between the plates). From the results, significant losses due to impedance mismatches were observed, which arise from the large geometrical variations between adjacent traces [12]. Firstly, the measured lines were not uniform; geometrical variations were observed in the distance between the wires which led to changes in the impedance. Consequently, there is the presence of parasitic odd-modes due to uneven ground potential for coplanar waveguide (CPW) lines, and the line becomes a $\lambda/2$ resonator which can prohibit transmission at certain frequencies. This in turn limits the usable frequency range of a transmission line.

In forming transmission lines on woven fabrics, it is noted that the distance between yarns vary (Figure 2.1), where yarns are formed from bundles of fibres twisted together. Consequently, one can deduce that an asymmetrical CPW would result, which gives rise to parasitic modes excited at high frequencies and a limited bandwidth of operation. Cottet *et al*. [12] noted variations with regards to the location of fibres within the yarn as well as the location of the yarns within the fabric. These irregularities arise from the deformability of the textile as well as the manufacturing process. On the other hand, the issue of limited operating bandwidth may not arise for the case of non-woven fabric, as they are not made from warp (length) and weft (width) yarns interwoven at right angles, but obtained through bonding or felting.

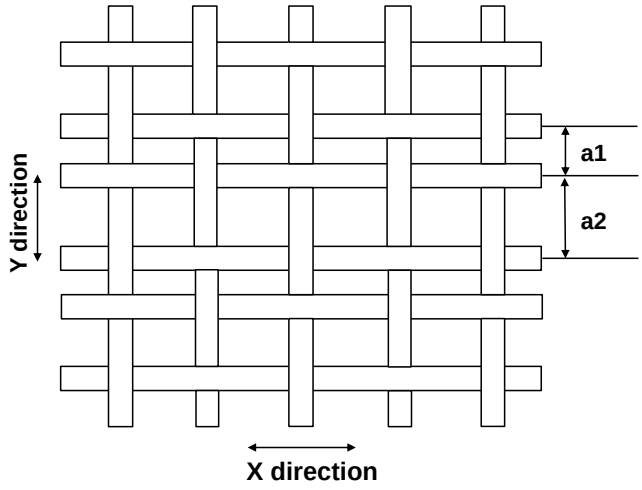

a1, a2 represent the distance between yarns

Figure 2.1 Variations in textile geometry (a1≠ a2), adapted from Cottet *et al.* [12]

Seager *et al*. [14] demonstrated a fabric antenna operating at 406 MHz using embroidered conductive threads. The spiral antenna was based on a cross dipole configuration and was designed for the purpose of achieving size reduction. While a reduced Q-factor was observed for the fabric antenna compared to a copper spiral antenna, the former was more resistant to bending when subjected to simple flexing experiments [14].

The main drawback of using conductive threads lies in the minimum dimension achievable. For instance, the minimum achievable spacing between two embroidered traces using an industrial machine is limited to about 1-1.5 mm [48].

For high frequency applications, a need arises for fine pitch (line width/spacing) with accurate dimensions (minimal dimension tolerances). Furthermore, fine pitch would enable a higher degree of module integration. In addition, embroidered traces on fabrics may not be very flexible, particularly when dense circuitries are embroidered into the fabric. Furthermore, embroidered transmission lines were found to have usually large losses which reduce the usable frequency range to 2-4 GHz [48].

2.1.3 Conductive Fabrics

Locher *et al*. [15] evaluated a textile antenna design using conductive fabrics. Prior to that, they investigated the sheet resistance variation with strain stress for a knitted conductive fabric, where it was observed that the resistance values with respect to the elongation differs in the x- and y- direction. A conductive fabric of a woven type (*Nora*) [49] was found to provide the lowest sheet resistance (0.02Ω/□), though the elasticity is less compared to the knitted fabric. In addition, the knitted fabric has a tendency to curl [15], which makes the adhesion to the substrate difficult. Locher *et al*. [15] also studied different methods of obtaining a proper adhesion of the conductive fabric to the textile substrate, with considerations given to the retention of the trace dimensions upon adhesion and ensuring that the attachment does not alter the sheet resistance of the conductive fabric or the dielectric properties of the textile substrate. 'Heat-n-bond' adhesive sheets (activated by ironing) were found to be the best option, since an even layer of adhesion can be obtained and the material does not penetrate through the conductive fabric or textile substrate. This is in contrast to sewing where wrinkling occurs beyond a minimum seam spacing. Furthermore, a liquid textile adhesive was not ideal as it was difficult to obtain an even distribution of the adhesive.

Locher *et al.* [15] reported that the plating thickness of the fabrics was restricted to several hundred nanometres [15] in order to maintain textile properties. As such, the implication of using conductive fabrics is that significant losses would result at higher frequencies due to the skin effect. This is particularly so in the millimetre wave regime where the skin depth at 60 GHz is 0.27 μm. The skin depth is a function of frequency and describes the current distribution in a conducting

material. The alternating current density is maximum at the surface and decreases with increasing depth in the conducting material. The skin depth is represented by equation (2.1) [50]:

$$\delta = \sqrt{\frac{2}{\omega\mu\sigma}} \tag{2.1}$$

where δ is the skin depth over which magnetic fields are attenuated by a factor of $1/e$, $\omega=2\pi f$ is the frequency of operation (rad/s), μ is the magnetic permeability of the conducting material (H/m) and σ is the conductivity of the conducting material (S/m). At 0 Hz, the entire thickness of the conducting material is utilised for the electric current. At higher frequencies, the current flows between the outer surface of the conducting material and the skin depth. This reduces the cross-sectional area and results in an increase of the conductor resistance. Ideally the metal thickness should be five times that of the skin depth to minimise the metal losses.

2.1.4 Screen Printing

A few researchers [39, 51] have considered screen-printing on fabrics towards realising flexible electronics. While this technique offers finer feature sizes compared to those obtained using embroidered traces, the minimum pitch achievable by screen-printing is typically limited to line width/spacing of around 100/100 μm [52] on common substrates such as Kapton, Mylar and glass. While it is possible to define smaller feature sizes of 50/50 μm on the screen [53], this is at the expense of increased screen costs. Another advantage of screen printing is that no surface modifications are required for the substrate to obtain continuous traces.

Merilampi [54] investigated screen printing on fabrics, where fabrics were considered to be a possible substrate for printed radio frequency identification (RFID) tags. While the temperature tolerance depends on the fabric type, most fabrics can withstand the curing temperature of printed thick film (PTF) ink. In addition, the average thickness of PTF is dependent on the substrate material, where the variation is most obvious on porous, rough substrates (eg. paper and fabric). Different fabric absorbs different amounts of ink, due to different woven structures and surface finishes. This affects the morphology of printed film.

In the area of smart fabrics, an EU project (Microflex) [55] was started in Southampton University with the goal of developing processes and materials, to fabricate microelectromechanical systems (MEMS) devices which are printed onto fabrics [55, 56]. Most of the processes and devices fabricated were noted to be implemented using screen printing [56, 57].

On the other hand, Pourdeyhimi *et al*. [40, 58] screen-printed coplanar waveguide (CPW) transmission lines onto non-woven fabrics (Tyvek and Evolon). In contrast, woven fabrics were not found to be suitable substrates for screen-printing due to their pore sizes (spaces between yarns and pores among fibres in the yarns). Consequently the printed resolution on a woven fabric would be constrained by the yarn diameter and yarn spacing. The printed CPW transmission lines onto the nonwoven fabrics yielded dimensions of 1400/400 μm (linewidth/spacing). However, as the dielectric properties of the Tyvek and Evolon fabrics were unknown, the printed line dimensions were not based on 50Ω impedance, but rather on the possible dimensions achievable while keeping the signal transmission intact [59]. While the characteristic impedance values of the CPW lines were measured [40], no information was available on the transmission line losses with respect to frequency. From the work done by Karaguzel *et al*. [40, 58] there exist a gap to build upon in terms of investigating the minimum dimensions achievable (ie fine line printing) on fabrics from the electrical perspective, particularly for high frequency (≥ 20 GHz) applications.

Unlike conductive threads and tape, obtaining conductive traces on fabrics after screen printing involves a low temperature curing process, due to the upper temperature limit which the fabric material could withstand. For instance, Pourdeyhimi *et al*. [58] considered conductive inks with curing temperatures of 110-120 °C in printing onto fabrics. Printing onto low temperature substrates necessitates sourcing for pastes and inks which could be cured or sintered at lower temperatures.

Though no surface treatments are required for the substrate during screen printing, the printed trace characteristics (eg. minimum width/spacing realisable, final

thickness, surface quality) are influenced by a myriad of factors such as the mesh count, mesh thickness, emulsion layer thickness, the paste property [60] and its interaction with the mesh and substrate during printing [60]. For instance, the printed thickness (*t*) obtained after curing can be estimated using equation (2.2)[61]:

$$t = [(Mesh\ thickness \times Opening\ ratio) + Emulsion\ thickness] \\ x\ (Wet\ to\ dry\ ratio) \quad (2.2)$$

With respect to equation (2.2), the actual thickness obtained is further dependent on the mesh-paste interaction, and the paste adhesion onto the substrate. This could give rise to residual paste on the mesh after printing, which affects the printed thickness on the substrate. The mesh-paste interaction also affects the levelling of the paste, and the resulting surface roughness of the printed traces [60].

In general, the viscosity of pastes and inks (inkjet printing) affects the spreading and slumping of the printed features. This in turn influences the printed line width and line cross-sectional profile [62]. As such a paste with a higher viscosity would be preferable for fine line printing since this would result in reduced paste spread. The minimum printed line width attainable would be affected by the screen mesh count along with the paste spread. In screen printing traces onto fabrics, Pourdeyhimi *et al*. [58] suggested that the surface tension of the paste used (relative to surface of nonwoven) would have a significant effect on the printed lines since this affects the dispersion of the ink into the substrates.

2.1.5 Aerosol Deposition

Aerosol deposition (AD) [63] may be another viable technology for depositing conductive traces onto fabrics with the main advantage of using this process being that the deposition is done at room temperature. Although the mechanism to date has not been fully clarified [63], the deposition behavior has been much investigated [63, 64]. As illustrated in Figure 2.2, this process involves the acceleration of metallic particles (sub-micron to micron range) by a gas flow. Upon impact onto a substrate, the particles undergo deformation and a portion of the particle kinetic energy is converted into a bonding energy between the particle and the substrate [63]. Base anchor layers are then formed. Akedo *et al*. [63] have

demonstrated that a dense and hard layer could be formed on a polycarbonate substrate at room temperature using ceramic particles.

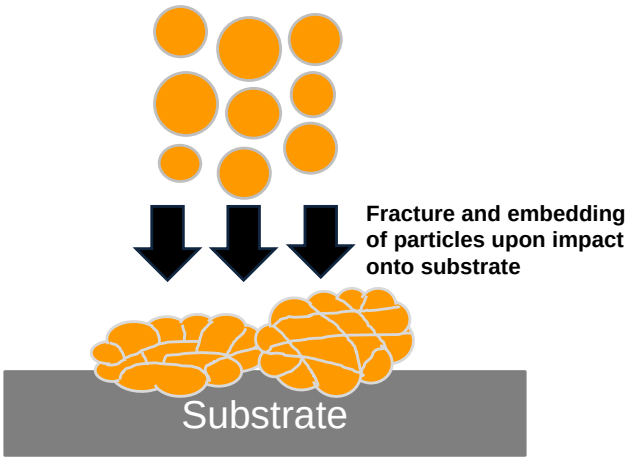

Figure 2.2 Diagram showing the aerosol deposition process, adapted from Akedo *et al.* [63]

In addition, Imanaka *et al*. [64] have used the AD process to realise multi-layer ceramic capacitors in a RF module. AD was selected in this application as the deposition temperature was lower than the temperature which could be withstood by the epoxy resin [64]. Furthermore a thick ceramic film is realisable using AD, where the high dielectric constant of the ceramic film aids in the miniaturisation of the capacitor footprint in the module.

The particle-substrate interaction in AD is specific to the particle and substrate considered. From literature, work has been done on ceramic films [63, 64], metal-dielectric composites [65] and dielectric films [66]. Lim *et al*. [67] used AD to investigate the deposition of a copper film on glass substrates, but observed that the copper film delaminated from the glass surface during a tape test. The results indicate the lack of a base anchor layer present for the copper film formed [67]. As copper particles are relatively soft in comparison with ceramic particles, the results suggest that considering a different particle size [67] or adjusting the velocity speed of the metal particles may aid in strengthening the impact between particle-substrate.

2.2 Inkjet Printing for Fine Pitch Resolution

From literature, Muller *et al*. [19] achieved fine line printing through screen printing onto low temperature co-fired ceramic (LTCC) substrates, where screens with a high mesh count and finer wire diameter were used. On LTCC, fabrication capabilities of 50/50 µm were achievable [19, 20]. Baras *et al*. [20] also employed screen printing to realise passive components on LTCC in the millimetre-wave regime (up to 67 GHz). The performance for a particular circuit design was found to be repeatable across different runs, with 10 samples considered in each run. This suggests that there is a good repeatability of the circuit dimensions. Furthermore, the conductor thickness obtained from screen-printing is well over the skin-depth at millimetre wave frequencies, which minimises the conductor loss due to the skin-depth effect at those frequencies. Nevertheless, Baras [68] noted that the edges of printed lines at any resolution were rather rough due to the rheology of the printing paste used [68], and the edge roughness was on the order of some 2-3 µm. Apart from that, the surface roughness of the substrate may also influence the surface roughness of the printed traces when considering substrates with non-negligible surface roughness.

Unlike screen-printing, inkjet printing does not require any patterned screen masks. Being a direct write technique, traces could be directly patterned without the need masks or photolithography steps unlike in the printed wiring board (PWB) industry [69]. In addition, highly dense and finer pitch metal traces targeted for future highly integrated electronic devices can possibly be achieved using inkjet printing, where it is expected that trace width dimensions would be decreased from the current 35 µm to less than 20 µm in 2010 [70].

From literature, fine pitch has been achieved with inkjet printing on smooth surfaces [71-73]. Azucena *et al.* [71] used inkjet printing to obtain a coplanar transmission line with transition dimensions of 100/100 µm on glass. Shaker *et al*. [72] demonstrated a resolution of 50/65 µm for a meander line which was inkjet printed on liquid crystal polymer (LCP). In addition Takano *et al*. [73] has demonstrated 5 µm and 40 µm wide lines in the printing of terahertz metamaterials on a high resistivity silicon substrate. These structures were printed using a super-

fine inkjet printer developed Murata *et al*. [17, 74]. These conventional packaging substrates, while possessing smooth surfaces, yield only limited degrees of flexibility and user comfort if considered for body sensors. Therein lies a potential to exploit inkjet printing to realise printed fine line traces on fabrics - achieving higher density integration on a conformal "substrate", along with the weight reduction of sensors by replacing bulky wires with conductive traces for data transfer.

In terms of the high frequency performance of printed interconnects, a few authors [71, 75] have measured the insertion loss of coplanar transmission lines which were inkjet-printed onto glass substrates. Azucena *et al*. [71] reported higher insertion losses of 3-4 times for the inkjet printed transmission lines compared to electroplated copper transmission lines, which could be attributed to the lower DC conductivity of the printed lines after thermal sintering [71]. From a system perspective, Xie *et al*. [76] demonstrated a wearable bio-patch module comprising of a system-on-chip (SoC) die, where the interconnects were realised using inkjet printing. The inkjet printed interconnects were tested to 10 MHz to ascertain that digital signals could be transmitted, and the overall size of the module was found to be comparable with commercial products [76].

Unlike commonly used substrates such as FR4, glass or polyimide, fabrics have not been extensively studied, particularly in the area of inkjet printing. While Karaguzel *et al*. [77] has evaluated inkjet printing onto fabric, the deposition involved a non-conductive test fluid (mixture of glycerol, water, 4 % red acid dye). One of the fabrics used in their work was Tyvek, which is a high density polyethylene with a high surface volume fraction SVF (50 %) nonwoven fabric. The fibres in Tyvek are 0.5–10 μm, and the nondirectional fibers (plexifilaments) are first spun and then bonded together by heat and pressure without binders. The Tyvek substrate used by Karaguzel *et al*. [77] was surface treated on one side to facilitate inkjet printing.

Inkjet printing onto fabrics necessitates the use of a conductive ink which can be cured at low temperatures. Typically, fabrics can withstand temperatures up to around 200 °C [78]. For the case of the Tyvek fabric, the material starts to soften at

118 °C and melts at 135 °C. At present, there are not many commercial conductive pastes or inks which can be sintered at low temperatures. Table 2.1 shows a list of such possible pastes and inks which could be considered for application onto fabrics. With the exception of Intrinsiq's copper-based ink which is cured via photonic curing or infrared (IR) laser, most of the conductive inks and paste can be cured/sintered within a range of 100-180 °C. Several of the products in Table 2.1 (from Intrinsiq, Nanomas Technologies, Harima Chemicals, Kunshan Hisense) are formulated using nanoparticles with particle sizes ranging from 3-45 nm. This is due to the size dependent melting point of nanoparticles. Small particle sizes (nm) significantly reduces the melting point of nanoparticles from the bulk melting point, thereby allowing for very low processing temperature for sintering nanoparticles into conducting films.

From Table 2.1, it can also be observed that inkjet inks typically possess higher conductivities compared to screen printed pastes, though the trace thickness obtainable for a single printed layer are much smaller. Whereas the silver inks typically comprise of solvents and silver nanoparticles, silver paste formulation (Figure 2.3) include organic and inorganic components [79].

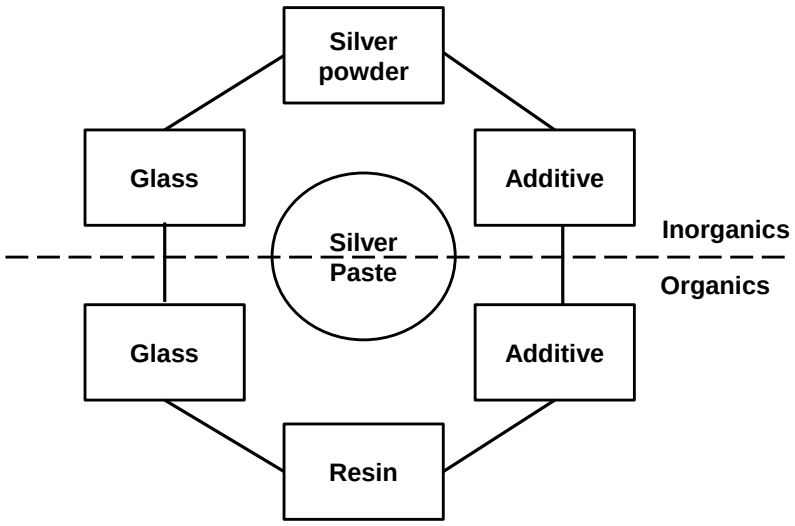

Figure 2.3 Typical composition of silver pastes, adapted from Zhang [79]

Table 2.1 Conductive pastes and inks with low temperature drying conditions

Company	Product Code	For use in	Average Conductivity (S/m)	Remarks
Creative Materials	125-13	Screen print & Picodot jetting	$2.5x10^6$	Fine line widths and spaces. Very resistant to flexing and creasing. Best properties obtained when curing at 170°C-180°C for several minutes. Can also be cured within a range of 50°C-150°C.
	124-29	Screen print & Picodot jetting	$8.3x10^5$	Very resistant to flexing and creasing. Best properties obtained when curing at 100°C for several minutes. Can also be cured within range of 50°C-150°C.
Dupont	5064H	Screen print	$4.4x10^6$	Drying Condition: 130°C (10-20 min).
	PV416		$2.5x10^5$	Fine line print capability. Drying Condition: 130°C-180°C (5-60 min).
	9169		$2.2x10^6$	Fine line print capability. Drying Condition: 120°C-170°C (5-30 min).
Intrinsiq	CP-002	Screen print	$4.8x10^6$	Copper-based paste. Drying Condition: 60°C for 15-30 min. Sintering Condition: IR laser at room temperature or Xenon flash lamp system (photonic curing).
	CI-002	Inkjet	$1.2x10^7$	Copper-based ink. Drying condition: 50°C-60°C (15-30 min) Sintering condition: IR laser at room temperature or Xenon flash lamp system (photonic curing).
Advanced Nano Products	DGP 40LT-15C	Inkjet	8.7×10^6	Curing temperature: 120°C-150 °C; Plastic films.
Harima Chemicals	NPS-JL	Inkjet	2×10^7	Curing condition: 120°C-150°C (60 min); for low temperature substrates.
Kunshan Hisense	Jet-100	Inkjet	4×10^7	70°C-150°C (30 min); Paper, PET, PI, Silicon.
	Jet-200			100°C-150°C (30 min); Paper, PET, PI, Silicon.
	Jet-600C			100°C-150°C (30 min); PET, PI, Silicon.

Due to the higher conductivity obtainable, inkjet printing may be a viable technique for high frequency applications, since the trace thickness required at those frequencies is much less due to the skin effect phenomena and could be obtained by printing several layers. Beyond achieving printability, Smith *et al*. [22] introduced an equation to predict the printed line width based on the measured contact angle values, as shown in Figure 2.4.

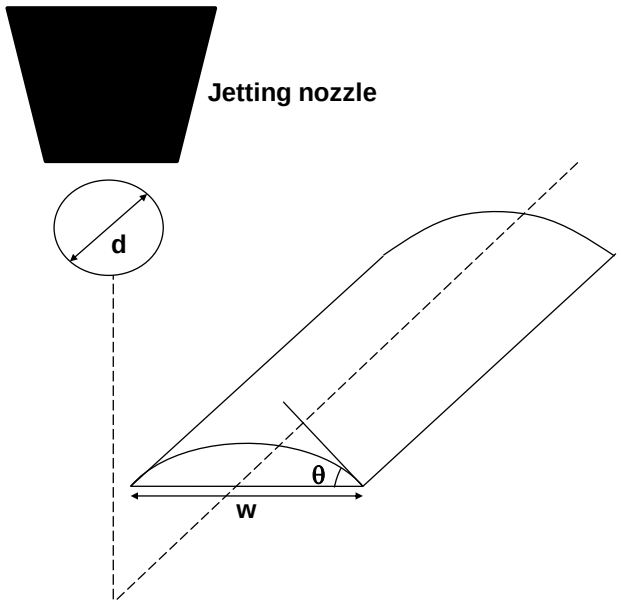

Figure 2.4 Diagram showing the relationship between final track width and contact angle, adapted from Smith *et al.* [22]

$$w^2 = \frac{\frac{\pi d^3}{6\Delta x}}{\frac{\theta}{4(\sin\theta)^2} - \frac{\cos\theta}{4\sin\theta}} \tag{2.3}$$

From equation (2.3), *w* represents the final track width, θ is the equilibrium contact angle in radians, d is the dot diameter and Δx is the dot spacing. The assumption made was that the contact angle of the ink on the substrate is low, such that the drop becomes a cylindrical cap shape. However, it was noted that this equation was verified on smooth substrates possessing negligible surface roughness and porosity [22]. For substrates with non-negligible surface roughness such as fabrics, it is unclear if equation (2.3) would still be valid, i.e. yield an accurate estimation of the printed line width. Further investigations would be needed to determine the validity of the equation for substrates with non-negligible surface roughness.

2.2.1 Surface Modifications

This section discusses surface modification techniques used in literature. These modifications are used to improve the substrate surface to facilitate good printability when overprinting with silver inks/pastes.

(a) Planarisation Layers

Challenges exist in using inkjet printing to define conductive traces or electronic circuitry onto textiles. This is since fabrics are porous materials with surface roughness. The effect of substrate roughness is particularly significant due to the slight metal thickness achievable for a single inkjet printed layer (typically < 1 µm). There is little literature addressing this issue in inkjet printing, as most researchers consider substrates with relatively smooth surfaces for the printing [22, 80-84]. To overcome the surface roughness, a planarisation layer(s) would be required prior to the overprinting of silver traces by inkjet printing. This type of surface modification is further illustrated in Figure 2.5.

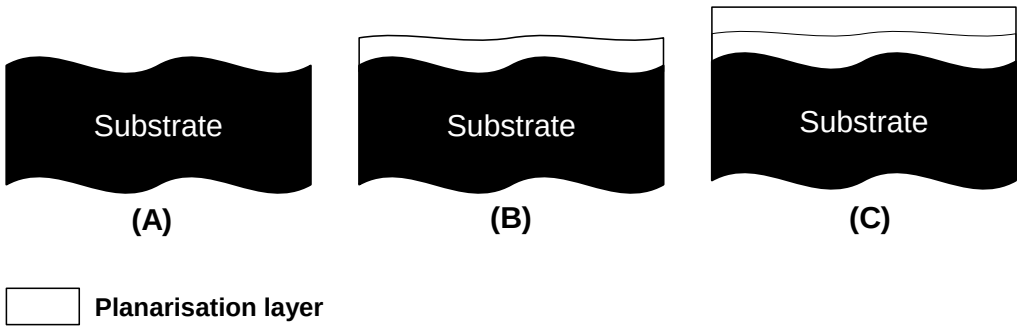

Figure 2.5 Diagram showing the use of planarisation layer to overcome the surface roughness of the substrate (A) No planarisation layer (B) One layer of planarisation (C) Two layers of planarisation

Denneulin *et al*. [27] applied an intermediate layer on paper substrates via inkjet printing, where the layer was realised using UV curing. In particular, an UV-curable ink was developed to yield surface properties such as smoothness, absorption capacity and surface energy which are homogeneous for most of the substrates considered. Conductive patterns were then overprinted using a carbon nanotube (CNT) ink which was also an in-house formulation [27].

Li *et al*. [26] also introduced an intermediate layer on textiles, prior to overprinting with silver inks. Specifically the planarisation layer was applied via screen printing onto a polyester/cotton textile, following which the layer was UV-cured. Due to an insufficient wettability of the silver ink onto the planarisation layer, 2-3 layers of silver ink were overprinted [85]. Similar to Denneulin *et al*. [27], the UV-curable insulator ink used by Li *et al.* [26] could be tailored to match the surface energy of the silver ink, such that de-wetting would not occur [85].

Similarly Hakola *et al*. [28] over-printed silver onto an UV-curable insulator layer (deposited via inkjet printing), where they ensured that the insulator layer was properly cured prior to printing the silver ink. From the specification provided it was noted that the equipment used for UV curing [86] comes from a major industrial manufacturer.

However Yakoub *et al*. [87] encountered de-wetting issues in overprinting silver onto a UV-cured insulator layer deposited via inkjet printing. Both silver and dielectric inks were commercial formulations. It was noted that the de-wetting observed could be due to curing equipment used for the curing (Fe-doped Hg lamp from 200-500 nm) [88]. This is since ink manufacturers typically recommend a specific light source for curing the inks, according to the ink formulations [89, 90]. To resolve the de-wetting issue to obtain printability, Yakoub *et al*. subjected the samples to plasma treatment followed by a second round of UV curing [87] to tune the substrate surface for improved wettability with silver ink used.

(b) Coatings for Improved Line Resolution

Andersson *et al*. [91] evaluated the application of coatings as a form of surface treatment prior to inkjet printing, though the pre-coatings [92] which were used were targeted for enhanced imaging in graphics (e.g. photography and paintings) rather than for the printing of conductive inks. In their work [91], the main objective was to achieve improved print quality with better line definition compared to uncoated substrates. Prior to inkjet printing, the pre-coatings were applied onto polyimide and polyethene (low temperature substrates). The study concluded that the coatings improved the print quality significantly. For instance a 200 µm wide trace printed on polyethene substrates resulted in line widths which

were 1.5-2 times the designed trace, as compared to around 4.5 times on the uncoated substrate [91].

Lin *et al*. [93] also sought to improve the resolution of inkjet printed traces through the deposition of a hydrophobic layer onto a hydrophilic substrate (polyimide) using microcontact printing. Such 'surface energy patterning' enhances the control of the ink flow and spread, which in turn improves the printed resolution. Inkjet printed patterns with gap dimensions of 15 μm could be obtained from applying this technique. The results from these studies suggest that hydrophobic coatings could be useful in obtaining finer printed line widths/gaps.

(c) UV/Ozone Treatment for Tuning Wettability of Surfaces

The use of UV/ozone was originally proposed for cleaning sample surfaces [94]. However, several authors have used it to alter the surface tension of samples such that the surfaces are more hydrophilic, with the extent of hydrophilicity dependent on the UV/ozone exposure time [95-98]. For instance Ma *et al*. [98] used UV-ozone treatment to tune the wettability in polydimethylsiloxane-based (PDMS-based) microfluidic devices. In particular, it was observed that UV–ozone treatment uses less energy than oxygen plasma during the surface modification process of PDMS [99], resulting in a slower change in the water contact angle of the surface [100]. As such UV-ozone treatment was used to tune the wettability of PDMS [98].

(d) Plasma Treatment for Tuning Wettability of Surfaces

The use of plasma treatment was observed to affect only the top layer of textiles (<100 nm) [101], resulting in changes to the adhesion properties. Yuen *et al*. [102] combined both plasma treatment with pre-coating for digital inkjet printed cotton fabrics. Their main objective was to investigate the effect of plasma treatment on a cotton fabric prior to inkjet printing. Oxygen was used as the plasma medium for the inkjet printing. Plasma treated cotton samples with and without the application of a pre-coat were evaluated, prior to inkjet printing. SEM images reveal that plasma treatment aided the filling up of the fibre cracks when the pre-coat is applied, yielding a more uniform film on the fabric surface. Overall, the use of

plasma treatment improves the adhesion of the dye (in digital inkjet printing) with the pre-coat.

Zander *et al*. [103] studied the effect of plasma and UV ozone treatment on polyethylene (PE) polymer. The plasma treatment involved the injection of helium and oxygen at atmospheric pressure (13 % of oxygen in plasma gas mixture. Compared to UV ozone treatment, plasma treatment was a more efficient technique to modify the PE surfaces due to the shorter treatment times (few seconds compared to several minutes using UV ozone method). In both methods, the treated films were stable for 21-30 days. Nevertheless, modifying the substrate surface using plasma has to be determined by experimental trials, which could take time.

2.2.2 Post Processing of Printed Traces after Deposition

Though inkjet printing is a direct write technique, one common feature it shares with screen printing is that both require curing or sintering after deposition to obtain functionalisation of the printed patterns. In screen-printing, the firing temperature of the ink is typically around 850 °C for common ceramic-metal inks [104], which restrict the use of low temperature and low cost substrates for applications such as RFIDs and sensors. Polymer-based thick film inks have lower processing temperatures of 120 °C, but this property is at a trade-off with the electrical performance [104]. There has been increasing interest to extend the range of substrates to include low temperature substrates, targeted for wider applications such as wearable electronics.

In post-processing the pastes and inks, there has been a big motivation towards adopting laser sintering, which localises heating to the materials to be sintered (local processing). This stimulates densification [62] of the nano-particles while avoiding the degradation of the substrate. A main advantage of such a local processing is the possibility of inducing chemical reactions or heating a deposited material beyond the temperature which is possible with conventional heating, since conventional heating would be limited by the heat tolerance of the substrate, which can be < 200 °C for fabrics [62].

Researchers [69, 105-107] have investigated the use of laser sintering on conventional inks and pastes which have typically been processed at temperatures above 800 °C. In 2007, Kinzel *et al*. [105] investigated the laser sintering process in detail for a silver based thick film ink with a firing temperature of 850 °C. From the micrographs of laser sintered traces, low laser powers and high scanning speeds were found to be insufficient to sinter the ink (a portion of the trace was removed during the cleaning step). On the other hand, the use of higher laser powers and low scan speeds result in the melting of the ink which then group together, forming voids in the trace. In addition, damage to the substrate was observed [105]. As it was challenging to determine the temperature inside the ink and the substrate in situ, Kinzel *et al*. [105] used numerical modelling to compute for the temperature profile. The simulation results show that temperatures above the damage level of the substrate can be confined to within a layer of a few microns.

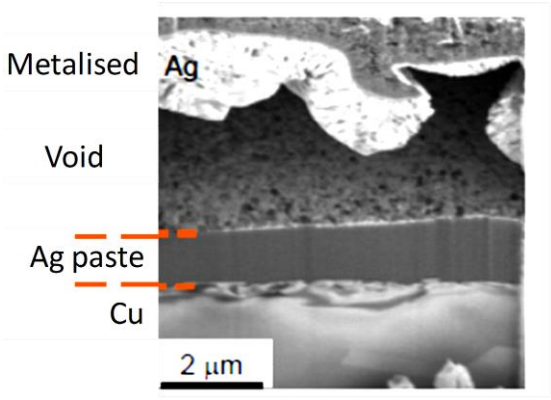

Figure 2.6 Cross-section from continuous wave laser sintering [69] © 2008 IEEE

Laakso *et al*. [106] studied laser sintering on silver nanoparticle inks using a fibre coupled diode laser at 940 nm at a continuous wave mode. In their work the fibre laser was chosen (940 nm wavelength) so that the light was not highly absorbed into the substrate (i.e. to obtain localised heating). The substrate used in this case was polyimide. While the two silver inks tested were both nanoparticle-based, different beam sizes and laser powers were required during the sintering process. This implies that a customisation of the laser sintering parameters may be required for inks of different formulations.

In addition, Laakso *et al*. [106] also faced other issues in the use of laser sintering. For instance one of the silver nanoparticle inks considered required significant beam defocusing to minimise damage to the sintered ink. Beam defocusing refers to the heating of the same area for a longer period but at a reduced intensity. One drawback of using heavy defocusing is that the surrounding substrate areas may be affected by the laser, which no longer results in localised heating. Another issue encountered by Laakso *et al.* [106] in laser sintering was the thickness variation of the inkjet printed trace, in which areas with extremely thin printed layers (partially transparent) were only partially sintered [106]. This phenomenon could be attributed to the beam passing through the thin, almost transparent trace, and could be alleviated by using multiple sintering passes, or drying in the oven for the recommended duration by the ink manufacturer. Conversely, the authors suggested that thick prints may be partially sintered if the thermal penetration depth is much less than the printed trace thickness. This hypothesis was supported by the work of Maekawa *et al*. [69, 107], who observed the presence of a gap between the sintered trace and the silver paste as shown in Figure 2.6. This gap is attributed to the gas generated by the evaporation of the solvents which are trapped beneath the metallised surface [69]. Due to the wavelength of the yttrium aluminium garnet (YAG) laser, there is little absorption into the paste once metallisation has occurred on the paste surface with the remaining laser energy being reflected. As such when the paste is too thick, it is difficult for heat to conduct through the entire depth of the trace [107].

Overall, the temperature required to cure or sinter the paste/ink is a function of the melting temperature of the metal. For instance, the melting temperature of silver is around 960 °C, and the sintering temperature is around 800 °C. While it is possible to lower the curing or sintering temperature on substrates, this would typically be at the expense of the final conductivity value obtained [108]. The recent work done by Laakso *et al.* [106] and Maekawa *et al.* [69] indicates an increasing interest to apply laser sintering onto commercial nanoparticle inks which have typically been sintered through furnace sintering (or thermal curing), such that low temperature substrates can be used. However, the laser parameters to be used are dependent on the substrate considered and the targeted application. To obtain the desired sintered

profile require the experimentation and optimisation of various laser parameters.

Apart from the use of laser sintering for sintering silver inks on low temperature substrates (eg. paper, plastic films), Novacentrix introduced a photonic curing method involving intense pulsed light [108, 109] to heat the conductive inks without damaging the low temperature substrates. This technique uses a pulsed photonic source to irradiate the particles which could momentarily heat the particles to temperatures [108, 109] high enough to enable sintering. Sears *et al.* [110] investigated the photonic curing process on silver nanoparticles and compared the measured resistance values obtained from other curing techniques (furnace and laser sintering). The trace resistance from photonic curing was observed to be significantly higher compared to furnace and laser sintering [110]. In addition, this curing technique has been limited to a few inks (Metalon®, Intrisiq), and its effect on the post-cured resistivity on other inks have yet to be investigated. To optimise the curing conditions for different materials, parameters such as the cure area, surface area energy density and pulse length of the discharge would have to be considered. While photonic curing is a relatively fast process, the use of specialised equipment for such curing [109] may restrict the widespread usage of this technique, since such equipment are not readily available and require significant financial investments.

2.3 Conclusions and Research Gaps

This chapter has described a review of the techniques which are commonly used to realise conductive traces on fabrics. In particular, techniques for realising fine pitch interconnects are identified. The main points drawn from literature are:

- The use of conductive threads, conductive fabric and tapes were not considered to be suitable for high frequency applications due to the minimum dimensions obtainable (i.e. conductive threads), where fine pitch are required for high frequency applications. For conductive fabrics, the metal plating thickness of several hundred nanometres is not sufficient to alleviate the skin depth effect at higher frequencies, which results in significant losses.

- The potential techniques for realising fine pitch interconnects for high frequency applications include screen printing, aerosol printing and inkjet printing. The advantage of utilising screen printing is that no surface modifications are required to obtain continuous traces on the substrates. Thus screen printing is ideal for use in the dielectric characterisation of fabrics in Chapter 4, where the analysis can be simplified without the consideration of an intermediate layer in the characterisation process. In addition, due to the thicker traces obtainable (> 5 μm) from screen printing (relative to inkjet printing), the electromagnetic modelling of the RF performance of interconnects (Chapter 7) is facilitated. This is because the computational requirements for solving large aspect ratio models (e.g. structures with small trace thickness relative to the substrate thickness) in three-dimensional (3D) simulators are significantly higher.

- The feasibility of using inkjet printing to obtain fine pitch interconnects for high frequency applications have been discussed. From literature, there has been little work reported on realising inkjet printed traces on fabrics, and this would be further investigated in this thesis. Specifically as fabrics possess inherent surface roughness, investigations would be performed to alleviate the surface roughness through surface modification techniques. Another research gap pertains to the effect of surface roughness on the printed line widths, since the equation proposed by Smith *et al*. [22] has only been validated for traces printed on smooth substrates. These investigations are performed in Chapter 5 of this thesis. Obtaining a smooth planarisation layer using appropriate surface modification techniques facilitates the overprinting of silver ink using inkjet printing. This is with the goal of obtaining clear linear traces which are electrically conductive, which is essential for wearable electronics applications. This work is further investigated in Chapter 6 of this thesis.

Chapter 3. Characterisation of Material Properties and Electrical Performance of Interconnects

This chapter provides an overview of techniques used in literature to characterise the material properties and electrical performance of interconnects. This includes the characterisation of the dielectric properties (dielectric constant, loss tangent) of substrates, and the wettability of surfaces. A review is also carried out on the high frequency characterisation of interconnects and the effect of surface roughness on the high frequency performance.

3.1 Characterisation of Substrate Dielectric Properties

In RF/microwave and high speed applications, it is crucial to obtain accurate values of the substrate dielectric property at the frequency of interest. For instance, the design of controlled impedance structures for high speed applications necessitates knowledge of the dielectric properties of possible materials in order to select the material which meets the required specifications. As shown in Figure 3.1, the dielectric property is a significant factor influencing signal integrity since it determines the width and length of transmission lines at a particular frequency of interest [111]. Variations in the impedance values arising from changes in the dielectric constant would introduce undesired impedance mismatches and increase the loss of the board. For RF applications [33, 112], an accurate knowledge of the dielectric properties is essential to design components such as antennas and filters (in terms of the required dimensions), as well as to miniaturise the component footprint and minimise their loss.

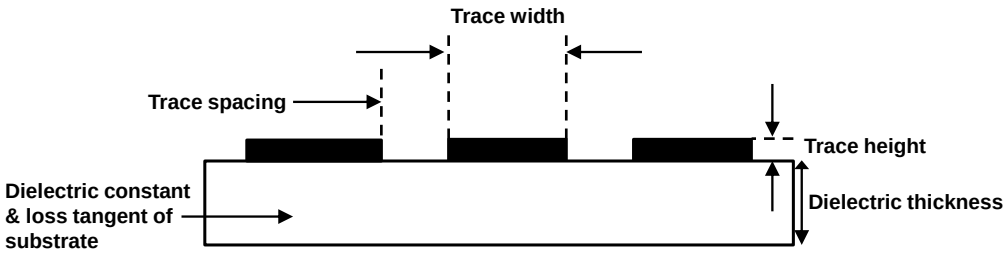

Figure 3.1 Diagram showing the parameters which have to be considered in RF and high speed applications

As fabrics are not typically used for high frequency applications (gigahertz range), little information is available from the manufacturers on the dielectric properties in that frequency domain. This is in contrast to typical laminates used for high frequency applications [113], which are formulated to yield low losses along with a range of dielectric constants for various design considerations. As such this necessitates a need for the dielectric properties to be characterised to the gigahertz range.

From literature there exist a myriad of techniques for extracting the dielectric properties of materials ranging from low loss to lossy. The techniques available can be generally classified under two broad categories - discrete (frequency) or broadband [114]. The discrete frequency techniques involve resonant techniques which yield values at a few resonant modes [115], while the broadband techniques involve sending electromagnetic waves through the material under test, and allow frequency values to be swept over a certain band. Figure 3.2 provides more information on the frequency range covered by the various techniques. Generally, resonant techniques are useful for measuring low loss materials, while transmission line methods are useful for broadband measurements, though they do not have sufficient sensitivity to measure very low loss samples due to the significant effect of metal losses [114]. Baker-Jarvis *et al*. [114] have also classified the resonant and transmission line methods according to the material type, the ease of sample preparation and the relative accuracy of the method [114].

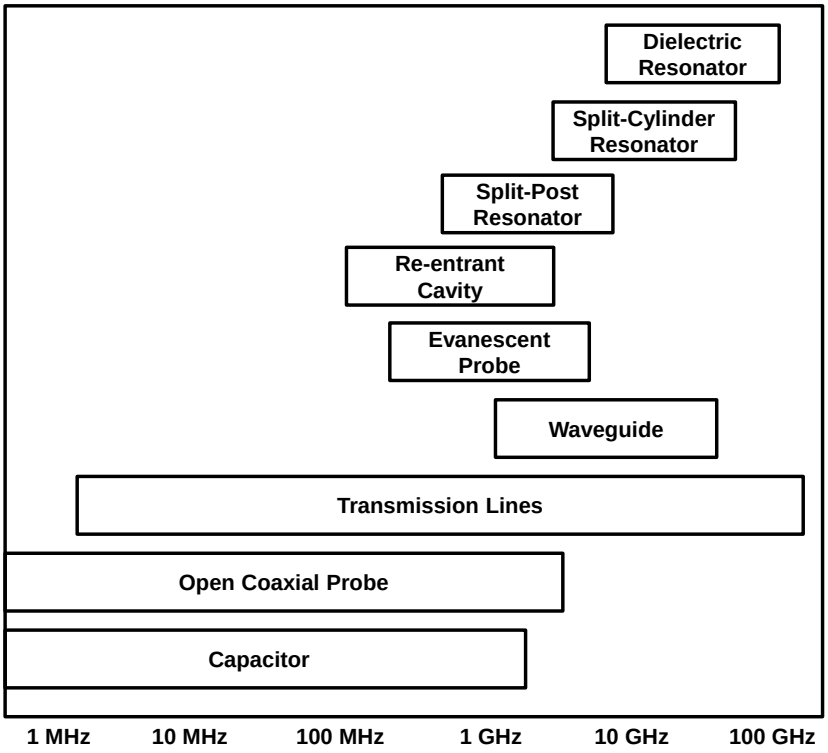

Figure 3.2 Frequency range covered by various dielectric characterisation techniques, adapted from Baker-Jarvis *et al.* [114]

However challenges arise in the dielectric characterisation of fabrics. Firstly, fabrics are flexible and compressible which along with fabrication variations could result in geometrical variations [33] of the test structures. Furthermore, transitions such as that from coaxial probe to transmission lines can no longer be assumed to be identical [114]. For instance Cottet *et al*. [12] used copper fibres incorporated into fabrics to realise transmission lines for measurements. However they observed large variations for the permittivity values, due to the geometrical inaccuracies of the transmission line structures realised by the copper fibres. Another contributing factor for the result variations arises from the non-repeatable coaxial-transmission line transitions at both ends of the DUT. Lee *et al*. [116] attempted to minimise the errors introduced by these transition mismatches and the connector repeatability through repeating the line measurements and using the results with the smallest connection repeatability. The advantage of this technique lies in that broadband dielectric measurements can be made utilising short transmission lines [116]. More importantly, no prior knowledge of the substrate dielectric constant is required, and it is not necessary to use transmission lines with characteristic impedances of 50Ω. This versatility enables substrates with unknown dielectric constant values to be

measured. However, one drawback of this technique is that the process of extracting for the dielectric constant can be time consuming, since each measurement is repeated ten times. Following this the measured data with the minimum error cost would be used to extract for the effective dielectric constant of the substrate [116].

Declercq *et al*. [33] extended the work of Lee *et al.* [116] by combining the two-line approach with a matrix pencil technique to reduce perturbations observed in the extracted dielectric properties. The matrix pencil method is applied as an averaging technique when combined with the two-line method to extract for the dielectric properties of fabrics. Declercq *et al*. [33] observed that the matrix pencil method yielded a poor estimation of the attenuation constant used for extracting the loss tangent of certain fabrics, which was attributed to the non-ideal test structure [33]. In addition, issues arising from the non-repeatable connector-to-line transition and the geometrical tolerances of the lines were noted to give rise to inaccuracies of the calculated permittivity values for some of the fabrics tested [33].

Researchers have also utilised waveguide and cavity techniques to measure the dielectric properties of fabrics at the lower gigahertz range. For instance, Zhu *et al*. [117] extracted the dielectric properties of fabric samples using a rectangular waveguide system (2.6-3.95 GHz) which consists of two identical waveguide cavities with transition parts, a shorting plate and a waveguide sample holder. However Lee *et al.* [118] in using a similar technique observed fluctuations in their results, due to the presence of air gaps for the carbon nanotube (CNT) film measured, which resulted in numerical inaccuracy during the extraction process. Kennedy *et al*. [119] have also conducted measurements on fabric between 0.82 – 4.0 GHz using a thin sheet dielectric tester. The tester employs a rectangular cavity to measure the in-plane component of dielectric constant (ε_r) and loss tangent of thin samples (< 3 mm) with ε_r < 10. The drawbacks of such measurement techniques lie in that waveguide systems are costly, and the waveguide dimensions limit the frequency range over which the dielectric properties could be extracted.

From literature, there have also been groups that make use of the ring resonator or T-resonator to measure the dielectric properties of substrates [112, 120, 121]

including paper [112]. A limitation of using the resonator technique is that the dielectric properties can only be extracted at discrete frequencies, corresponding to the resonant peaks. Figure 3.3 shows a typical ring resonator structure:

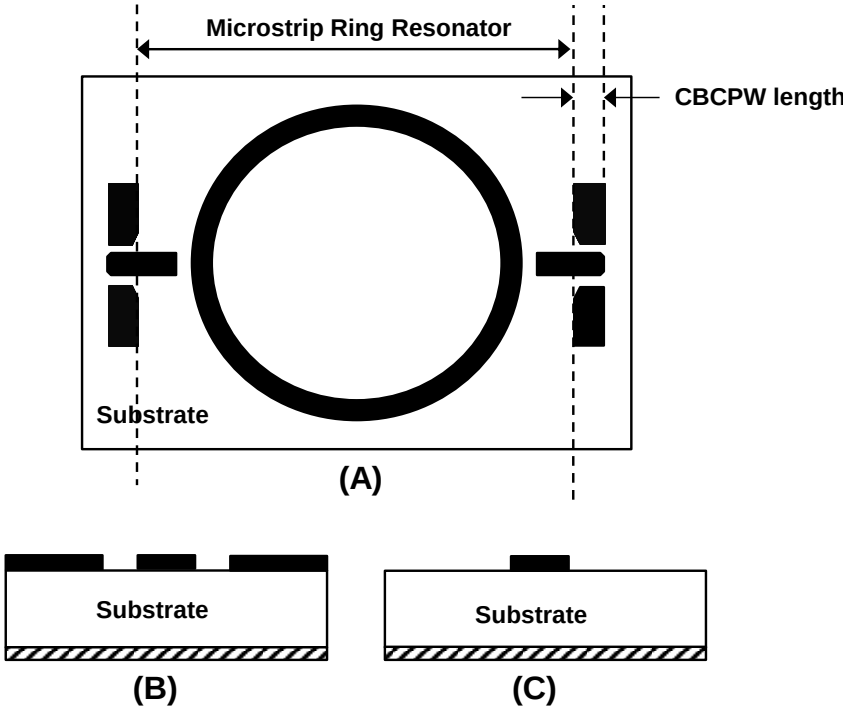

Figure 3.3 (A) Top view of overall resonator structure (B) Cross-section of CBCPW length section (C) Cross-section of ring resonator (microstrip configuration)

The structure is designed to produce periodic resonant peaks in the *S*-parameter (S_{21}) results during measurements, and analytical equations are used to determine the dielectric constant and loss tangent. While the dielectric constant can be extracted based on the resonant peaks and the ring dimensions [120], the extraction of the loss tangent (dielectric loss) is more challenging. To obtain the dielectric loss, the conductor and radiation losses need to be subtracted from the total loss at each resonant peak, both of which are based on analytical formulae. Thomson *et al*. [120] highlighted issues in extracting for the loss tangent from the calculated conductor and radiation losses up to 110 GHz based on the current analytical formulae available. This is since the formulae [122, 123] were not considered beyond tens of gigahertz. As such, in their extraction of the conductor loss, Thomson *et al* used a formula which yielded reasonable values for the extracted loss tangent [120]. Similarly the formula used to extract the radiation loss was one

which did not diverge beyond the error tolerance set within the measured frequency band from 30-110 GHz.

With regards to the extraction of the conductor loss, it is noted that resonator structures realised by inkjet printing would not be suitable for use. This is due to the small thickness of the printed structures, following which the significant conductor losses from the metal thickness would affect the 3-dB bandwidth and the extraction accuracy of the loss tangent values [112]. While this technique could be used to extract for both low loss [120] and medium loss [112] substrates, the resonator structures are typically based on microstrip and/or conductor backed coplanar waveguide (CBCPW) configurations as shown in Figure 3.3. The realisation of such configurations would require two metal layers and vias to connect the ground in both layers.

A summary of the possible techniques which could be used for the dielectric characterisation of fabric materials is shown in Table 3.1.

Table 3.1 Dielectric Characterisation Techniques for Fabrics

Researchers	Technique Used	What it Involves	Parameter (s) Extracted	Advantages	Disadvantages
Cottet *et al*. [12]	Parallel plate capacitors	Varying capacitor plate sizes and plate distances	Effective dielectric constant	Simple	• Dielectric constant extracted only at DC.
	Transmission line structures	CPW lines of varying lengths realised using fabrics with copper fibres		Standard transmission line designs	• Geometrical inconsistency of the CPW dimensions realised with copper fibres, which results in the excitation of parasitic modes and limits the frequency of extraction.
Zhu *et al.* [117] Kennedy *et al*. [119]	Rectangular waveguide	Waveguide Cavities	Dielectric constant , Loss tangent	Precise	• Limited frequency range of extraction.
Thomson *et al*. [120] Yang *et al*. [112]	Ring resonator, T-resonator	Resonator with resonant points at multiples of $\lambda/2$.		No need for special test fixtures, as the test structures are printed onto the substrate.	• Extraction at discrete frequency points. • Current analytical formulae for extracting conductor and radiation losses were not formulated for frequencies beyond tens of gigahertz.
Lee *et al*. [116]	Transmission line structures	Two microstrip lines of varying lengths; evaluation of ABCD matrices.	Effective dielectric constant	Knowledge of substrate dielectric constant is not required as the line impedance can be non-50Ω.	• Inaccuracies arising from non-repeatable connector-to-transmission line transitions. • Time consuming; the measurements for each sample were repeated 10 times to obtain the measured data with the minimum calculated error cost.

3.2 Electrical Characterisation of Printed Interconnects

In terms of electrical characterisation in the time domain, Wilson *et al*. [40] determined the characteristic impedance of screen printed CPW on non-woven textiles using time-domain reflectometry (TDR) measurements. Xie *et al*. [76] demonstrated an integrated bio-patch module, where inkjet printing was used to realise the interconnects. The printed interconnects were evaluated for the transmission of digital signals, which includes the system clock at 1 MHz and digitised bio-signal with a data rate of 150 kb/s. The results confirmed that the printed interconnects could be used for such applications [76].

(a) Low Frequency Range

Literature abounds on the electrical characterisation of printed traces in the low frequency regime (DC and megahertz range), which relates to the applications considered. Amongst them, printed electronics is one key area which many authors have reported on. For instance, Merilampi *et al*. [51] considered the electrical characteristics (DC resistivity) of screen printed traces for use in RFID tags [51, 54]. Additionally, Sanchez-Romaguera *et al*. [124] and Yang *et al*. [112] reported RFID tag modules on paper substrates, but using inkjet printed interconnects. In these cases, the RFID modules were considered for use in the frequency range of 860-960 MHz (UHF band). Others such as Jang *et al*. [35] demonstrated a light emitting diode (LED) board display using inkjet printed interconnects.

Printed traces have also been extensively used in silicon solar cells and hybrid circuits. As such there are also researchers who focused on the paste formulation to improve the DC performance of the printed traces for use in such applications. Park *et al*. [34] reported on a nanoparticle-based silver paste formulation, where the DC conductivity was investigated with varying sintering temperatures (250 °C -450 °C). Georgiou *et al*. [125] also investigated the formulation of silver inks for improving the printability and DC conductivity of the inkjet printed electrodes used in inverted organic photovoltaic devices.

To extract for the DC resistivity values, the use of four point probe measurements is usually considered in literature [18, 36, 38, 51]. A typical four point probe

measurement arrangement is shown in Figure 3.4. The key advantage of this technique lies in that the effect of the probe contact resistances is removed, which could be of a similar order of magnitude as the resistance of the test sample (R_{DUT}). The test sample in this context refers to the printed traces. With this set-up the current flowing through the voltage path is very small due to the high input impedance of the voltmeter. Thus the voltage drops across the wire resistance (R_w) and contact resistance (R_c) become negligible and the measured voltage is mainly attributed to the voltage drop across the DUT.

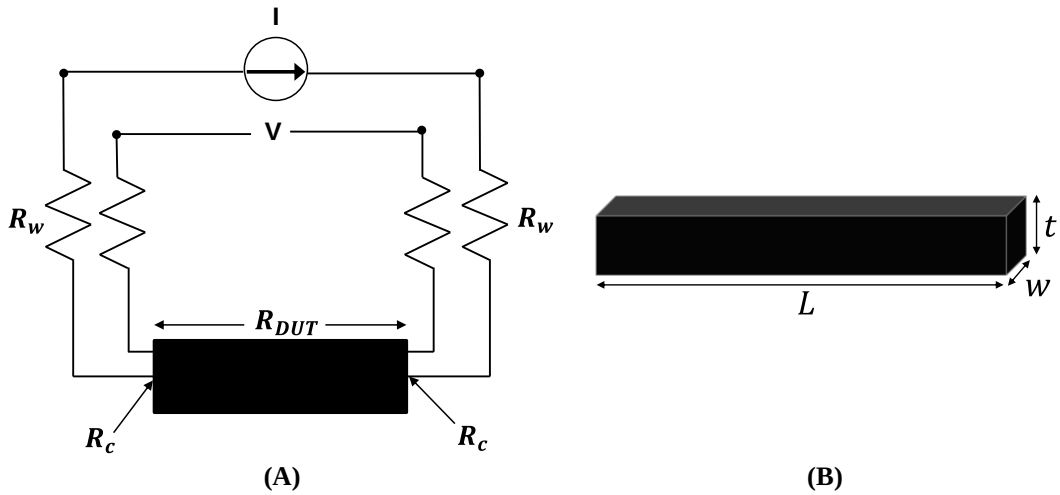

Figure 3.4 Concept of four-point probe resistance (A) Schematic showing the measurement for a printed trace (B) Details of the printed trace dimensions

With reference to Figure 3.4, the resistivity of the sample can be extracted using equation (3.1):

$$R_{DUT} = \frac{\rho L}{A} = \frac{\rho wt}{A} \tag{3.1}$$

where ρ is the resistivity of the printed trace, L refers to the length of the trace, w refers to the trace width and t is the trace thickness. The four point probe measurements can be performed using either a collinear probe arrangement (i.e. probes equi-distant apart) [126] or using four contacts placed at the periphery of the test sample [126]. For the case of the latter, a few assumptions are made during measurements. Firstly, it is assumed that the contacts are positioned at the circumference of the sample and that they are sufficiently small. In addition the thickness of the sample should be uniform and the sample surface is assumed to be continuous, without the presence of holes [126].

(b) RF and Microwave Frequencies

Apart from DC, some work on the RF characterisation of interconnects in the gigahertz range have been done [18, 71, 75]. For instance, Azucena *et al*. [71] have characterised the insertion loss of inkjet printed transmission lines (CPW) up to 6 GHz and 20 GHz respectively. Kim *et al*. [18] characterised the insertion loss of CPW lines up to 30 GHz, where the effect of increased sintering temperature on the loss was also investigated. As expected, higher sintering temperatures result in lower losses, which imply lower DC resistivity values. However little information were provided on whether the measured results were within an expected benchmark, as there were no simulation results presented on the expected insertion loss.

The RF design and simulation process typically use transmission lines with ideal characteristics (rectangular cross-section, negligible surface roughness) for simplification. However fabrication techniques yield transmission lines with non-ideal characteristics such as trapezoidal cross-section [127, 128] and non-negligible surface roughness [129], which affect the conductor losses at the higher gigahertz frequencies. Thus to accurately model the RF performance of transmission lines necessitate that these non-ideal effects be considered in the simulation process. Salmeron *et al*. [23] used a 2.5D simulator to model the RF performance of transmission lines up to 1.2 GHz and correlated it with measurements. At 1.2 GHz (i.e. lower gigahertz range), the non-ideal characteristics of the measured transmission line are not significant. In addition, the limitation of using a 2.5D simulator is that the solver uses surface meshing techniques. This approach does not adequately capture the conductor losses in the vertical axis, unlike a 3D simulator which is based on volume meshing techniques.

In terms of electrical characterisation, *S*-parameters were developed [130] to characterise high frequency structures (e.g. transmission lines). At high frequencies, the wavelengths of signals are much smaller than the physical length of the conductors, and power transmission can be considered in terms of travelling waves. *S*-parameters are defined in terms of voltage travelling waves [130], which are measurable using network analysers. The use of *S*-parameters is widespread across

both the RF measurement and design domains, since the parameters can be widely imported and used for simulation in RF design softwares (e.g. *Advanced Design System, CST, ANSYS HFSS*). Figure 3.5 shows a schematic illustrating the use of *S*-parameters for a two-port device.

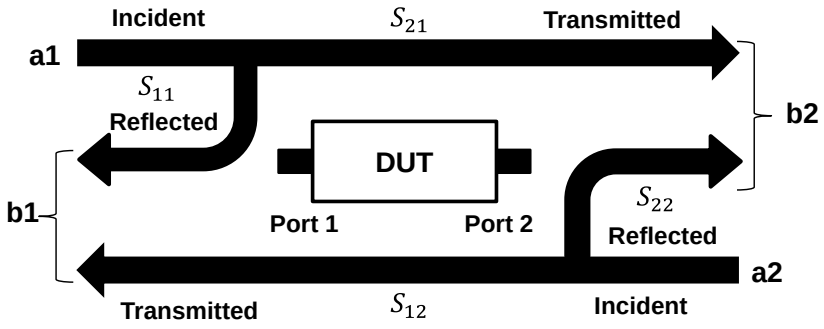

Figure 3.5 Schematic showing the use of *S*-parameters for a two-port device

An N-port device has N^2 S-parameters, which implies that a two-port device has four parameters. The first number following the "*S*" for S-parameters is the port where the signal emerges and the second number is the port where the signal is excited. Thus from Figure 3.5, S_{21} represents the signal coming out of port 2 relative to the RF signal excited at port 1, and is commonly referred to as the insertion loss. On the other hand, S_{11} represents a reflection measurement as the input and output ports are the same, and is usually referred to as the return loss. In Figure 3.5, the voltage travelling waves are represented by the incident terms (a1, a2) and output terms (b1, b2).

To date the transmission lines realised by printing (e.g. inkjet printing [18, 23, 71], aerosol printing [129, 131]) are CPW structures, which are planar. A typical CPW structure is shown in Figure 3.6, with the ground planes and inner conductor labelled. In Figure 3.6(A), the ground planes are connected together to minimise parasitic effects over high frequencies.

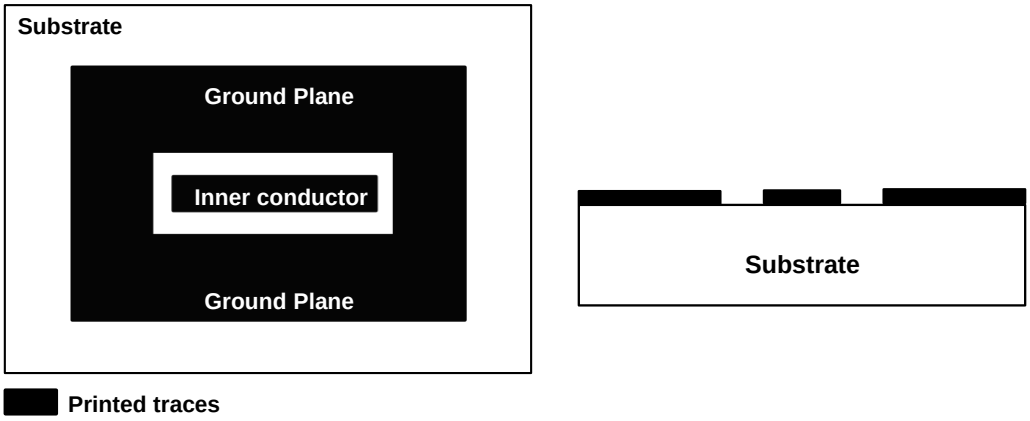

Figure 3.6 Diagram showing a CPW transmission line structure (A) Top view, with the ground planes connected (B) Cross-section view

At present technological limitations exist in fabricating multi-layer transmission line structures (e.g. microstrip, stripline) using inkjet printing or screen printing. This is because vias need to be fabricated to connect the ground plane layers together to avoid parasitic effects. The fabrication of vias may be possible through the use of different processes, but this may significantly increase the prototyping costs. For instance, Oh *et al*. [132] proposed the use of laser ablation (a non-conventional process) to form vias to connect multi-layer interconnects. On the other hand, Yang *et al*. [133] made use of insulator layers which could be dissolved by the organic solvents of the conductive inks to form vias. However such a consideration may limit the insulator materials which could be used in multi-layer board fabrication. In addition, the insulator properties may also compromise on the device or module performance since the insulator may not be easily substituted. Another technology for fabricating the vias is the conventional printed circuit board (PCB) processes [132]. Nevertheless the overall cost of the fabricated device using a hybrid process of inkjet printing/screen printing combined with PCB process may be significantly higher, compared to a device fabricated entirely using the PCB process. However such a situation may change in future as interest gain in realising printed transmission lines for high frequency applications, which could create a market for hybrid fabrication processes [134].

3.3 Surface Roughness Modelling

At higher frequencies, the onset of skin effect causes current crowding into traces with surface roughness profiles, which results in increased attenuation. As these effects may lead to signal integrity problems at microwave frequencies, a need arises to consider the effect of surface roughness on printed traces.

Most of the work pertaining to the investigation of surface roughness pertains to etched copper traces on a PCB [135-137]. This is because the copper foils on PCBs are typically roughened to improve the adhesion to dielectric substrates.

Hammerstad *et al*. [135] introduced a factor to estimate the loss of a trace for a given surface roughness value. However the factor is valid for values ≤ 2, which implies that the model is not valid for very rough surfaces. Furthermore it is assumed that the trace profiles are saw-tooth shaped, triangular or square. Huray *et al*. [136] introduced an analytical modelling of the power loss for a rough copper trace by considering the copper profiles as 3D snowball structures, based on their observations from SEM images. Nevertheless these models may not be applicable for traces obtained by technologies such as inkjet printing, as the trace profiles may tend to be more spherical due to the agglomeration of the metal nanoparticles during sintering. On the other hand, some researchers [138, 139] have used full-wave solvers to simulate the roughness profiles of traces, which is computationally intensive.

Recently Curran *et al*. [129] proposed a model to calculate the resistive losses in transmission lines. In one of the equations, a variable (P) was used to represent the shape of the surface roughness, with P = 2 used for traces with a saw-tooth profile. Nevertheless this P value is unknown for traces with different trace profiles [140] which are obtained from other fabrication technologies, and further work would be needed to determine those values.

To characterise the surface roughness, stripline configurations are typically considered in the design of the test samples. This is because such a configuration allows for the surface roughness on both the top and bottom side of the trace to be

taken into account. Due to the current fabrication limitations, it is challenging to fabricate multi-layer structure using screen printing or inkjet printing processes to study the surface roughness phenomenon. This may be more feasible in future with the emergence of hybrid processes as discussed in Section 3.2(b).

3.4 Contact Angle Analysis

From the manufacturing perspective, the contact angle analysis is a method commonly used for analysing the wettability of surfaces. Wettability can be observed from the way a water droplet spreads out on clean glass to how it changes shape to a large round droplet on a non-stick Teflon frying pan (Figure 3.7).

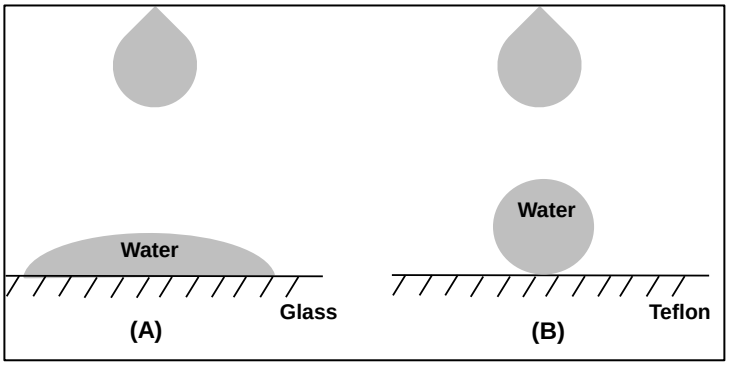

Figure 3.7 Diagram showing (A) A water droplet on clean glass surface and (B) A water droplet on a Teflon surface

Contact angle analysis is a commonly used technique to ascertain the change in wettability of samples after surface modifications. When a liquid droplet is deposited onto a surface, the droplet would adjust its shape to expose the minimum surface area possible (i.e round shaped). The surface tension can be described by Young's equation [141] as shown in equation (3.2):

$$\gamma_s = \gamma_L \cos\theta + \gamma_{SL} \tag{3.2}$$

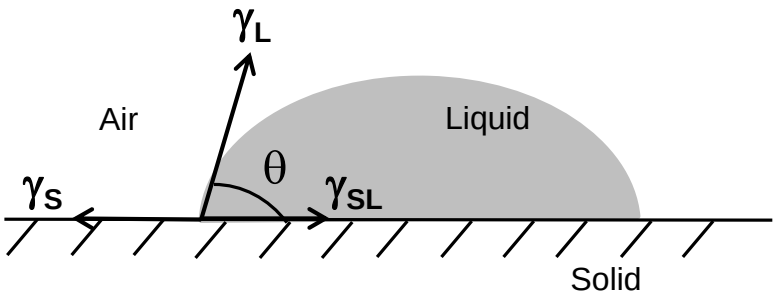

Figure 3.8 Diagram illustrating Young' equation

With reference to Figure 3.8, θ refers to the contact angle, γ_s and γ_L refers to the solid and liquid surface tension while γ_{SL} refers to the solid and liquid boundary tension. Owen-Wendt-Rabel-Kaelble [142] proposed equations for determining the surface energy of polymers by using two reference liquids with known dispersive and polar components, where one of the liquids needs to have a polar component > 0.

Nevertheless, a few assumptions lie behind reliable contact angle measurements. The first assumption is that the reference liquid used does not dissolve the surface of the test sample, which could contaminate the reference liquid thus changing its properties. As such care needs to be taken with regards to selecting a suitable reference liquid which would not interact with the surface of the test sample. Another assumption is that the sample surface is homogeneous such that uniform contact angles could be obtained across the sample. Yet in some cases it was unclear if the reference liquid used had an effect on the test sample. For example, in measuring films which have been cured using UV exposure, little information is available in literature on their cure status [29, 30]. As such it is assumed that the films are fully cured.

The use of contact angle analysis on materials such as paper and fabrics is challenging as they are porous and rough. A droplet of liquid deposited on these materials not only spreads on the surface but also penetrates the depth of the material. This in turn changes the wetting properties of the liquid. Samyn *et al*. [143] reported that water droplets on uncoated papers are unstable and penetrate immediately into the porous substrate. As such the contact angle measurements of the water droplets on paper substrates were obtained 1 second after contact [143].

For such rough substrates, two key models [144, 145] are typically used to describe the effect of surface roughness on the contact angle of liquid droplets. Wenzel [144] suggested that surface roughness increases the surface area of a solid (non-porous) as shown in Figure 3.9, which changes the surface contact angle. Subsequently Cassie *et al*. [145] extended the work of Wenzel to consider for a porous surface, where they considered pockets of air trapped below the liquid resulting in a composite surface.

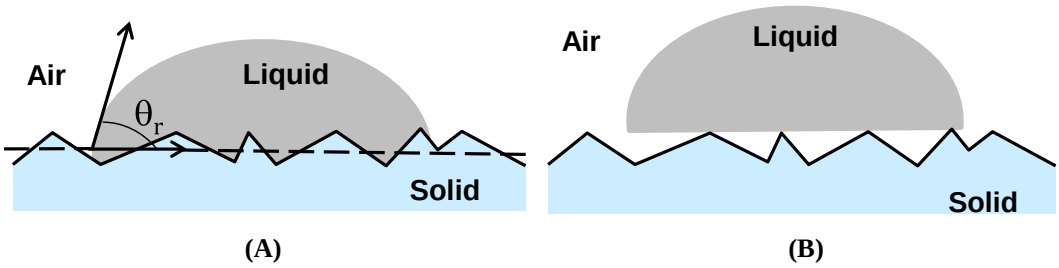

Figure 3.9 (A) A liquid droplet on a rough non-porous surface and the corresponding contact angle (θ_r) (B) A liquid droplet on a rough surface with pockets of air below the liquid

3.5 Conclusions and Research Gaps

In this chapter, the characterisation aspects related to the research presented in this thesis have been reviewed. In particular, literature on the electrical performance and the material properties characterisation were presented. The associated research gaps are summarised as follows.

- In terms of material characterisation, the dielectric characterisation of substrates is paramount for high frequency applications. From literature, issues were encountered in the repeatability of the dielectric properties of fabrics, which are mainly attributed to the non-identical effects of the test set-up considered. The issue of repeatability in the dielectric characterisation in the higher gigahertz range (≥ 20 GHz) is further investigated in Chapter 4 of this thesis.

- In considering transmission line structures for the dielectric characterisation of substrates (including fabrics), the current formulae for extracting the conductor losses in transmission lines are not formulated for frequencies beyond tens of gigahertz [120, 122]. This research gap necessitates an approach to improve

the analytical equations in characterising the dielectric properties of Tyvek, which have not been characterised. This work is detailed in Chapter 4 of this thesis.

- In the deposition of traces using inkjet printing, contact angle analysis is a commonly used technique to determine the wettability of a liquid onto a surface. However research is lacking on the applicability of contact angle measurements on partially cured films, as little information is available on the final cure status of UV-curable films. This is further investigated in Chapter 6 of this thesis (refer to Section 6.4.3).

- From literature, the RF measurements of printed transmission lines up to 30 GHz have been reported, but there are no simulation models available to predict the transmission lines performance up to 30 GHz. The correlation of simulation with measurement results has been reported up to 1.2 GHz, for RFID applications. Thus a research gap exists to accurately model the RF performance of printed interconnects in the higher gigahertz range (≥ 20 GHz), by taking into account the non-ideal characteristics of the printed transmission lines. This work is detailed in Chapter 7 of this thesis.

Chapter 4. Understanding the Properties of Substrates – Characterisation of Dielectric Properties

4.1 Introduction

The need for an accurate knowledge of the substrate dielectric properties (dielectric constant, loss tangent) at the frequency of interest [146, 147] is essential for high speed and RF applications. Knowledge of these parameters enables designers to select the appropriate substrates when designing for controlled impedance structures. In addition, the dielectric properties data are essential for designing the dimensions of passive components, miniaturising the component footprints and minimising their RF losses. However as Tyvek has not been used in high frequency applications, its dielectric properties are not available from manufacturers compared to conventional high frequency laminates [113], for which the dielectric properties have been characterised over broadband frequencies [31, 113]. Consequently the work in this chapter seeks to characterise the dielectric properties of Tyvek over broadband frequencies up to 20 GHz (due to constraints of the available equipment). To validate the approach, the results are verified using RO3006 as the reference substrate.

Several techniques are available for the dielectric characterisation of materials [112, 116, 117]. However most require customised test fixtures [148, 149] or specialist equipment [117, 150]. In contrast the use of transmission line structures [12, 33, 116] is appealing since they enable broadband dielectric measurements to be made. Furthermore these structures can be readily realised through a variety of techniques such as embroidered traces [12], screen printing [40] or inkjet printing.

Nevertheless, one challenge in the dielectric characterisation using transmission line structures is the suitability of the analytical equations for use in the higher frequencies. Accurate theoretical equations are essential for extracting the loss tangent using the transmission line structures. However the conductor loss

formulae available [122, 123] were not intended for calculating the transmission line characteristics beyond tens of gigahertz. Thompson *et al*. [120] circumvented this by comparing different formulae and used the equation which yielded reasonable values for the loss tangent, in extracting for a low loss material up to 110 GHz. Another challenge in the dielectric characterisation lies in the non-repeatability of the transition from connector to transmission line structure during RF measurements [12, 33, 116]. Lee *et al*. [116] minimised the SMA transition non-repeatability through the use of an error cost function, but this approach would be time consuming as ten measurements were performed for each test structure, following which the error cost for each measured data set was computed.

In view of the above limitations, a new methodology for dielectric characterisation is proposed. This combines analytical equations found in the literature [122, 123] with simulation models which are used to describe the conductor losses of the measured transmission lines, up to 20 GHz. To address the issue of transition repeatability, the RF measurements were performed using a probe station setup. With this setup, RF probes are used instead of SMA connectors. This eliminates non-identical SMA transitions arising from variations in the manual soldering and the subsequent error in the extraction process.

4.2 Methodology

The methodology used for the dielectric characterisation is shown in Figure 4.1. The dielectric constant is extracted from analytical equations based on the approach by Lee *et al.* [116]. This makes use of two line lengths, which can be non-50 Ω in impedance. This approach which allows for non-50 Ω lines to be considered is particularly useful for extracting the dielectric properties of Tyvek using screen printing, where information on the degree of the paste spread is uncertain and thus the realisable dimensions are also uncertain. Transmission lines designed at 50 Ω may be non-50 Ω after screen printing depending on the extent of the paste spread. The paste spread is dependent on a myriad of factors such as the screen mesh parameter and the paste characteristics [151]. From previous work, the paste spread was found to vary for different paste-substrate combinations, which requires a separate characterisation.

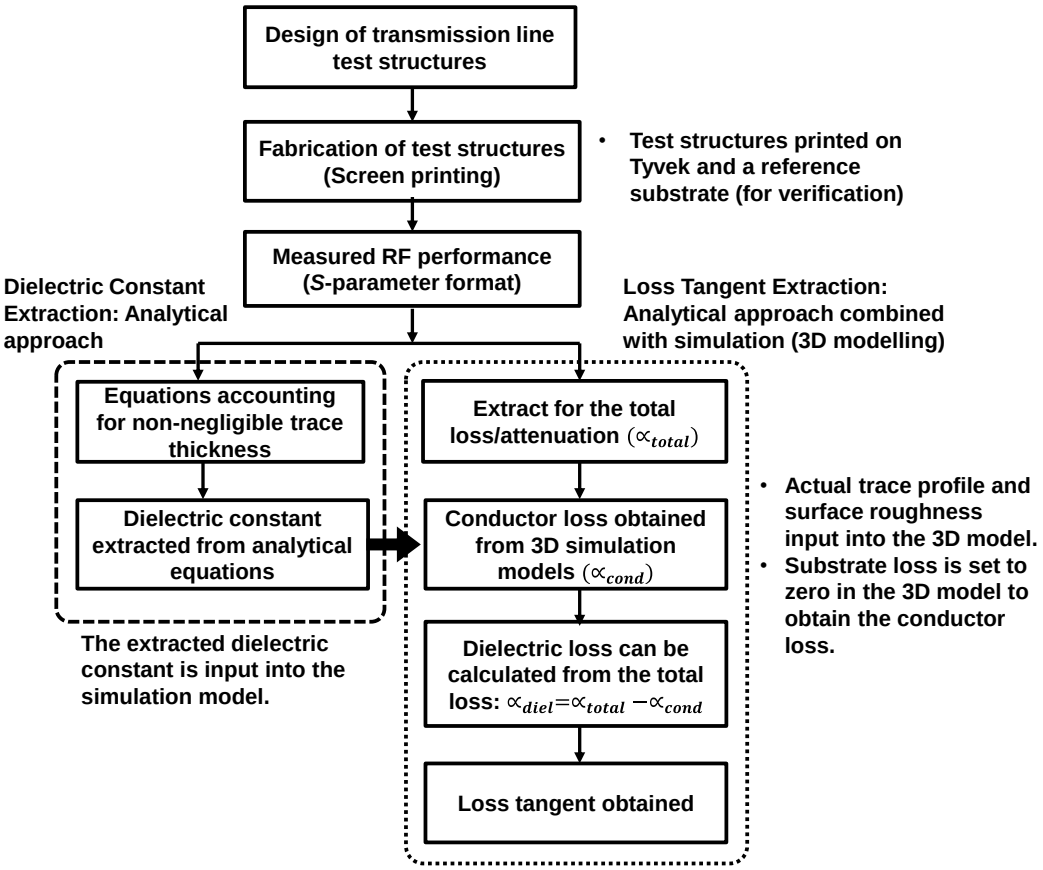

Figure 4.1 Methodology for characterising the dielectric properties of Tyvek

On the other hand, the loss tangent is extracted using on a novel approach combining analytical equations with 3D simulation. Instead of relying solely on analytical equations this approach was adopted because to the author's best knowledge, the analytical formulas available for describing conductor losses in CPW structures [122, 123] were not intended for the millimetre-wave domain [120]. This approach improves the analytical approach.

With reference to Figure 4.1, to extract for the loss tangent, the total loss for a short transmission line is first obtained based on the approach by Eisenstadt *et al*. [152]. Next, the conductor loss is obtained from the 3D simulation model. The 3D model incorporates the actual measured trace profile parameters (trace width, height, DC conductivity values), where the profile parameters are characterised through a non-contact technique. The DC conductivity values are obtained from two point probe measurements of traces with lengths of 4 cm to 10 cm and widths ranging from 0.3 mm to 1 mm. With the conductor loss obtained from simulation, the dielectric loss

can be calculated from the total loss. Consequently the loss tangent can then be extracted using the equations detailed in Section 4.2.3.

4.2.1 Extraction of Dielectric Constant

The dielectric properties obtained using the technique proposed by Lee *et al*. [116] and considered by Declercq *et al.* [33] are effective values, which comprise of a mixture of air and the material under test. In this section, the extraction by Lee *et al.* [116] is extended to obtain the actual dielectric constant (ε_r) values from the effective values.

(a) Extraction of Actual Dielectric Constant from Effective Values

The complex effective permittivity is generally represented as shown in equation (4.1), where ε'_{eff} is the effective dielectric constant and ε''_{eff} is the effective loss tangent. *j* represents the imaginary part of equation (4.1):

$$\varepsilon^*{}_{eff} = \varepsilon'{}_{eff} - j\varepsilon''{}_{eff} \tag{4.1}$$

$$\varepsilon^*{}_{eff} = \varepsilon'{}_{eff} - j(\tan\delta)_{eff} \tag{4.2}$$

The final equation for the complex permittivity as proposed by Lee *et. al*.[116] is given as:

$$\varepsilon^*{}_{eff} = \left[\frac{1}{\beta_0 \Delta d}\cosh^{-1}\left\{\frac{1}{2}Tr\left(M_1 M_2{}^{-1}\right)\right\}\right]^2 \tag{4.3}$$

where β_0 is the phase constant in free space, Δd is the length difference between 2 microstrip lines, M_1 and M_2^{-1} are ABCD matrices which are obtained from *S*-parameter matrices. The significance of using *S*-parameters is described in Section 3.3(b) of Chapter 3. From equation (4.3), *Tr* represents the trace defined as the sum of the diagonal elements in the matrices. Consequently ε'_{eff} can be extracted from the real part of equation (4.3), which is equivalent to equation (4.2). To extract the real dielectric constant from the effective value, the equation proposed by Ghione *et al.* [153] for a CPW configuration was considered (with reference to Figure 4.2):

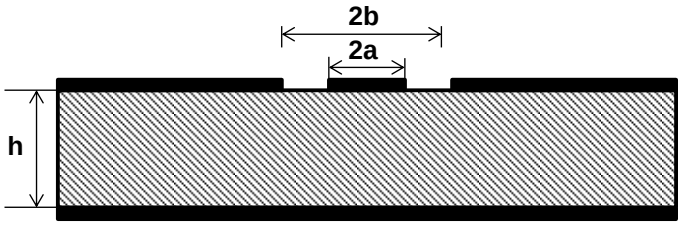

Figure 4.2 Coplanar waveguide structure with a lower ground plane

$$\varepsilon'_{eff} = \frac{1 + \varepsilon_r \frac{K(k')}{K(k)} \frac{K(k_1)}{K(k_1')}}{1 + \frac{K(k')}{K(k)} \frac{K(k_1)}{K(k_1')}} \tag{4.4}$$

where

$$k = \frac{a}{b} \tag{4.5}$$

and

$$k_1 = \frac{\tanh\left(\frac{\pi a}{2h}\right)}{\tanh\left(\frac{\pi b}{2h}\right)} \tag{4.6}$$

With reference to Figure 4.2, 2*a* represents the trace width while 2*b* is the summation of the trace width and the gaps on both sides of the trace. *h* represents the substrate thickness. From equation (4.5) and equation (4.6), *k* is the complete elliptic integral of the first kind and $k_1' = \sqrt{1 - k_1^2}$.

Due to the non-negligible trace thicknesses, their effects were accounted for in the extraction of the effective dielectric constant, where:

$$\varepsilon'^{t}_{eff} = \varepsilon'_{eff} - \frac{0.7\left(\varepsilon'_{eff} - 1\right) t/(2a)}{\left[\frac{K(k)}{K'(k)}\right] + 0.7t/(2a)} \tag{4.7}$$

Next, letting

$$f = \frac{K(k')}{K(k)} \frac{K(k_1)}{K(k_1')} \tag{4.8}$$

By substituting equation (4.8) into equation (4.4), one can obtain the actual dielectric constant ε_r as:

$$\varepsilon_r = \frac{\varepsilon_{eff}'^{t}(1+f)-1}{f} \tag{4.9}$$

4.2.2 Extraction of Loss Tangent

With reference to equation (4.1) and (4.2), the loss tangent (ε_{eff}'') can then be extracted from the imaginary part of equation (4.2). The extraction of the loss tangent requires first determining the total attenuation constant $\propto_{total}$ [152], where:

$$e^{-\gamma l} = \left\{\frac{1 - {S_{11}}^2 + {S_{21}}^2}{2S_{21}} \pm X\right\}^{-1} \tag{4.10}$$

where

$$X = \left\{\frac{({S_{11}}^2 - {S_{21}}^2 + 1)^2 - (2S_{11})^2}{2S_{21}}\right\}^{1/2} \tag{4.11}$$

From equation (4.10), γ represents the propagation constant of the transmission line. This approach is recommended for transmission line lengths within λ/2, where λ is the wavelength at the maximum frequency considered. This implies the consideration of a shorter transmission line as the maximum frequency increases. Otherwise, the extraction would involve the conversion of the measured *S*-parameter phase value (ranging from -180 °C to +180 °C) to the actual phase value in radians, which complicates the extraction procedure.

Once γ is determined, the total attenuation $\propto_{total}$ can be obtained, where:

$$\propto_{total} = real(\gamma) \tag{4.12}$$

Assuming that the radiation losses are negligible, the total attenuation comprises of the conductor loss ($\propto_{cond}$) and dielectric loss ($\propto_{diel}$):

$$\propto_{total} = \propto_{cond} + \propto_{diel} \tag{4.13}$$

The conductor losses are obtained from the *S*-parameters of the 3D simulation model of the transmission line (in *CST* software), with the actual trace profiles input into the model. In addition, the substrate loss is set to zero in the 3D model, hence only the conductor losses are obtained.

Finally the loss tangent can be obtained from the dielectric loss as shown in equation (4.14). In this case the dielectric loss is extracted by subtracting the conductor loss from the total attenuation in equation (4.13). Subsequently $\propto_{diel}$ can be manipulated to yield [122]:

$$\tan\delta = \frac{\alpha_{diel}\,\lambda_0(\varepsilon_r' - 1)\sqrt{\varepsilon_{eff}'}}{\pi\varepsilon_r{}'(\varepsilon_{eff}' - 1)} \tag{4.14}$$

where λ_0 is the wavelength in free space.

4.3 Materials

This section details the specifications of the substrate, screen and silver paste used for realising the test structures.

4.3.1 Substrates

The reference substrate used in this work (RO3006) is a ceramic-filled PTFE laminate typically used for high frequency applications [31], with dielectric properties well characterized up to 40 GHz (Dielectric constant = 6.15 ± 0.15, loss tangent = 0.002) [31]. The laminate is supplied in a 305 x 457 mm sheet with a laminate thickness of 1.28 mm and 17 µm electrodeposited copper on both sides. In order to prepare a single-sided laminate, the copper on one side of the laminate was chemically removed using the standard printed circuit board (PCB) process – lamination, UV exposure, development, etching and stripping. The resulting surface roughness is around 1 µm. The single-sided laminate is used for the trace deposition using screen printing.

The substrate to be characterised, Tyvek [154], is a white matt material which is polyethylene based and is treated for solvent inkjet printing. It has a slightly textured surface on one side, and a smooth paper like surface on the other side (i.e. treated surface). The treated surface has been coated to be receptive of solvent inks, and is used for printing in this work. The datasheets of RO3006 and Tyvek can be found in Appendix B1.

4.3.2 Screen Specifications

For the screen printing, a 29 inch 325 mesh screen was used, with a 45° tilt. The emulsion thickness is 12 μm and the mesh thickness is 62 μm ± 2 μm. The mesh opening ratio is 39 %. An estimation of the paste thickness can be calculated from equation (4.15) [61]:

$$Wet\ thickness \approx Mesh\ thickness\ x\ Opening\ ratio + Emulsion\ thickness \quad (4.15)$$

Assuming that the wet / dry ratio of a conventional silver paste is about 70 %, the estimated wet thickness after printing is around 36 μm.

4.3.3 Screen Printing Paste

The silver paste used is a silver polymer thick film ink from Johnson Matthey (S-020) [155]. The paste has a silver content of 64.0 % and a solids content of 72.56-74 %. The paste viscosity is 17-32 Pas (Brookfield RVT, Spindle 6 at 20 rpm, 25 °C), and the recommended curing condition is at 15 min at 120 °C in a box oven where a sheet resistance < 15 mΩ/sq at 25 μm is provided in the datasheet.

4.4 Test Structure Design and Electromagnetic Modelling

This section describes the modelling aspects of the transmission line structures for frequencies from DC up to 30 GHz.

4.4.1 Structures for DC and RF Characterisation

Three types of structures are included in the screen design (with reference to Figure 4.3):

- ***DC test structures (5 cm and 10 cm lengths)***

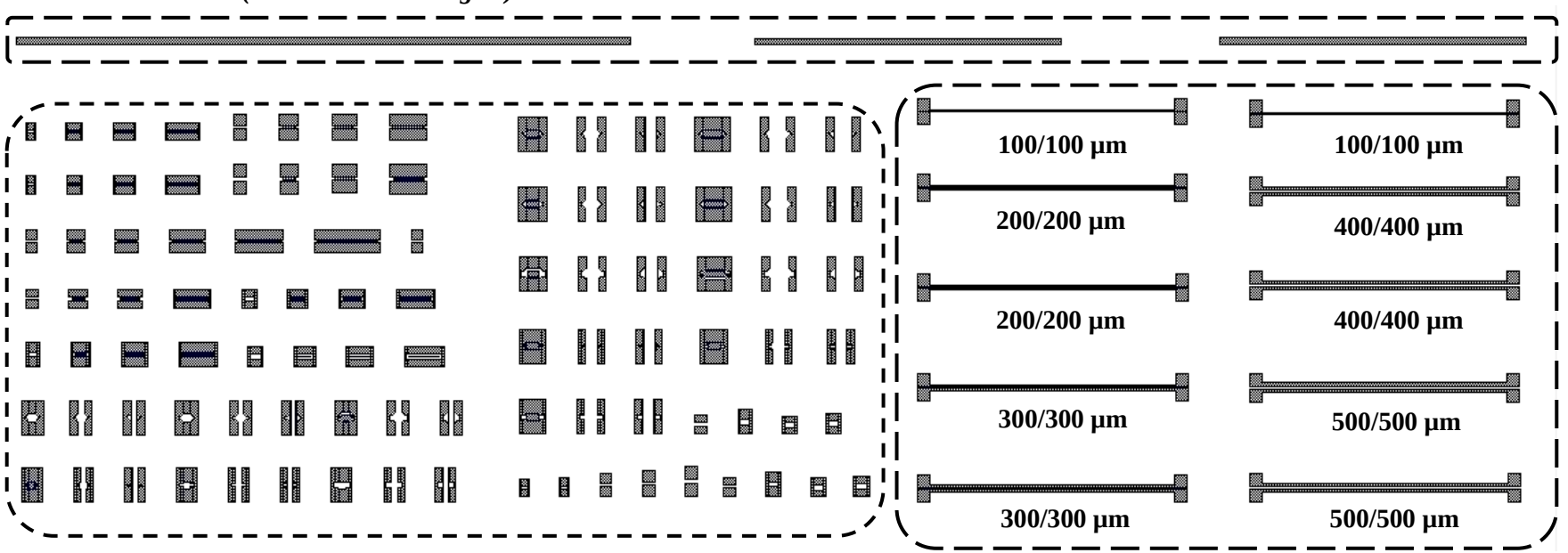

- ***CPW test structures***
- ***DC test and minimum gap structures (4 cm lengths)***

(A) Overview of designed test structures

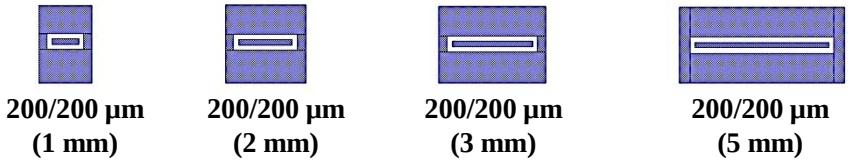

(B) Magnified view of CPW test structures with w/s = 200/200 µm

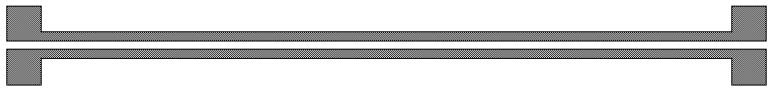

(C) Magnified view of DC test structures with w/s = 500/500 µm

Figure 4.3 Test structures designed for the dielectric characterisation of RO3006 and Tyvek

- DC test structures: Two point probe structures (4 cm long) with width/gap ranging from 100/100 μm to 500/500 μm were designed. One objective was to use the structures to characterise for the DC conductivity of the printed traces. To ascertain the effect of the probe contact resistance, longer DC structures of lengths 5 cm and 10 cm (with 1 mm widths) were also included in the designs.

- Minimum gap realisable: The 4 cm long two point probe structures could also be used for the dual purpose of determining the minimum width and spacing realisable on the substrates, where the gap between two DC structures is designed to be the same as the trace widths (shown in Figure 4.4).

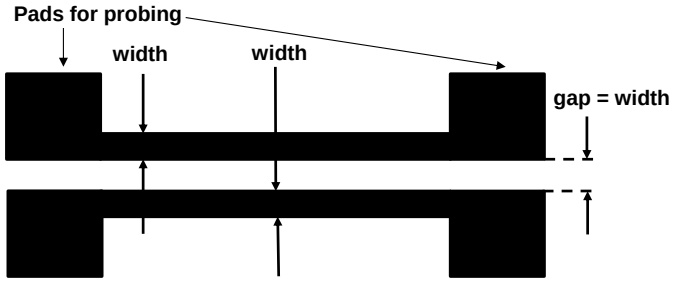

Figure 4.4 DC test structure which is also used to determine the minimum width/gap obtainable

- RF test structures: Coplanar waveguide (CPW) structures were designed for the high frequency electrical characterisation, where an electrical signal is sent down a central line with ground lines on both sides. This is known as the ground-signal-ground (GSG) configuration. CPW structures with dimensions ranging from 100/100 μm to 100/350 μm were designed, with lengths ranging from 1 mm to 5 mm (in steps of 1 mm). Figure 4.5 shows a typical coplanar waveguide test structure where w represents the signal width. g , g_1 and g_2 refer to the gaps between the trace and ground planes, while h represents the substrate thickness.

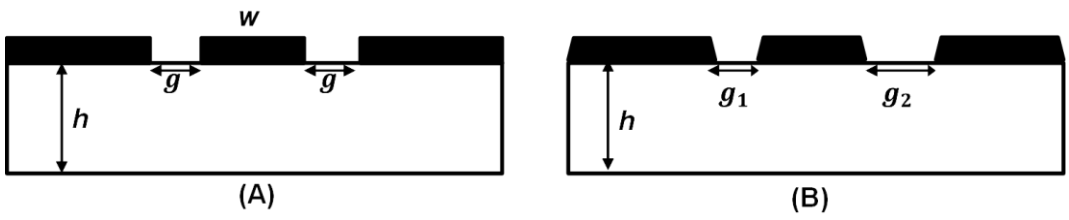

Figure 4.5 Cross-section of coplanar waveguide structure (A) Ideal (B) Actual

As shown in Figure 4.5(B), the actual fabricated CPW structure may yield inconsistent structure dimensions, where $g_1 \neq g_2$. In addition, the actual trace profile would be trapezoidal rather than the assumed rectangular profile shown in Figure 4.5(A), which may give rise to conductor edge effects [156]. The effect of these non-ideal characteristics can be modelled and taken into account in the 3D simulator.

For the CPW test structures, varying gaps were considered in the designs, with the respective dimensions shown in Table 4.1. As the degree to which the paste would spread is unknown, the designs with varying widths and gaps were considered to compensate for the paste spread, such that CPW structures could be realised without being shorted-circuited by the paste. As such the designs include non-50 Ω test structures which can be used for the extraction of the dielectric properties. The impedance values were calculated using *Linecalc*™. A dielectric constant of 6.5 was used for RO3006 from the datasheet provided [31]. For Tyvek, a value of 1.9 was used. This value is based on previous results obtained using the approach by Lee *et al*. [116], which involves coaxial-to-microstrip transitions.

Table 4.1 Dimensions of designed CPW test structures

Set	CPW structure (width/gap), μm	Characteristic Impedance on RO3006 (Ω)	Characteristic Impedance on Tyvek (Ω)	CPW Lengths (mm)
1	100/100	69.1	103.9	1,2,3,5
2	350/100	49.6	70.0	
3	200/100	57.5	84.8	
4	400/100	47.8	66.6	
5	300/100	51.6	74.0	
6	200/200	71.4	101.3	
7	200/300	80.2	109.1	
8	300/250	67.9	90.8	
9	100/350	99.9	138.9	

4.4.2 3D Model Setup

A 3D electromagnetic simulator (*CST*) was used for the simulation of the test structures. The transient solver was used to simulate the test structures in this work as it is suited for electrically large structures (physical dimensions >> wavelength). The length of the CPW structures range from 1-5 mm, where 2 mm corresponds to the half wavelength at the highest frequency of operation (30 GHz) on RO3006 substrate. In a transient simulation, the test structure is excited with a broadband signal and the response monitored in time domain (Figure 4.6). A discrete fourier transform is then applied to the time signals to obtain the broadband electrical response of the model in the frequency domain (i.e. *S*-parameter matrices).

Figure 4.6 also shows the simulated 3D structure for a typical CPW structure on RO3006 substrate. Waveguide ports were defined on either end of the CPW structure as excitation sources. The waveguide port dimensions were defined within a quarter of the wavelength (corresponding to the highest frequency considered) to avoid parasitic effects on the *S*-parameter results at the higher frequencies. The model was simulated from 0-30 GHz using the transient solver, with the field energy for the solver termination set at -40 dB. This termination criterion is essential to ensure that the electromagnetic energy in the computational domain has decayed sufficiently. An open boundary was defined for the entire structure. Setting the boundary conditions defines a finite computational domain, otherwise the entire structure would be computationally intensive.

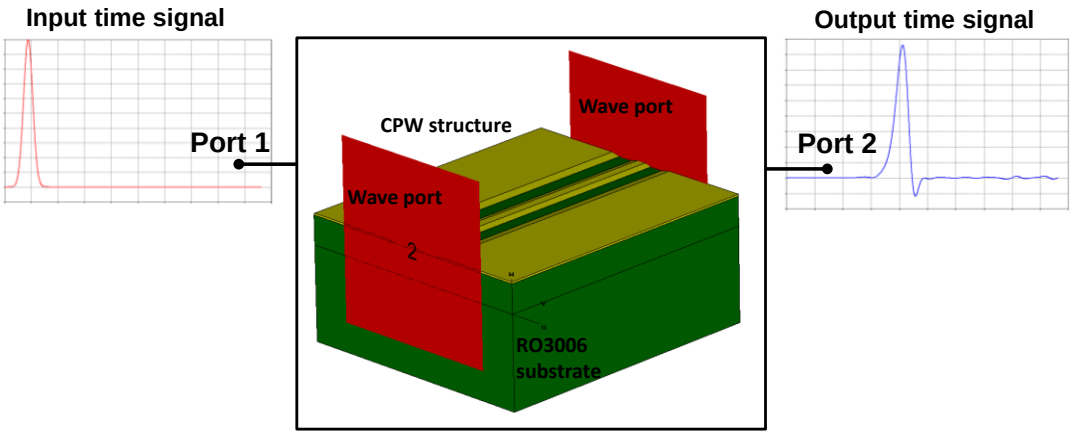

Figure 4.6 3D model of CPW test structure

4.4.3 Assumptions made in 3D Electromagnetic Modelling

The use of 3D electromagnetic modelling offers one the flexibility to isolate parameters and investigate the effect of one parameter on the overall result. Consequently the goal in this modelling is to isolate the conductor loss for the loss tangent extraction. With this data the dielectric loss can be obtained from the total loss using equation (4.13). Equation (4.14) would then be utilised to extract for the loss tangent.

A few assumptions were made in the 3D modelling. Firstly, it is assumed that the trace conductivity is constant throughout broadband. The trace conductivity value is obtained from the DC conductivity (σ) through equation (4.16):

$$\sigma = \frac{1}{\rho} = \frac{l}{RA} \tag{4.16}$$

where ρ is the resistivity, l is the trace length, R is the DC resistance and A represents the cross-sectional area of the trace.

In addition, the surface roughness of the trace is modelled using the tabulated impedance macro in *CST*. This macro makes use of the Hammerstad model [135] for modelling the surface roughness effects. This model assumes that the trace thickness is much higher than the skin depth ($t >> \delta$) [135]. It is also noted that the skin depth (δ) of the screen printed traces meets the condition of $\delta > 0.75\ H_{sr}$, where H_{sr} represents the surface roughness of the trace [129]. Due to the assumption that $t >> \delta$ this macro computes for one-dimensional (1D) geometry where the electric field is the same on either side of the material. Even when a two-dimensional (2D) geometry is modelled, the field inside the trace volume is not being computed. The implication of the tabulated impedance macro is that it is only suitable for modelling traces which are sufficiently thick compared to the skin depth.

4.5 Experimental Procedure

This section describes the parameters used in the experimental process, which includes the thermal curing of the printed structures, the RF measurements using a probe station and the non-contact profile characterisation of the traces for the simulation models.

4.5.1 Thermal Curing Parameters

The RO3006 substrate was cured at a temperature of 150 °C for 45 min. The Tyvek substrates on the other hand were cured at 100 °C for 35 min. A lower temperature was used for Tyvek as the maximum temperature which the substrate can withstand is 110 °C. In the curing of the substrates, it was crucial to ensure that the Tyvek substrates were not exposed to a prolonged period of curing. While an extended period of curing would improve the sintering among the particles and thus the DC conductivity, this would also introduce significant warpage in the substrate and make it challenging for RF measurements to be performed, where the substrate would be attached to the metal chuck via vacuum suction.

4.5.2 RF Measurement Setup

The accuracy of the extracted dielectric constant using the approach by Lee *et al.* [116] would be affected by the reproducibility of the transition region from the connector (at the end of the RF cable) to the CPW transmission line [116]. Typically, coaxial connectors are used for this transition [116, 157]. However the connection of the coaxial connectors to the CPW lines involves a manual soldering process, which degrades the reproducibility of the coaxial-to-CPW transition. The coaxial-to-CPW transition would be non-identical at the ends of the CPW line which reduce the accuracy of the approach [33]. On the other hand, the use of coplanar probes allows for a precise contact of the probe tips to the transmission lines (over-skating distance in the range of μm). As such coplanar probes were used for the RF measurements due to the improved reproducibility. A typical coplanar probe (GSG configuration, 500 μm pitch) is shown in Figure 4.7(A), while Figure 4.7(B) shows how a CPW structure is electrically characterised using a pair of coplanar probes.

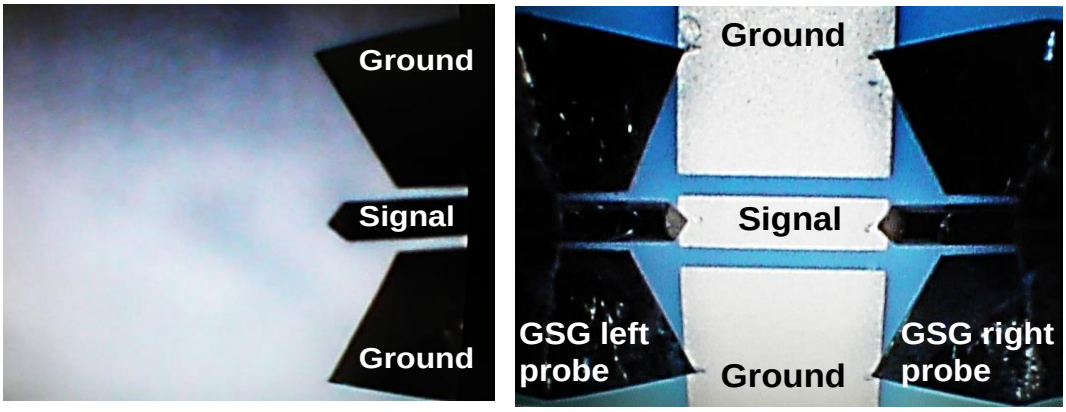

Figure 4.7 (A) View of a coplanar GSG probe (500 μm pitch) (B) Measurement of a CPW structure using a pair of GSG probes

The RF characterisation of the test substrates were performed using an Agilent E8361A PNA network analyser (10 MHz – 67 GHz). Two pairs of coplanar probes of 350 μm and 500 μm pitches (ACP-350 and ACP-500, Cascade Microtech) were used for the RF measurements due to the different pitches considered in the CPW structures. Prior to measuring, a Line-Reflect-Match (LRM) calibration was performed to remove the effects of the cables. Two frequency ranges were considered, 0.1-20.1 GHz and 0.1-30.1 GHz, with the number of frequency points set at 201. The averaging factor was set at 10 with the IF bandwidth at 5 kHz. Right angle male-female adaptors were used for the transition from the ends of the RF cables to the GSG probes. The substrates measured were held down using a vacuum chuck. In addition, the substrates were taped along the 4 sides. This step is particularly crucial for flexible substrates such as Tyvek, where the material could be easily warped due to the thin substrate thickness. The RF probe measurement setup is shown in Figure 4.8.

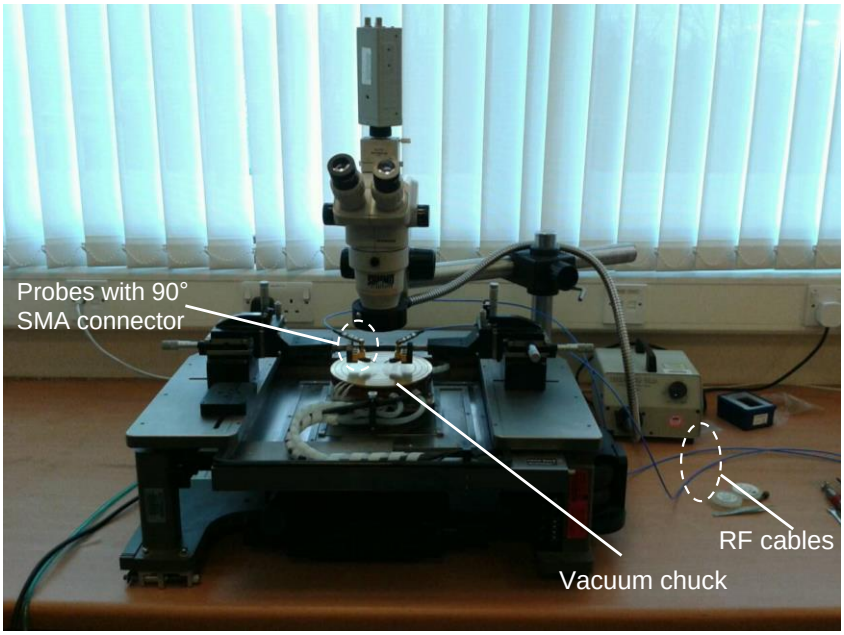

Figure 4.8 Close up view of the RF probe station

4.5.3 Trace Profile Characterisation

The trace profiles were characterised using a 3D laser non-contact measurement system (LEXT OLS-4100, Olympus). In the measurements, a differential interference contrast (DIC) laser observation was used with a x20 objective lens. The DIC option is useful in obtaining a sharper view of the RO3006 and Tyvek substrates which have rough surfaces, particularly for roughness in the range of nanometres to micrometres [158]. The cut-off wavelengths used for extracting the average surface roughness values (R_a) were 80 μm and 250 μm. These correspond to transmission line measurements of 1 mm and 2 mm. The cut-off wavelengths were selected as recommended in the manual for determining the surface roughness [158]. The cut-off wavelengths were set such that the scan length would be at least 5 times larger.

4.6 Results and Discussion

In this section, the basic characterisation results pertaining to the printed structures are presented in Section 4.6.1. A comparison of the losses obtained from analytical equations and 3D modelling is also shown in this section. Section 4.6.2 goes on to verify the proposed methodology by using it to extract the known dielectric properties of RO3006. Section 4.6.3 presents the dielectric characterisation results

of Tyvek. Sections 4.6.2 and 4.6.4 also include uncertainty analysis of the proposed methodology. Lastly the methodology is validated against another technique (Section 4.6.5), and a discussion is provided on its limitations in Section 4.6.6.

4.6.1 Characterisation of Printed Structures

(a) Minimum Gap Obtainable

Figures 4.9 (A)-(F) show some the test structures fabricated via screen printing on RO3006 and Tyvek.

From the printed DC test structures described in Section 4.4.1, test structures with spacings of 100 μm were observed to be shorted (trace widths and ground), due to the paste spread. Minimum spacings of 200 μm and 300 μm were obtained on RO3006 and Tyvek respectively. The larger spacing which was obtained on Tyvek could be attributed to the silver paste viscosity value (17-32 Pas), which likely resulted in more spread and increased the possibility of the traces being shorted together [21]. These results agree with those obtained by Karaguzel [21], where traces printed with lower viscosity silver pastes (12 Pas, 32 Pas) were observed to spread more compared to those printed using a higher viscosity paste (49 Pas) [21]. For the CPW test structures, only designs with gaps of 200 μm and above could be realised without any short-circuited traces.

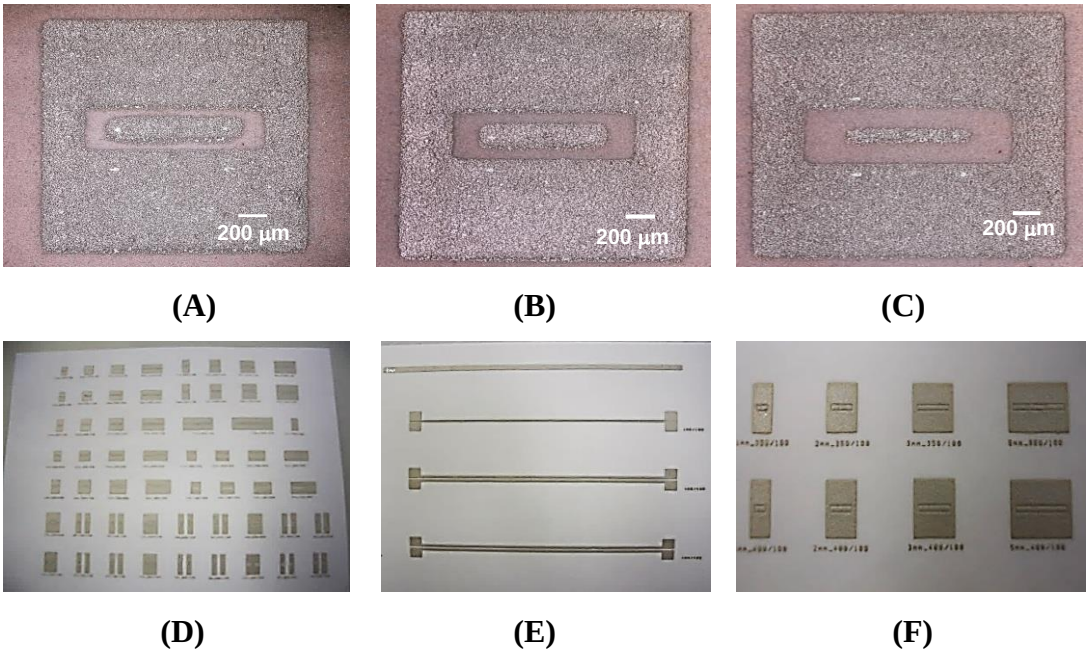

Figure 4.9 Fabricated test structures (A) CPW with width/spacing of 200/200 µm on RO3006 (B) CPW with width/spacing of 300/250 µm on RO3006 (C) CPW with width/spacing of 100/350 µm on RO3006 (D) Overview of CPW structures on Tyvek for RF measurements (E) DC test structures on Tyvek (F) Magnified view of CPW test structures on Tyvek

(b) DC Conductivity Values

The resistance values of the DC test structures (described in Section 4.4.1) were measured with a multi-meter and the DC conductivity computed according to equation (4.16). In the calculation of the trace cross-sectional areas in equation (4.16), it was assumed that the traces have rectangular trace profiles. The DC conductivity values extracted from the 10 cm long DC test structures were observed to vary by around 10-20 % compared to the shorter test structures. As such, the averaged conductivity value (from all the measured values) was used in the simulation model. The computed DC conductivity values of the measured test structures can be found in Appendix B2 of this thesis.

(c) Comparison of Results – Analytical Equations versus 3D Modelling

As mentioned in Section 4.2, analytical formulae are available for describing conductor losses in CPW structures [122, 123]. However these formulae have not been verified in the millimetre-wave domain [120]. In this section, we compare the results for the conductor loss obtained analytically [122] to those obtained via 3D modelling.

From Gupta *et al*. [122], the conductor loss of a CPW (dB/unit length) is represented as:

$$\alpha_c = 4.88x10^{-4} R_s \varepsilon_{re} Z_o \frac{P'}{\pi S}\left(1+\frac{W}{S}\right)\left\{\frac{\frac{1.25}{\pi} ln\frac{4\pi W}{t} + 1 + \frac{1.25t}{\pi W}}{\left[2+\frac{W}{S}-\frac{1.25t}{\pi S}\left(1+ln\frac{4\pi W}{t}\right)\right]^2}\right\} \tag{4.17}$$

where Z_0 is the characteristic impedance of the CPW, R_s is the surface resistivity of the conductors. *W* is the trace width while *S* represents the gap between the trace and ground planes. In addition:

$$P' = \left(\frac{K}{K'}\right)^2 P \tag{4.18}$$

where

$$P = \begin{cases} \dfrac{k}{\left(1-\sqrt{1-k^2}\right)(1-k^2)^{3/4}}, & for\ 0 \le x \le 0.707 \\ \dfrac{1}{(1-k)\sqrt{k}}\left(\dfrac{K'}{K}\right)^2, & for\ 0.707 \le x \le 1 \end{cases} \tag{4.19}$$

$$k = \frac{W}{W+2S} \tag{4.20}$$

In equations (4.19) and (4.20), *K* is the complete elliptical integral of the first kind and *K'* is represented as:

$$K'(k) = \mathrm{K}(k') \tag{4.21}$$

where

$$k' = \sqrt{1-k^2} \tag{4.22}$$

The conductor loss of a CPW structure was simulated with measured dimensions of 300/150 μm for the trace width/gap. Compared with the screen design dimensions of 200/200 μm, this represents a paste spread of around 50-100 μm for the width and gaps. The dimensions of the same structure were input into *Matlab* to compute for the conductor loss based on the analytical equations by Gupta *et al*. [122]. The results obtained are shown in Figure 4.10.

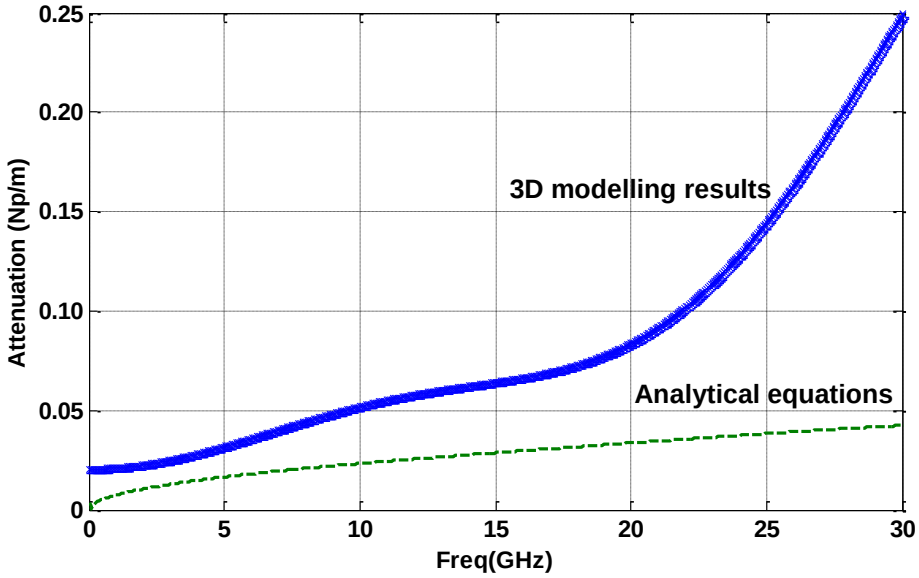

Figure 4.10 Comparison of attenuation obtained via analytical equations and simulation

From Figure 4.10, the attenuation obtained from analytical equations [122] follow a linear trend up to 30 GHz, and starts to deviate from the 3D simulation results beyond 20 GHz. Compared to the simulation results in Figure 4.10, the analytical equations based on a quasi-static approach were observed to under-estimate the conductor losses in the millimetre wave regime (≥ 30 GHz).

4.6.2 Characterisation of RO3006

(a) Dielectric Properties of RO3006

The measured parameters of a CPW structure used to extract for the dielectric properties of RO3006 are shown in Table 4.2. The notations used are with reference to Figure 4.11. The trace parameters were averaged from measurements at 3 locations of the trace (as indicated in Figure 4.11).

Table 4.2 Measured parameters of a 1 mm CPW structure (with reference to Figure 4.11)

Trace Parameters	Values	Remarks
Target g_1/w/g_2	200/ 200/ 200 µm	Design value
Actual g_1/w/g_2	148/ 259/ 149 µm	Measured value; averaged
θ_{1a} , θ_{1b}	12.3°, 12.7°	Lower signal trace angles
θ_{2a} , θ_{2b}	8.3°	Lower ground traces angles
θ_{3a} , θ_{3b}	9.4°	$\theta_{2b} = \theta_{2a}$ and $\theta_{3b} = \theta_{3a}$ in simulation model.
R_a of signal trace	0.79 µm	Using a cut-off wavelength of 0.08mm
R_a of ground plane	1.1-1.2 µm	Using a cut-off wavelength of 0.25mm
Trace thickness, t	20 µm	Averaged value
Average DC conductivity	2.6 x 10^6 S/m	Averaged value
Skin depth	1.8 µm	At 30 GHz

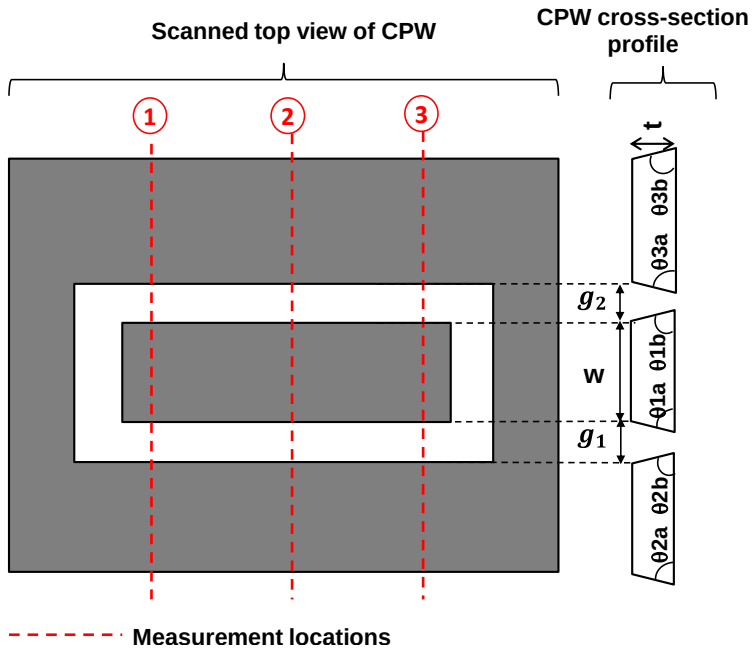

Figure 4.11 Schematic showing how the CPW structure is profiled using non-contact measurements and the parameters used in the simulation model

Figure 4.12 shows the top view of the measured structure on RO3006. The corresponding trace profile is shown in Figure 4.13, where a trapezoidal profile is observed for the signal and ground traces.

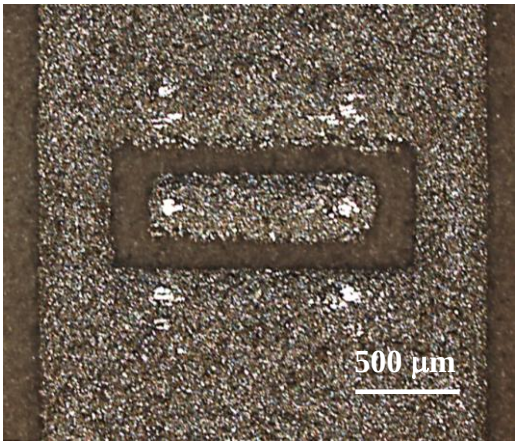

Figure 4.12 Measured CPW test structure on RO3006

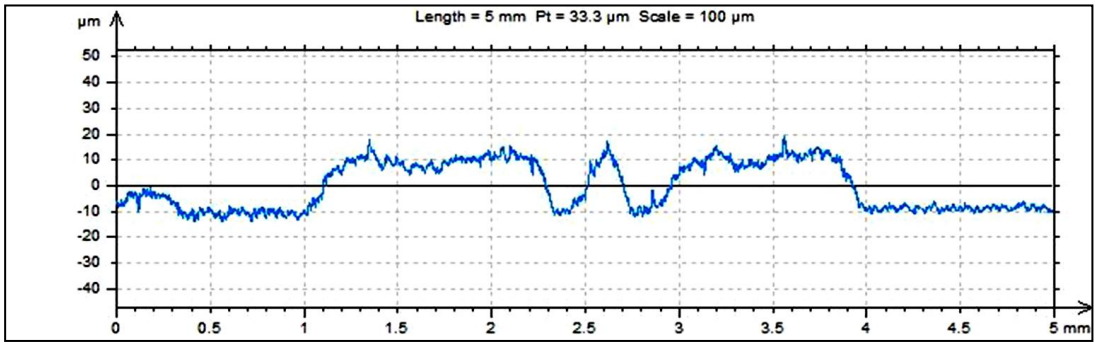

Figure 4.13 Measured trace profile of the CPW test structure

Figure 4.14 shows the correlation between simulation and measurement results, with a relatively good match up to 25 GHz. The fluctuations observed beyond 25 GHz are attributed to limitations of the measurement setup as elaborated later in this section.

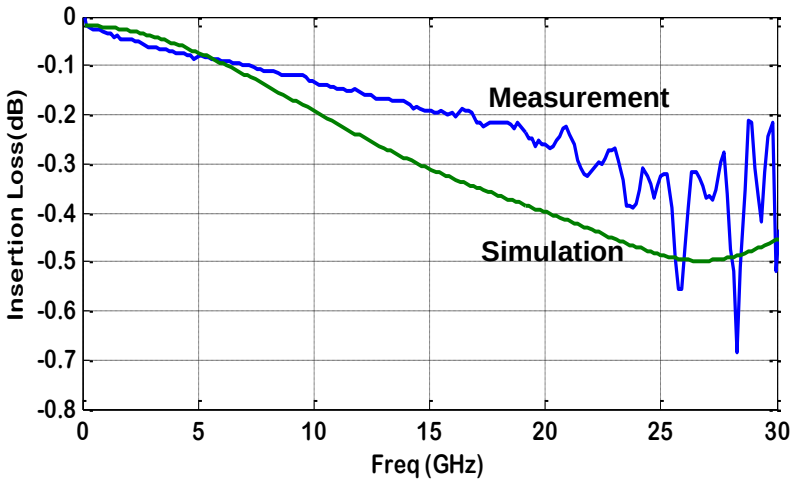

Figure 4.14 Correlation of insertion loss between measurement and simulation

From Figure 4.14, the observed discrepancy in the insertion loss results from 10-25 GHz may be due to the DC conductivity used in the simulation model, which is an averaged value and may not be accurate (i.e. an estimate) for the specific structure measured.

To validate the simulation model, the characteristic impedance value (Z_0) was considered, where the simulation and measurements were correlated. If the simulation model is a good representation of the measured transmission line, the Z_0 values are expected to yield a good match. The results are shown in Figure 4.15. From the figure, a variation of around 10 % is obtained between simulation and measurement results beyond 5 GHz, which is within the acceptable range of ± 10 %.

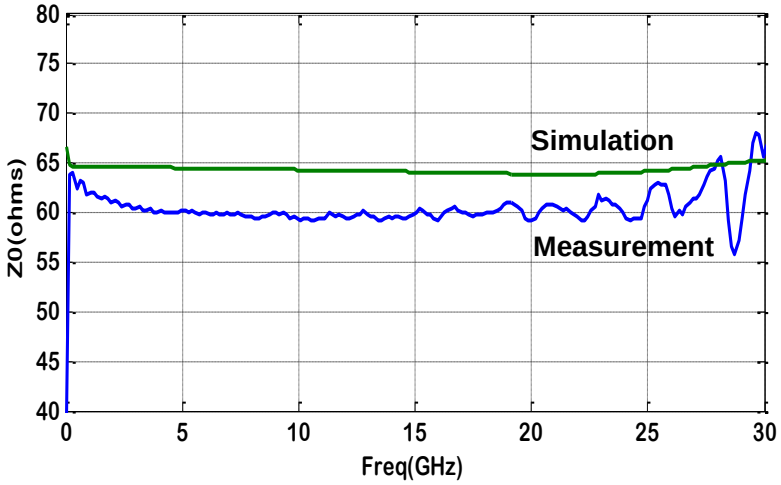

Figure 4.15 Correlation of Z_0 between simulation and measurement

The extracted dielectric constant and loss tangent for RO3006 are shown in Figure 4.16 and Figure 4.17. From Figure 4.16, the extracted dielectric constant ranged from 6.5-7.0 (beyond 3 GHz). These values were obtained after accounting for the trace thickness, and deviate from the manufacturer's value of 6.5 by around 6 %. However the results are not stable in the low frequency range (≤ 3 GHz), as the difference in the electrical lengths of the transmission lines becomes small in this region [116]. In addition, the lower frequency range from 10 MHz -3 GHz is near the instrumentation limit of the network analyser. Due to the input circuit characteristics of the PNA the test signal level is attenuated by more than 20 dB below 1 GHz. As such, the performance within this range could be improved by

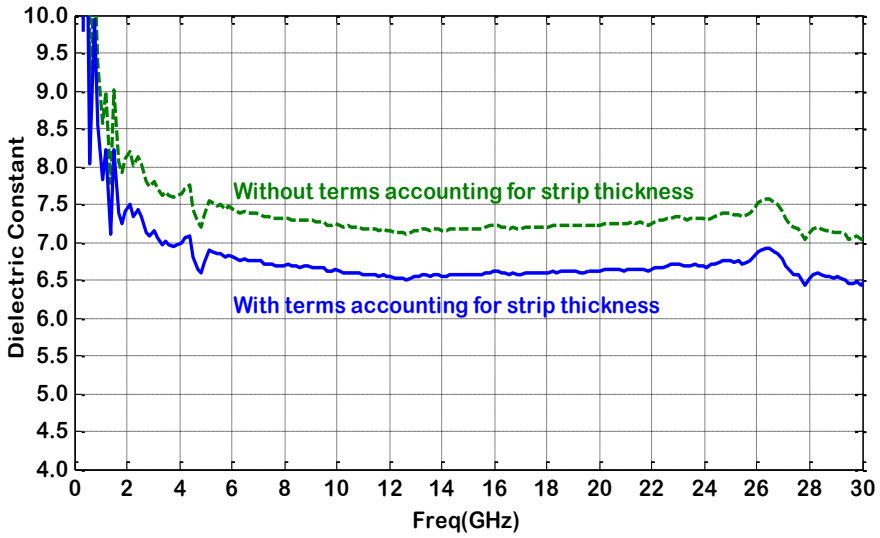

Figure 4.16 Extracted dielectric constant versus frequency for RO3006

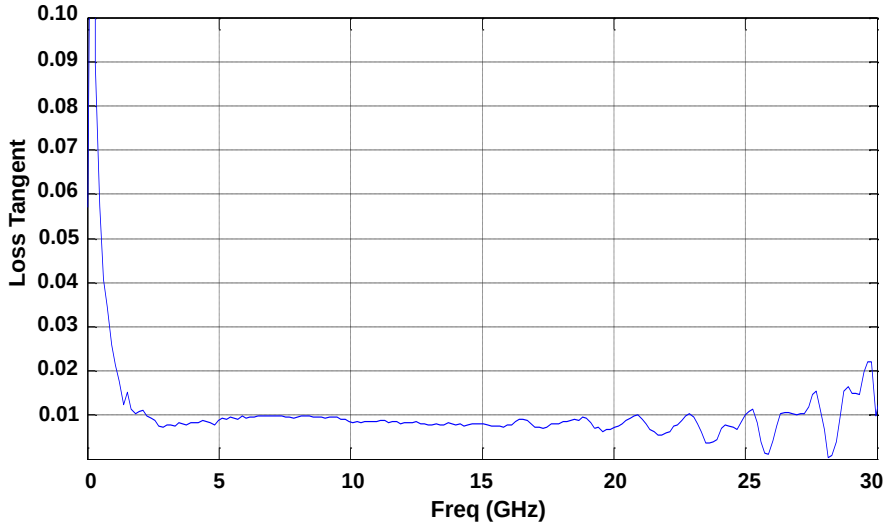

Figure 4.17 Extracted loss tangent versus frequency for RO3006

reducing the intermediate frequency (IF) bandwidth further or increasing the averaging factor so as to improve the signal-to-noise ratio. This would however result in a trade-off in the time required for the RF measurements.

The extracted loss tangent shown in Figure 4.17 was around 0.01 from 5-25 GHz, beyond which significant fluctuations in the values could be observed. This phenomenon was also observed in Figures 4.14 to 4.16. The significant fluctuation beyond 25 GHz can be attributed to the upper frequency limit of the right angle adaptors. These adaptors were of SMA coaxial types with upper frequency limits ranging from 12.4-18 GHz [159, 160]. Thus although the ACP-350 probes could be used up to 40 GHz [161], this is dependent on having a compatible adaptor

version with a similar upper frequency limit (i.e. 2.92 mm K adaptor). For the RF measurements performed in this work, the upper frequency of the measurement setup is limited by the specifications of the right angle adaptors used.

(b) Extracting for Low Loss Substrates – Uncertainty Analysis

The significant variation in the extracted loss tangent of RO3006 highlights the challenge in extracting for low loss substrates (loss tangent < 0.01). This can be better understood by performing an uncertainty analysis for equation (4.14). From equation (4.14):

$$\tan\delta = \frac{\alpha_{diel}\,\lambda_0(\varepsilon_r' - 1)\sqrt{\varepsilon_{eff}'}}{\pi\varepsilon_r'\left(\varepsilon_{eff}' - 1\right)}$$

Letting

$$A = \frac{\alpha_{diel}\,\lambda_0(\varepsilon_r' - 1)}{\pi\varepsilon_r'}$$

Equation (4.14) then becomes:

$$\tan\delta = \frac{A\sqrt{\varepsilon_{eff}'}}{\left(\varepsilon_{eff}' - 1\right)} \tag{4.23}$$

Differentiating with respect to $\partial\varepsilon_{eff}'$ yields:

$$\frac{\partial(\tan\delta)}{\partial\varepsilon_{eff}'} = \frac{0.5A(\varepsilon_{eff}'-1) - A\varepsilon_{eff}'}{(\varepsilon_{eff}' - 1)^2\sqrt{\varepsilon_{eff}'}}$$

Therefore

$$\frac{\partial(\tan\delta)}{\tan\delta} = \frac{0.5A(\varepsilon_{eff}'-1) - A\varepsilon_{eff}'}{(\varepsilon_{eff}' - 1)^2\sqrt{\varepsilon_{eff}'}} \times \frac{\partial\varepsilon_{eff}'}{\tan\delta} \tag{4.24}$$

It can be observed from equation (4.24) that the variation of the extracted loss tangent is a function of the ratio $\frac{\partial\varepsilon_{eff}'}{\tan\delta}$. Subsequently for a given change in $\partial\varepsilon_{eff}'$, a substrate with a low loss tangent value ($tan\,\delta$) would result in a higher variation

of the extracted loss tangent $\frac{\partial(tan\,\delta)}{tan\,\delta}$ compared to a more lossy substrate. In the case of the RO3006 substrate, a value of 0.2 was obtained for $\partial\varepsilon'_{eff}$. Using a value of 0.002 for the loss tangent from the datasheet [31], $\frac{\partial(\tan\delta)}{\tan\delta}$ is observed to be multiplied by a factor of 100 times from the ratio $\frac{\partial\varepsilon'_{eff}}{tan\,\delta}$. The variation in the extracted loss tangent of RO3006 is also shown in Figure 4.18, where a range of 100-200 % is observed up to 15 GHz. This variation is observed to increase significantly beyond 20 GHz due to the upper frequency limit of the measurement setup.

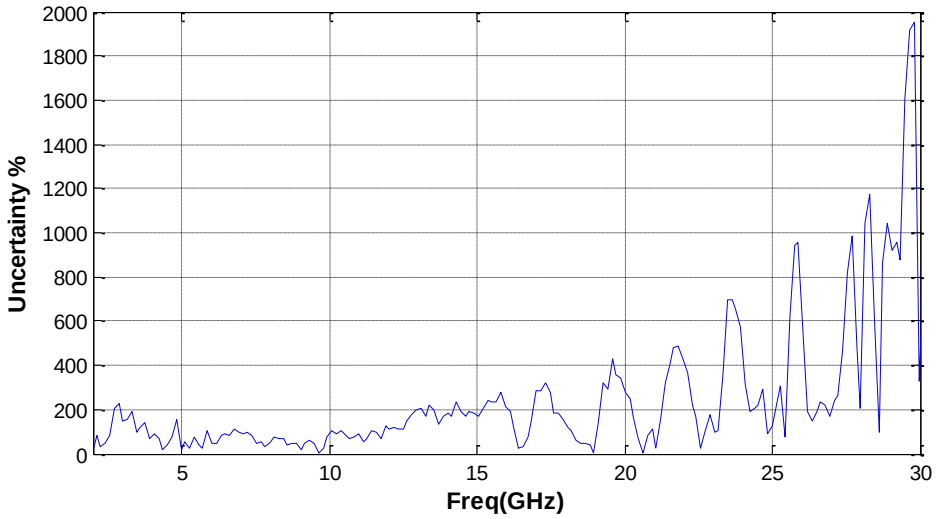

Figure 4.18 Variation of extracted loss tangent across 0.1-30.1 GHz

4.6.3 Characterisation of Tyvek

(a) Dielectric Properties of Tyvek

Due to the limitations of the measurement setup highlighted in Section 4.6.4, the upper frequency limit for reliable measurements was observed to be around 20 GHz, which is the upper limit of SMA connectors. The dielectric properties of Tyvek were extracted using the same procedure as RO3006 up to 20 GHz. The measured test structure and trace profiles are shown in Figure 4.19 and Figure 4.20. Table 4.3 shows the measured CPW parameters used for the extraction, where the notation used is referenced to Figure 4.11.

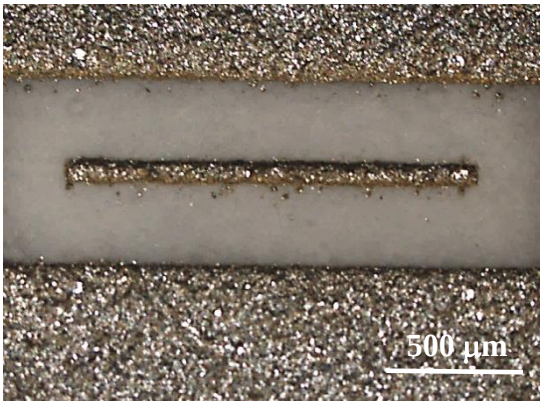

Figure 4.19 Measured CPW test structure on Tyvek

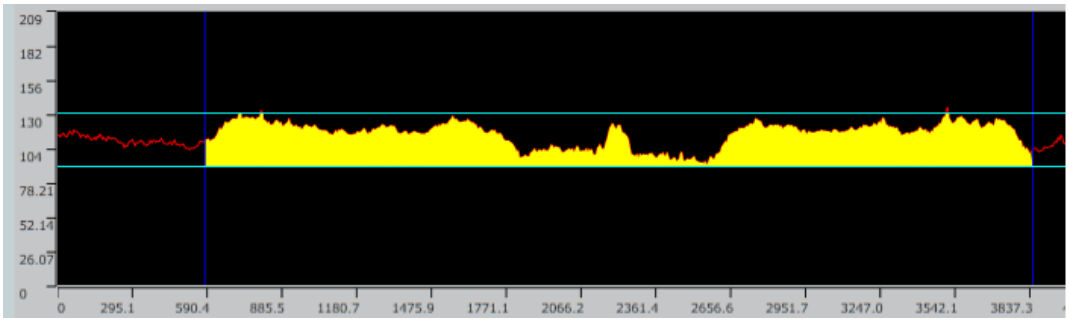

Figure 4.20 Measured trace profile of the CPW test structure on Tyvek

Table 4.3 Measured parameters of a 2 mm CPW structure on panel 1 (with reference to Figure 4.11)

Trace Parameters	Values	Remarks
Target g_1/w/g_2	350/ 100/ 350 µm	Design value
Actual g_1/w/g_2	335/107/319 µm	Measured value, averaged
θ_{1a} , θ_{1b}	39.9°, 39.9°	Lower signal trace angles
θ_{2a} , θ_{2b}	12.7°	Lower ground traces angles
θ_{3a} , θ_{3b}	21.3°	$\theta_{2b} = \theta_{2a}$ and $\theta_{3b} = \theta_{3a}$ in simulation model.
R_a of signal trace	1.5 µm	Using a cut-off wavelength of 0.25 mm
R_a of ground plane	1.3-1.4 µm	
Trace thickness, t	22 µm	Averaged value
Average DC conductivity	1 x 10^6 S/m	Averaged value
Skin depth	3.6 µm	At 20 GHz

Figure 4.21 and 4.22 show the extracted dielectric constant and loss tangent of Tyvek using the proposed methodology. From Figure 4.21, the dielectric constant of Tyvek remains stable at 1.9 over a broadband frequency range from 0.1-20.1 GHz. This value is expected as Tyvek, being a textile substrate, is porous and

contains a significant amount of air [12]. The corresponding loss tangent shown in Figure 4.22 range from 0.05-0.12 from 2-20 GHz, for which the loss is significantly higher compared to RO3006 by an order of magnitude. However compared to other textile substrates [33, 162], the loss tangent lies in a similar order of magnitude. The implication is that Tyvek is a lossy substrate, defined by $\tan\delta > 0.05$ [163], and an intermediate layer of dielectric is required (between the trace and the substrate) to alleviate the substrate loss.

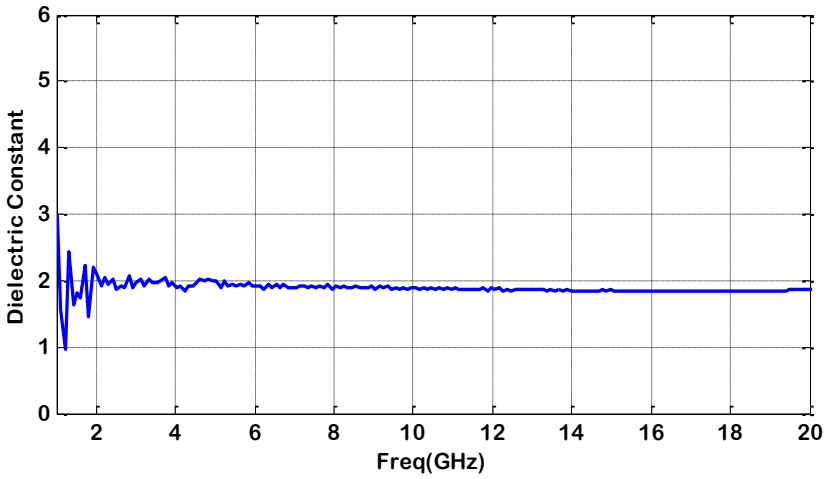

Figure 4.21 Extracted dielectric constant versus frequency for Tyvek

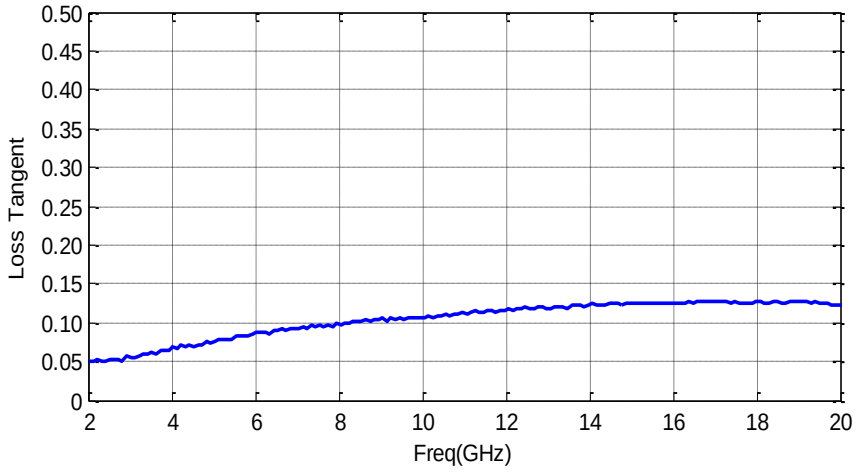

Figure 4.22 Extracted loss tangent versus frequency for Tyvek

(b) Repeatability of Results

To ascertain the repeatability of the results, the same design was measured on a second Tyvek substrate (i.e. panel). A typical panel is shown in Figure 4.9(D). The measured parameters are shown in Table 4.4. The dielectric properties were then extracted using the same procedure for the first panel and the results compared.

Table 4.4 Measured parameters of a 2 mm CPW structure on panel 2 (with reference to Figure 4.11)

Trace Parameters	Values	Remarks
Target g_1/w/g_2	350/ 100/ 350 μm	Design value
Actual g_1/w/g_2	324/ 109/ 338 μm	Measured value, averaged
θ_{1a} , θ_{1b}	36.7°, 40.4°	Lower signal trace angles
θ_{2a} , θ_{2b}	18.7°	Lower ground trace angles
θ_{3a} , θ_{3b}	20.2°	$\theta_{2b} = \theta_{2a}$ and $\theta_{3b} = \theta_{3a}$ in simulation model.
R_a of signal trace	1.7 μm	Using a cut-off wavelength of 0.25 mm
R_a of ground plane	1.2-1.3 μm	
Trace thickness, t	27 μm	Averaged value
Average DC conductivity	1 x 10^6 S/m	Averaged value
Skin depth	3.6 μm	At 20 GHz

From the results in Figure 4.23, there is a good repeatability in terms of the extracted dielectric constant for Tyvek. However, a significant variation is observed for the loss tangent values extracted for the 2 panels as shown in Figure 4.24. The extracted loss tangent for panel 1 ranges from 0.05-0.12 over 2-20 GHz. However panel 2 yields a significantly lower loss tangent of 0.01. This variation is attributed to a difference in the Z_0 values of the structures, as shown in Figure 4.25. Though both structures have similar printed dimensions, the Z_0 values between the two structures vary by 15-20 Ω from 0.1-20.1 GHz. In addition, the Z_0 values were observed to deviate by 20-50 Ω from the simulation model which was modelled without any air gaps (Figure 4.25).

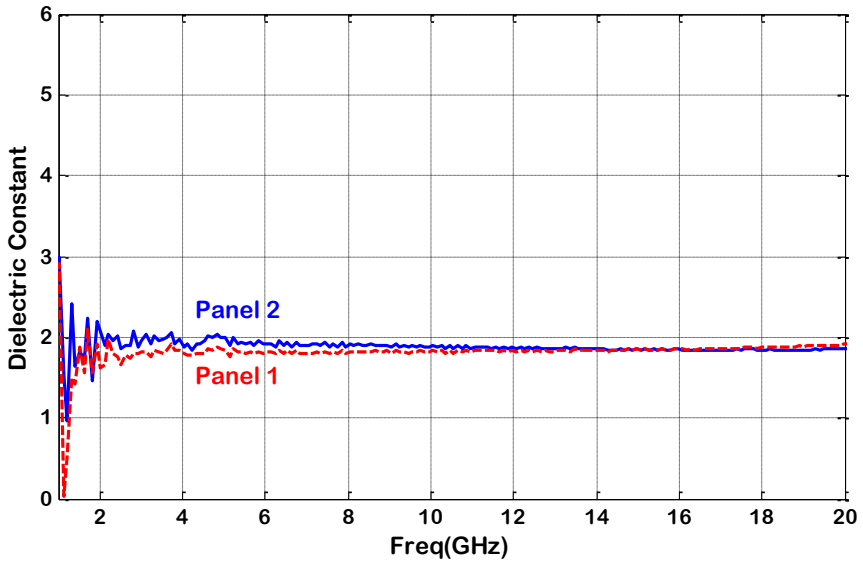

Figure 4.23 Extracted dielectric constant versus frequency for the Tyvek panels. A typical panel is shown in Figure 4.9(D)

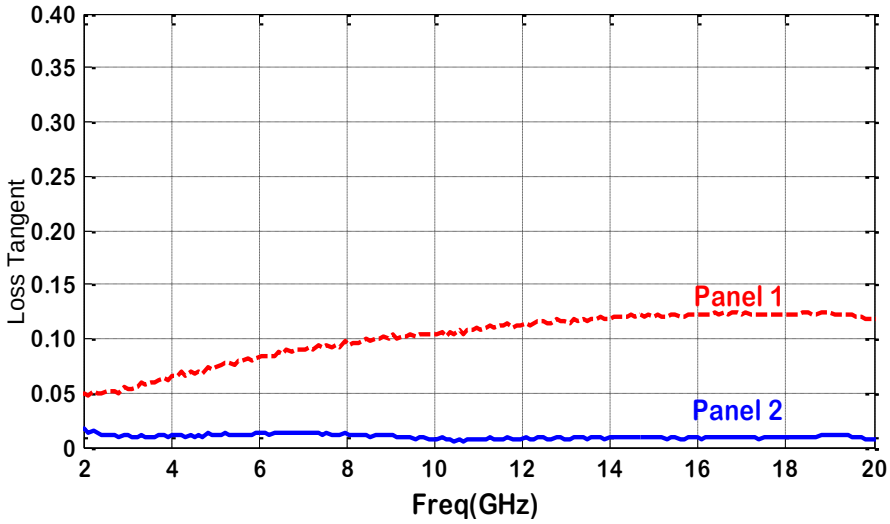

Figure 4.24 Extracted loss tangent versus frequency for the Tyvek panels

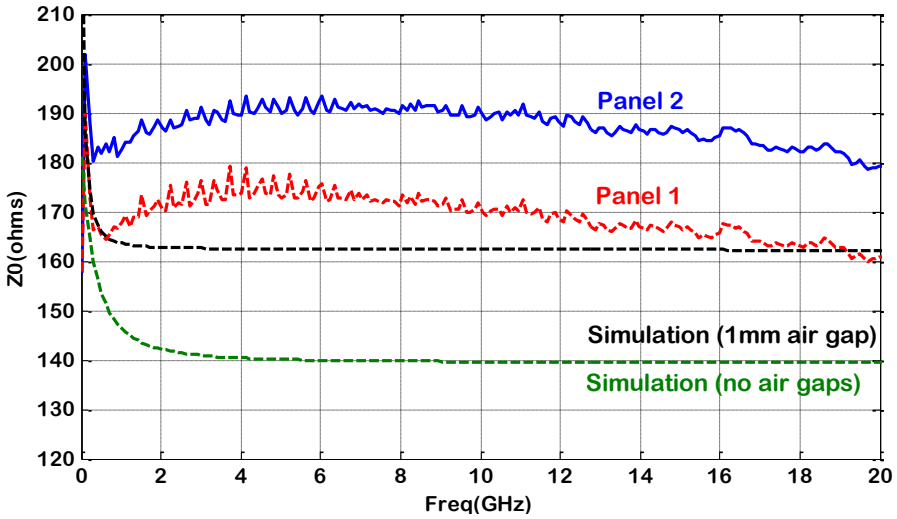

Figure 4.25 Comparison of Z_0 –Measurements versus simulation

The variation of the Z_0 values in Figure 4.25 could be due to the nature of Tyvek. As a textile material, Tyvek is flexible and compressible and the presence of air gaps underneath the substrate is inevitable if the vacuum suction is not sufficiently strong during measurements. This would in turn result in variable characteristic impedances along the transmission line [33]. The effect of air gaps reduces the overall capacitance (C) of the CPW structure. From equation (4.25), Z_0 would be increased, assuming the effects of resistance and conductance are negligible:

$$Z_0 = \sqrt{\frac{L}{C}} \tag{4.25}$$

where L represents the inductance of the CPW structure. The increase in Z_0 increases the impedance mismatch of the CPW structure with the RF probes, thus resulting in a higher insertion loss. As shown in Figure 4.26, the insertion loss variation between two structures of the same design printed on different panels is 0.5 dB at 20 GHz. When the air gap effect is accounted for in the simulation model as shown in Figure 4.25, a better match is observed between the Z_0 values for the simulation and measurement results.

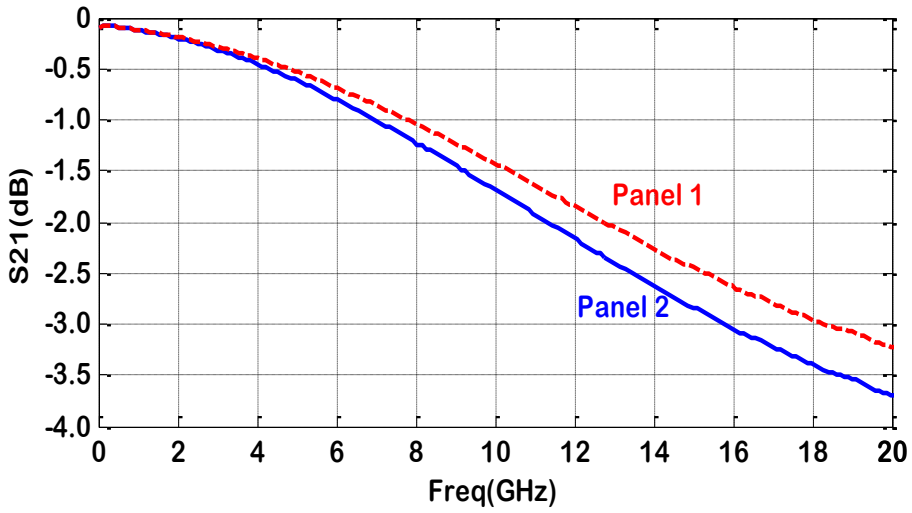

Figure 4.26 Comparison of the insertion loss between Tyvek panels 1 and 2

From the results obtained for Tyvek, the extraction of the dielectric constant using the approach by Lee *et al.* [116] is more robust as the technique is based on two lines of similar geometrical structure but with varying lengths. As such the effect of air gaps is being offset during the extraction procedure. On the other hand, the loss tangent extraction is based on the measured *S*-parameter results of a single CPW transmission line. While the Z_0 values from simulation and measurement are correlated, this value may vary for the same design measured on different panels due to the effect of air gaps. The extent of air gaps present would vary from panel to panel giving rise to the poor repeatability observed.

4.6.4 Uncertainty Analysis (Dielectric Constant)

Due to the variation observed for the extracted dielectric constant values, an uncertainty analysis was performed. Starting from equation (4.9):

$$\varepsilon_r = \frac{\varepsilon_{eff}'^{t}(1+f)-1}{f}$$

$$\Rightarrow \frac{\partial \varepsilon_r}{\partial \varepsilon_{eff}'^{t}} = \frac{1+f}{f}$$

$$\Rightarrow \partial \varepsilon_r = \left(\frac{1+f}{f}\right) \times \partial \varepsilon_{eff}'^{t}$$

$$\therefore \frac{\partial \varepsilon_r}{\varepsilon_r} = \left(\frac{1+f}{f}\right) \times \frac{\partial \varepsilon_{eff}'^{t}}{\varepsilon_r} \quad (4.26)$$

With reference to equation (4.26), f is defined by equation (4.8) and is a function of the structure geometry (i.e. trace width, gap and substrate thickness). The accuracy of the extraction for $\partial\varepsilon'^{t}_{eff}$ is dependent on the repeatability of the probe-to-CPW transition [116]. The calculated uncertainties using equation (4.26) are shown in Table 4.5.

Table 4.5 Variation of extracted dielectric constant values

Substrate	ε_r	$\partial\varepsilon'_{eff}$	f	$\frac{\partial\varepsilon_r}{\varepsilon_r}$ (%)
RO3006	6.5	0.2	1.02	6.1
Tyvek Panel 1	1.9	0.06	1.27	5.6
Tyvek Panel 2		0.05	1.28	4.7

From the results in Table 4.5, the uncertainty of the extracted dielectric constant lies within 10 % for both RO3006 and Tyvek, where the substrates were measured up to 30.1 GHz and 20.1 GHz respectively.

4.6.5 Validation with Resonant Cavity Technique

The results from the transmission line method were compared to the resonant cavity technique [164]. This method makes use of the shift in resonant frequency and quality factor to calculate the dielectric properties when a sample is placed in the cavity. Measurements are typically performed at only one or a few frequencies [164]. The cavity resonator used is as shown in Figure 4.27, where the samples were characterised at 2.45 GHz.

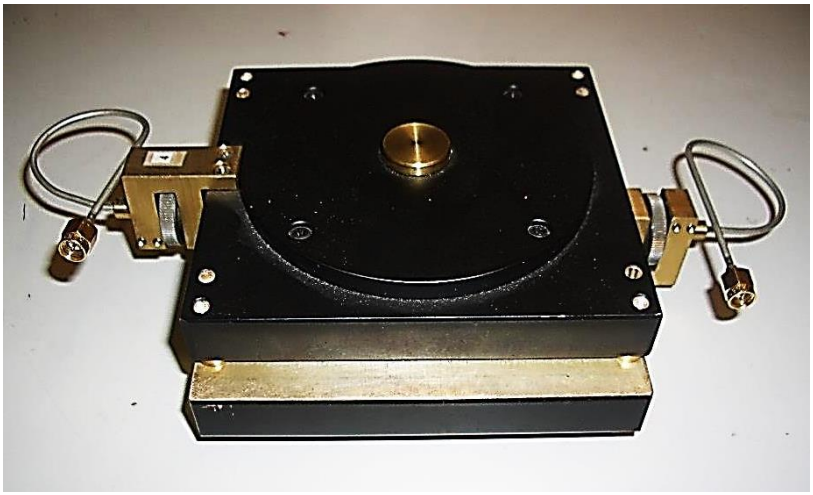

Figure 4.27 Setup of cavity resonator

For the RO3006 substrate, values of 6.81 and 0.00087 were obtained for the dielectric constant and loss tangent. The extracted dielectric constant is within 5 % of the data provided by the vendor, with a dielectric constant of 6.5 [31]. The corresponding loss tangent also agrees well with the loss tangent of 0.002 provided in the datasheet [31].

For Tyvek, the range of dielectric constant obtained using the resonant cavity technique is 1.46-1.53, with loss tangent values in the range of 0.0024-0.0072. The extracted loss tangent values are an order of magnitude smaller compared to the values obtained in Section 4.6.4. This variation may be due to the presence of air gaps in the cavity as the thickness of Tyvek (330 μm) is significantly smaller compared to RO3006 (1.28 mm). In turn this could have resulted in inaccuracies during the extraction using the resonant cavity technique.

4.6.6 Limitations of Proposed Methodology

The proposed methodology has a few limitations. The first lies in the surface impedance model used for the 3D simulation, in that this macro assumes for a 1D trace geometry, and does not take into account the conductor edge effects present in the printed traces. These conductor edge effects have been reported to affect the conductor loss [156], particularly for long transmission line lengths. To simulate for the actual 3D trace profile (with conductor edge) is possible but at the expense of significant computational time, since the skin depth is very small compared to the trace thickness and a fine mesh is required to capture the skin effect adequately.

In addition, a limitation exists in the modelling for the surface roughness in *CST*. The current model is based on the Hammerstad model [135], which considers trace roughness profiles with rectangular, triangular and square grooves [165] such as the profile shown in Figure 4.28(A) and Figure 4.28(B). However screen printed traces observed using SEM display spherical trace profiles (Figure 4.28(C)) which are formed by inter-particle necking during sintering. Consequently the trace continuity is affected by the degree of inter-particle neck formation and porosity of the resulting traces [18, 37, 166]. One implication of such printed trace profiles is that the Hammerstad model may not suffice, as the model is not valid for trace

profiles which are significantly different or where defects such as cracks are present in the traces [165].

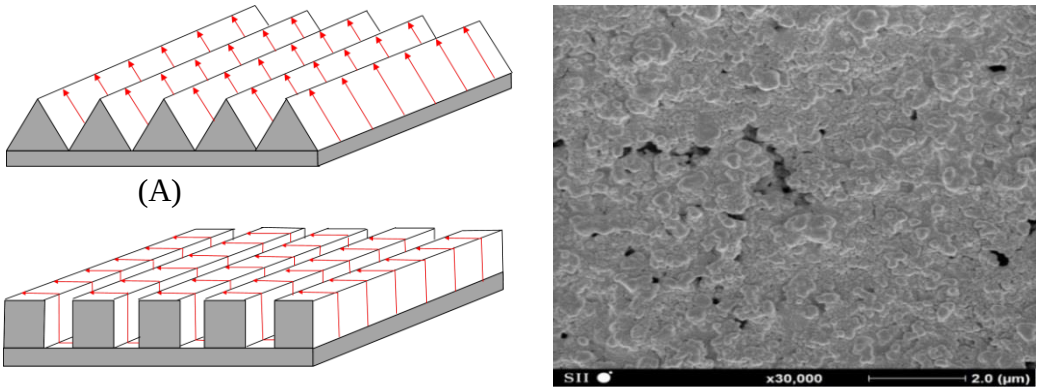

Figure 4.28 Surface roughness with (A) triangular profile; (B) square profile transverse to current flow (C) Top profile of screen printed traces after sintering

Lastly due to the analytical formula (based on transmission line structures) used to extract for the loss tangent, a significant variation of the extracted loss tangent was obtained for RO3006 from an uncertainty analysis performed in Section 4.6.2(b). Another technique which yields a smaller variation is required for the loss tangent extraction of low loss substrates.

4.7 Conclusions

In this work, a novel methodology was used to enhance the analytical approach for dielectric characterisation based on transmission line structures. This is since the conductor loss formulas available were not intended for calculating the transmission line characteristics beyond the higher gigahertz frequencies, and conventional analytical equations based on the quasi-static approach were found to underestimate the conductor losses beyond 20 GHz.

The approach was first validated on a high frequency laminate with well-characterised dielectric properties (RO3006), where a variation of 6 % was obtained for the dielectric constant compared to the manufacturer's data. The extracted loss tangent was an order of magnitude larger than the value specified in the datasheet. This is attributed to analytical formula (based on transmission line structures) used to extract for the loss tangent value. An uncertainty analysis in

Section 4.6.2(b) showed that the loss tangent variation, $\partial(\tan\delta)$, is increased significantly for substrates with low loss tangent values, where the loss tangent variation is a function of the effective dielectric constant variation $(\partial\varepsilon'_{eff})$ and the loss tangent $(\tan\delta)$. The implication in using transmission line structures for low loss substrates is that the loss tangent is over-estimated and a different characterisation technique is required. For Tyvek the loss tangent variation is expected to be lower, due to two factors. Firstly, Tyvek contains a significant amount of air, which implies that the effective dielectric constant is lower (shown in Table 4.5). Secondly the loss tangent of Tyvek is an order of magnitude higher compared to RO3006. Due to these factors, the resulting ratio $\frac{\partial\varepsilon'_{eff}}{tan\,\delta}$ which influences the loss tangent variation is lower for Tyvek.

The dielectric properties of Tyvek were extracted up to 20 GHz, due to the upper frequency limitations of the adaptors used in the measurement setup. Values of 1.9 and 0.05-0.12 were obtained for the dielectric constant and loss tangent. Compared to other textile substrates [33, 162], the loss tangent lies in a similar order of magnitude. However the implication is that Tyvek is a lossy substrate, defined by $\tan\delta > 0.05$ [163], and an intermediate layer of insulator is required between the metal traces and the substrate in order to alleviate the effects of the substrate loss. This aspect is further investigated through the use of surface modification techniques (detailed in Chapter 5), and subsequent studies on the overprinting of silver ink onto the insulator to obtain measurable resistances (detailed in Chapter 6).

To ascertain the degree of the results variation, an uncertainty analysis of the dielectric constant was performed. The variation of the dielectric constant for both RO3006 and Tyvek were observed to be within 10 %, for measurements up to 30 GHz and 20 GHz respectively.

Lastly, the limitations of the proposed methodology arising from the modelling aspect are discussed. For trace thickness on a similar order of magnitude compared to the skin depth (i.e. thin traces) and traces with significant surface roughness relative to the skin depth [129], a more sophisticated model is required to capture the conductor losses accurately.

Chapter 5. Surface Modification for Robust Line Trace Deposition onto Substrates – Overcoming Surface Roughness

5.1 Introduction

Following the dielectric characterisation of Tyvek in Chapter 4, the significant substrate loss requires the deposition of an insulator layer to alleviate the loss. In addition the inherent surface roughness of Tyvek necessitates an insulator layer to significantly planarise the substrate surface. To address these issues, surface modification using an UV-curable insulator [167] is considered in this chapter. The insulator is deposited via inkjet printing and has been selected because it has already been formulated for flexible substrates.

However a challenge in depositing an insulator layer on Tyvek lies in the porosity of the substrate. In inkjet printing onto Tyvek using silver ink, the silver nanoparticles were observed to penetrate into the fibres (Appendix A). Thus to simplify the analysis of the parameters affecting the deposition of a smooth planarisation layer, a non-porous reference substrate (RO3006) is used in this chapter. As RO3006 is a copper-cladded substrate, it reveals substrate roughness after the top metal layer is etched away, leaving copper dendrite imprints on the etched substrates. The degree of substrate roughness present on RO3006 is a trade-off for good adhesion of the cladded copper to the laminate.

In considering inkjet printing for high frequency applications, the presence of non-negligible substrate roughness would increase the printed interconnect losses at higher frequencies, due to the skin depth effect. As such, the first objective of the work considered in this chapter is to achieve lower surface roughness on RO3006 intended for the inkjet printing process, with the goal of decreasing the interconnect losses at higher frequencies. In particular, the use of a UV-curable insulator [167] is investigated to planarise the surface of RO3006 to alleviate the surface roughness. The resulting surface roughness was then compared to the

untreated RO3006 and RO3006 modified using a hydrophobic coating. The planarisation techniques are selected based on their compatibility with inkjet printing towards obtaining fine pitch traces, the requirements of which are described in Section 2.1 of Chapter 2.

The second objective of this chapter is to investigate the effect of substrate roughness on printed line widths deposited via inkjet printing. To date there is little literature addressing this issue in inkjet printing, as most researchers consider substrates with relatively smooth surfaces for the printing [22, 37, 95]. In addition, it is of interest to print onto an untreated substrate (i.e. with minimal processing), as this translates into a lower cost of production. In this chapter, inkjet printing trials were performed onto the untreated RO3006 substrates, and the results analysed in terms of the line width variation. Specifically the goal is to ascertain if the equation by Smith *et al*. [22] for estimating the printed line width is applicable for substrates with non-negligible roughness.

5.2 Materials

This section describes the materials used in the inkjet printing process. The substrate of interest is RO3006, which is subjected to surface modifications to planarise the substrate surface. Two silver inks with different surface tension values were used to overprint on the RO3006 substrate with/without surface modifications.

5.2.1 Substrates

The details of RO3006 can be found in Section 4.3.1 of Chapter 4, with the corresponding datasheets provided in Appendix B1 of this thesis.

5.2.2 Conductive Inks

For inkjet printing, two nanoparticle-based conductive silver inks were used with a Dimatix inkjet printer. The first [168] comprises of 30-35 wt % silver (DGP 40LT-15C, Advanced Nano Products), with a surface tension of 35-38 mN/m. The volume resistivity is 11-12 μΩ-cm at a curing temperature of 120-150 °C (duration of 30 min). The second ink [169] is a composition of 20 wt % silver (SunTronic

EMD 5603, Sun Chemicals), with a surface tension of 27-31 mN/m. The corresponding volume resistivity of this ink is 5-30 μΩ-cm at 150-300 °C (sintering duration of 30 min). Both of the inks were selected based on their compatibility with the inkjet printer and the surface modified substrates.

5.2.3 Substrate Modifications

To reduce the substrate roughness, the surface treatments considered for RO3006 for inkjet printing include: coating with a hydrophobic solution and ink-jetting an UV-curable insulator.

(a) Hydrophobic Coating

The use of a hydrophobic coating serves two purposes in this work. The first aim is to use the coating surface modification technique to deposit a thin insulator layer and planarise the substrate surface. The second aim is to investigate whether finer trace widths [91, 93] could be obtained with the hydrophobic coating, which would result in a higher contact angle of the deposited silver ink.

The hydrophobic coating considered was a 2 wt % fluorochemical acrylate polymer based in a hydrofluoroether solvent (EGC-1700, 3M Novec Electronic Coating). After application, the coating dries to a transparent film with a thickness of around 1 μm (by dip-coating) according to the datasheet [170]. The corresponding surface energy of the film is in the range of 11-12 mN/m. The measured contact angle of water onto the coating is around 134°. The coating was applied by brushing to minimise the contamination of the solution by the substrate.

(b) UV-Curable Insulator

An UV-curable insulator (Solsys Jettable Insulator EMD 6200, Sun Chemicals) was applied to the surface of RO3006. The aim of using EMD 6200 is deposit a planarisation layer (Figure 5.1), in this case via inkjet printing. EMD 6200 is a research sample, with an ink viscosity of 7-9 mPas at 45 °C and a surface tension of 23-27 mN/m. At a temperature of 25 °C, the ink viscosity is 10-30 mPas with a relative density of 1.02-1.1 [167].

Figure 5.1 Cross-section of surface modified RO3006, with EMD 6200 deposited as planarisation layer

(c) Abrasive Sheet

To investigate the effect of surface roughness on the printed line widths, a silicon carbide abrasive paper backed sheet [171] was used (Norton T489) to roughen the substrate surface. The abrasive sheet has a grit range of P1200 and average particle sizes of 15.3 ± 0.1 µm. The sheet dimensions are 229 mm x 279 mm.

5.3 Experimental Procedure

5.3.1 Sintering Conditions

The RO3006 substrate has a melt temperature of 327 °C [172], which does not pose a problem in the curing of the conductive tracks at the recommended sintering conditions. The printed tracks were sintered at 180 ºC for 40 min.

5.3.2 Inkjet Printing

A commercial drop-on-demand mode inkjet printer (DMP 2831, Fujifilm Dimatix Inc.) was used for the printing with a 10 pl print head, as shown in Figure 5.2. The printing cartridge comprised of 16 nozzles. Prior to printing onto the surface modified substrates, a characterisation process of the inkjet printing using the Dimatix printer was performed. The results of the characterisation process are detailed in Appendix C1 of this chapter.

In the printing of conductive inks onto the surface modified substrates, a single jetting head with a 5 kHz waveform was used. The silver inks were jetted out at temperatures of 25 ºC (DGP 40LT-15C and EMD 5603). The separation of the cartridge from the substrate was set at 0.8 mm. The dot spacing (Δx) was set at 20

µm (in both x and y direction as shown in Figure 5.2) and the substrate was heated at 60 ºC (platen temperature) during the printing of the silver ink to aid in the solvent evaporation of the deposited drops. The substrates were held in place on the platen via suction through vacuum holes on the platen.

The test patterns for printing were created in DMP-2831 through the Pattern Editor function, which allows one to input the trace width and spacing dimensions for a test pattern or a group of test patterns. This function also enables a repetitive array of pattern blocks to be printed, and was utilised to realise the test structures in Appendix C1. Apart from the Pattern Editor, one can also import bitmap and gerber file formats into DMP-2831. In this case the resolution for the drop spacing needs to be defined in the bitmap file prior to importing (e.g. 20 µm drop spacing corresponds to a resolution of 1270 dots per inch). Figure 5.2 shows a schematic of the drop spacing in the definition of a printed line, and how a printed line width would compare with the line width defined in Dimatix. Further details of the line width variation for different defined widths on a substrate are described in Appendix C1.

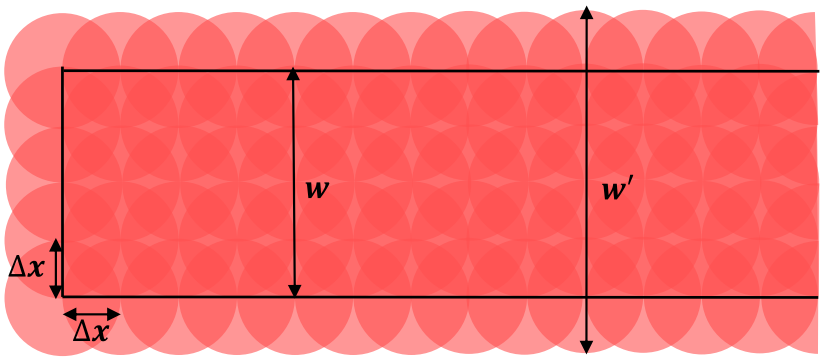

Figure 5.2 Schematic of a printed line of width *w'* compared with the size (*w*) established in the Pattern Editor function in Dimatix

5.3.3 UV Coating Parameters

To obtain a smooth coating of the EMD 6200 onto RO3006, several printing trials were considered. These trials were performed to evaluate the effects of different curing intensities and platen temperatures.

The UV lamp used (PEL365, Printed Electronics Limited) for the curing of EMD 6200 is a 365 nm light-emitting diode (LED) as shown in Figure 5.3. Prior to printing using the UV ink, the cartridge printhead was manually covered with a red tape to limit the UV exposure to the ink while it is in the fluid module. In addition, due to the separation between the UV unit and the print cartridge, the pattern file to be printed was modified with a 90 mm offset such that the UV unit would travel far enough to expose the desired pattern. Prior to the UV curing, the cure dosages (mJ/cm^2) were measured using a UV intensity meter (Integration Technology). This meter measures for the cure dosage of a circular footprint of 1 cm^2 as the UV lamp moves across the area.

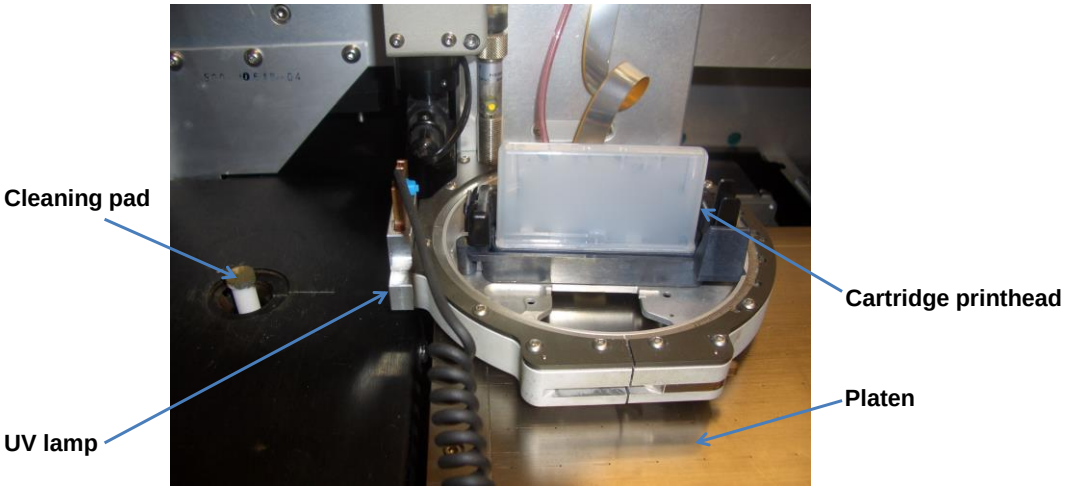

Figure 5.3 UV lamp attached beside Dimatix printhead

Prior to the printing trials described in Table 5.1, the jetting waveform (at 5 kHz) for EMD 6200 was adjusted to minimise satellite drops. In addition, the drop velocity for EMD 6200 was tuned to 7 m/s for the jetting process. The ink was jetted at a temperature of 45 ºC as recommended in the datasheet. For the curing stage, a dosage (un-doped mercury) of 200-400 mJ/cm^2 was recommended for the processing of EMD 6200 [90]. The cure intensities obtained for levels 1, 2 and 3 using the UV lamp are 831 mJ/cm^2, 1359 mJ/cm^2 and 2048 mJ/cm^2 respectively, following which a colorless coat was observed after curing. The time duration for curing a footprint of 4 x 1 cm^2 is around 14 min. To obtain a smooth coating, several printing trials were considered. These trials were performed to evaluate the effects of different curing intensities and platen temperatures. The respective process parameters are summarised in Table 5.1.

Table 5.1 Printing trials involving different curing levels and platen temperatures

Trial No.[1]	No. of coat(s)[2]	UV cure level[3]	Platen Temperature (°C)	Curing Condition
1	1	1	25	In-line
2	1	1	60	In-line
3	1	2	60	In-line
4	1	3	60	In-line
5	2	2	60	In-line
6	2	1	60	In-line & Off-line[4]
7	2	1	60	In-line

[1]The printed area coverage is around 4 x 1 cm in each trial. [2]Colorless coating observed after curing. [3]The corresponding cure intensities are provided in Section 5.3.3. [4]For the off-line curing, 3 rounds of raster curing was used.

5.3.4 Contact Angle Measurements

Contact angle measurements with different liquids were performed to ascertain the surface energy of the surface modified substrates as well as the ink-substrate interaction. The first involved measuring the contact angles of water (triply distilled water) onto the surface modified substrates. In addition, the contact angles of another reference liquid (diiodomethane) on the substrates were obtained, following which the surface energies of the surface modified substrates could be extracted using the Owen-Wendt-Rable-Kaelble method [142], as shown in Table 5.2. The surface energy of the hydrophobic coating calculated using two reference liquids was around 10 mN/m, which agrees well with the value provided in the datasheet.

Table 5.2 Contact angle values measured for untreated and surface modified RO3006 substrate using water (triply distilled) and diiodomethane

Surface Treatment Applied	Measured Contact Angle (°)[5]		Measured Surface Energy (mN/m)[6]
	Water	Diiodomethane	
Untreated RO3006	118.3	90.1	14.6
Hydrophobic coating	134.1	96.6	9.9
EMD 6200 coating	92.9	21.0	48.0

[5]Averaged contact angle measurements. [6]Surface energy calculated using the Owens-Wendt-Rabel-Kaelble method.

The contact angle measurements using the two reference liquids were performed using the Dataphysics OCA 20 instrument (DataPhysics Instruments GmbH, Germany). The droplet volumes used in the measurements were 2.0 µl and a minimum of five measurements were obtained for each reference liquid on the surface modified substrates [142].

In addition, contact angle measurements to ascertain the ink-substrate interaction were performed using a Fibro Dat 1100 contact angle tester (Fibro System AB, Sweden). A minimum of three measurements were obtained for each surface modified substrate, recorded after 10 s following the droplet deposition. The droplet volumes used in the measurements were 4.0 ± 0.5 µL. The measured contact angles (averaged) of the silver inks with the various surface modified substrates are shown in Table 5.3.

Table 5.3 Measured contact angles for untreated and surface modified RO3006 substrate

Surface Treatment Applied	Measured Contact Angle (°) - Silver Inks
Untreated RO3006[7]	47
Hydrophobic coating[7]	76
EMD 6200 coating[8]	50

[7]Using DGP 40LT-15C silver ink (Advanced Nano Products). [8]Using EMD 5603 (Sun Chemicals)

5.3.5 Surface Profile Characterisation

The surface roughness of the printed traces were characterised using a non-contact technique, based on the confocal gauge point principle (Talysurf CLI 2000, Taylor Hobson). This technique is considered to be more suitable than contact techniques for soft substrates, as RO3006 is PTFE-based. This equipment is typically used for step height (i.e thickness) measurements and surface roughness characterisation. The measured data were subsequently post-processed with a 3D analysis software (Talymap, Taylor Hobson).

The measurement range used for the surface modified RO3006 samples was 300 µm, with a resolution of 10 nm. Evaluation lengths of 3 mm were used for the characterisation, with the sampling spacing set at 0.5 µm. During the post-

processing, a Gaussian filter size cut off of 0.8 mm was used, which is the recommended cutoff according to ISO 4288-1996 [173]. This cut off also represents the sampling length, following which an evaluation length of 3 mm yields a sample size of 4. The surface roughness was measured at different areas of the substrate, and a total of 11 measurements were obtained and averaged. A summary of this characterisation process is shown in Figure 5.4.

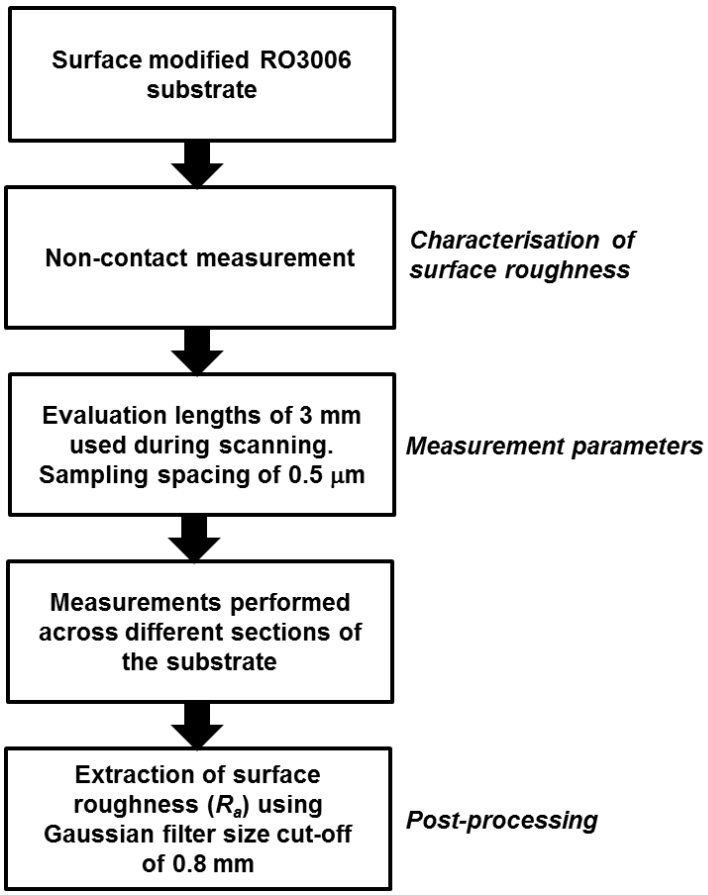

Figure 5.4 Surface morphology characterisation process

High resolution field emission gun scanning electron microscope (FEGSEM) images (1530 VP, Carl Zeiss) of the surfaces were used to aid in the qualitative analysis of the inkjet printed traces after curing. This equipment is able to capture surface features of materials up to a resolution of 1 nm, which is useful for imaging the nano-particle sized silver ink deposited using inkjet printing.

5.3.6 Sample Preparation for Analysis

The RO3006 samples were prepared for FEGSEM analysis using a PCB cutter with a guillotine blade. This was found to yield more consistent even edges compared to immersing the RO3006 substrate in liquid nitrogen and snapping it, due to the thickness of the substrate (1.28 mm). However, one challenge in using the PCB cutter lies in that some of the samples obtained were partially bent, due to the PTFE composition of the RO3006.

5.4 Results and Discussion

This section describes the results obtained on RO3006 substrate. This includes the optimisation of the printing parameters to reduce the surface roughness of RO3006 using a UV-curable insulator. The surface morphology characterisation results and the effect of surface roughness on the printed line widths are also described.

5.4.1 Printing Results on Untreated RO3006

This section presents the results of overprinting silver ink onto the untreated RO3006. In particular, two point probe structures were printed to extract for the resistivity values. These structures were selected as a compromise between the accuracy of the results obtained, against the time required to print more complex four point probe structures.

The test structures are shown in Figure 5.5, and Table 5.4 shows the dimensions defined in Dimatix via an imported bitmap file. The test structures were overprinted with two silver layers, and thermally cured at 150 °C for 30 min (for 2 rounds), in order to ascertain the effect of time on the resistivity values. Prior to the thermal curing, the substrate was left overnight (12 h) on the heated platen at 60 °C after the printing was completed. The measured resistance and corresponding resistivity values are shown in Table 5.5.

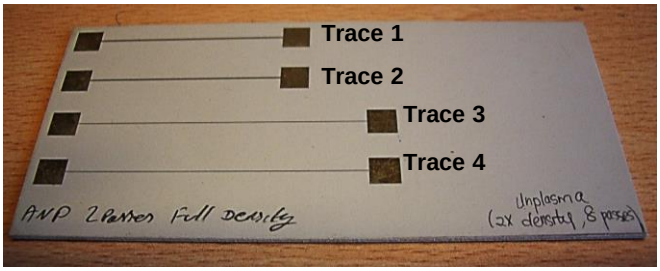

Figure 5.5 Printed two point probe test structures

Table 5.4 Dimensions of two point probe structures defined in Dimatix

Trace (s)	Line width (µm)	Line length (mm)
1,2	**250**	**35**
3,4	**100**	**50**

Table 5.5 Extracted resistivity values for 2 layers of overprinted silver on untreated RO3006

Trace[9]	Printed width (µm)	Trace Thickness (µm)	Resistance, 60°C platen (Ω)	Resistance after 1st cure (Ω)	Resistance after 2nd cure (Ω)	Extracted Resistivity (Ω-cm)
1	267	3.0	-	19.8	18.1	4.18E-05
2	250	2.7	34.0	18.4	17.4	3.41E-05
3	111	2.6	147.0	73.5	70.2	4.00E-05

[9]Trace notation is with reference to Figure 5.5.

From Table 5.5, the variation of the printed trace widths from the defined values ranged from 6.8-11 %. These printed line widths may be influenced by the surface morphology of RO3006, since it has been reported that the substrate surface roughness changes the contact angle of liquid drops [144]. Specifically, the relationship between the substrate surface roughness and the printed line width is investigated further in Section 5.4.4.

Furthermore, the resistance values in Table 5.5 indicate that leaving the substrate on the platen to cure for an extended period of time does not aid a sufficient sintering of the nanoparticles, since this process is also dependent on the sintering temperature. However, heating the substrate at a lower temperature (60 °C) could possibly have aided the evaporation of the solvents from the printed traces, which would facilitate the nanoparticle sintering when the substrate was placed in the oven. This is observed from the resistance values after two rounds of thermal

sintering at 150 °C, where the resistance variation was observed to be negligible (≤ 5 %). This suggests that the nanoparticle sintering may have reached saturation.

In characterising for the trace morphology, it was challenging to distinguish between the trace thickness and the substrate roughness of RO3006, since the trace thickness was about 2-3 µm and the average substrate roughness was around 0.6-0.7 µm (i.e. around the same order of magnitude). The substrate profile of the untreated RO3006 along with the printed trace profile is shown in Figure 5.6. To alleviate the surface roughness of RO3006, a UV-curable insulator was used to modify the substrate surface. This is further discussed in Section 5.4.2 of this chapter.

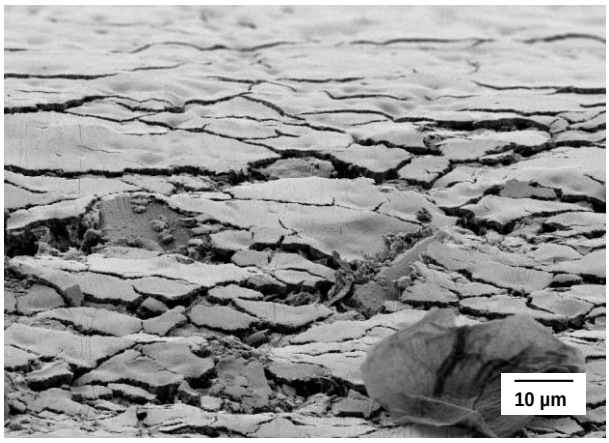

(A)

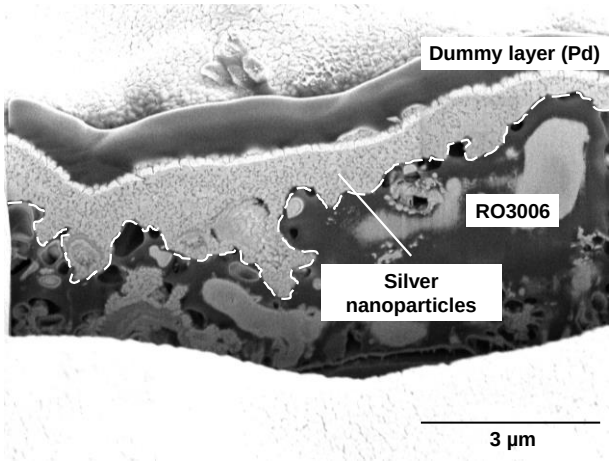

(B)

Figure 5.6 SEM images showing (A) RO3006 profile (B) overprinted silver trace profile on RO3006

Lastly the effect of overprinting multi-layer silver on the resulting trace parameters was investigated. From Table 5.6, when the number of overprinted silver layers was increased from 2 to 4, the thicknesses of traces 1 to 4 were observed to increase by 0.7-1.7 µm, where the increase was non-proportional to the number of overprinted silver layers. Assuming that the deposited ink volume is constant [22], and that the cross-sectional areas of each overprinted layer will be the same, this non-proportionality may arise from the corresponding increase in the printed trace widths. The printed trace widths were observed to increase by a factor of 1.4-1.9 times (from Table 5.6), which could have offset the increase in the trace thickness. In particular, the second to fourth silver layers were each overprinted after 30 min intervals, with the substrate left on the heated platen at 60 °C during and after printing. Consequently the silver layers may not be fully dried at 60 °C, as verified from the resistance results in Table 5.5. As such there may be an absence of a (or a weak) contact line pinning in the first silver layer to constrain the width of the subsequent overprinted layers [174]. Overall the results obtained highlight the importance of the sintering temperature to obtain sufficient nanoparticle sintering, and to control the trace morphology (line width). Studies by Xu *et al*. [174] show that if each silver layer has dried prior to the overprint of the next layer, the trace width will remain unchanged with increasing layers of overprinted silver.

Table 5.6 Extracted resistivity for printed traces on untreated RO3006

Trace[10]	Trace thickness (2 layers, in µm)	Trace thickness (4 layers, in µm)	Printed width (2 layers, in µm)	Printed width (4 layers, in µm)
1	3.0	4.7	267	360
2	2.7	3.3	250	376
3	2.6	3.3	111	208
4	2.4	3.7	118	208

[10]Trace notation is with reference to Figure 5.5.

5.4.2 UV Curing of EMD 6200 on RO3006

This section details the investigation on the effect of the platen temperature and curing level on the surface roughness of the deposited EMD 6200 layer. A single layer coat of EMD 6200 deposited on RO3006 was first studied to understand the interaction between EMD 6200 and the substrate. This is detailed in Section 5.4.2

(a). Subsequently optimisation trials were performed for a double layer coat and the results discussed in Section 5.4.2(b).

(a) Effect of Platen Temperature and Cure Levels

In Trials 1-3 from Table 5.1, the effects of the platen temperature and curing levels were investigated for a single layer coat. The ink-substrate interaction can be better understood through a consideration of the *Z* number. The *Z* number is the inverse of the Ohnesorge number (*Oh*), and relates the viscous forces to the inertial and surface tension forces. This parameter is used as a dimensionless analysis of the effect of the ink properties on the drop formation [175-177], i.e. the printability of a fluid. A difference in the ink viscosity results in a change of the *Z* number and the corresponding droplet volume [178]. From equation (5.2),

$$Z = Oh^{-1} = \frac{\sqrt{\gamma \rho a}}{\eta} \tag{5.2}$$

where γ, ρ and η are the surface tension, density and viscosity of EMD 6200, with the respective values provided in Section 5.2.3(b). *a* represents the characteristic length, which is defined as the nozzle diameter in this case. For a 10 pl cartridge, the nozzle diameter is calculated to be around 27 µm. At 25 °C, which approximates the platen temperature without heating (room temperature), the calculated *Oh* is 0.75 for an average ink viscosity of 20 mPas (viscosity range from 10-30 mPas). The reciprocal *Z*=1/*Oh* yields a value of 1.33, which is close to the lower bound for stable drop formation, where $1 < Z < 10$ [179]. The value of the *Z* number increased to 3.33 at a higher temperature of 45 °C with an ink viscosity of 8 mPas (viscosity range from 7-9 mPas).

In printing with the platen temperature at room temperature (18-20 °C), the ink was found to de-wet upon contact with RO3006, due to a mismatch of the surface energies (Figure 5.7(A)). One possible way to reduce the de-wetting would be to lower the viscosity of the deposited ink, by heating the platen to aid in the degree of spreading [178]. From the data in Section 5.2.3(b), EMD 6200 is observed to have a reduced viscosity of 7-9 mPas at a temperature of 45 °C, compared to a

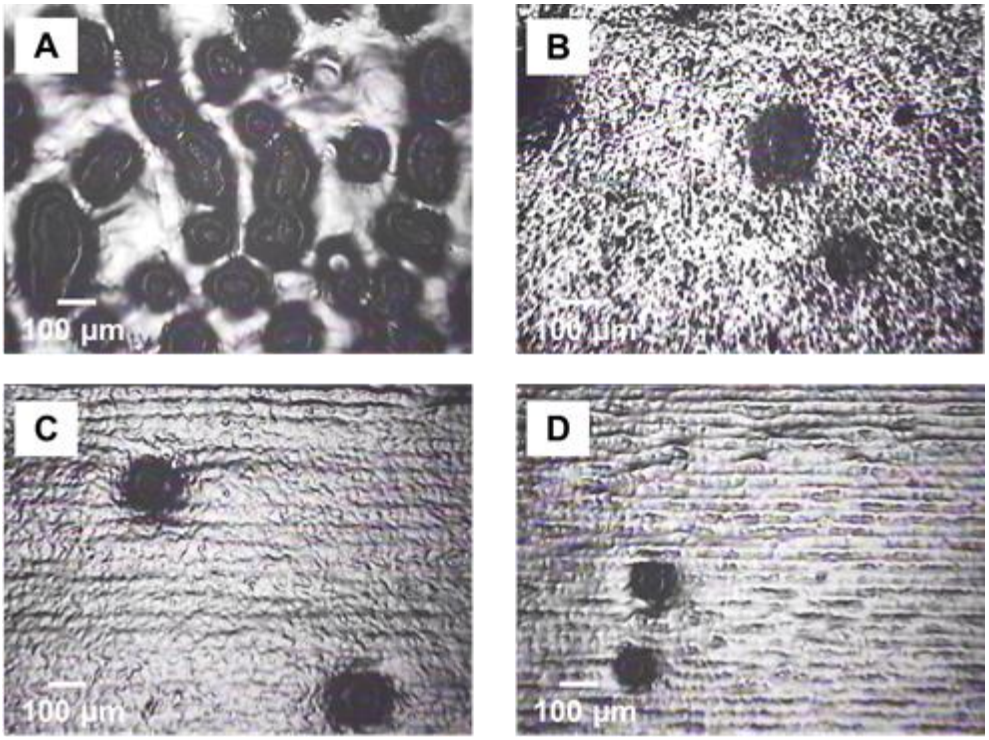

Figure 5.7 (A) Ink de-wetting phenomenon in Trial 1 (B) Improved wetting in Trial 2 (C) Trial 3 (D) Trial 4 Colorless coats were observed after curing

viscosity of 10-30 mPas at 25 °C. Therefore, the platen was heated to a maximum temperature of 60 °C to increase the mobility of the ink, and improve the ink-substrate interaction. From Figure 5.7(B), it can be observed that the de-wetting phenomenon could be reduced with platen heating. This is consistent with the works of Gao *et al.* [180] and Schiaffino *et al*. [181], where it was suggested that a printed bead is likely to become unstable under conditions of a higher contact angle and/or contact line freezing, induced by a lower target temperature as one of the key determinants [180]. In their work [180], molten droplets were deposited onto a surface with varied temperatures. These solidify upon contact with the surface since the target temperature (T_f) is lower than the jetting temperature (T_j). This work bears some resemblance to those of Gao *et al*. [180], in that the ink also undergoes solidification (albeit through a photochemical process), and the platen temperature is varied. In this case $T_{j1} < T_f < T_{j2}$, where T_{j1} represents room temperature (18-20 °C) and T_{j2} represents a platen temperature of 60 °C. Apart from Gao *et al*. [180] and Schiaffino *et al*. [181], Bhola *et al*. [182] has also investigated the effect of varying the substrate temperature (23 °C to 73 °C) on the

the spread of molten droplets. It was suggested that a reduction of the substrate temperature would result in an increase in the liquid viscosity [182], leading to reduced wettability (and vice versa). In addition, the lower substrate temperature would induce a solidification of the liquid adjacent to the substrate, which could limit the droplet spreading [182].

The de-wetting observed for EMD 6200 at room temperature could also be attributed to the surfactant package of the UV-curable ink, which affects the ink wettability. From literature, Rebros *et al.* [183] noted that the variation of a surfactant results in a significant change of the contact angle [183]. From the ink formulation perspective, EMD 6200, being an UV ink (100 % solids), has no solvents to be removed. As such, an increased spreading with a lower ink viscosity is aided by the relatively faster solidification through UV curing. This is in contrast to solvent-based silver inks which require a removal of the solvent contents by evaporation. As the solvent contents are reduced, the silver particles are less inclined to wet the substrate surface. On the other hand, the results for EMD 6200 suggest that the surfactant package of EMD 6200 promotes a wetting of the substrate surface [184], as the mobility of the ink particles increases due to a lower ink viscosity.

Following on the results in Trials 1 and 2, an increase of the curing levels in Trials 3 and 4 (from Table 5.1) was observed to yield continuous coats. However the surface texture of the coated layers were observed to deteriorate with increased cure dosage, i.e the coated dielectric has a surface roughness relative to the level of UV energy used (Figure 5.7(C), (D)). In addition, surface defects were visible throughout the coated layers in all 4 cases, which could be due to the low ink viscosity, following which any contamination on the surface would provide a locus for the de-wetting of the ink.

It was important to minimise the effects of surface defects, which could result in discontinuities of the printed traces. This led to the approach of building up layers of EMD 6200 by printing a second coat, so as to cover the surface defects. To obtain a smooth coating using this approach, it is important to optimise the control of the UV dose as this affects the curing of the insulator layer. Optimum conditions

of the UV curing were achieved in Trials 5-7 (Table 5.1).

In Trial 5, the effect of using an intermediate setting (cure level 2) was studied for a double layer coat, which was printed after the in-line curing for the first coat was completed. Compared to the first coat, the second coat revealed a visibly rougher surface, which could be due to the higher curing dosage at level 2. Similarly, when off-line curing for each of the layers was introduced in Trial 6, a visibly rougher surface was observed after the off-line curing of the second coat (Figure 5.8(A), (B)). This could be due to an over-curing of the layers during UV exposure, resulting in an excess hardening of the coated layer [185]. The use of a lower curing level (level 1) for both coats in Trial 7 was found to significantly improve the final coated surface (Figure 5.8(C), (D)).

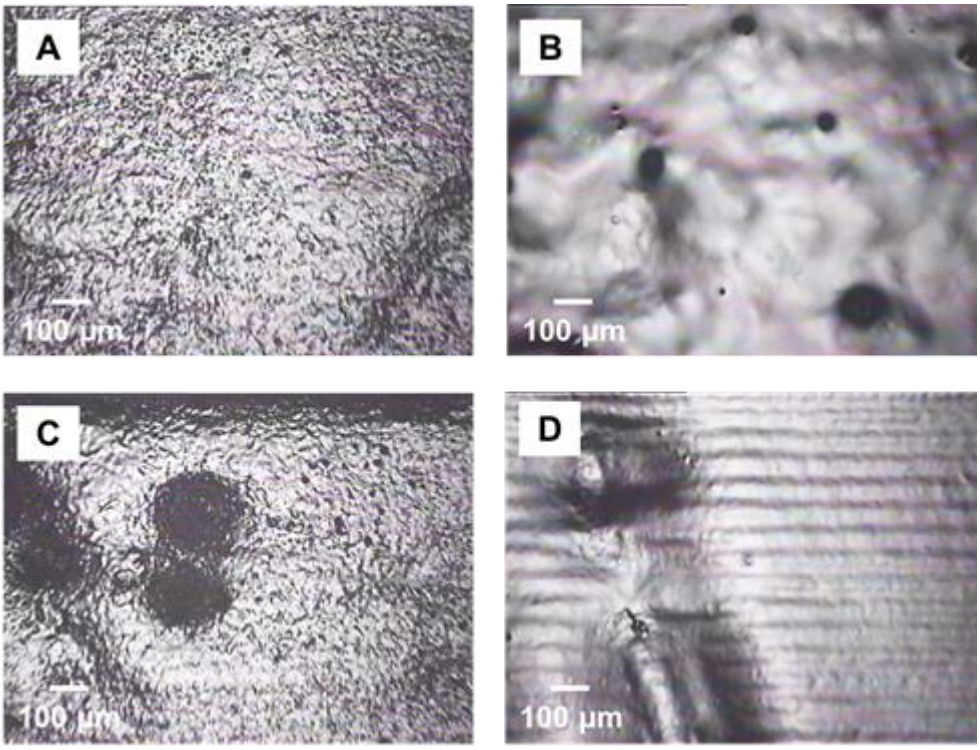

Figure 5.8 (A) Trial 6 – First coat after off-line curing (B) Trial 6 - Second coat after off-line curing (C) Trial 7 – First coat (D) Trial 7 – Second coat Colorless coats were observed after curing

The average surface roughness (R_a) for Trial 7 was 0.52 µm. The coated thickness has a slightly concave profile, and the thickness profile characterisations show that the surface of the printed dielectric has a non-uniform height, where the height at

the edges is higher than the height in the center region. This may be attributed to the coffee stain effect [186], where the fluid flows outwards to compensate for the evaporative effect for a pinned contact line. Further investigations would be required to better understand this phenomenon but this is outside the scope of this research.

(b) Optimisation for a Two Layer Coat using EMD 6200

As an extension of the experiments in Section 5.4.2(a), the effects of different platen temperature and cure levels on the coated thickness of EMD 6200 were investigated. The platen temperature was varied between 30-60 ºC, in steps of 10 ºC, while the cure levels considered were level 1,1 and 1,2, for the first and second coat respectively. The rationale for considering a two stage curing is to under-cure the first layer (cure level 1), followed by a curing of both layers simultaneously. The results obtained are shown in Figure 5.9.

A few implications can be deduced from the results in Figure 5.9. Firstly, it was observed that a minimum temperature of 30 ºC is sufficient to improve the ink mobility and minimise the de-wetting phenomenon (Figure 5.10(A), (B)). From Figure 5.9, the thicknesses of EMD 6200 are comparable when the platen temperature is set at 60 ºC, regardless of the cure levels.

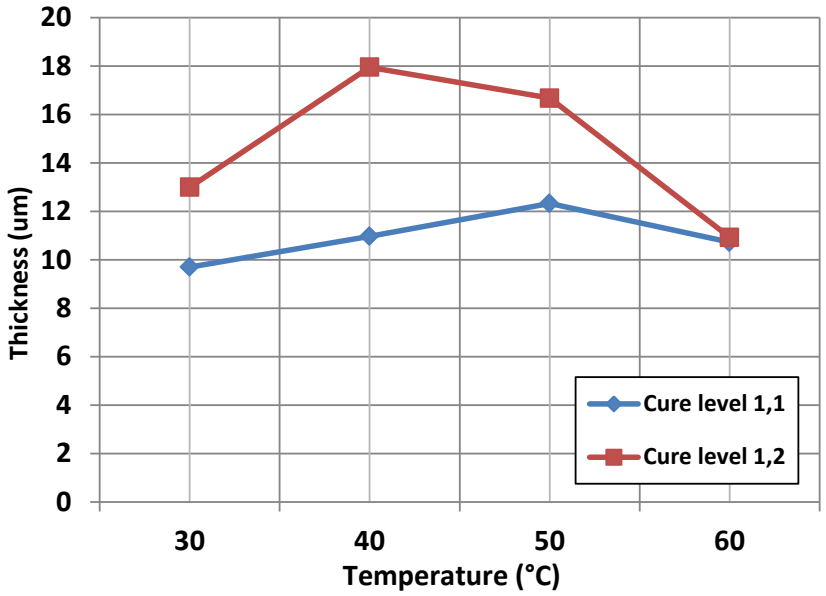

Figure 5.9 Effects of platen temperature and UV cure levels on the cured EMD 6200 thickness

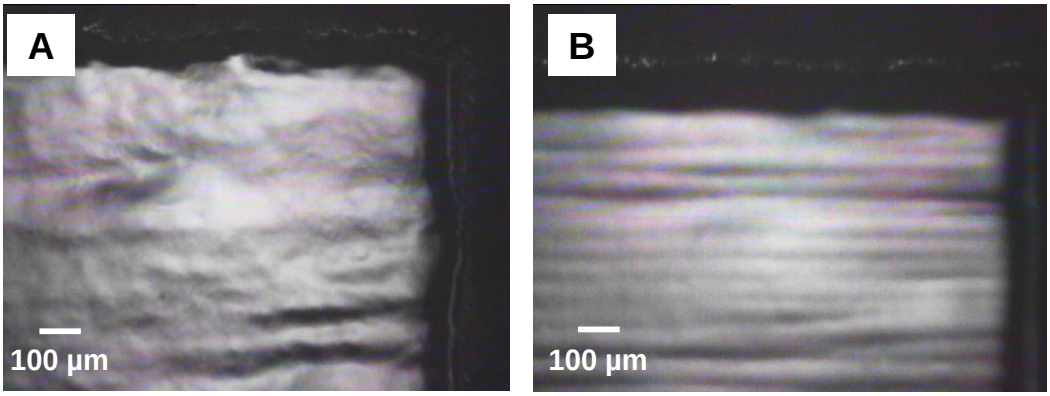

Figure 5.10 Coated EMD 6200 with platen temperature set at 30ºC, cure levels 1,1 (A) After first coat (B) After the second coat

At lower platen temperatures (40-50 ºC), an increase in the coated thicknesses was observed with a higher cure dosage (level 1,2). This phenomenon could be attributed to a reduced coffee stain effect [186], where a lower platen temperature results in a slower rate of evaporation of the volatiles in the ink prior to UV curing. Combined with a stronger cure level, the ink components would be cured at a faster rate.

Further results in Table 5.7 also suggest that the cured EMD 6200 is sensitive to the effects of heating, resulting in a thicker layer. The table shows the average thickness of EMD 6200 before and after thermal curing (150 ºC, 30 min).

Table 5.7 Average thickness of EMD 6200 before and after thermal curing

Platen Temperature (ºC)	Cure Level	Average Thickness (µm)
40	1,1	20.3[11]
40	1,1	10.4[12]
40	1,2	23.6[11]
40	1,2	18.0[12]
30	1,2	25.3[11]
30	1,2	13.0[12]

[11]Before thermal curing. [12]After thermal curing.

A significant reduction of the thickness by at least 20 % was observed in the post curing stage. As the ink is 100 % reactive, this suggests a possible shrinkage of the cured matrix. As the matrix is a polymer with some degree of porosity and a glass

transition temperature, this shrinkage could be due to the expulsion of air as the polymer softens and compacts. In addition, RO3006, being an unreinforced ceramic-filled PTFE material, was found to warp after the thermal sintering. This was because the substrate was etched to remove the top copper layer and was exposed to elevated temperatures. The warpage of RO3006 went beyond the upper limit of 106 µm (fine range) when measured with a contact stylus (Talysurf CLI 2000, Taylor Hobson). One implication of this substrate warpage would be in the fabrication of multi-layer circuits based on inkjet printing, where misalignment issues may arise in attempting to align one metal layer with another.

The surface roughness values for cure levels 1,1 and 1,2 are comparable, with slightly lower values obtained for reduced cure levels. The values of R_a range from 0.47-0.52 µm and 0.52-0.67 µm for cure levels 1,1 and 1,2 respectively.

5.4.3 Results of Surface Morphology Characterisation

Following the characterisation procedure in Section 5.3.5, the surface roughness results obtained after the various surface modifications are presented in the form of an error bar plot (Figure 5.11). The values are also listed in Appendix C2.

While the use of a hydrophobic coating changed the surface tension of RO3006 (discussed further in section 5.4.4), the measured thickness of the coated layer was observed to be negligible as shown in Figure 5.12 and Figure 5.13. Thus the use of the hydrophobic coating did not yield a lower surface roughness as expected. Instead the R_a was found to be comparable to the untreated RO3006. It is believed that this is due to the low solids content in the hydrophobic solution (around 2 %), which could have been deposited in the pores of the substrate during the coating process.

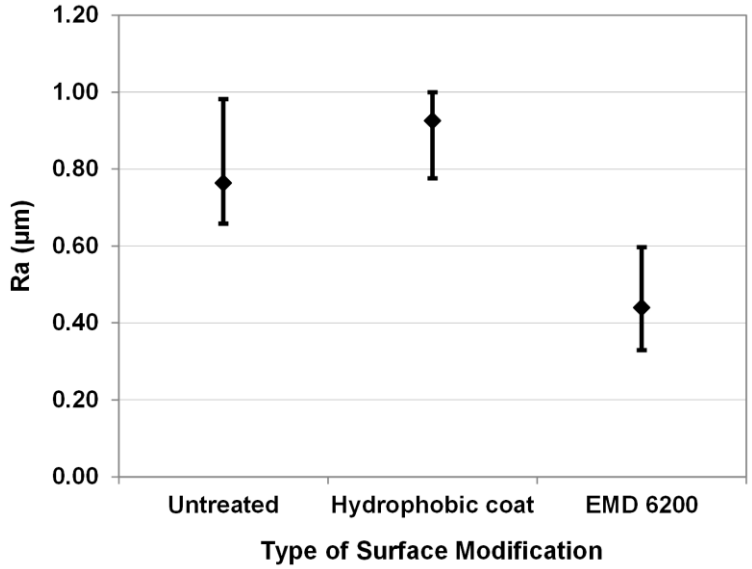

Figure 5.11 Error bar plots for the average surface roughness (R_a) obtained after the different surface modifications

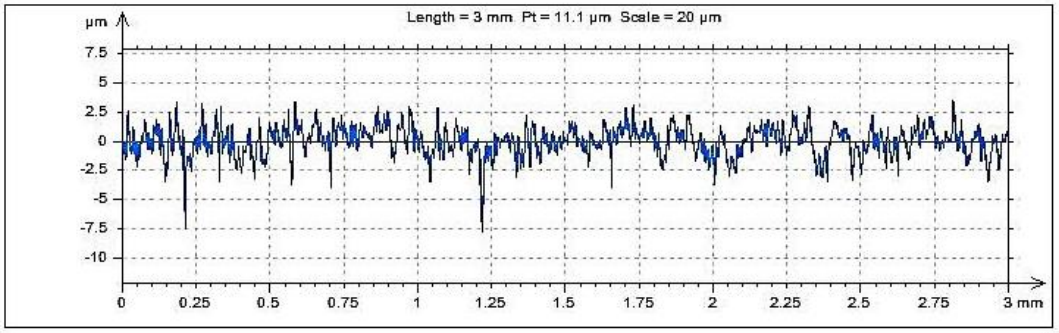

Figure 5.12 Substrate roughness without hydrophobic coating (R_a: 0.91 µm)

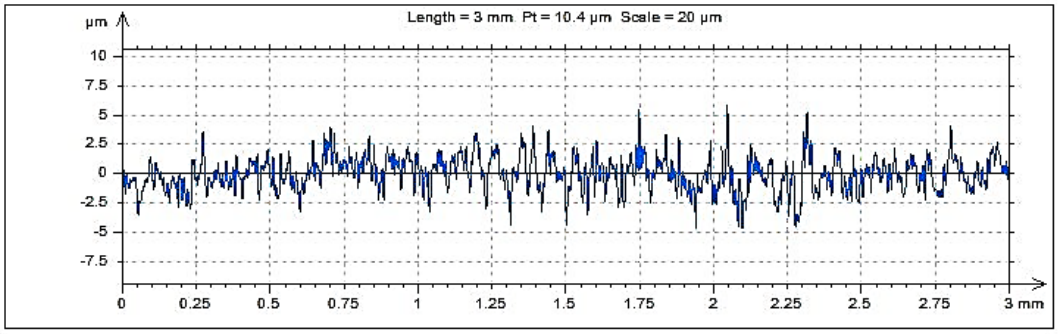

Figure 5.13 Substrate roughness with hydrophobic coating (R_a: 1.07 µm)

As such, obtaining a thicker coat would require either several times of dip-coating (where thicknesses of around 1 µm can be obtained through dip-coating) [170], or using a hydrophobic coating with a higher solids content. Due to concerns of contaminating the sample solution (limited volume) by the substrate, dip-coating

was not used to apply the coating onto RO3006, and it is planned to include the suggested applications to obtain a thicker hydrophobic coat in future work.

5.4.4 Effect of Substrate Roughness on Printed Line Widths

Wenzel [144] considered the effect of surface roughness on the contact angle through a roughness factor. Smith *et al.* [22] printed conductive tracks onto several substrates, and introduced a simple empirical model relating the printed width to the equilibrium contact angle. Nevertheless, data on the substrate surface roughness were not available, and it was unclear what their effect on the printed line widths were. As a result, the good agreement obtained between the calculated and the printed widths [22, 176] could be due to the negligible surface roughness of the substrates considered (e.g. glass) for inkjet printing. The substrate roughness was found to influence the printed line widths significantly in this work, and a surface roughness factor was introduced to account for the increased line widths.

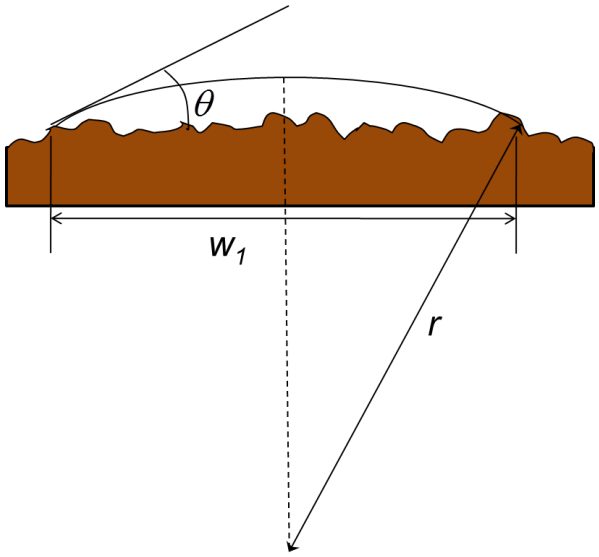

Figure 5.14 Diagram showing relationship between surface roughness and printed line width

With reference to Figure 5.14, the surface roughness increases the actual width of a printed trace. In this case, the authors consider:

$$w_1 = w_0 \times k_r = (2r \sin\theta) k_r \tag{5.3}$$

where k_r in equation (5.3) represents the surface roughness factor, and w_0 represents the width of a trace on a smooth surface (of negligible surface

roughness). Substituting w_1 into the equation by Smith *et al.* [22], we obtain a modified expression for the trace width as shown in equation (5.4), taking into account the surface roughness:

$$w_1{}^2 = \frac{\frac{\pi d^3}{6\Delta x}}{\frac{\theta}{4k_r(\sin\theta)^2} - \frac{\cos\theta}{4k_r \sin\theta}} \tag{5.4}$$

The final expression for the actual trace width can be expressed in equation (5.5) as:

$$w_1 = \sqrt{\frac{(2\pi d^3 k_r)}{3\Delta x\left[\frac{\theta}{\sin^2\theta} - \frac{\cos\theta}{\sin\theta}\right]}} \tag{5.5}$$

where θ (in radians) is the contact angle formed by the droplet on the substrate, Δx is the dot spacing and d is the droplet diameter. This equation assumes that the surfaces are of low or negligible porosity, as porous surfaces could result in a penetration of the silver nanoparticles into the surface [24]. The effect of porosity is typically considered in literature for coated substrates such as paper [24, 187-189], where the pore size distribution and network structure of the coating layer would affect the speed of ink penetration into the pores [187]. Much of the literature involving coated layers considered dye-based inks [187-189], though Öhlund *et al.* [24] considered the conductivity obtained from printing silver based inks onto coated papers [24].

For substrates without coatings, porosity could be considered in terms of the water absorption into the substrate according to the IPC-TM-650-2.6.2 test method (i.e. material immersed in distilled water at 23 °C for 24 hours) [190]. Öhlund *et al*. [24] considered a polyimide film (Kapton HN, Dupont) as a nonporous reference substrate in their work, which had a water absorption of 2.8 % [191]. Apart from Kapton, Smith *et al.* [22] also considered Teflon, sodalime glass, carbon fiber and glass fiber reinforced epoxy compositions for their equation which relates the trace width to the contact angle. The corresponding water absorption of these materials were in the range of 0.01-0.5 % [192, 193]. In this work, the RO3006 substrate has

a water absorption of < 0.1 % [31]. From Figure 5.15, the planarisation layer (EMD 6200 coat) considered in this work were observed to be porous. For the purpose of simplification, these coated surfaces would be excluded from consideration using equation (5.5).

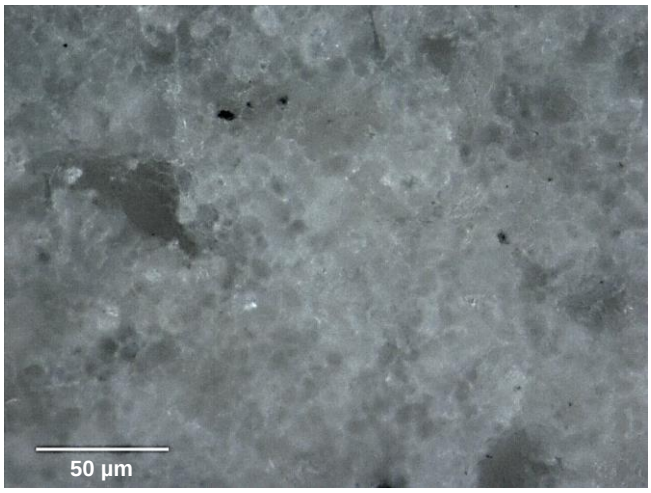

Figure 5.15 Top view of EMD 6200 coat

Test lines of 1 cm length were printed onto the surface modified substrates, as shown in Figure 5.16. The printed line widths were subsequently measured using an optical microscope (Smartscope Flash 200, Optical Gauging Products), and the best fit values were obtained and averaged. These measured values were compared with the calculated values from the empirical formula introduced by Smith *et al*. [22] The values are shown in Table 5.8.

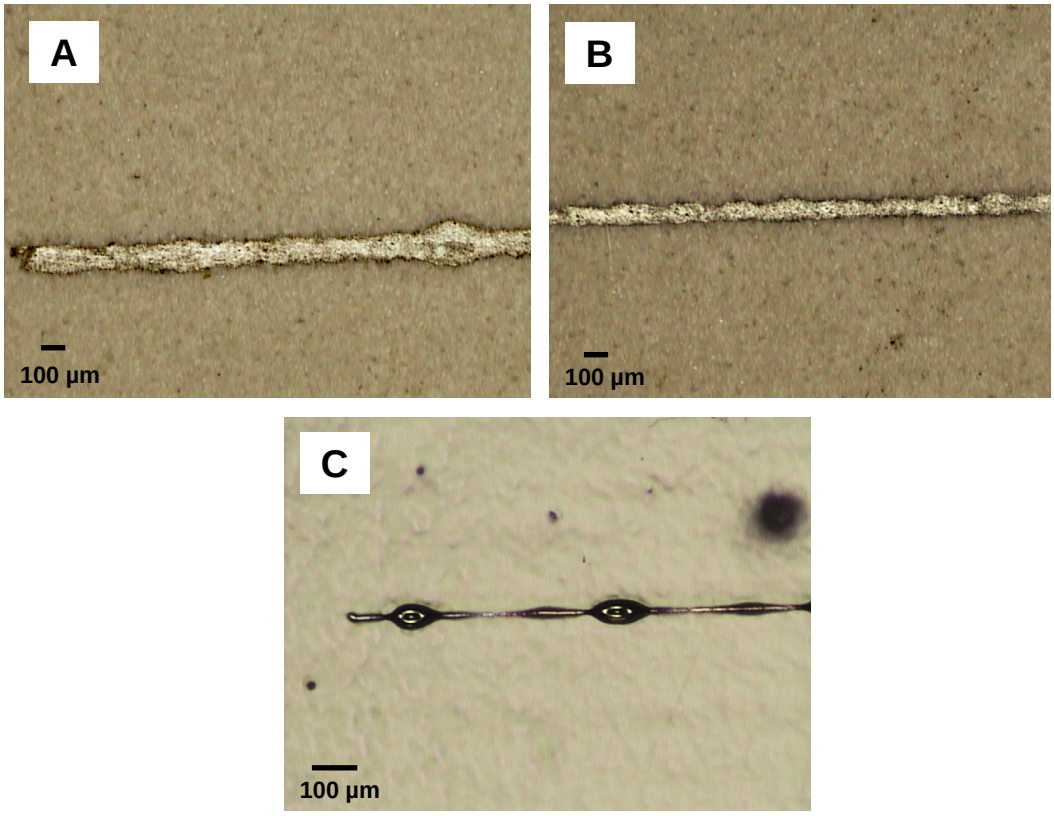

Figure 5.16 Test lines printed on (A) Untreated RO3006 (B) Hydrophobic-coated RO3006 (C) EMD 6200 coated RO3006

Table 5.8 Comparison between predicted and measured line widths on surface modified substrates

Surface Modification	R_a (µm)	Measured Contact Angle (°)[13]	Line Width (µm)		
			Smith *et al.* [21]	Equation (5.5) with k_r =1.2	Measured
Untreated	0.76	47	57.7	83.3	88.2
Abrasive sheet (P1200)	0.80	67	46.0	57.8	54.1
Hydrophobic coating	0.93	76	41.5	50.9	48.2

[13]Average contact angle measurements.

From equation (5.5), it can be deduced that finer line widths can be obtained by printing onto a high contact angle substrate. This is verified by the lower line width variation observed on the hydrophobic coated RO3006 (Table 5.8) compared to the other surfaces. For the untreated and hydrophobic coated RO3006 substrate, a value of 1.2 was used for k_r to predict the line widths as shown in Table 5.8. This value of k_r is for a range of $R_a \leq 1$ µm. To validate this range, a third sample was obtained by applying an abrasive sheet to the RO3006 substrate to roughen the surface, where a measured R_a of 0.8 µm was obtained. Test lines of 1 cm length

were then printed and equation (5.5) used to predict the line width, for which the results are also shown in Table 5.8. A variation of within 10 % was observed between the predicted and measured line widths.

The relation between the correction factor and the static contact angle (θ) is further investigated as shown in equation (5.6), where k_r can be represented as a function of θ and w_1:

$$k_r = f\left[\left(\frac{\theta}{(\sin\theta)^2} - \frac{\cos\theta}{\sin\theta}\right) {w_1}^2\right] \tag{5.6}$$

From equation (5.6), it can be deduced that k_r would decrease as θ increases, since a higher contact angle results in a reduced line width. As w_1 is in the range of µm, this implies that k_r would be more significantly affected by changes in w_1 (i.e. the ${w_1}^2$ parameter) compared to variations in θ which are in units of radians. From equation (5.6), a closer match between the measured and predicted line width by Smith *et al.* [22] can be observed as θ approaches 90° (i.e. $k_r \rightarrow 1$). This is expected because as k_r approaches the value of 1, w_1 can be estimated using the equation by Smith *et al.* [22]. This is also graphically represented in Figure 5.17 which plots the measured static contact angle against the predicted line widths, with and without the factor k_r. This is based on the results in Table 5.8.

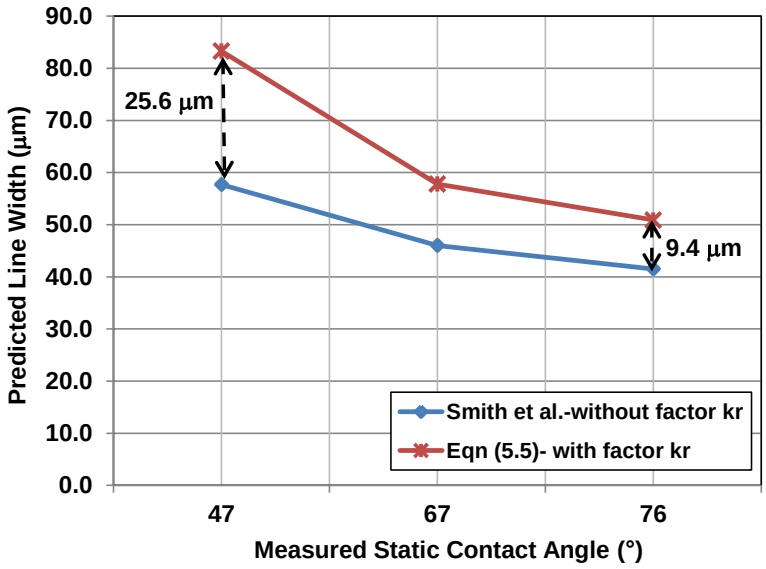

Figure 5.17 Graph of measured static contact angle against predicted line width

5.4.5 Effect of Printing Silver Inks onto EMD 6200

In printing the test line onto double-coated EMD 6200 using EMD 5603, partial de-wetting was found to occur at a platen temperature of 60 ºC (Figure 5.16 (C)). Bulges were observed for the printed trace, which occurred at regular intervals [80, 81]. The width of the connecting ridge between adjacent bulges was reduced from an initial 60 µm (printed width) to 10 µm. In some line sections, breaks in the connecting ridges were observed (Figure 5.16 (C)). This line thinning down to 10 µm could be attributed to the pumping of the ink from the ridge to the bulge arising from a pressure difference [80]. In addition, it could be due to the fine dimensions being considered for printing. In particular, the width of the ridge was observed to be smaller than the diameter of single printed drops on the substrate (as shown in Figure 5.18), which had diameters of around 30 µm. Compared to the calculated drop diameter of 26.7 µm from a 10 pl print head, this suggests that negligible spreading (i.e. de-wetting) of the conductive ink had occurred. This was also verified using contact angle calculations in equation (5.7). While the measured contact angle of the ink-substrate was 45 ± 5º (at room temperature), the printed drops were observed at a platen temperature of 60 ºC. The corresponding contact angle for the printed drops calculated using equation (5.7) was around 102 ºC [80], where:

$$\frac{b_0}{d} = \left(\frac{4sin^3\theta}{(1-\cos\theta)^2(2+\cos\theta)} \right)^{1/3} \tag{5.7}$$

In equation (5.7), b_0 is the width of a drop on the substrate, d is the diameter of the droplet and θ is the contact angle. This significant increase in contact angle suggests a minimal spreading of the printed droplets.

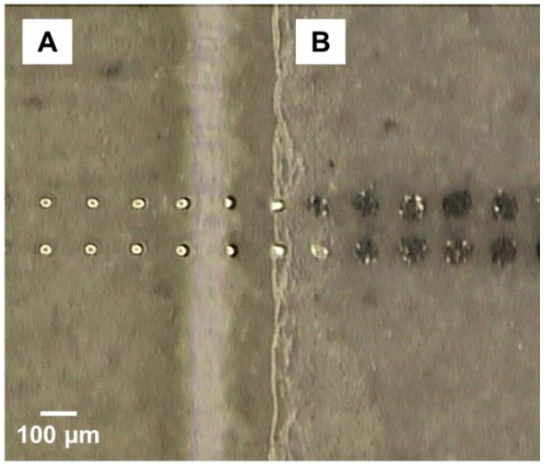

Figure 5.18 Printed drops on (A) EMD 6200 coating (B) Untreated RO3006 substrate

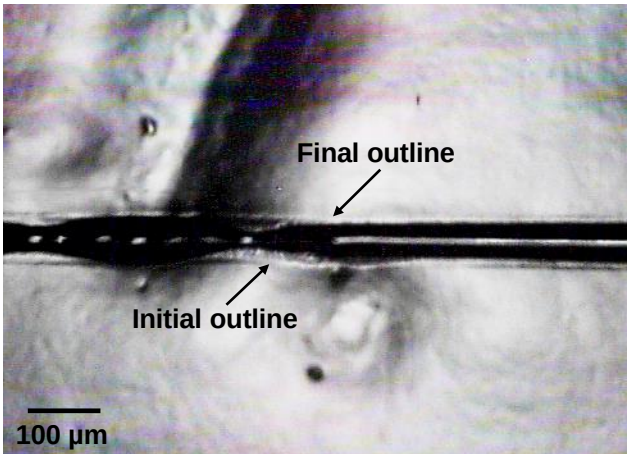

Figure 5.19 Top view showing the initial and final outline of a printed trace on EMD 6200 coat

As observed in Figure 5.19, an initial trace outline was observed after printing, which subsequently shrunk to that defined by the metal trace. This de-wetting phenomenon was also investigated using dynamic contact angle measurements. The static and advancing contact angles of acetone onto the double-coated EMD 6200 were measured, as the surface tension of acetone was found to be close to that of EMD 5603 (25.2 mN/m at 20 ºC). The measured results are shown in Table 5.9. From Table 5.9, the static contact angle (θ) was found to be close to the advancing contact angle (θ_a), which is near the boundary condition for an unstable line (i.e. $\theta > \theta_a$) [80, 194]. Another factor contributing to the line instability could be due to the movement of the contact line during the drying process, as the substrate is heated by the platen below with a temperature of 60 ºC [81, 180, 181].

Unlike the UV-curable ink (EMD 6200), as EMD 5603 becomes more mobile, the surfactant package of the ink results in the silver nanoparticles being less likely to wet the surface as the solvent is removed [184].

In addition, the charging of the surface during the UV exposure could be another possible factor for the de-wetting observed. The charging of the dielectric layer could vary according to the curing system used, where the extent of curing (e.g. curing depth) may differ compared to another system. Furthermore, there is a possibility of a degradation of the LED used in the UV curing, resulting in an uncertainty of the curing dosage and thus the extent of the dielectric cured during printing.

Table 5.9 Static and advancing contact angles for acetone onto EMD 6200 coating

Measurement	Static Contact Angle (°)	Advancing Contact Angle (°)[14]
1	26.4	30.1
2	30.5	28.7
3	26.7	23.3
4	27.3	27.0
5	31.2	32.6
6	30.4	32.0

[14]Three drops dispensed/measured for obtaining the advancing contact angles.

One possible way of alleviating the de-wetting phenomenon could be to use a conductive ink with a higher concentration or viscosity [195]. In this case, the DGP 40LT-15C ink (30-35 % solid content) was used for printing onto EMD 6200. While no de-wetting was observed, the metal trace formed was found to deposit beneath the UV dielectric, and no resistance values could be measured. This could possibly arise from an incompatibility of the solvents in the silver ink with EMD 6200, in which the solvent could be partially dissolving the film and providing a path to the base of the insulator. Further investigations would be required to understand this phenomenon.

5.5 Conclusions

This chapter has described the investigations on surface modification techniques to reduce the surface roughness of a flexible PTFE-based substrate (RO3006). The main results are presented as follows.

Firstly, methods for reducing the surface roughness have been described, by considering surface modification techniques - hydrophobic coating and the use of a UV-curable jettable insulator to form a planarisation layer onto RO3006. In particular, the jetting parameters of the UV-curable insulator were optimised to obtain a smooth layer over the substrate roughness, with an average surface roughness of 0.44 μm obtained. De-wetting was observed when overprinting silver onto the UV-cured insulator as discussed in Section 5.4.5. The de-wetting phenomenon observed necessitates further investigation to understand and address the de-wetting phenomenon, with the goal of obtaining conductive traces with overprinted silver ink. In cases where printability could be obtained, no measurable resistance was obtained for the printed traces, as highlighted in Section 5.4.5 also. Further investigations are also required to understand this phenomenon. These further investigations are described in Chapter 6 of this thesis.

Secondly, the importance of matching the surface energy of the substrate to the ink is highlighted by the use of the UV-cured insulator for jetting onto RO3006. While this can be achieved with ink modification, the author has shown that this is possible within the parameters of heating the platen, which is a more flexible approach. The results obtained indicate that a minimum temperature of 30 °C is sufficient to improve the ink mobility and minimise the de-wetting phenomenon. However RO3006, being an unreinforced ceramic-filled PTFE material was found to warp after being subjected to a thermal sintering temperature of 150 °C for 30 min. One implication of the substrate warpage could be in the fabrication of multilayer circuits based on inkjet printing, where misalignment issues may arise in attempting to align one metal layer with another.

The successful deposition of the UV-curable insulator onto RO3006 to alleviate the surface roughness may be used to reduce the substrate loss effect. From the results

obtained, the insulator thickness of two coats after thermal curing was observed to be in the range of 10-25 μm (Table 5.7). This suggests a possibility of using a thick insulator layer to alleviate the substrate loss of Tyvek due to the higher loss tangent as described in Chapter 4. However this would first require eliminating the de-wetting of the silver ink when overprinting onto the insulator, which will be addressed in Chapter 6 of this thesis. In addition, simulation via electromagnetic modelling is essential to ascertain the optimal insulator thickness for a particular design, in order to meet the performance specifications. The optimal thickness should sufficiently alleviate the substrate loss for improved RF performance while not significantly increasing the surface roughness of the insulator. This area of work could be investigated more in the future.

Lastly, as discussed in Section 5.4.4, the substrate roughness was also observed to affect the printed line width significantly, and a surface roughness factor was introduced in the equation of Smith *et al*. [22] to take into account this phenomenon. The surface roughness factor is valid for $R_a \leq 1$ μm. The proposed equation improves the correlation for printed line widths on substrates with non-negligible surface roughness within 10 % accuracy. However, the proposed equation excludes substrates with coatings. This is because the planarisation layer (EMD 6200) considered in this work was observed to be porous, which could result in a penetration of the silver nanoparticles into the planarisation layer. Future work would seek to investigate the relationship between the degree of porosity of coatings and the printed line widths, obtained via inkjet printing.

Chapter 6 . Surface Modifications for Robust Fine Line Trace Deposition onto Substrates - Overcoming De-wetting

6.1 Introduction

The results obtained in Chapter 5 revealed some challenges in obtaining clear linear traces as the silver ink was observed to de-wet when overprinted onto the UV-curable insulators. This leads to a need to understand and eliminate the de-wetting phenomenon to obtain traces with measurable resistances, with the ultimate goal of printing onto fabrics.

In this chapter, the focus is not on tuning the ink formulations or properties, but on understanding the processing parameters to eliminate de-wetting when the surface energies of the UV-curable insulator and silver ink are not matched. The objective of this chapter is to investigate the conditions for realising electrically conducting traces using commercial ink formulations, especially where the curing equipment available may be non-optimal. Specifically this involves the elimination of de-wetting through surface modification techniques (thermal and UV-ozone post-treatments) to obtain measurable resistance for silver traces overprinted onto the UV-curable insulator layers. At this stage, optimisation of the electrical resistivity of the printed traces is not investigated, as literature abounds in this area [196, 197].

To simplify the study and analysis of the parameters affecting de-wetting, glass was used as the substrate in this work. Firstly as glass is non-porous, the influence of substrate porosity on the UV-curable insulator layer can be ignored, particularly since the curing light source is non-optimal. For the case of a porous substrate, the application of a UV-curable insulator ink would result in ink penetration into the substrate, as well as the ink spread on the substrate surface. This phenomenon would be complicated by the use of a non-optimal light source for curing, which would likely yield a partially cured insulator layer with resulting ink properties (eg. viscosity, surface hardness) which deviate from the ink datasheet. Another

challenge in applying insulator layers on textiles lie in the substrate surface roughness. Previous results (Appendix A) from applying an insulator coat (SU-8) onto Tyvek yielded an uneven coating, where the parameters used for conventional silicon wafer processing were not found to suffice. In this chapter, two UV-curable insulator materials were deposited and the effects of curing time and curing atmosphere (with and without surface modifications) on the inkjet printability of a commercially available silver ink were investigated. A number of different techniques (water contact angle measurements, XPS analysis, focused ion beam-scanning electron microscopy and optical microscopy) were used to characterise the samples at different stages of the process in order to evaluate the surface properties and printability.

6.2 Materials

This section provides details of the glass substrate used, and the specifications of the UV-curable insulator inks and the silver ink used for overprinting onto the insulator.

6.2.1 Substrate

The substrates used for coating with UV-curable inks were twin frosted glass slides of dimensions 76 mm x 26 mm with thicknesses in the range of 0.9-1.0 mm (Fisherbrand P/N 1156-2203, Fisher Scientific). The glass slides were cleaned with acetone and wiped using cleanroom wipes prior to usage.

6.2.2 UV-Curable Insulator Inks

Two UV-curable inks were selected for evaluation with the silver ink. EMD 6415 is a commercial product (SunTronic Solsys Jettable Insulator EMD 6415, Sun Chemical) which is formulated to yield a hard and non-porous surface after curing, such that it would be compatible with the overprinting of silver. The ink has a viscosity of 11-13 mPas at 50 °C and a surface tension of 35-37 mN/m [89]. The specified cure dosage for EMD 6415 (un-doped mercury source) is from 100-300 mJ cm^{-2}. The second ink (SunTronic Solsys Jettable Insulator EMD 6200, Sun Chemical) is a research sample formulated for use with flexible substrates, with an

ink viscosity of 7-9 mPas at 45 °C and a surface tension of 23-27 mN/m [90]. At a temperature of 25 °C, the ink viscosity is 10-30 mPas with a relative density of 1.02-1.1 [90]. The corresponding cure dosage required for EMD 6200 is 200-400 mJ/cm^2. Both inks are formulated to react by radical polymerisation and are colourless after coating.

6.2.3 Silver Ink

The ink used for the inkjet printing of metal traces is a composition of 20 wt % silver (U8726/M20177, Sun Chemical), with a surface tension of 27-31 mN/m. According to the datasheet, the ink contains no resin binders. The ink was selected based on its compatibility with the inkjet printer and EMD 6415. M20177 is formulated with a surfactant package to improve the spreading on the substrate surface. Nevertheless it is noted that M20177 has a similar surface tension to EMD 6200, which implies that the wettability of the silver ink onto EMD 6200 may not be as good compared to EMD 6415.

6.3 Experimental Methods

This section details the process of applying the UV-curable inks onto the glass slide substrates. It also describes the equipment and parameters used in the curing, surface modification and inkjet printing processes. Silver inks are printed onto two types of substrate configurations: plain glass slides and glass slides coated with UV-cured insulator layers. The plain glass slides are used as reference samples to evaluate the traces printed on glass slides coated with the UV-cured insulator layers.

6.3.1 Ink Drawdown Process

To coat glass slides with the UV-curable insulator, a drawdown process was used. The drawdown process for coating the UV-curable insulator onto the slides is shown in Figure 6.1.

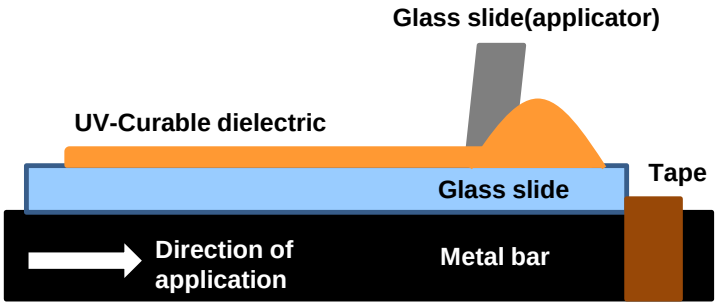

Figure 6.1 Diagram illustrating the draw down process of the UV insulator onto glass slide samples

A glass slide was first placed on top of a metal plate and prevented from sliding by adhesive tape placed at one end of the bar. The UV-curable insulator ink was then deposited onto the glass slide using a disposable pipette. Another glass slide was then used as an applicator to spread the ink across the glass substrate towards the raised tape at the other end of the metal bar, at an angle of 45°. Thicknesses of 20-30 μm (EMD 6200) and 10 μm (EMD 6415) were measured for the post-cured samples.

In this work, the samples prepared were compared to those supplied by the ink manufacturer (reference samples), which were drawn down using a K-bar to yield 24 μm thickness. The reference samples were exposed using a H-bulb mercury lamp [86].

6.3.2 UV Curing of the Insulator Materials under Inert and Ambient Atmospheres

The recommended equipment for curing the UV insulators is an undoped mercury (Hg) lamp [89, 90]. In this work, the exposure unit used (Pluvex1410 UV Exposure Unit, Mega Electronics) [198] comprised of UVA bulbs operating in the range 315-400 nm with peak wavelength at 352 nm (Blacklight F15W/350 BL, Sylvania) [199]. The wavelength was noted to be within the recommended spectral distribution, although it does not cover the full spectrum from 200-600 nm [86].

The power intensity was measured with a UV light metre (UV-340A, Lutron Electronic Enterprise Co. Ltd) which measures the instantaneous power intensity values in the range of 290-390 nm. Prior to measurements, the exposure unit was

turned on for two rounds of 300 s, where 300 s is the recommended duration for obtaining constant exposure values [198]. Each round started 3-5 s after the last round. Following this, various exposure times ranging from 50 to 400 s were set, in steps of 50 s. Readings using the UV light metre were taken 4 times for each exposure time, to allow for the power intensity values to stabilise. The average power intensity value from the last reading (stabilised value) was then used to calculate the energy dosage. From the results obtained, the average energy dosage of the UV equipment was found to be 1.35 ± 0.15 mW/cm^2. This power intensity value is observed to be two orders of magnitude lower compared to a value of 150 mW/cm^2 used by the ink manufacturer [86], resulting in a prolonged exposure time.

During UV exposure in air, oxygen can diffuse into the ink and affect the cure reaction in a process known as oxygen inhibition [200, 201]. This phenomenon is exacerbated with extended exposure times and prevents a full cure of the insulator layers (EMD 6200 and EMD 6415). In the absence of curing equipment with a light intensity strong enough to minimise oxygen inhibition, using an inert atmosphere [202] during curing can help to alleviate oxygen inhibition. In this work the effect of curing the samples under different exposure atmospheres (inert versus ambient) was investigated. Specifically silver traces overprinted onto the different UV cured samples were compared in terms of their wettability, with the goal of obtaining electrically conductive traces.

For the inert curing, the glass slide samples were encapsulated in a polyethylene bag (100 mm x 140 mm) filled with Argon gas. To minimise the oxygen present in the bag, argon gas was injected and expelled from the polyethylene bag three times before the final filling and sealing of the bag, Polyethylene was used in this work as it is largely transparent to UV light due to its simple chemical bonds [203]. To verify this, the power intensity values were measured again with the UV light metre inside a polyethylene bag. The measured values were observed to be comparable to those obtained without the polyethylene bag.

The UV dosages used for curing the insulator samples ranged from 150-600 mJ/ cm^2, in intervals of 150 mJ/cm^2. The upper limit of 600 mJ/cm^2 is in accordance with the recommendations of the ink manufacturer for good printability [184].

Another approach to alleviate the effects of oxygen inhibition is to use a secondary thermal cure, with the purpose of improving the cross-linking generated after the initial UV cure in an ambient atmosphere. From the literature [204, 205], authors have also used heat to promote thermal induced cross-linking of polymers. For instance Lee *et al*. [204] used microwave heating as an alternative to UV irradiation to generate thermally induced crosslinking in an acrylate. Samples which were subjected to a secondary thermal cure were placed in an oven for durations of 10 min at 150 °C.

6.3.3 UV-Ozone Treatment

UV-ozone treatment (UV/O_3) was used to modify the surface energy [95-98] of the insulator layers after UV curing. Based on previous work [206], poor wettability was obtained for silver overprinted on the EMD 6200 insulator layer. As such, the purpose of using UV-ozone treatment is to improve the wettability of the silver ink overprinted onto the insulator layer. Much literature abounds in the use of UV-ozone treatment to obtain more hydrophilic surfaces [207-209], with the extent of hydrophilicity dependent on the UV-ozone exposure time [95-98].

The equipment used was a UV ozone photogenerator (PR-100 UV ozone photoreactor, UVP Inc.), which is a low pressure mercury source operating in the shortwave UV region. The output spectrum of the source displays two peaks in the UV-C band at 254 nm and 185 nm [94]. The UV power intensity is reported to be 15 mW/cm^2 at a wavelength 254 nm and 1.5 mW/cm^2 at 185 nm (at 1" distance from the source) [210]. To maximise the UV intensity reaching the samples, the samples were placed close to the UV source using a metal support such that the distance between the source and the samples was reduced to around 1 cm.

The UV-ozone exposure times were set from 20 to 80 s, as the system was not new and it was expected that the level of intensity would be lower. Assuming a 50 %

power rate, the equipment would yield maximum nominal exposures of 150 mJ cm^{-2} to 600 mJ cm^{-2} (at 254 nm). Longer exposure times involving 3 min intervals [95] were also considered, in order to investigate a trend in the results obtained.

6.3.4 Silver Ink Printing onto Plain Glass and UV-Cured Insulator

A commercial drop-on-demand mode inkjet printer (DMP 2831, Fujifilm Dimatix Inc.) was used for the silver ink deposition. The cartridge comprised of 16 nozzles capable of delivering 10 pl drops per nozzle. In the printing of the silver ink onto the samples, a single jetting nozzle with a 5 kHz waveform was used to print straight lines in the direction of travel of the platen. The inks were jetted out at temperatures of 28 ºC, with the dot spacing in the direction of travel maintained at 20 µm. 25 mm long traces with widths of 100 µm, 500 µm and 1 mm were deposited by making multiple passes of the single nozzle to print parallel lines with a centre to centre spacing of 20 µm. Prior to printing, these traces were created using a pattern definition program available in the inkjet printer software [211], as mentioned in Section 5.3.2 of Chapter 5. The samples were heated at 60 ºC (platen temperature) during printing. Following that, the printed tracks were thermally sintered at 150 ºC for 60 min.

Some samples were overprinted with two layers of silver ink, to ascertain the effect on the resistance values. The second silver layer was printed after a 15 min interval following the printing of the first layer on the heated platen. After the second silver layer was printed, the samples were thermally sintered at 150 ºC for 60 min.

6.3.5 Sample Characterisation

A number of techniques were used to characterise the samples at different stages of the process in order to evaluate the surface properties and printability.

(a) Contact Angle Measurements

In order to realise conductive traces, it is crucial that good wettability first be obtained for the silver ink deposited onto the UV-cured insulator layer. To evaluate wettability, contact angle measurements were performed on the insulator layer and the respective surface energies were calculated. The contact angles were obtained

for coated glass slides cured under different conditions, with/without UV-ozone treatment.

An assumption behind obtaining reliable contact angle values is that there exists minimal absorption of the liquid into the test surface [212]. In this work, the UV-cured polymers considered have varying degrees of cross-linking under inert and ambient atmospheres. To minimise the interaction between the reference liquid and the UV-cured polymer, the choice of a suitable reference liquid becomes an important consideration in the contact angle measurements.

In addition to contact angle measurements, attempts were made to characterise the sample surfaces with the calculated surface energy values using the Owen-Wendt-Rabel-Kaelble method [142]. This method requires the contact angle measurements of the samples using two reference liquids, where triply distilled water and diiodomethane were used. In using diiodomethane for contact angle measurements, imprints and smudging were observed on the surfaces of EMD 6200 samples after wiping away the diiodomethane droplets, which suggested that the insulator layer may have been partially dissolved by diiodomethane. Apart from the incompatibility of the liquid with the polymer, the solubility observed could also have been due to the incomplete curing of the UV ink when cured under an ambient environment, particularly since EMD 6200 is noted to have a reduced cross-linking formulation. As the accuracy of the contact angle measurements depend on the purity of the reference liquids, what was observed may indicate a degradation of the purity of diiodomethane, which could have affected the contact angle results.

To eliminate the uncertainty arising from the interaction of a solvent with the polymer, only one reference liquid, triply distilled high purity water (Chromasolv for HPLC, Sigma-Aldrich), which does not react with the polymer, was used for the contact angle measurements. From the literature, the contact angles of water have been used to determine the wettability of polymers and corona treated surfaces [213].

The contact angle measurements of water were obtained using a Fibro DAT 1100 contact angle tester (Fibro System AB, Sweden), where a minimum of three static contact angle measurements were obtained for each surface modified substrate. The contact angle measurements (using the sessile drop method) were recorded for a period of 10 s following the droplet deposition. The measured values were observed to approximate the contact angles after 1 s droplet deposition. The droplet volumes used in the measurements were 2.0 ± 0.5 µl. These values were repeated using the sessile drop method with a Dataphysics OCA20 system, where a variation of ± 4° was observed compared to the values obtained with the Fibro DAT 1100.

(b) Focused Ion Beam- Scanning Electron Microscope (FIB-SEM)

To study the thin film and bulk material regions of the samples, a dual beam (FIB-SEM) microscope system (Nova 600 Nanolab Dual Beam, FEI) was used to do in-situ cross-sectioning of the printed silver trace on the glass slide. This method is preferable to manual cross-sectioning as with that approach the cleaved edge may be non-uniform and small pieces of glass may be deposited across the silver traces, contaminating the sample. Prior to making the cross-sections, dummy layers of palladium (~1 µm) were deposited onto the trace surfaces to serve as protective layers.

(c) Optical Microscope

A high power optical microscope (SMZ1500, Nikon) was also used to image the printed traces on the samples. The images were captured using x0.75 to x3 objective lenses.

(d) X-ray Photoelectron Spectroscopy (XPS)

XPS analysis using a K-Alpha, Thermo Scientific instrument was performed on the samples to analyse the chemical composition of the surfaces after UV curing and UV-ozone treatment, and analysed and compared to those of the reference samples obtained from the ink manufacturer. Spectra were acquired using Aluminium X-ray irradiation and quantification was obtained from survey spectra using the system software. Prior to the XPS analysis, the samples were cleaved in smaller

dimensions of around 2 x 2 cm^2 using a diamond cutter, such that multiple samples could be analysed in a single batch.

6.4 Results and Discussion

In this section, the results obtained on silver ink overprinted on glass and UV-cured insulator layers (with and without surface modifications) are presented. In addition, a discussion of the cracking phenomenon observed for silver traces overprinted on EMD 6200 is provided. The surface conditions of the samples are analysed using results from water contact angle measurements and XPS analysis. Lastly the relationship between printability and measurable resistance is discussed, followed by the demonstration of electrically conductive traces on ambient cured insulator layers.

6.4.1 Silver Ink Printability on Glass and UV-Cured Insulator Layers

The spreading of the silver ink on different substrates was investigated and Figure 6.2 shows examples of traces obtained after sintering that display different degrees of wettability.

Initially, traces were printed on plain glass (Figure 6.2(A)) and these displayed good wettability, without any de-wetting. For traces defined with 1 mm widths in the inkjet printer, dimensions of 1.7-1.9 mm were obtained for the printed traces on plain glass, indicating significant spreading.

Figure 6.2(B) shows the traces overprinted on the EMD 6415 UV cured insulator layer (UV cured in air for 230 s, 300 mJ/cm^2) and without any subsequent surface modifications. Beading of the silver ink is observed due to poor wettability. Some improvement in the wettability of the traces was obtained (Figure 6.2(C)) after the EMD 6415 sample was subjected to a secondary thermal cure (10 min, 150 °C) after UV curing to increase the cross-linking in the UV insulator layer. However, the insufficient wettability of the silver ink onto the insulator layers necessitated the use of UV-ozone treatment, following which good wettability was obtained, as shown in Figure 6.2(D), where clear linear traces can be seen. It was found that for

the UV curing conditions used here (ambient atmosphere) that a minimum ozone exposure time of 80 s was required for all the UV cure dosages in order to generate clear traces.

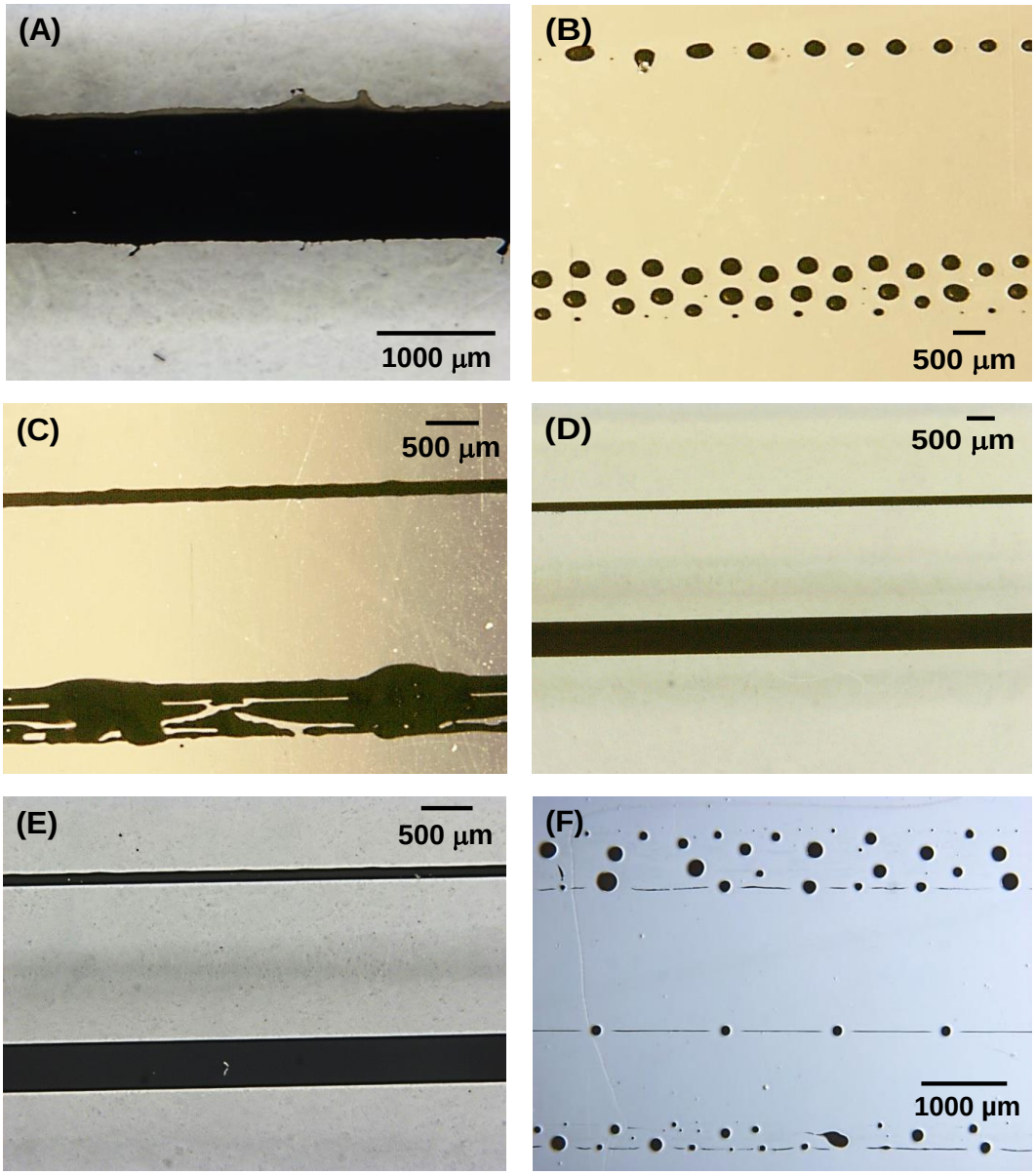

Figure 6.2 Optical microscope images of silver ink traces (single layer) after printing and sintering on different substrates: (A) Plain glass with 1 layer overprint; (B) EMD 6415 samples cured under an ambient atmosphere 300 mJ/cm2; (C) EMD 6415 sample cured under an ambient atmosphere (300 mJ/cm^2) with secondary heat cure applied (10 min); (D) EMD 6415 sample cured under an ambient atmosphere (300 mJ/cm^2) with UV-ozone treatment (80 s); (E) EMD 6415 sample cured under an inert atmosphere (300 mJ/cm^2) with UV-ozone treatment (20 s); (F) EMD 6200 samples cured under an atmosphere 600 mJ/cm^2;

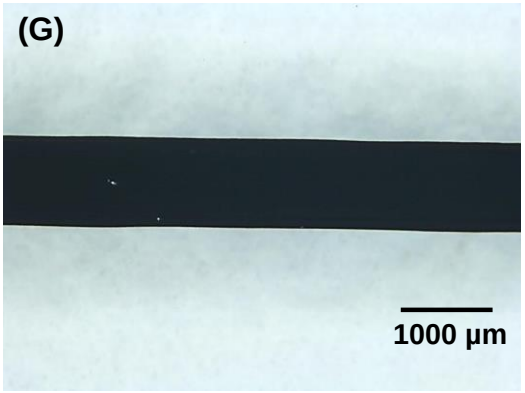

Figure 6.2 Optical microscope images of silver ink traces (single layer) after printing and sintering on different substrates: (G) EMD 6200 sample cured under an ambient atmosphere (600 mJ/cm^2) with UV-ozone treatment (6 min)

The insulator layers which were UV-cured under an ambient atmosphere were noted to remain tacky after the curing process and indicated that oxygen inhibition of the curing process may have taken place. In contrast, the manufacturer's reference samples that were cured with a more intense UV source were not found to be tacky. To investigate the effect of curing atmosphere EMD 6415 samples were UV-cured in the range of 150-600 mJ/cm^2 under an inert atmosphere and overprinted with the silver ink. Partial wettability similar to the image in Figure 6.2 (C) was observed. Under these conditions, the traces were not found to be tacky, but good printability was not obtained. However, in contrast to the air cured samples that required 80 s ozone exposure to achieve printability, good wettability of the silver ink on the inert atmosphere cured surfaces was observed after only 20 seconds of ozone treatment (Figure 6.2(E)). The difference is attributed to the variation in the degree of cross-linking obtained when UV curing the EMD 6415 samples under an ambient atmosphere. This was the case for all the UV cure dosages used, indicating that these are within the range for good printability. For EMD 6415 samples cured under both inert and ambient atmospheres, where silver ink traces were obtained, printed trace widths of 1.5-1.6 mm were observed for a designed trace width of 1 mm. This again indicates spreading of the silver ink, similar to that observed with a glass substrate.

EMD 6200 samples were also prepared and tested for printability of the silver ink. Similar to the EMD 6415 material, it was found that samples cured in an ambient atmosphere were not wettable (Figure 6.2(F)). UV-ozone treatment was again used

on these materials and the effect of curing in an inert atmosphere was also investigated. For samples cured under an inert atmosphere, the UV-ozone treatment time required to obtain good wettability was 3 min. This was doubled to 6 min when curing the sample under an ambient atmosphere (Figure 6.2(G)). Smaller printed trace widths of 0.96-0.98 mm were obtained for a 1 mm width defined in the printer. The results indicate that ozone treatment is a key factor in eliminating de-wetting, with the required ozone treatment influenced by the degree of cross-linking present in the UV-curable insulator layers. In turn the degree of cross-linking is influenced by factors such as the UV cure atmosphere (i.e. inert or ambient) as well as the ink formulations [214, 215].

6.4.2 Cracking in Silver Traces on EMD 6200

For the EMD 6200 samples cured in an inert atmosphere and subjected to ozone treatment, cracks could be observed for a single layer of silver ink overprinted and thermally sintered as shown in Figure 6.3(A). This phenomenon is exacerbated with two layers of silver overprint under the same UV exposure and ozone treatment conditions (Figure 6.3(B)), where pronounced hairline cracks were observed. In contrast, no cracks were observed for EMD 6415 samples which were exposed under an inert atmosphere and ozone treated. There were also no cracks observed for traces printed onto plain glass slides (Figure 6.2(A)), or for EMD 6200 samples cured under ambient atmosphere.

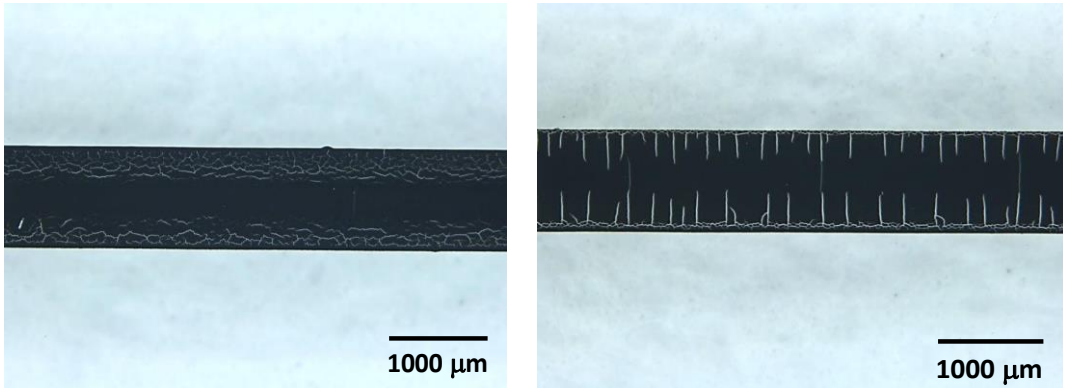

(A) **(B)**

Figure 6.3 EMD 6200 samples exposed under: (A) Inert atmosphere with UV-ozone treatment (3 min) with 1 layer overprint; (B) Inert atmosphere with UV-ozone treatment (3 min) with 2 layer overprint

For the single layer of silver overprint, the cracks were observed to occur at the edges of the 500 μm and 1 mm trace. This is attributed to the coffee stain effect where there is an outward fluid flow to compensate for the evaporative effect of a pinned contact line. Consequently the thickness at the trace edge is higher than the trace centre. From the literature, crack formations have been reported to occur for thicker films [216] and films which are above a certain critical thickness [217, 218]. When the silver overprint was increased to 2 layers, a wider crack area was observed for the smaller traces (100 μm and 500 μm), while the cracks for the 1 mm trace remained at the edges (Figure 6.3(B)). Compared to Figure 6.3(A), the crack area is also more obvious visually. This is since an increased layer of overprint also increases the line thickness, which would exacerbate the non-uniform solvent evaporation and gradient of solvent concentration [196]. The crack morphology in Figures 6.3(A) and 6.3(B) obtained by varying the layers of silver overprint was also observed to be different. While the trace in Figure 6.3(A) comprised of curved cracks, Figure 6.3(B) shows a straight array of cracks for 2 layers of silver overprint. From the literature, films with increased thickness have been found to yield an increase in the orderliness of the crack patterns [219, 220]. The resulting crack morphology is mainly attributed to changes in the humidity and temperature distribution of the evaporating (solvent) system [221].

Contrary to the observations of Lee *et al*. of the absence of cracks for narrower lines (100 μm widths) [196], the cracks in this study were seen to occur for both narrow and wide traces on the EMD 6200 samples cured under an inert atmosphere. While Lee *et al*. [196] reported cracks for silver printed directly onto polyimide (PI) and glass, the traces in this work were printed on an intermediate insulator layer. This suggests that stresses arising from the insulator layer and/or printed silver layer cause the occurrence of cracks. In this case the contact line of the silver trace is pinned to the insulator layer underneath [186]. As such any non-uniform shrinkage arising from the insulator layer (EMD 6200) expansion/contraction during and after sintering is likely to initiate stress. As EMD 6200 is formulated for flexible substrates, the dimensional shift that occurs is also expected to be larger compared to EMD 6415, for which no cracks were observed for samples cured under an inert atmosphere. The stress initiated could have

resulted in the cracks observed in the silver traces, where the traces are unable to shrink in-plane due to its adherence to the insulator layer [186, 222].

In addition, the cracks could stem from residual thermal stresses arising from the coefficient of thermal expansion (CTE) mismatch between the silver ink and the underlying UV insulator during thermal sintering and upon cooling after sintering. The silver traces on the EMD 6200 would experience compressive residual thermal stresses due to the higher CTE of the insulator (60-80 µm/°C) [184] compared to the silver trace (α_{Ag} = 19.6 µm/°C) [196, 216]. Furthermore an inhomogeneous stress distribution could have resulted during the solidification of the silver trace, where compression is generated in the bottom-most region (due to the CTE mismatch), while the top-most region could have remained in tension. Consequently the overall stress distribution of the trace-insulator configuration would be more tensile.

Another factor contributing to the crack phenomenon could be due to the rate of solvent release if the remaining solvent present in the silver ink is released too quickly during sintering. Thus if the rate of evaporation is fast compared to the rate of transport of liquid to the surface [223], pressure and moisture gradients would arise, which results in non-homogeneous shrinkage [223]. This in turn generates tensile stresses, and cracks are initiated when the stresses exceed the tensile strength of the material [196].

For EMD 6200 samples which were exposed to prolonged UV-ozone treatments for 20 min or longer, cracks were still evident on the silver ink printed trace after thermal sintering (Figure 6.4). This phenomenon was observed for EMD 6200 samples exposed under inert and ambient atmospheres, but was significantly pronounced for those exposed under ambient atmospheres (Figure 6.4(A)). The more pronounced cracking observed for samples exposed under ambient atmospheres could be attributed to a modification of the sample surface roughness due to the prolonged UV-ozone treatment time [209]. Jofre-Reche and Martin-Martinez reported changes to the surface topography of a polymer material with an increase in the UV-ozone treatment time. These changes were attributed to the ozone and atomic oxygen ablation and etching of the material surface [209]. The

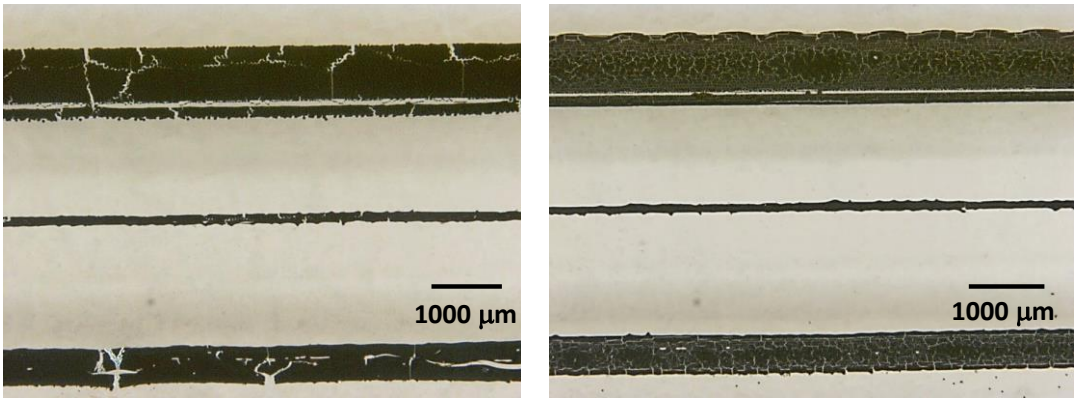

(A) (B)

Figure 6.4 Silver ink traces on EMD 6200 samples cured under: (A) Ambient atmosphere, followed by UV-ozone treatment (30 min) (B) Inert atmosphere followed by UV-ozone treatment (30 min)

EMD 6200 samples exposed under ambient atmosphere are expected to yield reduced cross-linking due to oxygen inhibition [214]. Compared to samples exposed under an inert atmosphere, this would result in an increased degree of softening of the polymer. Consequently the more pronounced cracking observed for the ambient exposed sample could be attributed to an increased ozone and oxygen ablation of the material [209]. Due to the colourless coating of EMD 6200, it was not possible to observe optically the surface topography of these samples.

In other research, the crack phenomenon observed has been shown to be controlled through the use of thinner films [224] and by tuning the insulator formulation [223, 224], which is out of the scope of this research. The occurrence of cracks was found to affect the measurable resistance of the printed silver traces [196], as discussed further in Section 6.4.5.

6.4.3 Contact Angle and XPS Results on Predicting Printability

This section discusses the results obtained from water contact angle measurements and XPS analysis. These techniques are used to characterise the samples after they have been UV-cured and exposed to UV-ozone treatments, to evaluate the surface conditions and gauge the printability of the samples.

For the contact angle measurements, Figure 6.5 shows the contact angles for water on the UV cured insulator layers and also indicates if printability of the silver ink was good. The contact angle results suggest that the values required for good wettability vary with the material and curing condition.

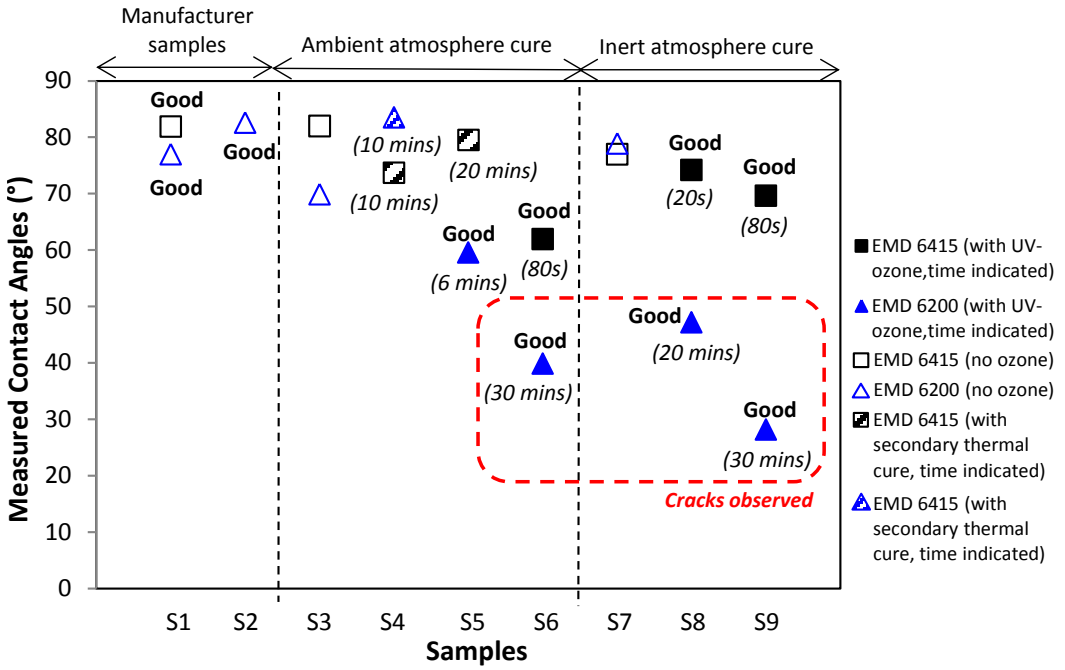

Figure 6.5 Measured contact angles of water on insulator layers prepared under different conditions. The notation "Good" refers to good silver ink printability where clear linear traces were obtained

With reference to Figure 6.5, for samples cured under an inert atmosphere (with a low intensity power source) and subjected to UV-ozone treatment, slightly lower values of 74° (EMD 6415) were obtained that gave good silver ink wetting. Samples cured under an ambient atmosphere and subjected to UV-ozone treatment yielded values ≤ 62° (EMD 6415) and ≤ 60° (EMD 6200) for good printability. In contrast, the highest contact angles of 77-83° were obtained for samples exposed to a high intensity power source (manufacturer samples), which generated highly cross-linked polymer networks where no de-wetting occurred during the overprinting of the silver ink. It can be observed that samples subjected to UV-ozone treatment yielded lower contact angles compared to those without. For EMD 6415 samples, the contact angles following UV-ozone treatment (S8 and S9) are not significantly lower (3-7°) compared to those without treatment (S7) due to the short ozone treatment times (20-80s). However, the decrease in contact angle is

more significant with longer treatment times [209], as observed for EMD 6200 samples S5 (10° reduction) and S6 (30° reduction) compared to S3.

An interesting phenomenon is observed for the samples exposed in an ambient atmosphere followed by a secondary thermal cure for durations of 10-20 min (S4, S5). For the EMD 6415 samples, the contact angle decreased after 10 min of thermal cure (Figure 6.2C), yet increased with a prolonged duration of 20 min. The results suggest that a shorter period of thermal cure would aid in the polymer cross-linking and in lowering the surface energy of the polymer. However, curing periods beyond 10 min suggest a hydrophobic recovery of the water contact angles with further thermal stimulation [225]. In contrast, a secondary thermal cure does not appear to improve the wettability for EMD 6200 samples. From Figure 6.5, 10 min of thermal curing resulted in a higher contact angle (by 13°) instead, when comparing S4 with S3. As EMD 6200 is formulated for flexible substrates, the ink would yield reduced cross-linking after curing compared to EMD 6415 [184]. The results imply a possible lack of thermally cross-linkable polymers in the ink. However, the results also suggest the possibility of using a secondary thermal cure to adjust the hydrophobicity of the layers to control the printing of silver inks to achieve finer line widths.

XPS analysis was also performed on the samples. Table 6.1 show the results for samples coated with EMD 6200 and EMD 6415 and cured under different conditions using a UV dosage of 600 mJ/cm^2. Comparing the EMD 6200 samples to the EMD 6415 samples, silicon groups were detected for EMD 6200 where the atomic concentration of silicon was around 10 %. This possibly indicates the presence of silane/silicone types in the ink formulation. For instance, polysiloxane is an elastomer used in certain inks and coatings to yield flexible films [226, 227].

It can be observed from Table 6.1 that the oxygen levels present in the inert cured samples are not significantly higher compared to the ambient cured or the reference samples. In addition, it is interesting to note from Table 6.1 that the oxygen levels of both EMD 6200 and EMD 6415 samples exposed under an inert atmosphere were comparable to the manufacturer's samples. However this did not result in good printability when the silver ink was overprinted onto the samples. This

phenomenon is similar to the contact angle results shown in Figure 6.5, where samples S3 and S7 yielded comparable contact angles with the manufacturer's samples (S1 and S2), yet de-wetting was observed when the silver ink was overprinted onto S3 and S7.

For samples subjected to UV-ozone post-treatment it can be observed that while the oxygen levels present in the samples were increased, a good wettability of the overprinted silver ink was also obtained, due to changes in the chemical bonds on the insulator layer surfaces [228]. This can be observed for the EMD 6200 sample (sample 2) in Table 6.1, which yielded good printability even though a higher oxygen level of 7 % was obtained relative to sample 3. For the EMD 6415 sample in Table 6.1, the oxygen level was noted to be comparable for samples 6 and 7 due to the short UV-ozone treatment time used for sample 7. However a good printability was obtained for sample 7 after the UV-ozone treatment, due to the increased wettability of the silver ink onto the surface modified insulator layer [208].

Table 6.1 Proportion (%) of the elements present in the EMD 6200 and EMD 6415 samples

No.	EMD 6200 samples	Atomic Concentrations					Remarks
		C 1s	O 1s	Si 2p	N 1s	P 2p	
1	Reference[15]	68.5	22.1	7.3	1.5	0.6	Good printability[16]
2	Ambient cure and UV-ozone (6 min)	57.4	28.7	11.1	2.1	0.7	Good printability[16]
3	Inert cure	66.4	22.3	10.2	0.9	0.3	De-wetting
4	Inert cure and UV-ozone (3 min)	61.4	26.4	10.3	1.4	0.5	Good printability[16]
No.	**EMD 6415 samples**	**C 1s**	**O 1s**	**Si 2p**	**N 1s**	**P 2p**	**Remarks**
5	Reference[15]	76.8	20.8	-	1.2	1.1	Good printability[16]
6	Inert cure	77.4	19.8	-	1.3	1.5	De-wetting
7	Inert cure and UV-ozone (20 s)	74.8	21.6	-	1.9	1.7	Good printability[16]

[15]Sample obtained from the ink manufacturer, which is exposed at 600 mJ/cm^2 using a high power UV source. [16]Good printability refers to clear linear traces being obtained when silver ink is overprinted onto the samples.

Overall, the contact angle provides a useful indication of printability through the ozone treatment duration required. On the other hand the XPS analysis results

provided an indication of the oxygen levels present on the sample surfaces, but may not suffice as an adequate gauge of printability since samples could have similar oxygen levels (inert cured versus manufacturer's samples), yet yield different printability results.

6.4.4 Measurable Resistance

Following the UV-ozone treatment of the insulators, single layers of silver ink were overprinted across the samples to form 0.5 and 1 mm (designed) trace widths which were 25 mm long. Three sets of such traces were printed onto the samples. After thermal sintering at 200 °C for 2 h the trace resistances were measured using a two point probe digital multi-metre. The use of two point probe measurements was considered to be appropriate since relative measurements were made amongst the samples. In this case the higher sintering temperature and time were used (compared to the printability trials) to improve the resistance values obtainable. The results are shown in Figure 6.6, where the average resistance value per unit length (i.e. normalised resistance) was plotted for 3 different samples. For each sample, the average resistance value was obtained from at least two measurements.

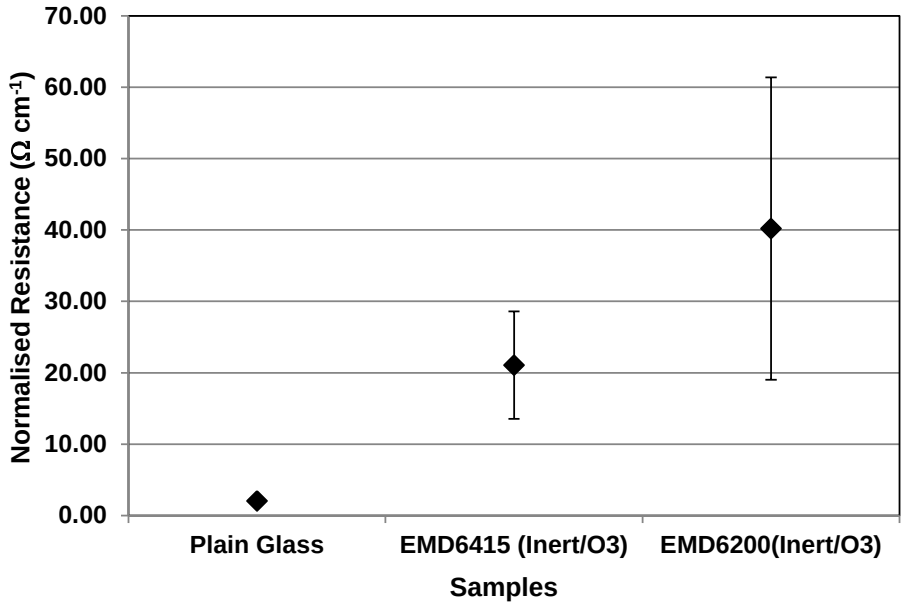

Figure 6.6 Comparison of normalised resistance values for 1 mm wide (design width) silver traces printed on plain glass, EMD 6415 and EMD 6200 insulator layers. The EMD 6415 and EMD 6200 samples were cured in an inert atmosphere with UV-ozone post-treatments of 20 s and 2 min respectively. The errors bars in the figure represent the maximum and minimum values.

Specifically these resistance values were divided by the corresponding trace length over which the resistance was measured (in cm) to normalise them. The results are presented without correcting for the trace widths or thicknesses. This is since the deposited ink volume is assumed to be constant [22], which implies that the cross-sectional areas of the traces would be the same (i.e. not affected by the trace spread) in the extraction of the resistance values.

From the measured resistance results, it was observed that only samples prepared on insulator layers exposed under an inert atmosphere and subjected to UV-ozone treatment gave conductive silver traces and yielded measurable resistances. This was the case for both EMD 6200 and EMD 6415 samples. From Figure 6.6, the normalised resistance for traces printed on plain glass consistently yield smaller values with smaller variation compared to the other samples. For 1 mm wide traces, the traces printed on plain glass yield normalised resistance values of 1.7-2.3 Ω/cm. This is at least 8 times lower compared to traces printed on EMD 6415 and EMD 6200 samples. In contrast, EMD 6415 and EMD 6200 samples yield a wide variation for the normalised resistance values. A range of 13.5-28.6 Ω/cm was obtained for EMD 6415 samples. For EMD 6200 samples prepared under the same conditions, this variation is slightly higher at 19.0-61.4 Ω/cm. Since the trace resistance is based on how good an electrical path is formed, the results could be possibly attributed to two factors. The first is the formation of cracks in the samples exposed in an inert atmosphere, which has been discussed in Section 6.4.2. Consequently a variation in the crack density in each trace would result in a variation of the measured resistances as the electrical contacts between nanoparticles are obstructed by the crack openings [196].

A second factor causing the variation of the resistance values could be the degree of cross-linking present in the insulator layers, which results in an inconsistency of the silver nanoparticle aggregation and hence the electrical path formed. This was further investigated using FIB-SEM. Figure 6.7(A) shows a FIB cross-section taken through the sintered trace to a part of the glass substrate underneath. From Figure 6.7(A), the silver nanoparticles deposited on plain glass were observed to be densely agglomerated without any clear boundary between the particles. In

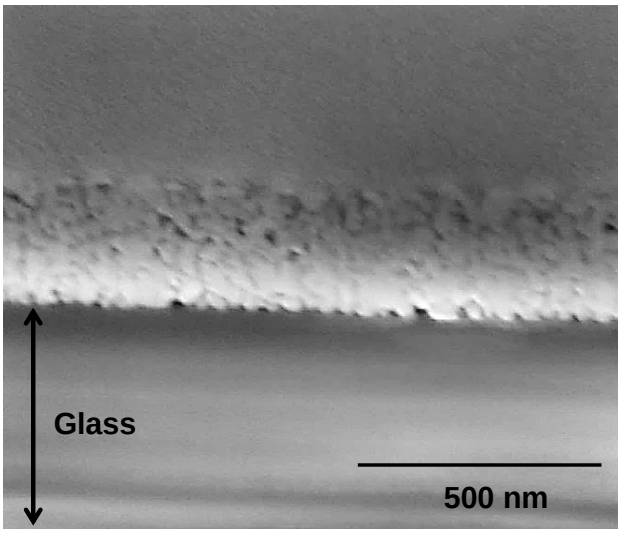

(A)

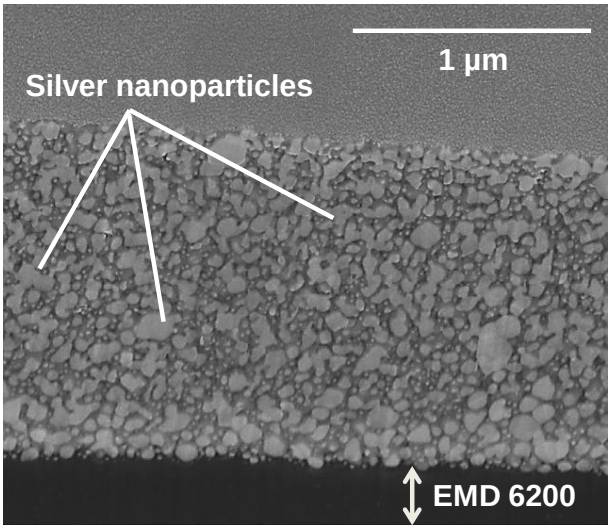

(B)

Figure 6.7 FIB cross-section of sintered trace on: (A) plain glass (B) EMD 6200 sample which was cured in an inert atmosphere and subjected to UV-ozone treatment for 2 min

comparison, the silver nanoparticles observed in Figure 6.7(B) which shows a section through the sintered trace and part of EMD 6200 are less densely aggregated and appear to be suspended. Furthermore, the silver layer appears to be thicker on the EMD 6200 compared to on glass, which could be partly attributed to the increased spreading observed on glass.

Further FIB-SEM cross-sections made for an EMD 6200 sample at the centre and edge of the silver trace indicate that the thickness is not uniform, as shown in Figure 6.8. Figure 6.8(A) shows the top view of the sintered trace while Figure

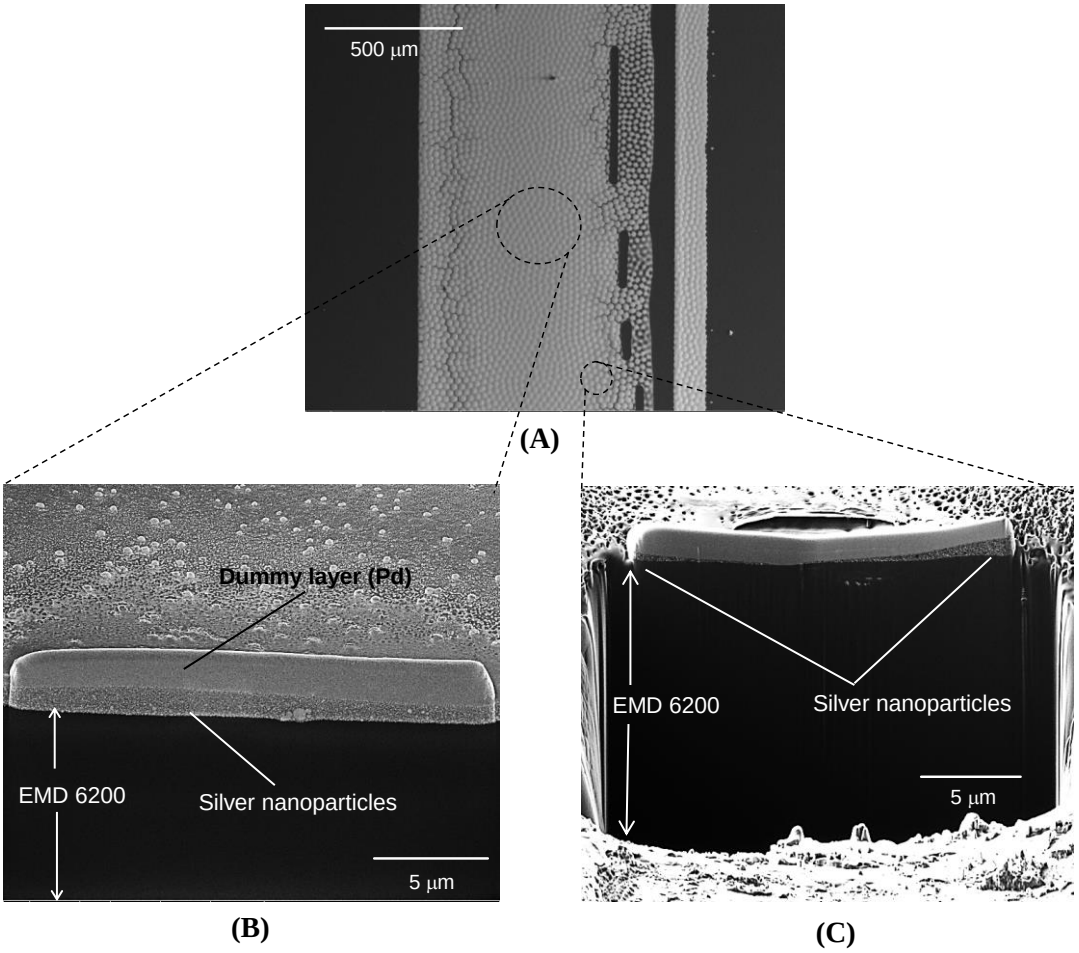

Figure 6.8 Silver ink printed on EMD 6200 which was cured in an inert atmosphere and subjected to UV-ozone treatment for 2 min: (A) Top view of sintered trace; (B) Cross-section taken in the trace centre region; (C) Cross-section taken near the trace edge

6.8(B) and Figure 6.8(C) show the cross-sections taken of the trace into the EMD 6200 insulator underneath. These cross-sections were taken at different locations (centre and edge) of the same trace in Figure 6.8(A), and dummy layers of palladium were deposited prior to making the cross-sections in Figure 6.8(B) and Figure 6.8(C).

From Figure 6.8(B), the thickness of the trace is 0.9-1.6 μm. This thickness reduces to ≤ 1 μm near the trace edge region as shown in Figure 6.8(C). In particular the trace thickness in the middle of the cross-section (Figure 6.8(C)) appears to be significantly smaller compared to the trace edges. The thickness variation could be due to the cross-section being taken near the junction of two dots located at the edge of the trace (Figure 6.8(A)), since further observation of

the trace in Figure 6.8(A) reveals a dot-like appearance.

The dot-like appearance observed are comprised of the deposited ink droplets which have not merged together, with the phenomenon being more obvious at the trace edge in Figure 6.8(A), where isolated droplets are observed. These isolated droplets could have been suspended in the insulator layer and thus prevented from agglomerating. As the polymer is not fully cross-linked, the lessened polymer cross-linkages in EMD 6200 could have enabled a diffusion of the silver nanoparticles through the insulator layer as the solvents in the silver ink penetrate the film, thereby providing a pathway underneath the insulator layer. This is consistent to the cross-section observed in Figure 6.7(B) of the sintered trace, where the silver nanoparticles appear to be suspended within the EMD 6200 insulator layer.

Overall, the results imply that the degree of cross-linking present in the UV-cured insulator could be another factor affecting measurable resistance, since a continuous path is required for current to flow. As such, while traces could be printed without de-wetting onto samples exposed under an ambient atmosphere with UV-ozone treatment, no resistance values were measurable for those samples. In particular, the larger 1 mm trace widths were observed to yield a change in the colour shade at the trace edges (Figure 6.9).

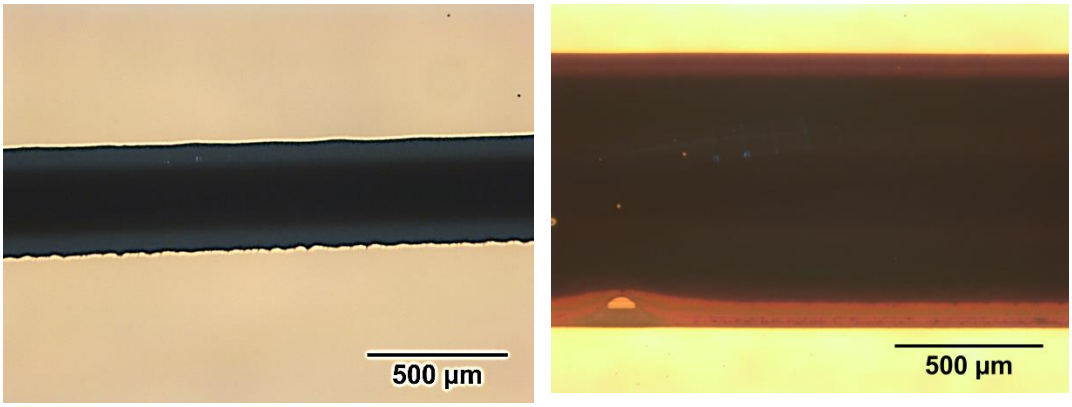

(A) (B)

Figure 6.9 Silver traces overprinted onto ambient cured insulator samples. (A) EMD 6415 sample exposed under an ambient atmosphere and followed with UV-ozone treatment (80 s) (B) EMD 6200 sample exposed under an ambient atmosphere and followed with UV-ozone treatment (6 min)

Goehring *et al*. [229] reported on such a phenomenon in the drying of colloidal dispersions. In particular, they observed a series of fronts when a colloidal suspension dries directionally, with distinct regions separating the liquid dispersion and the solid film [229].

While exposing the jettable insulators (EMD 6415, EMD 6200) under an inert atmosphere would be a more ideal condition for maximising the polymer cross-linkages [214], the thermal sintering of the silver traces resulted in the occurrence of cracks as discussed earlier in Section 6.4.2. A few approaches exist to alleviate the crack phenomenon observed. One possibility is to adopt a localised curing of the silver traces [230-232] such as laser sintering or the use of a xenon flash lamp. This has been adopted for the thermal sintering of silver traces on temperature sensitive substrates and is thus a possibility for fabric substrates. However it may also be possible to apply this technique for the overprinted silver traces without residual thermal stresses arising from the CTE mismatch of the silver ink and the insulator.

Yet the adoption of such a technique would require a silver ink with properties suitable for use with laser sintering. In addition, the use of a suitable laser source along with the optimisation of the laser sintering parameters for the ink is of critical importance [233]. Otherwise a non-ideal scalloped trace profile may result [231].

Another approach to alleviate cracks in the silver traces after thermal sintering involves a two stage drying process. Specifically the sample would be heated at a lower temperature (70 °C to 85 °C) to partially remove the solvents, following which it would be subjected to a higher temperature for a shorter time for the sintering of the nanoparticles. Nevertheless, if the temperature is too high or the thermal curing duration too long, cracks can still occur if the solvent present in the silver ink is released too quickly during sintering.

6.4.5 Electrically Conductive Traces on Ambient-Cured Insulator Layers

In view of the drawbacks of the above approaches, the author considered curing the samples in an ambient atmosphere, but overprinting upon it with multiple layers of silver ink to achieve measurable resistances. This is since crack formation is not an issue when curing the insulator samples under an ambient atmosphere. Due to the variation of the cross-linkages present in the ambient cured samples, the overprinting of multiple silver layers would aid in enhancing the proportion of the nanoparticles contacting and agglomerating during thermal sintering. In addition, the ambient cured samples would be thermally sintered for extended periods of time. This is to aid in the agglomeration of the nanoparticles to form conductive paths for measurable resistances.

Table 6.2 shows the resistances of 1 mm traces prepared from 2 layers of silver ink overprinted on ambient cured EMD 6415 samples. The insulator layers were UV exposed using a dosage of 600 mJ/cm^2 and ozone treated for 80 s. After printing the silver ink, the samples were thermally sintered at 150 °C for an extended period of 4 h, followed by 180 °C for 1 h. The extended period of 4 h followed by a second stage of sintering at 180 °C is adopted to aid in the agglomeration of nanoparticles as proposed in Section 6.4.4.

Table 6.2 Measured resistance values of 1 mm silver traces (2 layers) overprinted onto ambient cured EMD 6415 samples

Line No.	150 °C, 4 hours	180 °C, 1 hour
L1	1.47 kΩ	191.9 Ω
L2	0.37 kΩ	75.8 Ω
L3	70.8 Ω	39.9 Ω
L4	47.5 Ω	23.2 Ω
L5	1.79 MΩ	0.51 kΩ
L6	83.3 Ω	31.4 Ω
L7	1.71 MΩ	91.0 Ω

From the results in Table 6.2, resistance values were registered after 4 h of thermal sintering at 150 °C. However, 50 % of the resistance values are in the range of kΩ

and MΩ. After an additional hour of thermal sintering at 180 °C, most of the resistance values fall into the range of Ω, with the least resistance being 23.2 Ω.

The same procedure was performed for ambient cured EMD 6200 samples where two samples were subjected to a higher temperature thermal sintering of 180 °C, in steps of 2 h. The results obtained are also shown in Figure 6.10. It can be observed that sintering the overprinted traces at a higher temperature aids significantly in the agglomeration of the nanoparticles. From the FIB-SEM cross-section in Figure 6.11, increased clusters of silver particle agglomeration could be observed. After 4 hours of thermal curing, the measured normalised resistance values were in the range of Ω cm^{-1} (Figure 6.10). Following an additional 2 h of thermal curing at 180 °C, the reduction in the normalised resistance was around 12 %. This suggests that a thermal curing of the traces at 2 h may suffice since the reduction in the normalised resistance values is not significant after 4 h. However larger variations in the normalised resistance values (as indicated by the error bar plots) were noted after 4 h of thermal cure. This implies that the degree of aggregation of the silver nanoparticles varies from trace to trace (albeit with the same trace width), which

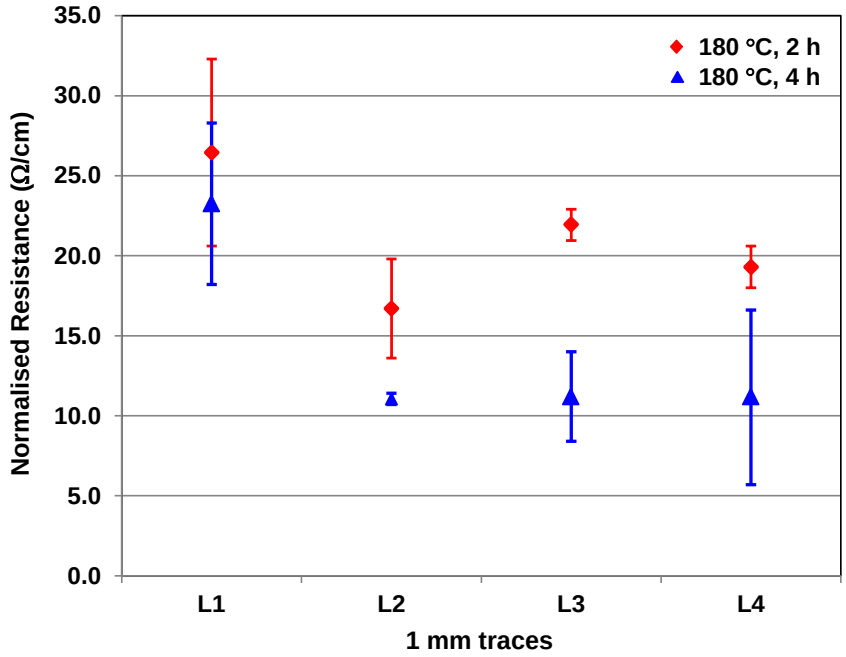

Figure 6.10 Variation of the normalised resistance values for 1 mm wide (design width) silver traces sintered for different periods of time at 180 °C. The results are for two layers of silver overprinted on ambient cured EMD 6200 samples

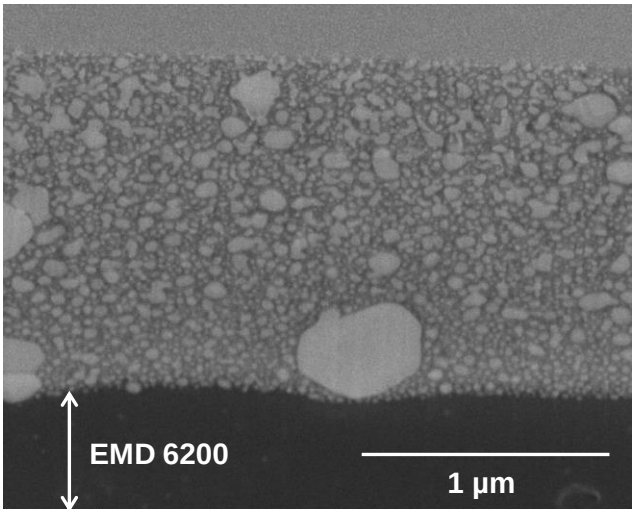

Figure 6.11 FIB cross-section showing clusters of agglomerated silver nanoparticles observed for two layers of silver overprinted on an ambient cured EMD 6200 sample

could be attributed to varying degrees of cross-linking present in different regions of the ambient cured insulator.

While the normalised resistance range obtained has to be further optimised, the results obtained show that the proposed approach is feasible for obtaining electrically conductive traces on ambient cured insulators, where the cross-linking in the samples is affected by oxygen inhibition. Compared to curing the samples under an inert atmosphere, this yields a more flexible solution towards obtaining electrically connected traces. Further work would also be needed to improve the repeatability of the printed trace resistances. One possibility would involve improving the thickness variation of the coated insulators, such that a more uniform curing and hence improved cross-linking can be obtained.

The results obtained are promising, following which a trial evaluation was performed using Tyvek as the substrate. This work is further described in Appendix D of this thesis. This trial evaluation considered only EMD 6415 due to the increased cross-linking formulation of the ink. From the results, samples prepared on insulator layers exposed under either inert or ambient atmosphere and then subjected to UV-ozone treatment yielded conductive silver traces with measurable resistances. However the resistance values are in the range of kΩ and MΩ, which implies that the UV insulator ink could have seeped through the porous

Tyvek substrate during the drawdown process. This may in turn have affected the polymer cross-linking in the insulator and the subsequent aggregation of the overprinted silver nanoparticles. Further work would be required to investigate the effect of substrate porosity on the polymer cross-linking of the UV insulator inks. Finally Figure 6.12 shows a summary of the operating window for achieving printability and measurable resistance on the UV-curable insulator layers, based on a UV power source intensity of 1.35 mW/cm^2.

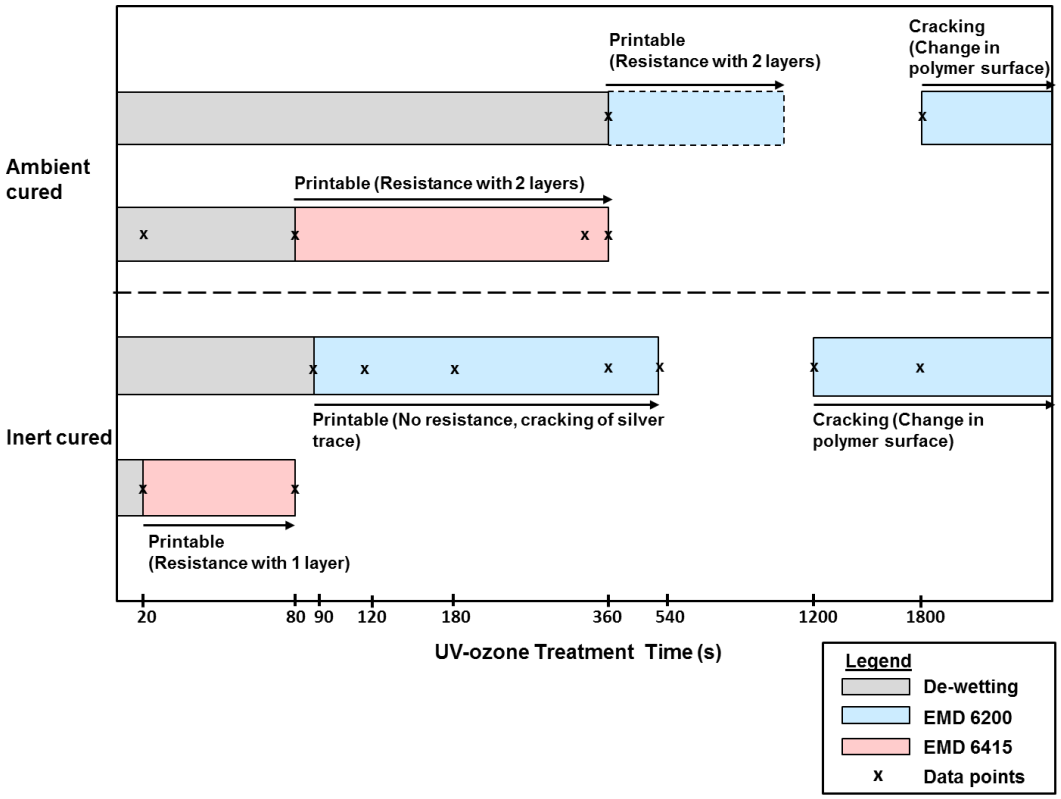

Figure 6.12 Summary of the operating window for achieving printability and measurable resistance on UV-curable insulator layers (UV cure dosages of 150-600 mJ/cm^2), with respect to the UV-ozone treatment time

6.5 Conclusions

This chapter has investigated the preparation of continuous silver ink traces with measurable resistances on UV cured insulator layers (EMD 6415, EMD 6200) with surface modifications. In particular, the goal was to identify suitable conditions for achieving electrically conductive traces using commercial ink formulations and where the curing equipment may be non-optimal. The important results of this work are summarised as follows.

Silver ink de-wetting was observed on a number of substrates and the influence of thermal and UV-ozone post-treatments as surface modification techniques to eliminate the silver de-wetting were investigated. These techniques were applied to insulator layers cured under both inert and ambient atmospheres. Good wettability of the overprinted silver ink on the insulator layers (EMD 6415, EMD 6200) was obtained with UV-ozone treatment, where the treatment time required was found to be a function of the material (ink formulation) and the curing atmosphere, which is thought to affect the degree of cross-linking.

One novel contribution arising from this work is that water droplet contact angle measurements provided an indication of changes in the surface condition of the insulator layers, but were not sufficient for predicting whether measurable silver track resistances could be obtained. Instead measurable resistance was found to be influenced by the occurrence of cracks. The results obtained also imply that the degree of cross-linking present in the insulator could be another factor influencing measurable resistance. In this case, contact angle measurements serve as a precursor, but are not able to predict the performance of the silver trace deposited onto the UV-curable polymers in the post-thermal sintering stage. To date little information is available in literature for contact angle measurements obtained on partially cured polymers. For contact angle measurements made on UV cured films [29, 30], no information was provided on the final cure stage of those films, therefore the authors assumed that they are fully cured. Future work would seek to investigate how the degree of polymer cross-linking affects the aggregation of the silver nanoparticles and the measurable resistance.

Another specific novelty of this work is that XPS analysis is not the only factor affecting printability. While the XPS results obtained provided an indication of the oxygen levels present on the sample surfaces, the use of XPS may not be a sufficient gauge of determining printability. This is because samples could yield comparable oxygen levels compared to the manufacturer's (i.e. reference) samples, yet have poor wettability when overprinted with the silver ink.

Subsequently the author demonstrated that measurable resistance can be obtained on samples cured under an ambient atmosphere, through the overprinting of

multiple silver layers and curing for an extended period of time. Further work is needed to optimise the resistivity range of the overprinted silver traces, and to improve the repeatability of the values. However the results at this stage suggest that compared to curing the samples under an inert atmosphere, this approach yields a more flexible solution for obtaining electrically conductive traces. In addition, a trial evaluation of overprinted traces on the EMD 6415 insulator layer was also performed using Tyvek as the substrate (Appendix D). In this case the same experimental parameters pertaining to the exposure and UV-ozone post-treatment of EMD 6415 on glass substrates were used. While measurable resistances could be obtained, the values were in the range of kΩ and MΩ. Hence another aspect of future work would seek to investigate how substrate porosity affects the polymer cross-linking for insulator layers subjected to UV exposure, as this has been little explored in literature for insulator layers deposited via inkjet printing.

Chapter 7 . Characterising the High Frequency Electrical Performance of Printed Interconnects

7.1 Introduction

As described in Section 3.2(a) of Chapter 3, literature abounds on the effect of sintering conditions on the DC electrical resistivity of printed traces [18, 34, 36-38, 234], which are typically obtained by screen printing or inkjet printing. However the electrical performances of printed traces in the higher frequency range (> 20 GHz) have been subjected to little investigation to date [18, 23].

Salmeron *et al*. [23] have correlated RF simulation results with measurements up to a frequency of 1.2 GHz for RFID applications. Kim *et al*. [18] characterised the RF performance of an inkjet-printed transmission line up to 30 GHz on silicon, in relation to increased sintering temperatures. Due to a lack of research, there is little information available on the RF performance of printed interconnects. To address this research gap, this chapter seeks to develop simulation models and validate them with experimental measurements, and to provide guidelines for modelling the RF performance of printed traces. A sub-objective of this work is to investigate how the paste property influence the DC conductivity of printed interconnects across the substrate, and the resulting effect on the RF performance. To date, there exists little literature which report on the variation of printed samples across a substrate, in terms of the DC electrical performance, because most researchers focus on measuring samples for repeatability [23], or measuring samples of a different variety [51, 235] for comparison.

Printed traces in this chapter refer to interconnects obtained by screen printing, but the methodology proposed is applicable for inkjet printed traces. Specifically, in order to accurately predict the RF response, the simulation models take into account non-ideal transmission line characteristics which are typically neglected during the design and modelling process (as discussed in Section 3.2(b) of Chapter 3).

The non-ideal transmission line characteristics in this chapter are defined as:

- ***Non-uniform printed dimensions***. The printed dimensions may vary across the line length due to the degree of wettability. For inkjet printed traces, the dimensions are influenced by the wettability of the ink onto the specific substrate [22] and the substrate roughness present [144, 206]. For screen printed traces, the paste wettability is also determined by the interaction between the screen mask and the paste [236] .
- ***Non-uniform DC resistivity/conductivity values***. This can be observed from Figure 7.1(A), the copper foil is observed to be continuous. In contrast the silver particles in screen printed traces are being held together by a binder as shown in Figure 7.1(B). Consequently the DC resistivity of the printed traces is influenced by the inter-particle agglomeration during the thermal curing process, where the electrical path is defined by the surface to surface contact.
- ***Trace cross-sections with non-rectangular profiles***. Perfect rectangular profiles are usually assumed in the modelling or design process for simplification. Yet such profiles are not representative of the fabricated traces which typically have trapezoidal profiles [127, 129].

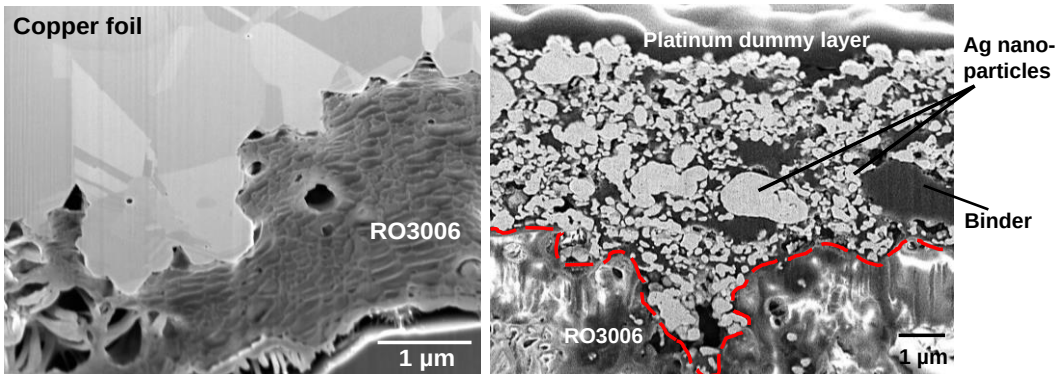

(A) **(B)**

Figure 7.1 FIB-SEM images of (A) Copper foil on RO3006 (B) Silver paste on RO3006 after thermal curing

- ***Surface roughness.*** At higher frequencies, the skin depth phenomenon causes current crowding in traces with surface roughness profiles, which results in increased losses and signal integrity issues [129]. When the skin depth becomes comparable to the trace thickness at the highest frequency considered, the effect

of surface roughness becomes considerable [129] and needs to be taken into account.

A methodology for modelling the above non-ideal characteristics is proposed in the next section. In particular, the non-uniform DC resistivity values necessitate a need to investigate the effect of varying DC resistivity on the RF performance of the transmission lines. The substrate used is a flexible high frequency laminate, RO3006 [31].

7.2 Methodology

The methodology adopted for this chapter is summarised in a flowchart in Figure 7.2.

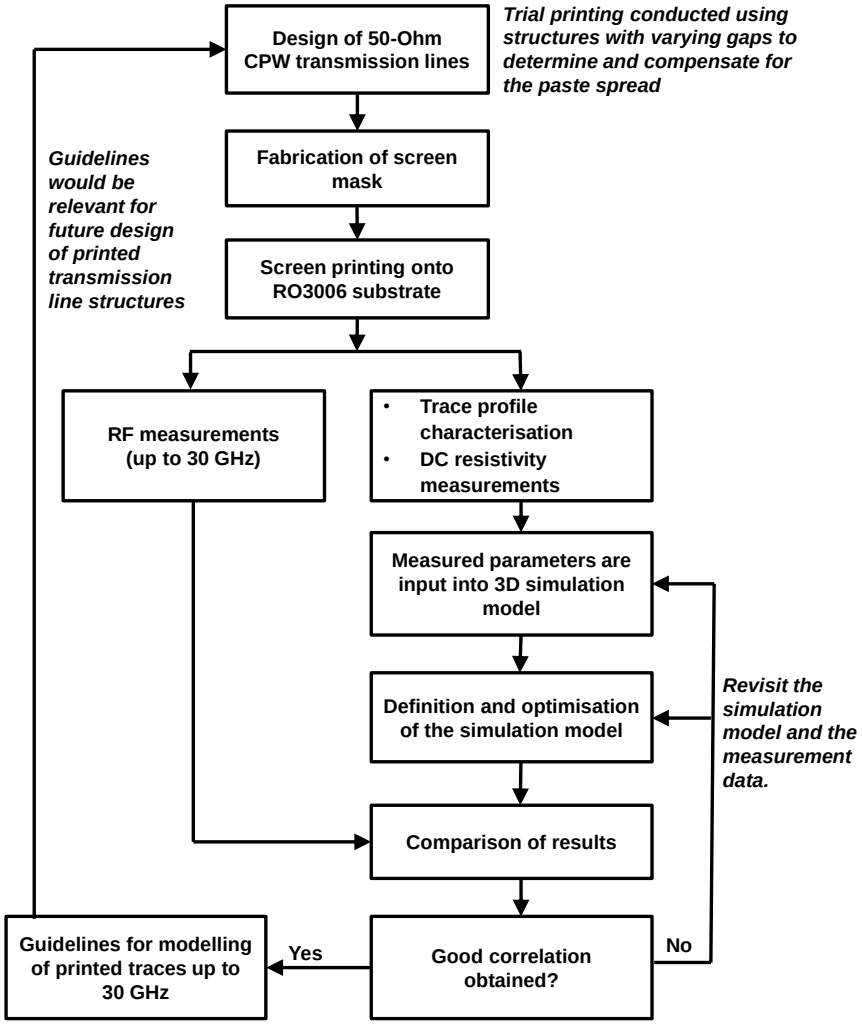

Figure 7.2 Proposed methodology for this work

The methodology used in this chapter is outlined in Figure 7.2, with the aim of obtaining 50Ω coplanar waveguide (CPW) transmission line structures. Such structures are essential to minimise signal reflections during measurements and maximise the power transfer [130]. However the paste spread on RO3006 is uncertain, which necessitates a trial test to determine this information for the specific silver paste used. The test structures for this trial include 50Ω CPW structures with zero spread. In addition CPW structures with the dimensions compensated to take into account paste spread (ranging from 25 μm to 150 μm) were included. Table 7.1 shows the compensated dimensions of the CPW structures with 250 μm pitch.

Table 7.1 50Ω CPW structures with paste compensation for varying spreads

	Width/spacing of CPW structure assuming different paste spread[17]				
	0 μm spread	**25 μm spread**	**50 μm spread**	**100 μm spread**	**150 μm spread**
Printed (Predicted)	150/45	175/50	200/50	250/70	300/80
Screen design	150/45	150/75	150/100	150/170	150/230

[17] based on the assumption that the paste spreads uniformly in the x-direction for both signal and ground traces.

Specifically, the CPW structures are designed with 250 μm pitch to enable RF measurements up to 30 GHz using microwave probes [237]. After the paste spread on RO3006 has been determined, the final 50 Ω structures can then be designed and realised via screen printing.

A number of techniques were used to characterise the samples in order to extract the trace profile and evaluate the electrical performance (DC and RF). These include four point probe measurements to obtain the DC resistivity of the printed traces. The trace profiles (e.g. signal width, signal-ground spacing) were characterised using a non-contact measurement technique. The data from these characterisations were then used to construct simulation models in *CST* [238], a three-dimensional (3D) electromagnetic (EM) simulator. After validating the simulation model and optimising it (in terms of meshing), the simulation results were compared against the RF measurements. A good correlation (± 0.5 dB) would

provide guidelines for the modelling of printed traces up to 30 GHz. If a poor correlation is obtained, the measured data used for the simulation model would be reconsidered. In addition, the assumptions made for the simulation model would be revisited.

7.3 Realisation of Transmission Line Structures

Due to the current fabrication constraints of the screen printing technology, it is challenging to fabricate multi-layer structures (Figure 7.3(A) and Figure 7.3(B)), as these require the grounds on different metallisation layers to be connected using vias to minimise undesired parasitic modes. Firstly, the realisation of the vias requires the use of laser drilling or chemical etching in printed circuit board (PCB) processes. This significantly increase the time and cost of producing the prototypes. In addition, issues may arise in aligning the vias between different layers since a manual screen printer is used to deposit the traces (i.e. larger dimensional tolerances). In view of these limitations, CPW structures are chosen as test structures since the signal and ground traces are coplanar (Figure 7.3(C)) and no vias are necessary for adequate grounding.

To study the effect of surface roughness, microstrip or striplines are typically used as test structures. This is further illustrated in Figure 7.3.

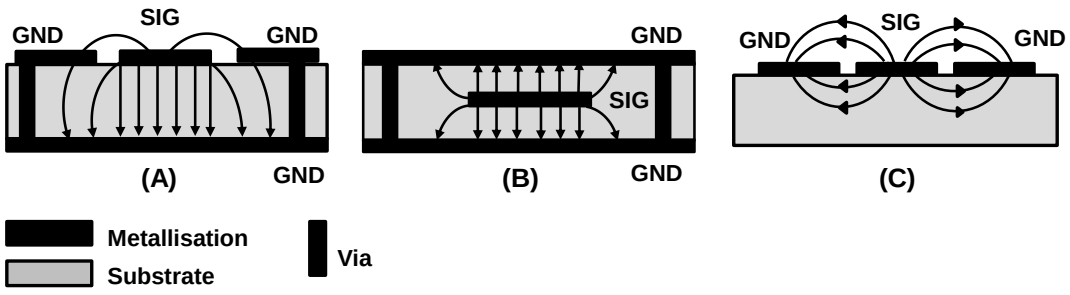

Figure 7.3 Electric field distribution of transmission line structures (A) Microstrip (B) Stripline (C) Coplanar waveguide

From Figure 7.3(A), the electric field distribution of the microstrip indicates that the conductor loss is influenced by the roughness on one side of the trace (i.e bottom side). For the case of the stripline configuration in Figure 7.3(B), the loss is influenced by the roughness on both sides of the trace. In the case where a CPW configuration is used as shown in Figure 7.3(C), the conductor loss would be

predominantly influenced by the roughness in the coplanar gaps since the electric field is confined around the ground-signal-ground (GSG) region. Curran [129] suggested that the effect of surface roughness in the coplanar gaps has negligible effect at DC and the lower frequencies, where a 1 mm long CPW structure with a coplanar gap of 1 µm was considered. It was claimed that the negligible effect is attributed to the smaller cross-sectional area occupied by the roughness in the gaps, relative to the roughness on the top and bottom sides of the CPW structure. However the roughness in the gaps was observed to have a significant impact at 50 GHz [129].

This phenomenon was further investigated in Appendix E1, where CPW structures with dimensions realisable by screen printing were fabricated. The fabricated CPW structures have gaps of 50 µm, which is the minimum dimension realisable by screen printing. The results obtained in Appendix E1 suggest that the effect of surface roughness from the coplanar gaps is negligible for 15 mm long CPW structures. As such, the effect of surface roughness was neglected in the modelling of the CPW structures in this chapter, which were designed with coplanar gaps of 75 µm.

7.3.1 Experimental Details

This section describes the experimental aspects of this work. This includes the materials and the test designs used in screen printing. The methodology for characterising the trace profile for simulation correlation is also detailed in Section 7.4.6.

(a) Substrates

The specifications of RO3006, the high frequency laminate used in this Chapter, are detailed in Section 4.3.1 of Chapter 4, with the corresponding datasheets provided in Appendix B1. As RO3006 is a low loss substrate (loss tangent = 0.002 at 10 GHz), the effect of the substrate loss on the overall CPW transmission line loss is negligible, where the overall loss is affected by the conductor, dielectric and radiation losses. Consequently the dominant loss then results from the conductor losses (assuming radiation losses are negligible), which could be accurately

captured using a 3D EM simulator to model the RF performance of printed traces. In addition the dielectric constant of RO3006 is well-characterised up to 40 GHz [31], which eliminates uncertainty in the dielectric property data used for the modelling (up to 30 GHz).

(b) Silver Pastes for Screen Printing

In this work, screen printing is used to fabricate the test structures. Compared to inkjet printing which yields thin layers, thicker traces are realisable using screen printing. This facilitates the modelling aspect, since the simulation model has to be meshed within the trace thicknesses to adequately capture the conductor losses. Thicker traces aid in limiting the overall aspect ratio (i.e. maximum versus minimum dimensions) of the simulation model and thus the computational resources which are required.

Two commercial silver pastes are used in this work, which are selected based on their suitability for fine line printing. Paste 1 is Rexalpha (RA FS 088, Toyo Co. Ltd), with a viscosity of 85 Pas and a silver content of 65-70 wt %. From the datasheet, the resistivity values are 8×10^{-5} Ω-cm (130 °C, 30 min) and 10×10^{-4} Ω-cm (100 °C, 30 min). Paste 2 is a research sample (CA-T31, Daiken chemical Co. Ltd) with a higher viscosity of 229 Pas and a silver content of 83.2 wt %. The corresponding resistivity is 1.4×10^{-5} Ω-cm (160 °C, 30 min).

(c) Test Structures for Screen Printing

An overview of the final designs is shown in Figure 7.4. The screen mask is divided into four regions to ascertain the repeatability of the printed test structures. Each region comprises of:

- 50Ω CPW transmission line structures designed for RO3006 and glass substrates. With reference to Figure 7.5(A), the linewidth/spacing (w/s) of the CPW structure on RO3006 is 150/75 µm while the w/s for the CPW structure on quartz is 350/50 µm. The CPW line lengths (*l*) are 2 mm, 7 mm and 15 mm. The details of the dimensions are shown in Table 7.2.

- Four point probe structures. As shown in Figure 7.5(B) these are used to extract the DC resistivity of the printed traces. The four point probe structures were positioned adjacent to the CPW transmission lines such that an in-situ measurement of the DC resistivity could be made for each CPW line for the simulation correlation. The rationale is that using an average conductivity value for the simulation correlation may not suffice, thus the need for four point probe structures to be placed beside the measured CPW lines for in-situ measurements. The widths of the test structures correspond to the signal (w) and ground (g) dimensions of the measured CPW lines, as listed in Table 7.3. There are 4 samples per trace width located in each region.

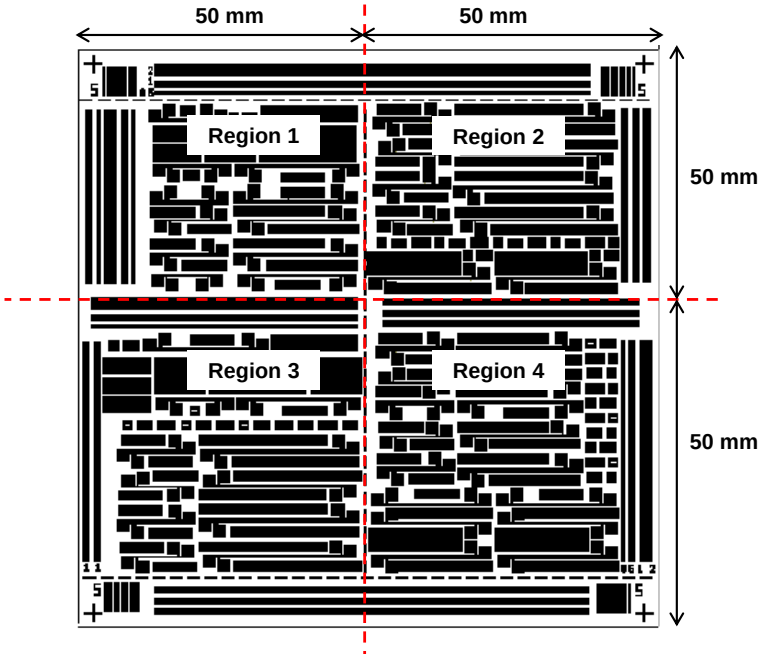

Figure 7.4 Final screen mask incorporating transmission line and DC test structures

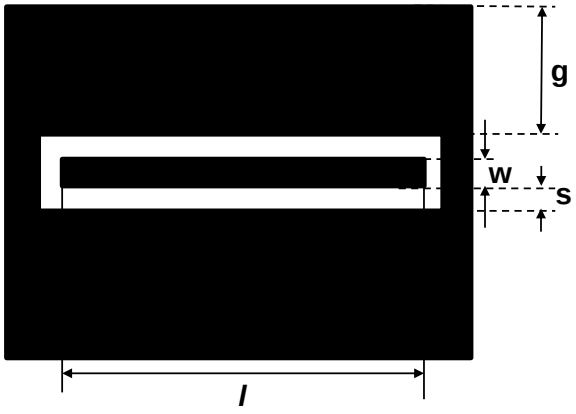

(A)

Figure 7.5 Test structures in the screen mask (A) CPW transmission lines

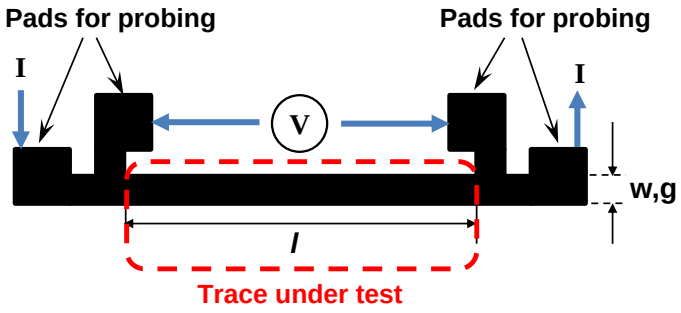

(B)

Figure 7.5 Test structures in the screen mask (B) Four point probe structure with current (I) applied through the outer pair of pads and voltage (V) measured from the inner pair.

Table 7.2 Dimensions of CPW transmission line structures

w (μm)	s (μm)	g (μm)	*l* (mm)	Remarks
150	75	690	2, 7, 15	RO3006
350	50	1750	15	Quartz[18]

[18]The CPW dimensions on quartz pertains to Appendix E1

Table 7.3 Dimensions of four point probe structures

w,g (μm)	*l* (mm)	Substrate
150 690	7,15	RO3006

(d) Screen Specification

The printing was performed using a manual screen printer (TOPRO ZT320) as shown in Figure 7.6(A), which had a suction function to hold the substrate in place. In addition, tape was used to fix the 4 sides of the RO3006 substrate to the chuck, as a slight warpage was observed for the PTFE-based substrate. The test structures were fabricated in a 320 x 320 mm screen, using a mesh count of 640 (i.e. 640 threads/inch), an emulsion thickness of 7 μm and an open area of 39 %. The screen mask had a mesh tilt of 22.5°. However a smaller area of 100 x 100 mm was utilised for the designs, due to constraints on the total design area possible (with respect to the screen size) in order to maintain the dimensional accuracy of the printed structures. Setting the usable area at 100 x 100 mm follows the guideline of setting the ratio between the design area and frame size to be within 1/9 (1/3 x 1/3).

Figure 7.6(B) shows a schematic of the screen cross-section and the paste deposited onto the substrate after screen printing.

Prior to printing, the sample surfaces were cleaned with acetone and dried using nitrogen gas. The squeegee durometer (i.e. physical hardness) used for printing is 80-85, and the print speed is around 200 mm/s, with the squeegee pressure controlled manually. The off-contact distance between the mesh and substrate was set at 1.5 mm. The samples were thermally cured at 130 °C for 1.5 hours after printing.

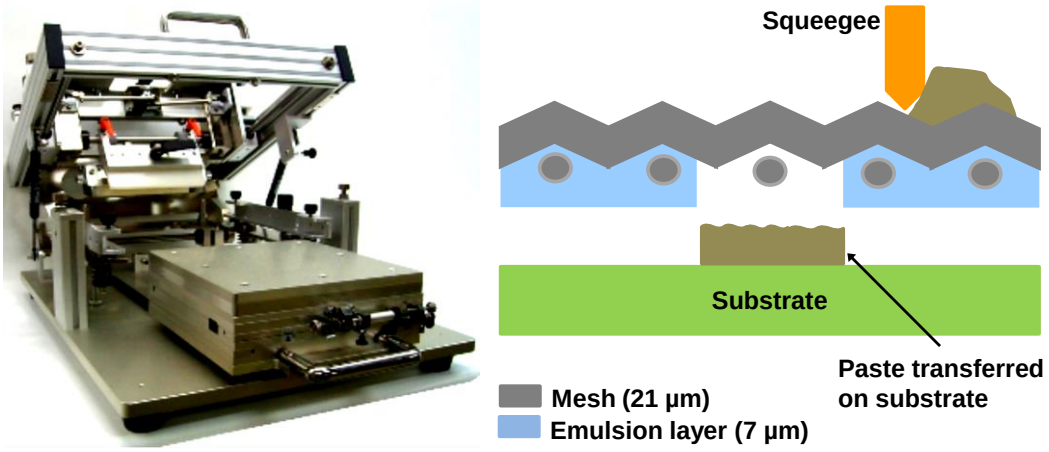

Figure 7.6 Screen printing (A) Manual screen printer used (B) Schematic showing cross section of the screen and the screen specifications used

(e) Electrical Measurement Parameters

(i) DC Measurements

The four point probe measurements were performed using a semiconductor parameter analyser (Agilent 4156C) connected to a DC probe station. The input current range was set from -1 mA to 1 mA in steps of 10 µA (i.e. 201 data points) and the corresponding voltage obtained from the four point probe structures. A total of 16 samples with trace widths of 150 µm and 690 µm were measured, with 4 samples (per trace width) located in each substrate region. Each sample was measured twice, and the average value used to calculate the DC resistivity.

(ii) RF Measurements

The RF measurement set-up is as described in Section 4.5.2 of Chapter 4. The frequency range is set from 0.1-30.1 GHz in the network analyser, with 201 measurement points. Microwave coplanar probes with 250 µm pitch (40A-GSG-250-DP, GGB Industries Inc.) were used for the two-port measurements [237]. An Intermediate Frequency (IF) bandwidth of 100 Hz was used along with an averaging factor of 64. Prior to measurements, a Line-Reflect-Reflect-Match (LRRM) calibration was performed, and the magnitude of the S_{11} parameter for a 600 µm coplanar line standard on the calibration substrate [239] was verified to be ≤ -40 dB at 30.1 GHz. As the RF measurements were performed on RO3006, a low loss substrate, the effect of substrate parasitics [240] were neglected.

(f) Characterisation of Trace Profile for EM Simulation

(i) Parameters to Extract DC Conductivity Values

To extract for the DC conductivity values, 3D non-contact laser measurements (LEXT OLS-4100, Olympus) are made for the 2 ends of each test structure. The lens magnification and imaging option used are as described in the next section, Section 7.3.1(f)(ii). The results of both ends are then averaged, with the assumption that the dimensions of the entire test structure are consistent. For each scanned region of the test structure, the cross-sectional area (averaged) is calculated from the trace region defined with a post processing function (Figure 7.7).

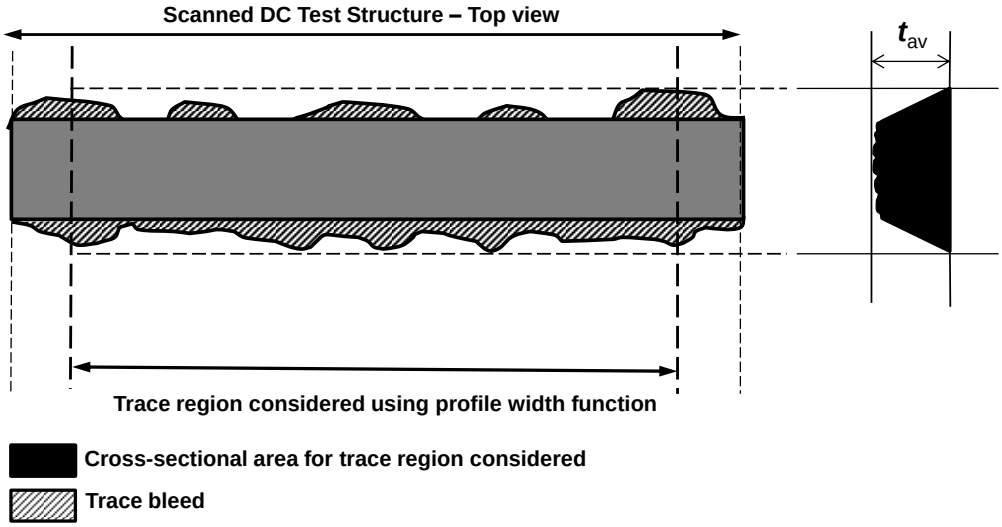

Figure 7.7 Schematic showing the determination of trace parameters for DC resistivity extraction

The corresponding average trace thickness (t_{av}) is determined manually using measurement lines in the software.

(ii) Transmission Line Parameters

To obtain a good correlation between simulation and measurement results, an accurate evaluation of the transmission line dimensions for use in the simulation model is critical. Figure 7.8 is a schematic showing the evaluation of the transmission line dimensions.

The entire transmission line profile is scanned in the 3D non-contact measurement system (LEXT OLS-4100, Olympus) using a x20 objective lens with a fast scan, which was found to be a compromise between speed and accuracy. Prior to this, a trial test was carried out to ascertain the suitable scan speed, the details of which can be found in Appendix E2.

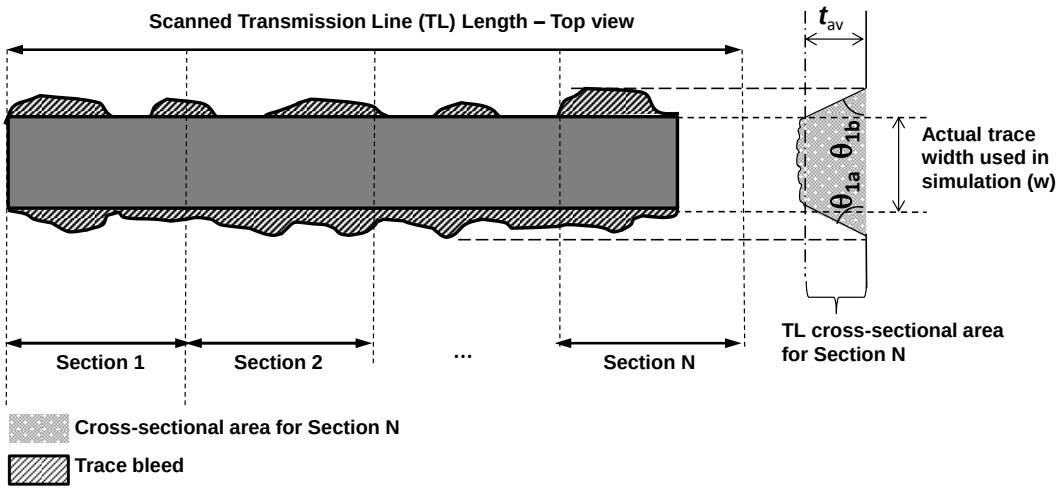

Figure 7.8 Schematic showing the evaluation of trace parameters using non-contact measurements

The x20 objective lens had a field of view of 80 μm. In particular, a differential interference contrast (DIC) - laser imaging was used for the scan. The DIC-laser option was used as it allows one to obtain a more accurate view of uneven surfaces (in range of a few nano-meters to a few micro-meters). This option is used for the RO3006 substrate which has non-negligible surface roughness. During measurements the brightness from the lens is automatically adjusted at each acquisition position.

During post-processing, levelling was performed for the scanned trace images. For glass substrates, an "inclination profile" option was used. However a manual correction was performed for the RO3006 substrate which displayed warpage after thermal curing, as RO3006 is a soft substrate. In this case the trace profile was corrected through the selection of three points on the image so as to specify the inclination plane for which to correct.

The profile width function was then used to yield an average value across individual sections of the scanned trace (Figure 7.9). In this case, a profile is defined as the trace parameters (i.e. width, height, cross-sectional area, trace edge angles) along a specified line on the trace. Each section was defined to be around 10-20 % of the total trace length, following which the average values of the trace parameters were extracted. For the RO3006 substrate, an increased number of sections were used. This is since some areas of the substrate are warped. As a result, the regions on the RO3006 substrate which can be considered level are smaller.

In particular, the regions with trace bleeding were not considered in the extraction of the trace width as the corresponding thicknesses were observed to be negligible. Aoki *et al*. [241] observed that the bleeding regions are not connected and as such may not contribute to the current flow. This is also highlighted in Figure 7.9, which shows a FIB-SEM of the side-view of a silver trace (after thermal curing) printed on a borosilicate glass substrate. Trace bleeding could be observed along the edges of the trace in Figure 7.9.

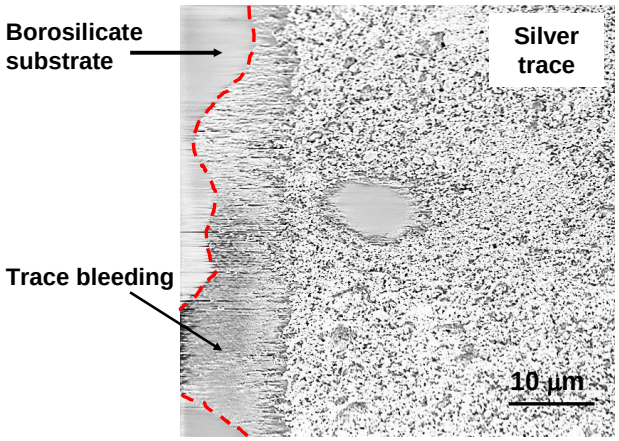

Figure 7.9 FIB-SEM showing silver trace with trace bleeding

Using the methodology described above, the profiles for a CPW structure as shown in Figure 7.10 were characterised. This includes the signal width (*w*), the signal-ground spacings (g_1, g_2), the conductor edge angles (θ_{1a} *to* θ_{3b}), and the conductor thicknesses (*t*). The angles θ_1, θ_2 used in the simulation correlation were compensated by 5° since the trace bleed regions on the trace periphery were excluded in the extraction of the trace width. The trace dimensions were extracted with an accuracy of around ±10 μm.

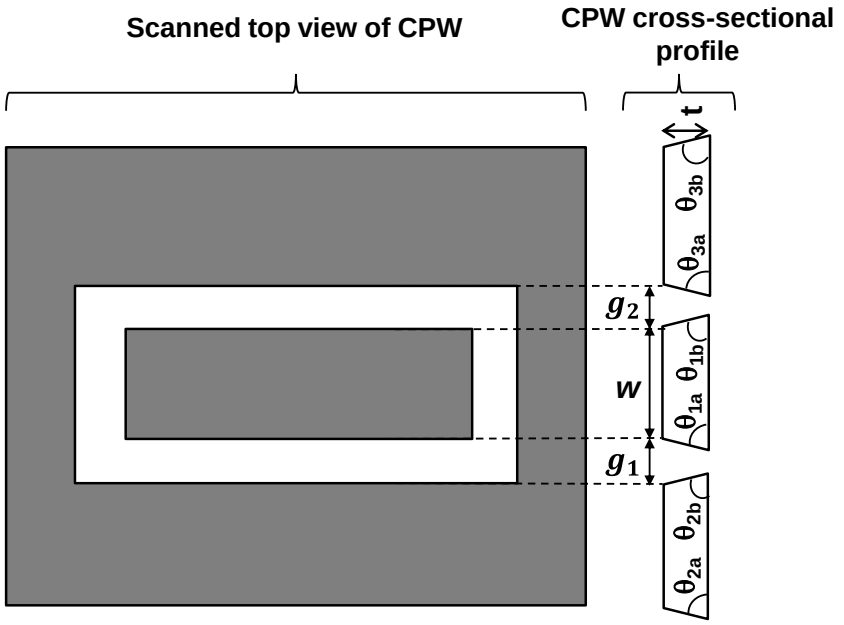

Figure 7.10 A typical CPW structure with notations to indicate the parameters extracted from the trace profile

7.3.2 Simulation Model Setup

A typical 3D simulation model used for the correlation of a CPW structure is as shown in Figure 7.11. The model is simulated using a Time Domain (TD) solver in *CST* which is suitable for the evaluation of electrically large structures. The solver uses hexahedral meshing to simulate the structures.

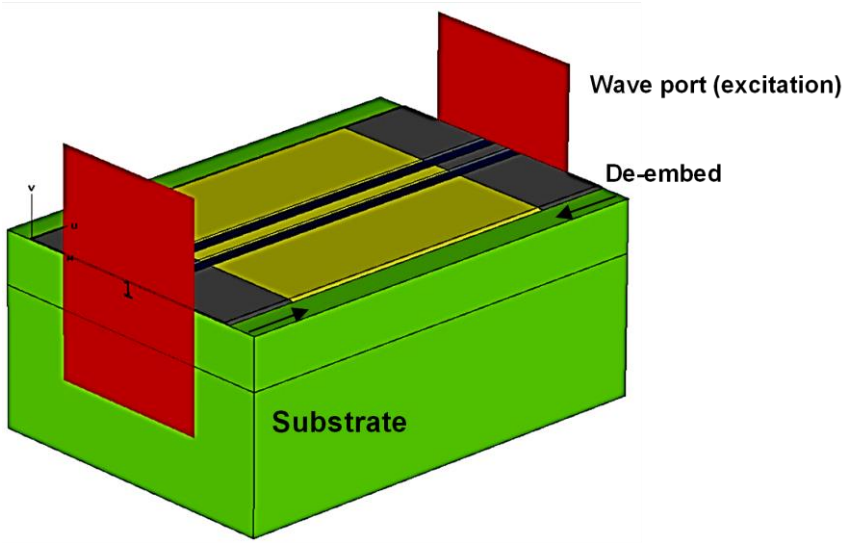

Figure 7.11 A typical simulation model of the CPW structure for the result correlation

Details of the waveguide ports used to excite the CPW structure can be found in Section 4.4.2 of Chapter 4. The accuracy set for which the simulation would terminate is -40 dB. Due to the symmetry of the reflection and transmission behavior of the signals, the *S*-parameter symmetry option (S_{11}= S_{22}) is utilised in the simulation. Through this setting, the simulation time can be reduced as the solver considers only the essential simulation runs.

(a) Considerations in the Modelling of Printed Transmission Lines

In simulating CPW structures obtained by screen printing, where the printed trace conductivity values are lower than the bulk metal conductivity, the conventional model setup which considers waveguide ports directly contacting the printed traces is no longer applicable. This is because the waveguide ports require contact with a perfect or lossy metal in order for the electromagnetic fields to be generated correctly. In this case the screen printed traces are defined as a “normal” material instead of a “lossy” material due to the need to mesh within the trace thickness. If a “lossy” material is defined, the simulator adopts a surface impedance formulation approach and only mesh at the surface of the trace. This approach does not compute for the field inside the trace volume and suffices for cases where the skin depth of the trace is much smaller than the trace thickness, by at least a factor of 5 times. To circumvent this, short lengths of transmission line (0.5 mm) defined with a perfect metal were used to contact the waveguide ports at both ends of the

transmission line, to ensure that the correct electromagnetic fields were being excited. A de-embedding function was then used to remove the perfect metal lengths electrically, such that only the lengths defined by the printed traces were being considered during post-processing. The de-embedding function is used to shift the reference plane (for *S*-parameter calculations) relative to the waveguide port by a specified length, which adjusts the phase information of the *S*-parameters.

In addition, due to the thin silver traces (~8.5 μm) and the non-negligible skin depth of 2.9 μm at 30 GHz, there is a need to mesh densely within the trace thickness in order to capture the skin effect on the transmission line loss (Figure 7.12). Apart from this, it was also important to mesh for the trace edges of the trapezoidal trace so as to capture the current crowding effect in those areas. The resulting mesh is shown in Figure 7.13.

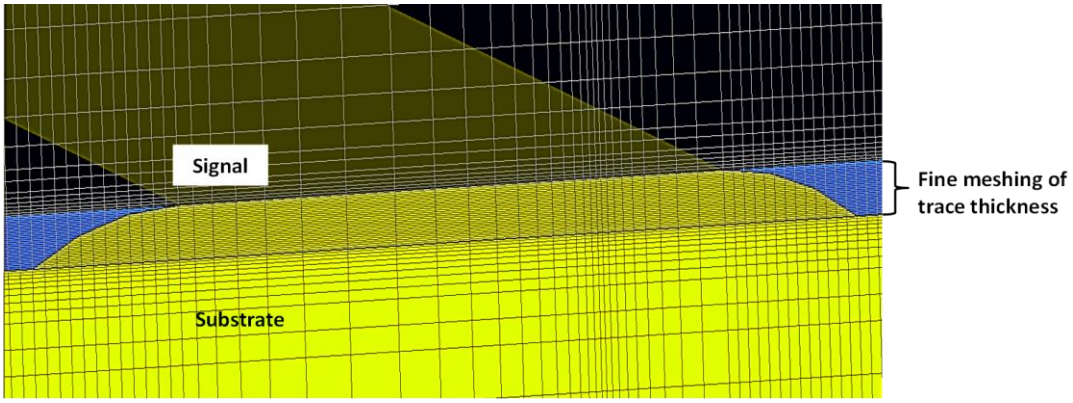

Figure 7.12 Meshing of traces at signal region to capture the skin depth

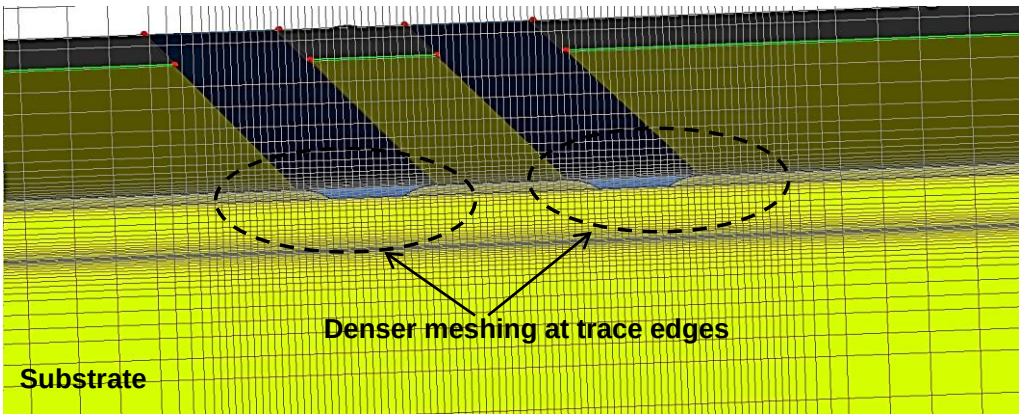

Figure 7.13 Mesh view of CPW structure showing denser meshing at the trace edges

Overall the meshing within the traces was optimised to balance between obtaining an adequate mesh versus over-meshing which results in significantly long computational time. The key meshing considerations are summarised in Table 7.4, where the *S*-parameter results for a CPW model with varying degrees of meshing were compared and optimised for a balance between the accuracy of the results and the simulation time required.

Table 7.4 Simulation settings for optimised model

	Setting 1	**Setting 2**	**Setting 3**	**Setting 4**
Meshing for trace thickness (z-direction)	Every 1 µm	Every 1.7/3 µm[19]	Every 1.7/9 µm[19]	Every 1.7/9 µm[19]
Inhomogeneous port accuracy enhancement	No	Yes	Yes	Yes
Electric shielding for ports	Yes	Yes	Yes	Yes
Energy balance	-40 dB	-40 dB	-60 dB	-40 dB
S-parameter symmetry	No	No	No	Yes
Total no. of meshes (hexahedral)	182,280	316,386	496,314	496,314
Total simulation time[20]	8h 3min 23s	6h 2min 24s	140h 24 min	19h 1min
Remarks	Insufficient meshing	Insufficient meshing	Long simulation time	Final setting

[19]1.7 µm represents the skin depth of the printed trace at 30 GHz. [20]A 64-bit Intel Xeon workstation with a random access memory (RAM) of 3 GB was used to perform the simulations. The operating system in the workstation is Windows XP.

From Table 7.4, an inhomogeneous port accuracy enhancement feature was activated for the 3D models since a broadband frequency range (0.1-30.1 GHz) is being considered. As the CPW line is an inhomogeneous structure, the waveguide port solver is less accurate for broadband frequencies as the interval between the upper frequency and the centre frequency is increased. As such activating the inhomogeneous port accuracy enhancement feature would aid in improving the *S*-parameter results.

In the optimised meshing, the trace thicknesses were meshed by a factor of skin depth/9 to adequately capture the loss due to the skin depth effect, where the skin depth refers to that at the maximum frequency. In comparing setting 3 with setting 4 (final setting), the simulation time could be reduced significantly (by 7 times)

through the use of the *S*-parameter symmetry and an energy balance of -40 dB, to obtain the same results.

(b) Use of Half Length Models

To reduce the simulation time and hardware resources required for simulating electrically long structures, attempts were made to simulate the CPW structures at 50 % of their actual lengths. The *S*-parameter results obtained for the half-length structure would then be cascaded to estimate the performance of the actual structure (100 % length). This procedure is performed in a circuit simulator (Advanced Design System 2014.01, Agilent Technologies) as shown in Figure 7.14.

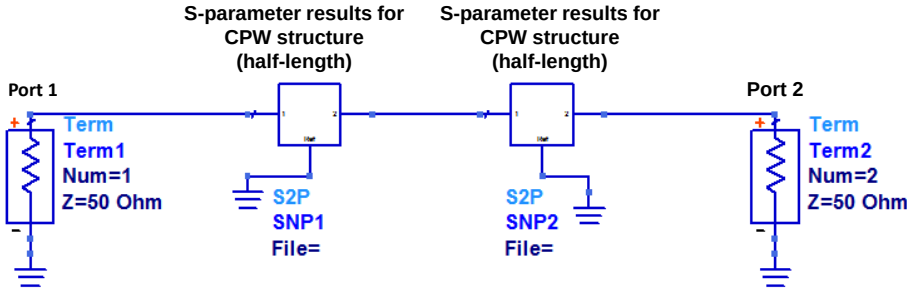

Figure 7.14 Schematic of cascaded *S*-parameter results

This approach is intended for a quick gauge of the results and to fine-tune the model where necessary to improve the correlation. The final model would then be simulated using the full length of the CPW structure to verify the results. A comparison of the insertion loss results obtained of a 7 mm long line using a full model versus a half-length model is shown in Figure 7.15.

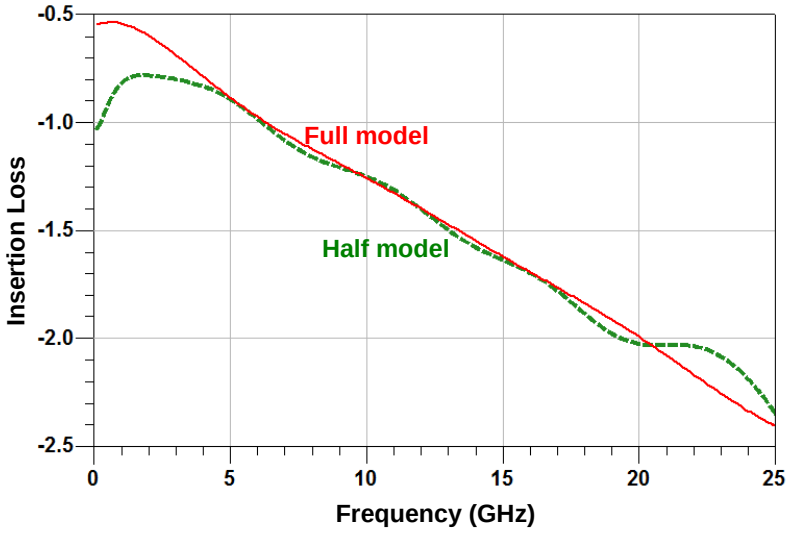

Figure 7.15 Comparison of results between a full CPW model and a half CPW model

From Figure 7.15 a good match is observed between the 2 models beyond 4 GHz. This suggests the feasibility of using a half-length model to estimate the performance, with the simulation of the full model used for the final model. With reference to the results shown in Figure 7.15, the time taken for the full model was 15 h 8 min involving 1.7 million meshes, while the time required for the half-length model was reduced by more than 50 % to 6 h 38 min involving 0.97 million meshes.

7.4 Results and Discussion

This section describes the verification of the simulation model in *CST*. In addition, the DC conductivity results for printed traces on RO3006 are discussed, along with the simulation correlation with measurements. Lastly, the influences of the DC conductivity and the trace edge profile on the RF performance of CPW transmission lines are discussed.

7.4.1 Verification of 3D Simulation Model

Following the optimised settings obtained for the simulation model in Section 7.3.2(a), the 3D model was subsequently verified by comparing the *S*-parameter results with those obtained from a Frequency Domain (FD) solver available in *CST*. As described in Section 3.2(b) of Chapter 3, *S*-parameters have been developed to characterise high frequency structures [130], and are measurable using network analysers.

The FD solver in *CST* uses a different meshing (tetrahedral meshing) to simulate a structure and is more typically used for electrically small structures. Figure 7.16 shows a comparison of the *S*-parameter results between the two solvers for a 7 mm CPW structure on RO3006.

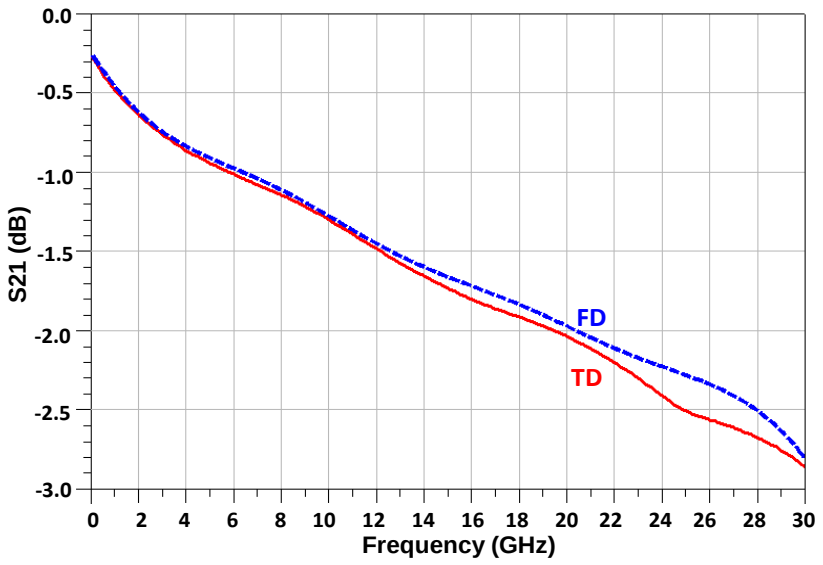

(A)

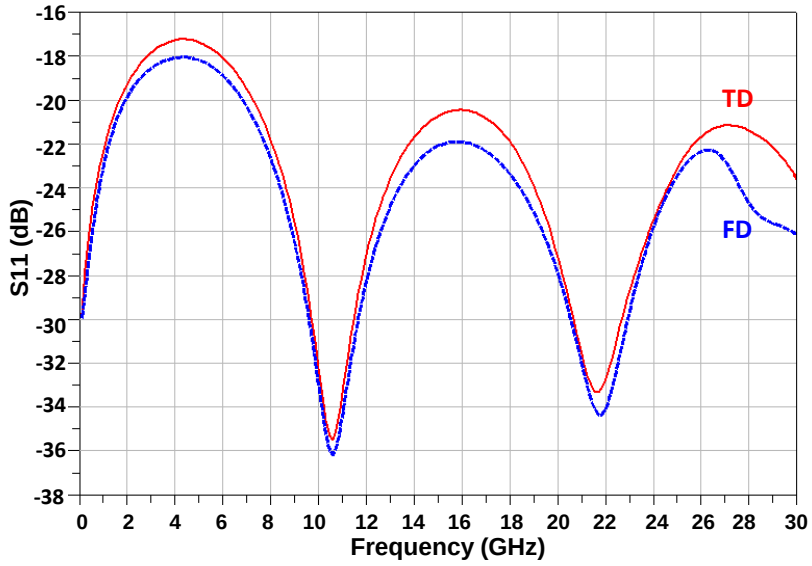

(B)

Figure 7.16 Comparison of *S*-parameters obtained from TD and FD solvers in terms of the (A) S_{21} (B) S_{11}

From Figure 7.16, a good agreement between the two models is obtained, with a variation of within 0.2 dB observed for the S_{21}. The variation observed between the two set of results could be attributed to numerical error and material characterisation, since the material characterisation is treated differently between the FD and TD models. Material characterisation in this case refers to the fitting of the dielectric properties of RO3006 across broadband. These dielectric properties were input using values from the RO3006 datasheet since they are not available in the materials library.

7.4.2 DC Conductivity Values

Figure 7.17 shows the results obtained for test structures with widths of 150 µm and 690 µm. The widths correspond to the signal and ground widths of a CPW line and the trace thicknesses range from 7.2-9.5 µm on RO3006 substrate.

From the results it can be observed that the average DC conductivity values after 1.5 hours of thermal cure were close to that provided by the manufacturer after 30 min of thermal curing (1.25 x 10^6 S/m), which suggests that the DC conductivity may have reached saturation point due to paste fillers present in the formulation. This implies that obtaining lower DC resistivity values may only be possible through the use of a different paste formulation. However the values were noted to vary across the 4 regions of the panel (regions with reference to Figure 7.4) as shown in Figure 7.17. The values used to plot Figure 7.17 are listed in Appendix E3.

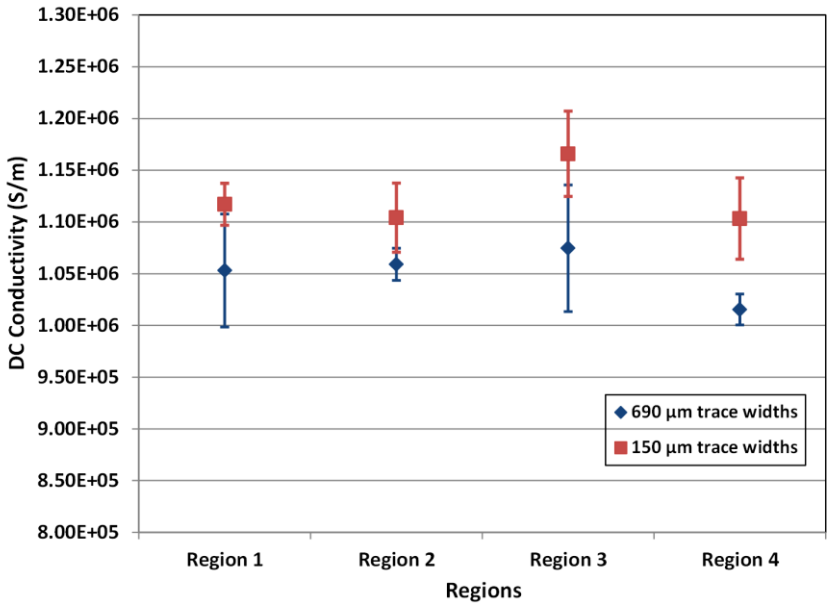

Figure 7.17 Standard deviation plot of the average DC conductivity in the different regions of the RO3006 substrate (with reference to Figure 7.4)

For the traces of 150 µm widths (16 samples), the average DC conductivity ranged from 1.10-1.17 x 10^6 S/m while for the traces of 690 µm widths (16 samples) the average DC conductivity was in the range of 1.02-1.07 x 10^6 S/m. The corresponding standard deviation was 2.0-4.1 x 10^4 S/m for traces of 150 µm widths and 1.5-6.1 x 10^4 S/m for traces of 690 µm widths. The variation of the DC

conductivity values may be attributed to the assumptions made during the extraction of the values using the four point probe measurement method. This technique assumes a uniform material (i.e. uniform thickness) over the measurement area. In contrast the printed traces on RO3006 were observed to yield non-uniform thicknesses as shown in Figure 7.18.

With reference to Figures 7.18(A)-(C), the red dots/regions represent the maximum trace thicknesses. From Figure 7.18(A) and 7.18(B), the traces printed using paste 1 onto RO3006 and glass substrates were observed to yield non-uniform thicknesses. This is also reflected in the corresponding cross-section profiles in Figures 7.18 (D) and 7.18(E), where a height variation of 4.8-6.8 µm was observed for printed traces using paste 1. In contrast, a smaller thickness variation of 1.5 µm was observed in Figure 7.18 (F) for printed traces using paste 2 (on glass). This particular trace was also observed to have a more uniform thickness from the top profile captured in Figure 7.18 (C).

Such a phenomenon could be mainly attributed to the paste levelling [60, 242] after screen printing, which results from the screen mask and paste interaction. Itoh *et al*. [243] and Buzby *et al*. [242] highlighted that the paste transfer from the screen mask to the substrate is non-ideal, because the paste adhesion is also affected by the wire meshes and the emulsion side walls, apart from the substrate surface. Buzby *et al*. [242] showed that the emulsion side walls are not perfectly smooth, which could have resulted in some paste adhesion to the side walls during printing. In addition, there would be some residual paste on the wire meshes during screen printing.

During the printing process, the paste formulation [60, 242] influences the extent of adhesion of the paste onto the mesh and substrate, thus affecting the uniformity profile of the printed trace. Phair *et al*. [60] suggested that an increased binder content in the paste formulation would increase the adhesion property of the paste onto the mesh, which results in an increased surface roughness of the printed trace. This agrees with the information from the silver paste datasheets, where paste 1 has a binder content of 8-10 wt % compared to a binder content of 5-7 % for paste 2.

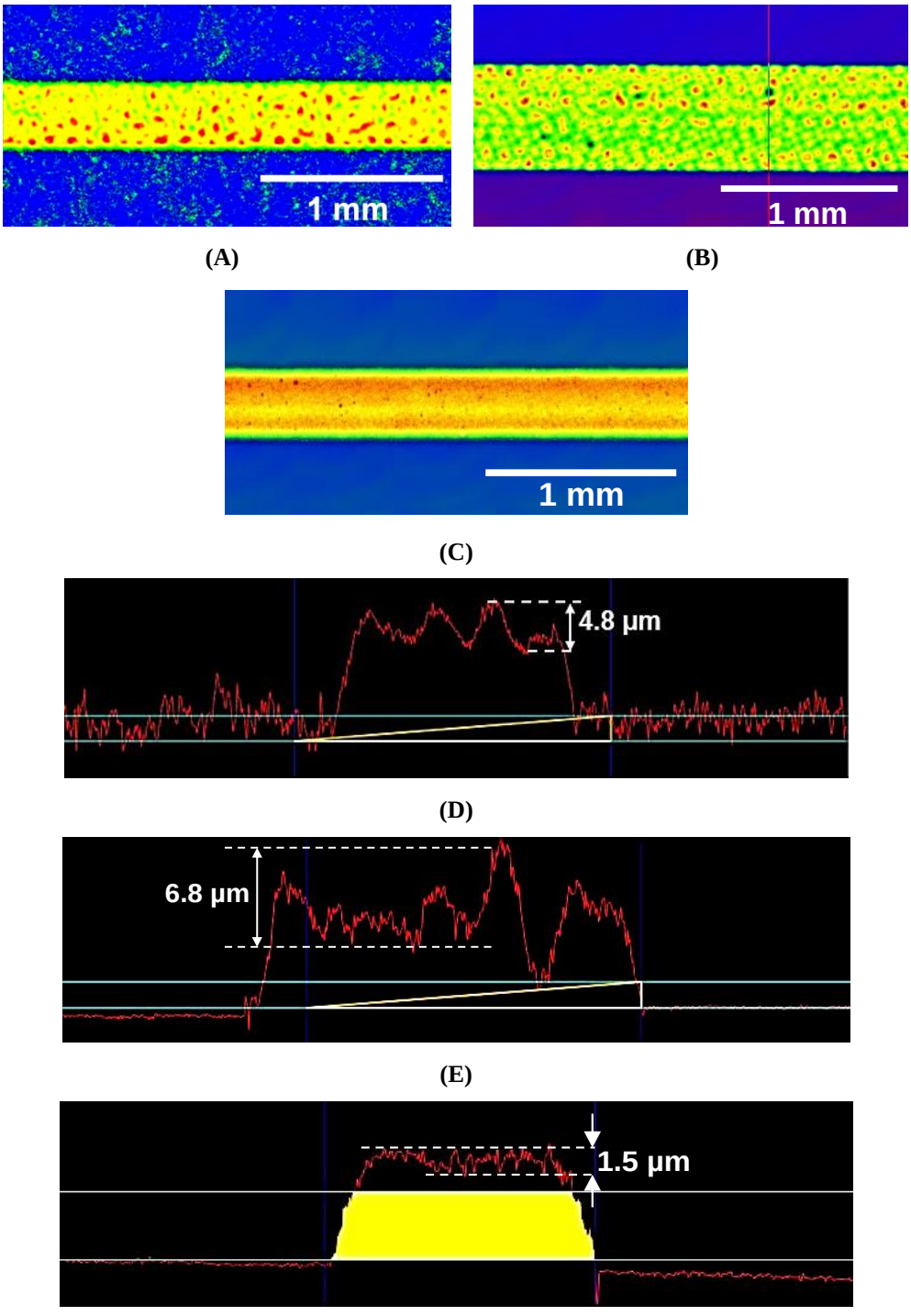

Figure 7.18 Diagram showing trace profiles of DC test structures (A)Top view of trace on RO3006; (B) Top view of trace on glass using paste 1; (C) Top view of trace on glass using paste 2; (D) Corresponding cross-section of trace in (A); (E) Corresponding cross-section of trace in (B); (F) Corresponding cross-section of trace in (C)

The screen mask-paste interaction on the printed trace profile is summarised in Figure 7.19. From literature (e.g. [60]), such a phenomenon has been reported to affect the mechanical and electrochemical characteristics of the trace. The results obtained in this section suggest that the mesh-paste interaction may also have a significant influence on the DC electrical performance.

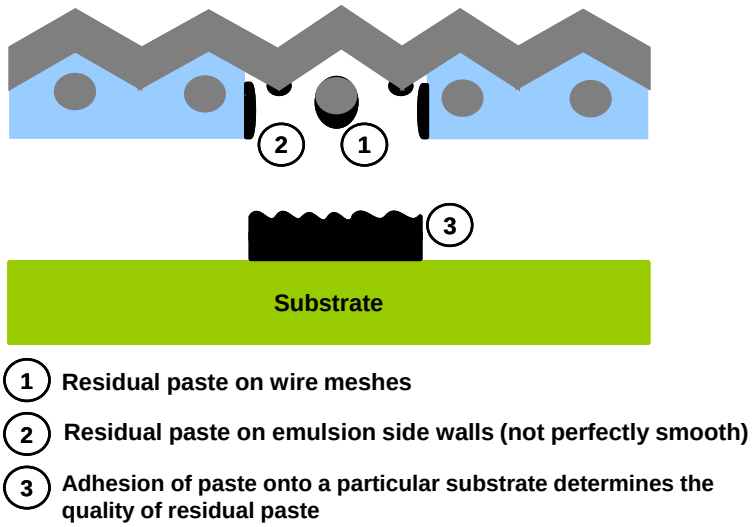

Figure 7.19 Factors influencing the paste-substrate interaction in the screen printing process

Overall, the results necessitate the selection of a suitable paste which yields uniform trace thicknesses and an improved consistency in the extracted DC conductivity values. This procedure of paste selection is recommended before the actual screen printing of the test structures. The results also suggest that due to the variation in the DC conductivity values, it is crucial to obtain an accurate DC conductivity value for a good simulation correlation with measurements for the printed CPW line considered.

7.4.3 Correlation of Simulation and Measurement Results

This section discusses the results obtained in correlating simulation and measurements. The proposed methodology is first verified on a short CPW line of 2 mm length, followed by a longer CPW line (15 mm) on RO3006. The 15 mm CPW line is considered as the dimensional variations are more significant for longer printed lines, and it is essential to verify that the proposed methodology is also applicable for longer line lengths.

(a) Correlation for a Short Transmission Line on RO3006

Figure 7.20 shows an optical microscope image of a typical CPW line printed on RO3006. The results correlation for a 2 mm CPW line are shown in Figure 7.21 and Figure 7.22, with the measured dimensions used in the simulation model listed in Table 7.5.

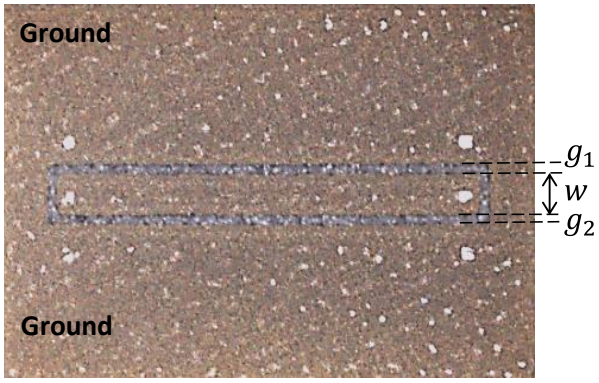

Figure 7.20 Optical microscope image of a printed CPW line (2 mm long)

Table 7.5 Trace parameters used in the simulation model, with reference to Figure 7.10

w (μm)	g_1, g_2 (μm)	t^{21} (μm)	θ_{1a}, θ_{1b} (°)	θ_{2a}, θ_{2b} (°)	θ_{3a}, θ_{3b} (°)	DC conductivity (S/m)
160	57,55	8.5	16.9,17.7	17.7,16.9	17.9,13.1	1.1×10^6

[21] t represents the average conductor thickness for the signal and ground traces

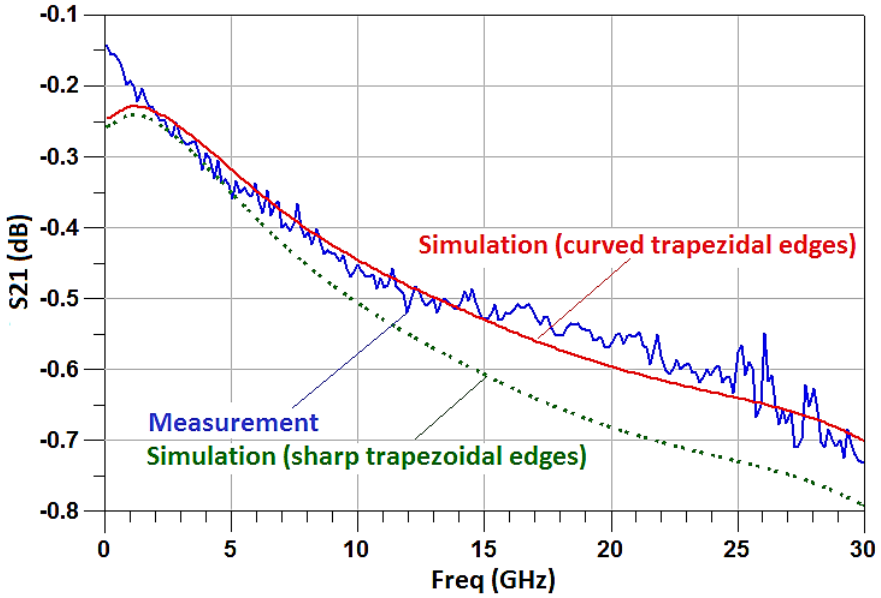

Figure 7.21 Correlation of measurement and simulation results (S_{21})

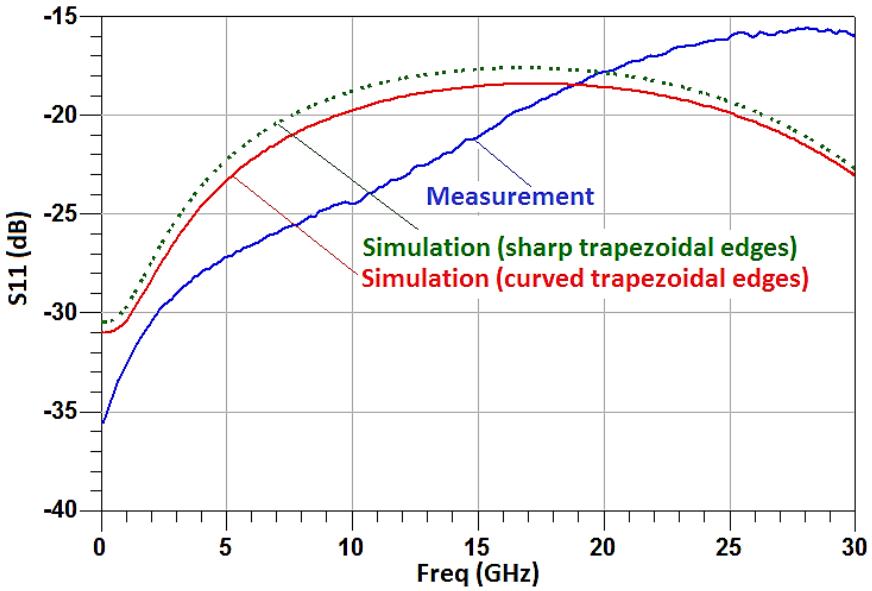

Figure 7.22 Correlation of measurement and simulation results (S_{11})

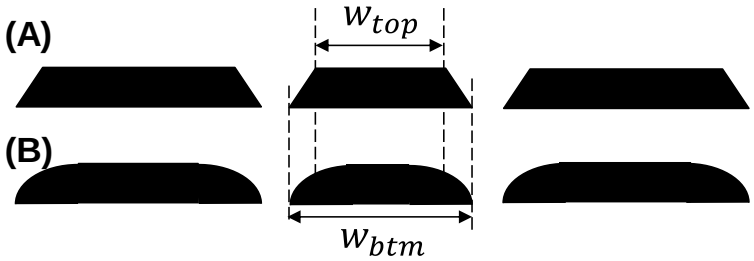

Figure 7.23 Trace edge profile considered in simulation (A) Sharp trapezoidal edge (B) Curved trapezoidal edge

From Figure 7.21, a good correlation is obtained between simulation and measurement results up to 30 GHz. The discrepancy observed at DC in Figure 7.21 could arise from inaccuracies in using the TD solver to solve at very low frequencies. From Figure 7.22, a similar trend is observed between simulation and measurements for the return loss results. The discrepancy observed in Figure 7.22 is with respect to the larger scale division used for the y-axis, relative to Figure 7.21. At 30 GHz a discrepancy of 7 dB is observed between simulation and measurements (Figure 7.22), which corresponds to a slight variation of 0.09 dB in terms of the insertion loss (S_{21}).

In particular, the effect of the trace edges was investigated for the 2 mm transmission line in the result correlation. When sharp trapezoidal edges were used to model the printed traces in the simulation model, the losses (S_{21}) were found to

be overestimated by about 14 % at 30 GHz as shown in Figure 7.21, with the effect on the return loss being negligible (Figure 7.22). Specifically the trace edge profiles considered are shown in Figure 7.23, where the widths of the top (w_{top}) and bottom surfaces (w_{btm}) of the traces are modelled as identical, with the same conductor edge angles, with the only difference located in the trace edges. In modeling the trapezoidal corners as curved edges, a good match could be obtained between the simulation and measured results. This effect has been little investigated in literature [129] and the results indicate that the trace edge profile may affect CPW structures more significantly due to the confinement of the electric fields around the ground-signal-ground region (Figure 7.3(C)). This phenomenon also agrees well with the observation made by Azucena *et al*.[71], in that the conductor losses are affected by the trace edge profiles of CPW structures since most of the current flows along the trace edges in those structures [71].

Apart from the trace edge profile, the effect of the DC conductivity on the RF performance was also investigated. Figure 7.24 shows the results obtained when the lower range of the measured DC conductivity (7.7×10^5 S/m) is considered. From Figure 7.24, an increase in the insertion loss by 0.03-0.05 dB/mm was observed throughout 0.1-30.1 GHz, with the increase of 0.05 dB/mm obtained at 30.1 GHz. This larger increase at 30.1 GHz is attributed to the significant effect of skin depth on the RF resistance at 30.1 GHz, relative to the resistance at DC [244]. As expected, a similar increase in the insertion loss arising from the DC conductivity variation was observed for the longer 15 mm CPW line. One implication of the results is that the variation in the DC conductivity values may be significant for the case of low loss transmission lines, which necessitates a consideration of this variation during the design stage.

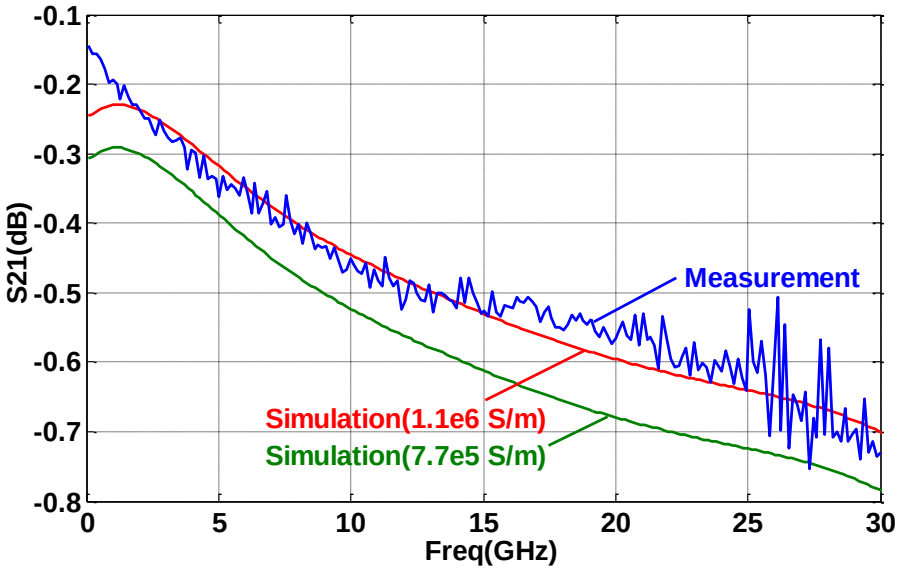

Figure 7.24 Insertion loss considering the lower DC conductivity value. The results are for another 2 mm CPW line with the same designed dimensions as the CPW in Figure 7.21

(b) Correlation for a Longer Transmission Line on RO3006

The methodology was also validated for a longer transmission line on RO3006 which is 15 mm long. A half-length model as described in Section 7.5(b) was first simulated, followed by the full length model for the final matching. The measured dimensions used in the simulation model are listed in Table 7.6.

Table 7.6 Trace parameters used in the simulation model, with reference to Figure 7.10

w (μm)	g_1, g_2 (μm)	t[22] (μm)	θ_{1a}, θ_{1b} (°)	θ_{2a}, θ_{2b} (°)	θ_{3a}, θ_{3b} (°)	DC conductivity (S/m)
160.8	54.5,60.1	8.1	15.8, 17.4	21.0,16.2	18.6,17.4	1.1 x 10^6 (Ground) 1.13 x 10^6 (Signal)

[22] t represents the average conductor thickness for the signal and ground traces

From the results in Figure 7.25 and Figure 7.26, a good correlation can be observed between the simulation and measurement for both the insertion loss (S_{21}) and return loss (S_{11}) results. The resonant points for S_{11} were observed to be within 0.2-0.8 GHz between simulation and measurement results, where the discrepancy was observed to increase beyond 20 GHz. The discrepancy may be attributed to the loop inductance in the measured structure which is not accounted for in the 3D model as a result of using a waveguide port excitation. Consequently the full return path could not be modelled and this could have resulted in a slight shift of the S_{11}

resonant points since current follows the path of least inductance at higher frequencies.

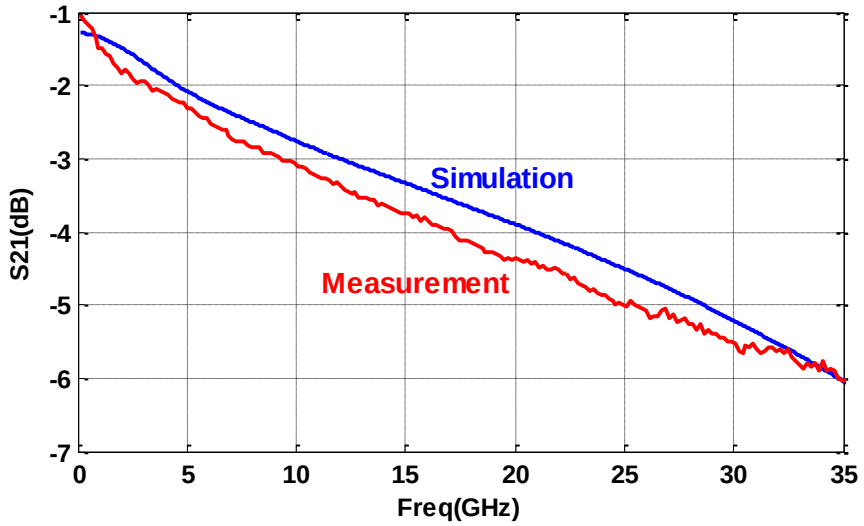

Figure 7.25 Correlation between measurement and simulation results (S_{21})

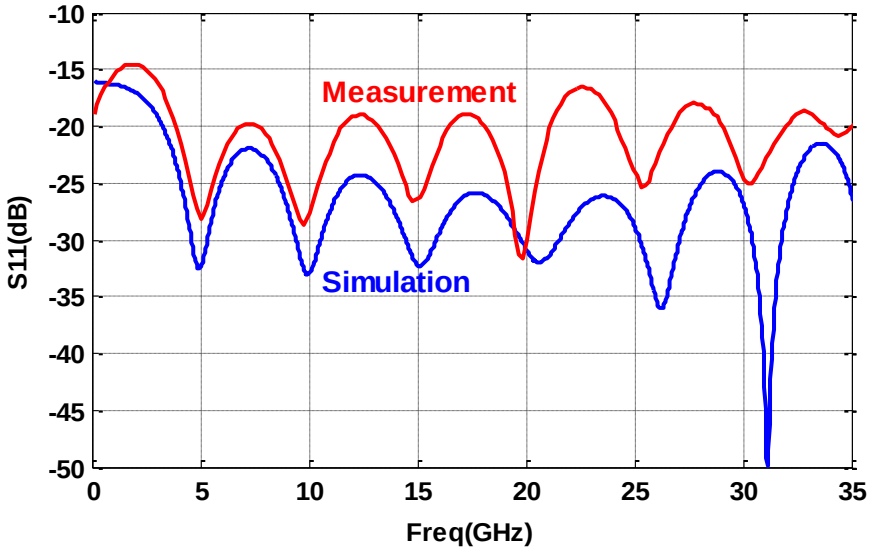

Figure 7.26 Correlation between measurement and simulation results (S_{11})

In addition, the simulation and measurement results for the insertion loss were observed to vary within 0.5 dB throughout the entire frequency range (Figure 7.25). The variations may be due to slight impedance mismatches arising from the dimensions considered in the 3D model and the actual printed dimensions. This is since the dimensions used in the simulation model were averaged from several sections of the printed trace and could vary slightly from the actual dimensions at different regions of the trace. Compared to the results obtained for the 2 mm CPW line in Figure 7.21, the impedance mismatch for the 2 mm CPW line may be

relatively insignificant due to the shorter line length and thus more consistent trace dimensions.

As an extension of the results in Section 7.4.3(a), the effect of the trace edges on the insertion loss is also investigated via simulation for this 15 mm CPW line. From Figure 7.27, the insertion loss obtained for the 15 mm CPW line from using sharp trapezoidal edges is observed to be overestimated by 1 dB from 30-35 GHz. This overestimation represents a deviation of around 20 % from the expected loss obtained from modelling the actual trace profile (i.e. curved trapezoidal edges). These results highlight the importance of modelling for the actual trace edges to accurately predict the transmission line loss, particularly where CPW structures are considered.

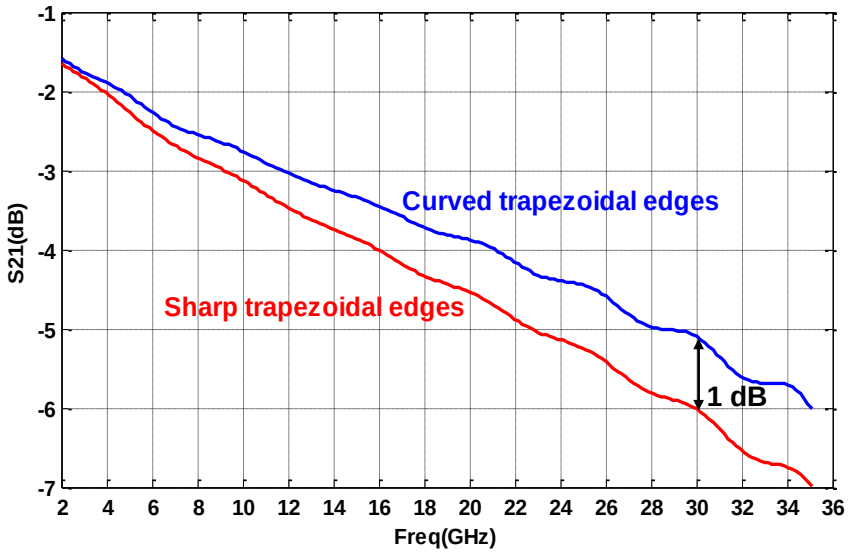

Figure 7.27 Correlation between measurement and simulation results (S_{21})

7.5 Conclusions

This chapter has discussed a methodology used to obtain an accurate simulation model such that a good prediction could be made on the RF performance of printed traces. The main results are presented as follows.

In terms of simulation, the guidelines for modelling printed traces are:

(1) Denser meshing within the trace thickness is essential to capture the loss due to the skin effect. In the optimised meshing, the trace thicknesses were meshed by a

factor of skin depth/9, where the skin depth refers to that at the maximum frequency. (2) Short transmission line lengths of perfect metal material were used to contact the waveguide ports in *CST* to circumvent inaccuracies of the *S*-parameter results arising from the lower conductivity of the printed traces compared to the bulk metal conductivity. (3) Denser meshing along the trace edges is essential to capture the current crowding effect. (4) Modelling the actual trace edge profile (e.g. rounded instead of sharp trapezoidal trace edges) is essential for CPW transmission lines to account for the proximity effect.

Specifically, the meshing was optimised for the simulation model based on a TD solver in *CST*. The *S*-parameter results of a model with the optimised meshing were then verified against those obtained from the FD solver in *CST*.

For the simulation correlation, the assumption made was that using an average DC conductivity value may not suffice. Thus the DC conductivity variation of the printed test structures was investigated for different regions of the substrate. Four point probe structures were positioned beside the measured CPW line, such that in-situ extractions of the DC conductivity values could be made for the corresponding CPW line. From the results, the average DC conductivity values were observed to vary across different regions of the RO3006 substrate, which may be attributed to the paste levelling after screen printing. The results obtained suggest that this phenomenon may have a significant influence on the DC electrical performance, and necessitates a paste selection procedure prior to the actual screen printing of the test structures. This is to ascertain that the paste used would yield uniform trace thickness and thus an improved consistency in the extracted DC conductivity values. The results also indicate the need for accurate DC conductivity values to be used for the simulation correlation of printed traces, since the values may vary across different regions of the substrate depending on the paste formulation and its interaction with the mesh and substrate during printing.

Using the proposed methodology, improved simulation models for printed transmission lines were obtained such that the high frequency performance of screen printed transmission lines can be accurately predicted. Good correlations were obtained between simulation and measurement results for a 2 mm CPW line

on RO3006. To validate the methodology correlation was also performed for a longer 15 mm CPW line on RO3006, where a good match was obtained. The results obtained are promising with respect to the goal of obtaining accurate 3D models to estimate the RF performance of printed traces. This methodology is also applicable for inkjet printed traces, and needs to be verified in terms of the simulation correlation with measurements. The verification of the methodology requires the following factors to be addressed. From the simulation aspect, the small thicknesses of inkjet printed traces after thermal sintering (≤ 1 µm for a single layer) [16, 245] necessitate excessively dense meshing during modelling, which results in computationally intensive models. From the measurement aspect, it will be challenging to distinguish between the small thickness and the surface roughness of RO3006 ($R_a \leq 1$ µm) during the trace profile characterisation, as both parameters are comparable. In addition, since the thickness of inkjet printed traces is of a similar magnitude to the skin depth at 30 GHz [129], the effect of surface roughness present in RO3006 needs to be accounted for in the modelling process. For inkjet printed traces on smooth substrates with negligible surface roughness (e.g. glass), measurement challenges are encountered from the poor adhesion of the traces onto the substrate surfaces, which results in partial trace removal when contacted with the DC probe leads or microwave probes (detailed in Appendix E4). This necessitates surface modification techniques (e.g. deposition of an intermediate insulator layer) to improve the trace adhesion.

The effect of trace edges on the RF performance has not been investigated thoroughly in the literature and this chapter described an investigation in this area for a 2 mm CPW line. When sharp trapezoidal edges were considered in the simulation model (for simplification purposes), the insertion loss was observed to be overestimated by about 14 % at 30 GHz. For a 15 mm CPW line at 30 GHz this overestimation was in the range of 20 %. The results indicate that the trace edge profile may affect CPW structures significantly due to the confinement of the electric fields around the ground-signal-ground region.

Lastly, the effect of the DC conductivity on the RF performance was also investigated. When the lower bound of the measured DC conductivity was used in

the simulation model, an increase in the insertion loss by 0.03-0.05 dB/mm was observed throughout 0.1-30.1 GHz. This implies that variation in the DC conductivity values may be significant for the case of low loss transmission lines, which necessitates a consideration of this variation during the design stage.

Chapter 8. Conclusions and Future Work

8.1. Summary

With the emergence of the Internet of Things (IoT), wearable electronics are becoming increasingly pervasive in everyday life. Most of the Wireless Body Area Networks (WBANs) currently operate at the IEEE 802.15.4 Zigbee standard, and there have been growing interest in investigating WBANs in the millimetre wave band, due to the advantages available. The aim of this thesis is to realise fine pitch (< 400 µm pitch) interconnects targeted for high frequency wearable electronics applications (20-30 GHz), based on printing technologies which offer fine pitch and higher frequencies of operation. To achieve this research aim four research challenges needed to be overcome. The first challenge involved overcoming the surface roughness of substrates (e.g. fabrics), as it results in ink spreading and affects the printed line resolution adversely. To overcome this necessitates a suitable surface modification technique to planarise the substrate surface and reduce the surface roughness. This work is covered in Chapter 5 of this thesis. The second research challenge was to obtain electrically conducting interconnects on the planarisation layer. The planarisation layer is commonly realised using UV-curable inks, but its properties (e.g. printability, electrical connection) after UV curing are strongly dependent on the ink formulation and UV source used. Thus the second research objective was to realise electrically conducting interconnects for the case where the surface energies of the ink and the planarisation layer are not matched, or when the UV source used is non-optimal. This work is described in Chapter 6 of this thesis.

From the electrical perspective, the dielectric properties (dielectric constant, loss tangent) of fabrics in the gigahertz range are not readily available from manufacturers, and the repeatability of the measured results is an issue. Therefore the third research objective was to characterise the dielectric properties of a non-woven fabric (Tyvek) up to broadband frequencies (≥ 20 GHz), with repeatable results. This work is covered in Chapter 4 of this thesis. The last research challenge pertained to a lack of information about the RF performance of printed interconnects, as most work reports on megahertz frequency applications or

presents the measured RF results. Thus the last research objective was to predict the RF performance of printed transmission lines, and to provide guidelines for the modelling of such structures. This work is described in Chapter 7 of this thesis.

8.2. Contributions to Knowledge

In this section, the main contributions from this research are summarised, along with the current limitations.

1. To characterise the dielectric properties of a non-woven fabric up to 30 GHz.

To realise interconnects for high frequency applications necessitates knowledge of the substrate dielectric properties, in order to calculate the dimensions of passive components, miniaturise their footprint and minimise the RF losses. In this work, the dielectric properties of a non-woven fabric (Tyvek) were characterised, using a substrate with well-characterised properties (RO3006) as a reference.

- *A novel methodology combining 3D modelling with analytical equations (based on transmission line structures) was proposed for dielectric characterisation up to 20 GHz, where the accuracy of the method was determined with experiments to be within 10 % for the dielectric constant.*

The accuracy of the method could be improved by modelling transmission lines with 3D profiles, which would enable the effects of non-ideal transmission characteristics to be included in the simulation. In addition, the proposed methodology is more suited for characterising lossy substrates, as the loss tangent variation is increased when the method is used on low loss substrates.

2. To reduce the surface roughness of substrates for trace deposition using inkjet printing.

For substrates with non-negligible surface roughness (≥ 1 μm), it was a challenge to realise fine pitch traces using inkjet printing, because of the ink spread which affects the trace definition. In this work, a UV-curable ink formulated for flexible substrates was used to form a planarisation layer onto RO3006 via inkjet printing.

Another sub-objective was to investigate the effect of surface roughness on the printed line widths, as most researchers consider smooth substrates in inkjet printing.

- *To minimise the de-wetting of the UV-curable ink, the mismatch of the surface energies between the ink and the substrate was addressed within the parameters of heating the platen (≥ 30 ℃), which is a more flexible approach compared to modifying the ink formulation.*

- *A surface roughness factor was introduced into the equation of Smith et al. [22], which improved the correlation of printed line widths on substrates with non-negligible surface roughness (valid for $R_a \leq 1$ μm) within an accuracy of 10 %.*

The proposed equation with the surface roughness factor excludes substrates with coatings because the planarisation layer considered was observed to be porous, which could result in a penetration of the silver nanoparticles into the layer. This work was published in ACS *Industrial & Engineering Chemistry Research*.

3. To realise electrically conducting traces using inkjet printing.

Silver ink de-wetting was observed when overprinting silver onto the UV-cured insulator layer, and this work seeks to realise continuous silver traces overprinted onto UV-curable insulators through surface modification techniques (thermal and UV-ozone post-treatments), when the UV light source used for the curing is non-optimal. Two UV curable dielectric materials were deposited and the effects of curing time and curing atmosphere on the inkjet printability of a commercially available silver ink were investigated.

- *Good wettability of the overprinted silver ink on the insulator layers was obtained following UV-ozone treatment of the insulator layers, where the treatment required was found to be a function of the ink formulation and the curing atmosphere.*

- *Water droplet contact angle measurements and XPS analysis provided an indication of changes in the surface condition of the insulator layers, but were not sufficient for predicting whether measurable silver trace resistances could be obtained.*

- *Measurable silver trace resistances were found to be influenced by the occurrence of cracks in the trace and possibly the degree of cross-linking present in the insulator.*

- *It was demonstrated that electrically conductive traces can be achieved on ambient cured samples, which yields a more flexible solution compared to inert cured samples.*

This work has been published in *Surface and Coatings Technology*. Using the approach outlined in this work, measurable resistances were demonstrated on Tyvek (described in Appendix D). The range of the resistance values obtained suggests potential for further optimisation of the process parameters to improve those resistance values. The influence of cracks on the measurable trace resistances also suggest that further investigations into the trace reliability may be important.

4. To predict the high frequency performance of printed interconnects.

Due to a lack of research, there is little information on the RF performance of printed interconnects. Thus a methodology was proposed to develop simulation models which were validated with experimental measurements. A sub-objective was to investigate how the paste property influences the DC conductivity of printed interconnects across the substrate, and the subsequent simulation correlation.

- *The proposed methodology was validated for screen printed CPW transmission lines of different lengths, where good correlations (±0.5 dB) were obtained between the simulation and measurement results.*

- *The variation of the DC conductivity values was investigated for different regions of the substrate, and the results suggest that the DC electrical performance is influenced by the paste levelling effect, which is due to the*

paste formulation and its interaction with the mesh and substrate during printing.

- *The simulation correlation results indicate that the trace edge profile has a significant effect on CPW structures (14-20 % over-estimation of the insertion loss), and necessitates a need to consider curved trapezoidal edges (as fabricated) in the modelling of printed CPW transmission lines.*

It is noted that this methodology when applied to printed traces of small thicknesses results in longer computational times (in terms of the simulation duration). This work was done in collaboration with Computer Simulation Technology (CST), and part of it was published in *IEEE Electronics Packaging Technology Conference (EPTC).*

Furthermore, some recommendations arise from this work. Firstly, due to the effect of paste levelling on the DC conductivity values, a need arises for a paste selection procedure prior to the screen printing, so as to identify a suitable paste for the specific application considered. This is particularly important for RF application, where a variation in the DC conductivity affects the insertion loss of the printed transmission lines, and the repeatability of the results. Secondly, the results necessitate obtaining accurate DC conductivity values for the modelling of screen printed traces, since these values may vary across different regions of the substrate. Such variations in the DC conductivity may have a significant effect on the predicted insertion loss of transmission lines with low losses.

8.2 Future Work

Much has been accomplished in this very challenging area of wearable electronics targeted for high frequency applications, and some work remains to drive this topic forward. This section presents a discussion of the possible topics arising from the research in this thesis.

1. Effect of substrate porosity in the overprinting of silver ink

The proposed equation (equation (5.5) in Chapter 5) which incorporates a surface roughness factor to predict the line widths on substrates with non-negligible surface roughness does not account for porous coatings. Further studies are necessary to investigate the relationship between the degree of porosity of the coatings and the printed line widths deposited via inkjet printing. The porosity measurements may be limited to the use of mercury porosimetry [246, 247], as the planarisation layer considered comprises of particles in the range of microns [206]. Yet mercury porosimetry is suited for coatings which are non-wettable by mercury [247]. This implies that if the coating considered interacts with mercury, a review of the current porosity techniques is necessary in order to identify a suitable approach for the porosity characterisation.

2. Effect of polymer cross-linking (UV-curable insulator)

(i) On the overprinted silver ink

Another possible research topic involves a quantitative assessment of how the degree of polymer cross-linking affects the aggregation of the inkjet printed silver nanoparticles and the measurable resistance. This is an extension of the results obtained in research objective 3, where the insulator is partially cured by a UV source. Furthermore, a research gap exists in terms of determining the surface energies of partially cured polymers. Most researchers consider water contact angle measurements [98, 143, 212], but the values only provide information on the surface wettability of the samples. Challenges [248] exist in the determination of the surface energy of partially cured polymers due to the requirement for two reference liquids which do not interact with the polymer [142]. To the author's best knowledge, there is also no information available on the final cure stage of UV-cured films [29, 30] considered by other researchers, and the author assumes that the films are fully cured.

(ii) When a porous substrate is considered

From the results obtained in Appendix D (under research objective 3), it is of interest to investigate the influence of the substrate porosity (e.g. different degrees of porosity) on the polymer cross-linking of UV-curable insulators which are deposited via inkjet printing. While the consideration of porous substrates in inkjet

printing increases the challenge of obtaining conductive traces deposited onto an insulator layer, this is an area which has been little explored in literature to date.

Li *et al.* [26] reported on the deposition of a UV-curable paste to planarise the surface of textiles using screen printing. This has an advantage in that the paste is more viscous with possibly larger particle sizes, which implies that the effect of a porous substrate is significantly reduced. However issues were encountered in the wettability of the silver ink when it was overprinted onto the planarisation layer. While Li *et al.* [26] circumvented this issue through the overprinting of 2-3 silver layers, the issue highlights the importance of matching the surface energies [248] between the silver ink and the substrate to ensure good wettability. Furthermore, the effect of the substrate porosity could be significant if the UV-curable paste is partially cured due to a non-optimal light source [248].

As discussed in Chapter 4 of the thesis, a thick planarisation layer is essential to alleviate the substrate loss of Tyvek. This need provides an additional impetus for further studies into the effect of substrate porosity on the polymer cross-linking. The area of research involving UV-curable insulators is also summarised in Figure 8.1.

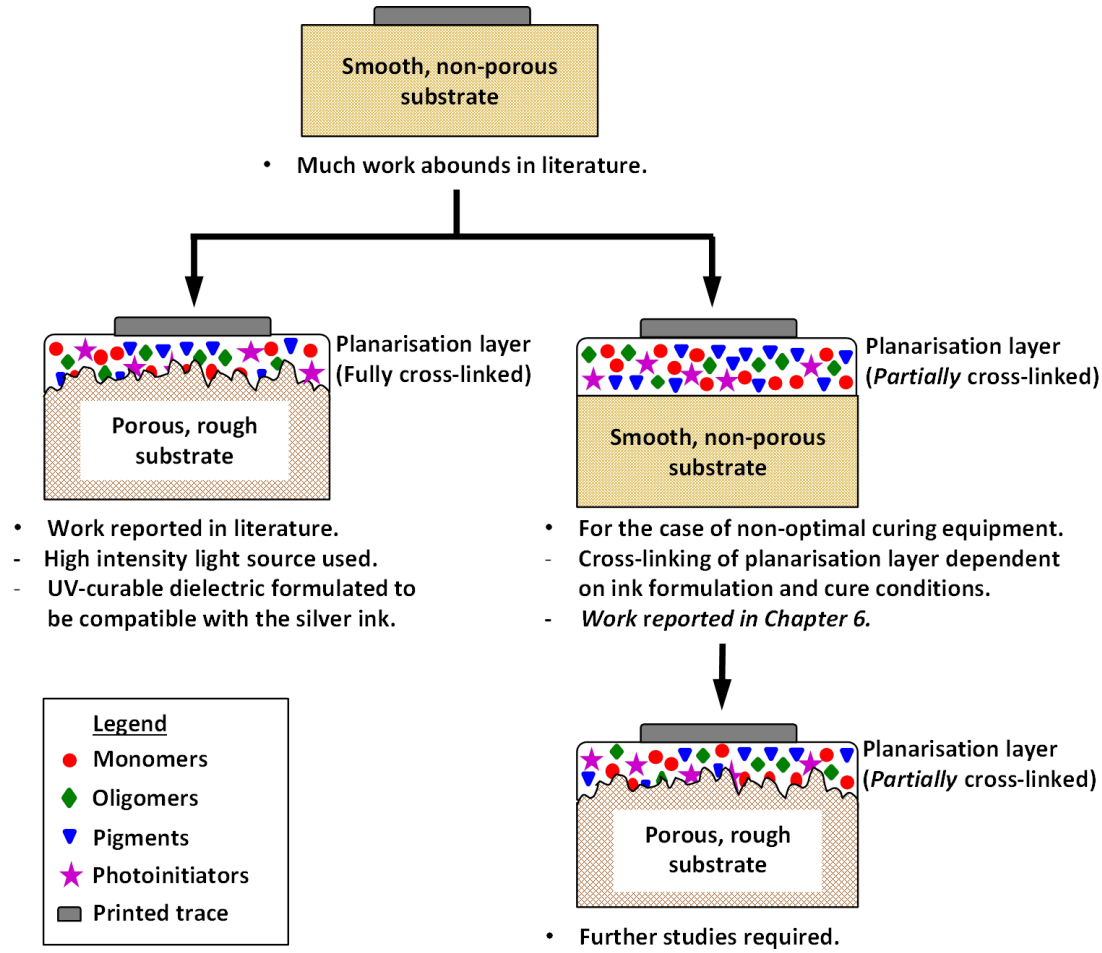

Figure 8.1 Diagram summarising the work done on UV-curable insulators [26-28, 87] and the possible area for further research.

3. RF performance of other printed interconnects

The methodology proposed in Chapter 7 (research objective 4) is applicable for inkjet printed traces. Yet the consideration of such traces on a substrate with non-negligible surface roughness necessitates that the effect of surface roughness be addressed and accounted for in the simulation process. This is due to the skin effect phenomenon relative to the small thickness of inkjet printed traces.

For inkjet printed traces on smooth substrates (e.g. glass), measurement challenges arise from the poor adhesion of the traces onto the substrate surfaces (Appendix E4). This leads to partial trace removal (and possibly areas which are electrically open) in the regions which are contacted by the DC probe leads or microwave probes. The poor adhesion necessitates surface modification techniques (e.g. deposition of an intermediate insulator layer) to improve the trace adhesion for electrical measurements.

Apart from inkjet printed traces, the application of the proposed methodology on traces obtained via aerosol deposition [63] is also feasible. However this requires that a good adhesion of the trace to the substrate [67] be first obtained, which necessitates an optimisation of the process parameters for the specific metal power-substrate considered [67]. As aerosol deposition is a spray process to coat metallic powders onto a substrate, the definition of fine pitch interconnects requires a lift-off process using photoresist [249, 250], which increases the complexity of fabricating the test structures.

References

[1] C. Chakraborty, B. Gupta, and S. K. Ghosh, "A Review on Telemedicine-Based WBAN Framework for Patient Monitoring", *Telemed. J. E. Health*, vol. 19, no. 8, pp. 619-626, 2013.

[2] S. Ullah, P. Khan, N. Ullah, S. Saleem, H. Higgins, and K. S. Kwak, "A Review of Wireless Body Area Networks for Medical Applications", *Int. J. Commun. Network Syst. Sci.*, vol. 2, no. 8, pp. 797-803, 2009.

[3] J. Lilja, V. Pynttari, T. Kaija, R. Makinen, E. Halonen, H. Sillanpaa, J. Heikkinen, M. Mantysalo, P. Salonen, and P. de Maagt, "Body-Worn Antennas Making a Splash: Lifejacket-Integrated Antennas for Global Search and Rescue Satellite System", *IEEE Antennas Propag. Mag.*, vol. 55, no. 2, pp. 324-341, 2013.

[4] J. Lilja, P. Salonen, T. Kaija, and P. de Maagt, "Design and Manufacturing of Robust Textile Antennas for Harsh Applications", *IEEE Trans. Antennas Propag.*, vol. 60, no. 9, pp. 4130-4140, 2012.

[5] J. C. G. Matthews, and G. Pettitt, "Development of Flexible, Wearable Antennas", in *3rd Eur. Conf. Antennas Propag*., Berlin, 2009, pp. 273-277.

[6] IEEE Standard for Local and metropolitan area networks - Part 15.4: Low-Rate Wireless Personal Area Networks (LR-WPANs)," IEEE, 2011.

[7] S. Lim, T. H. Oh, Y. B. Choi, and T. Lakshman, "Security Issues on Wireless Body Area Network for Remote Healthcare Monitoring," in *IEEE Int. Conf. Sens. Networks Ubiquitous Trustworthy Comput.*, Newport Beach, California, 2010, pp. 327-332.

[8] M. Haque, and S. I. Ahamed, "Security in Pervasive Computing: Current Status and Open Issues", *Int. J. Network Secur.*, vol. 3, no. 3, pp. 203-214, 2006.

[9] S. Patel, H. Park, P. Bonato, L. Chan, M. Rodgers, "A Review of Wearable Sensors and Systems with Application in Rehabilitation", *J. Neuroeng. Rehabil.*, vol. 9, no. 21, pp. 1-17, 2012.

[10] D. M. Pozar, *Microwave Engineering*; John Wiley & Sons, 2011.

[11] S. Chung, J. Lee, H. Song, S. Kim, J. Jeong, and Y. Hong, "Inkjet-printed Stretchable Silver Electrode on Wave Structured Elastomeric Substrate", *Appl. Phys. Lett.*, vol. 98, no. 15, 153110 (3 pp.), 2011.

[12] D. Cottet, J. Grzyb, T. Kirstein, and G. Troster, "Electrical Characterization of Textile Transmission Lines", *IEEE Trans. Adv. Packag.*, vol. 26, no. 2, pp. 182-190, 2003.

[13] T. Maleszka, and P. Kabacik, "Bandwidth Properties of Embroidered Loop Antenna for Wearable Applications", in *European Wireless Technol. Conf. (EuWIT)*, Paris,France, 2010, pp. 89-92.

[14] R. D. Seager, A. Chauraya, J. C. Vardaxoglou, and P. DeMaagt, "Towards a Compact Low Frequency Woven Antenna", in *IEEE Antennas Propag. Soc. Int. Symp. (APSURSI)*, 2009, pp. 1-4.

[15] I. Locher, M. Klemm, T. Kirstein, and G. Troster, "Design and Characterization of a Purely Textile Patch Antennas", *IEEE Trans. Adv. Packag.*, vol. 29, no. 4, pp. 777-788, 2006.

[16] N. Shirakawa, K. Murata, Y. Kajihara, K. Nakamura, Y. Kashiwagi, M. Nakamoto, H. Sato, T. Kojima, D. Komiya, K. Shimizu, and K. Masuda,

"Fine-Pitch Copper Wiring Formed with Super-Inkjet and Oxygen Pump", *Jpn. J. Appl. Phys.*, vol. 52, no. 5S1, 05DB19 (3 pp.), 2013.

[17] K. Murata, "Direct Fabrication of Super-Fine Wiring and Bumping by Using Inkjet Process", in *6th IEEE Int. Conf. Polym. Adhes. Microelectron. Photonics*, Tokyo, Japan, 2007, pp. 293-296.

[18] J.-W. Kim, Y.-C. Lee, J.-M. Kim, W. Nah, H.-S. Lee, H.-C. Kwon, and S.-B. Jung, "Characterization of Direct Patterned Ag circuits for RF Application", *Microelectron. Eng.*, vol. 87, pp. 379-382, 2010.

[19] J. Muller, R. Perrone, H. Thust, K.-H. Drue, C. Kutscher, R. Stephan, J. Trabert, M. Hein, D. Schwanke, J. Pohlner, G. Reppe, R. Kulke, P. Uhlig, A. F. Jacob, T. Baras, and A. Molke, "Technology Benchmarking of High Resolution Structures on LTCC for Microwave Circuits", in *1st Electron. Syst. Integr. Technol. Conf. (ESTC)*, Dresden, Germany, 2006, pp. 111-117.

[20] T. Baras, and A. F. Jacob, "Manufacturing Reliability of LTCC Millimeter-Wave Passive Components", *IEEE Trans. Microwave Theory Tech.*, vol. 56, no. 11, pp. 2574-2581, 2008.

[21] B. Karaguzel, *Printing Conductive Inks on Nonwovens: Challenges and Opportunities*, PhD Thesis, North Carolina State University, 2006.

[22] P. J. Smith, D. Shin, N. Reis, J. Stringer, and B. Derby, "Direct Ink-jet Printing and Low Temperature Conversion of Conductive Silver Patterns", *J. Mater. Sci.*, vol. 41, no. 13, pp. 4153-4158, 2006.

[23] J. F. Salmeron, F. Molina-Lopez, D. Briand, J. J. Ruan, A. Rivadeneyra, M. A. Carvajal, L. F. Capitan-Vallvey, N. F. Derooij, and A. J. Palma, "Properties and Printability of Inkjet and Screen-Printed Silver Patterns for RFID Antennas", *J. Electron. Mater.*, vol. 43, no. 2, pp. 604-617, 2014.

[24] T. Öhlund, Örtegren, J., Forsberg, S., Nilsson, H-E., "Paper Surfaces for Metal Nanoparticle Inkjet Printing", *Appl. Surf. Sci.*, pp. 731-739, 2012.

[25] G. Chinga-Carrasco, D. Tobjork, and R. Osterbacka, "Inkjet-printed Silver Nanoparticles on Nano-engineered Cellulose Films for Electrically Conducting Structures and Organic Transistors: Concept and Challenges", *J. Nanopart. Res.*, vol. 14, no. 11, 10 pp., 2012.

[26] Y. Li, R. Torah, S. Beeby, J. Tudor, "Inkjet Printed Flexible Antenna on Textile for Wearable Applications", *in Proc. 88th Text. Inst. World Conf.*, Selangor, Malaysia, 2012, pp.1-10.

[27] A. Denneulin, J. Bras, A. Blayo, and C. Neuman, "Substrate Pre-treatment of Flexible Material for Printed Electronics with Carbon Nanotube Based Ink", *Appl. Surf. Sci.*, vol. 257, no. 8, pp. 3645-3651, 2011.

[28] L. Hakola, K. Eiroma, J. Heilmann, K. Lehtinen, T. Mäkelä, and M. Vilkman, "Inkjet Printed Active Element on Paper Based on Conductive and Thermochromic Materials", in *NIP & Digital Fabr. Conf.*, Alaska, USA, 2007, pp. 932-935.

[29] C.-S. Liao, C.-F. Wang, H.-C. Lin, H.-Y. Chou, F.-C. Chang, "Tuning the Surface Free Energy of Polybenzoxazine Thin Films", *J. Phys. Chem. C*, vol. 112, no. 42, pp. 16189-16191, 2008.

[30] T. Gururaj, R. Subasri, K. R. C. Soma Raju, and G. Padmanabham, "Effect of Plasma Pretreatment on Adhesion and Mechanical Properties of UV-Curable Coatings on Plastics", *Appl. Surf. Sci*., vol. 257, no. 9, pp. 4360-4364, 2011.

[31] RO3000 Series Circuit Materials RO3003™, RO3006™ and RO3010™ High Frequency Laminates, Rogers Corporation, USA,2014.

[32] TLY Family of Low Loss Laminates, Taconic, 2012.

[33] F. Declercq, H. Rogier, and C. Hertleer, "Permittivity and Loss Tangent Characterization for Garment Antennas Based on a New Matrix-Pencil Two-Line Method", *IEEE Trans. Antennas Propag.*, vol. 56, no. 8, pp. 2548 -2554, 2008.

[34] K. Park, D. Seo, and J. Lee, "Conductivity of Silver Paste Prepared from Nanoparticles", *Colloids Surf., A*, vol. 313-314, pp. 351-354, 2008.

[35] S. Jang, Y. Seo, J. Choi, T. Kim, J. Cho, S. Kim, and D. Kim, "Sintering of Inkjet Printed Copper Nanoparticles for Flexible Electronics", *Scr. Mater.*, vol. 62, no. 5, pp. 258-261, 2010.

[36] K.-S. Kim, W.-R. Myung, and S.-B. Jung, "Effects of Sintering Conditions on Microstructure and Characteristics of Screen-Printed Ag Thin Film", *Electron. Mater. Lett.*, vol. 8, no. 3, pp. 309-314, 2012.

[37] C. Kim, M. Nogi, and K. Suganuma, "Electrical Conductivity Enhancement in Inkjet-Printed Narrow Lines Through Gradual Heating", *J. Micromech. Microeng.*, vol. 22, no. 3, 2012.

[38] J. F. Salmeron, A. R. Torres, J. Banqueri, and M. A. Carvajal, "Design and Characterization of Ink-jet and Screen Pdurinted HF RFID Antennas", in *4th Int. EURASIP Workshop on RFID Technol. (EURASIP RFID)*, Torino, Italy, 2012, pp. 119-123.

[39] B. Karaguzel, C. R. Merritt, T. Kang, J. M. Wilson, H. T. Nagle, E. Grant, and B. Pourdeyhimi, "Flexible, Durable Printed Electrical Circuits", *J. Text. Inst.*, vol. 100, no. 1, pp. 1-9, 2009.

[40] J. M. Wilson, C. R. Merritt, B. Karaguzel, T. Kang, H. T. Nagle, E. Grant, B. Pourdeyhemi, and P. D. Franzon, "High Frequency Characterization of Printed CPW Lines on Textiles Using a Custom Test Fixture", in *10th IEEE Workshop Sig. Propag. Interconnects*, Berlin, Germany, 2006, pp. 279-280.

[41] A. Vasylchenko, J. F. Farserotu, S. Brebels, W. De Raedt, M. Fernandez-Bolanos, A. M. Ionescu, and G. A. E. Vandenbosch, "Scalable Conformable Array for Multi-gigabit Body Centric Wireless Communication", in *5th Int. Symp. on Med. Inf. & Commun. Technol. (ISMICT 2011)*, Montreux, Switzerland, 2011, pp. 74-78.

[42] J. Muller, D. Stopel, T. Mache, A. Schulz, K. Drue, S. Humbla, M. Hein "Fineline Structuring on LTCC-Substrates for 60 GHz Line Coupled Filters", in *18th Eur. Microelectron. Packag. Conf.*, Brighton, United Kingdom, 2011. pp. 1-5.

[43] Probe Selection Guide, Cascade Microtech Inc., https://www.cmicro.com/products/probes (accessed Jun 5, 2015).

[44] P. Salonen, Y. Rahmat-Samii, M. Schaffrath, and M. Kivikoski, "Effect of Textile Materials on Wearable Antenna Performance: A Case Study of GPS Antennas", in *IEEE Antennas and Propag. Soc. Int. Symp. (APSURSI)*, Monterey, California, 2004, pp. 459-462.

[45] T. Maleszka, M. Preisner, and P. Kabacik, "Meshed Ground Plane Structures for Textile Antennas", in *Eur. Conf. Antennas Propag. (EuCAP)*, Berlin, Germany, 2009, pp. 713-717.

[46] Y. Ouyang, and W. J. Chappell, "High Frequency Properties of Electro-textiles for Wearable Antenna Applications", *IEEE Trans. Antennas Propag.*, vol. 56, no. 2, pp. 381-389, 2008.

[47] M. D. Janezic, D. F. Williams, V. Blaschke, A. Karamcheti, and C. S. Chang, "Permittivity Characterization of Low-k Thin Film from

Transmission-Line Measurements", *IEEE Trans. Microwave Theory Tech.*, vol. 51, no. 1, pp. 132-136, 2003.

[48] T. Maleszka, Wroclaw University of Technology, Poland, Private Communication, 2011.

[49] Conductive Metallized Nylon Fabric (Nora) Technical Data Sheet (PN# 1400101130), VTT/Shieldex Trading USA, NY, 2013.

[50] H. Johnson, *High-Speed Signal Propagation Advanced Black Magic*, Prentice Hall, NJ, 2003.

[51] S. Merilampi, T. Laine-Ma, and P. Ruuskanen, "The Characterization of Electrically Conductive Silver Ink Patterns on Flexible Substrates", *Microelectron. Reliab.*, vol. 49, no. 7, pp. 782-790, 2009.

[52] 125-13 Electrically Conductive Ink, Creative Materials Inc., 2013.

[53] Mitani Micronics Home Page. http://www.mitani-micro.co.jp/en/mask/screen.html (accessed Jan 7, 2014).

[54] S. Merilampi, *The Exploitation of Polymer Thick Films in Printing Passive UHF RFID Dipole Tag Antennas on Challenging Substrates*, PhD Thesis, Tampere University of Technology, 2011.

[55] Microflex Project website. http://microflex.ecs.soton.ac.uk/summary.html (accessed Mar 7, 2012).

[56] Y. Wei, R. Torah, K. Yang, S. Beeby, and J. Tudor, "A Novel Fabrication Process to Realise Piezoelectric Cantilever Structures for Smart Fabric Sensor Applications", in *IEEE Sens.*, Taipei, TW, 2012, pp. 1-4.

[57] S. P. Beeby, M. J. Tudor, R. N. Torah, K. Yang, and Y. Wei, "MICROFLEX Project - Microtechnology in Smart Fabrics", in *4th Int. Conf. Smart Mater., Struct. Syst. (CIMTEC)*, Montecatini Terme, Italy, 2012.

[58] B. Pourdeyhimi, E. Grant, H. T. Nagle, C. R. Merritt, B. Karaguzel, T.-H. Kang, and J. M. Wilson, *Methods and Devices for Providing Flexible Electronics*, U.S. Patent 20090286055, Nov 19, 2009.

[59] B. Karaguzel, Istanbul Technical University, Private Communication, 2011.

[60] J. W. L. Phair, M.Kaiser, A., "Leveling and Thixotropic Characteristics of Concentrated Zirconia Inks for Screen-printing", *Rheol. Acta*, vol. 48, no. 2, pp. 121-133, 2009.

[61] M. Yoshida, National Institute of Advanced Industrial Science and Technology (AIST), Japan, Private Communication, 2014.

[62] A. Pique, and D. B. Chrisey, *Direct-Write Technologies for Rapid Prototyping Applications*: *Sensors, Electronics and Integrated Power Sources*, Academic Press, 2002.

[63] J. Akedo, "Aerosol Deposition of Ceramic Thick Films at Room Temperature Densification Mechanism of Ceramic Layers", *J. Am. Ceram. Soc.*, vol. 89, no. 6, pp. 1834-1839, 2006.

[64] Y. Imanaka, N. Hayashi, M. Takenouchi, and J. Akedo, "Aerosol Deposition for Post-LTCC", *J. Eur. Ceram. Soc.*, vol. 27, pp. 2789-2795, 2007.

[65] J.-H. Park, and J. Akedo, "Highly Enhanced Dielectric Properties of Ferroelectric Nanocomposite Films Prepared by Aerosol Deposition Method", in *4th IMAPS/ACerS Int. Conf. Exhib.Cer. Interconnect Cer. Microsyst. Technol. (CICMT)*, Munich, Germany, 2008, pp. 467-470.

[66] M. Mori, N. Akita, S. Baba, and J. Akedo, "Fabrication and Characteristics of Dielectric Films by using Plasma Assisted Aerosol Deposition Method",

in *5th IMAPS/ACerS Int. Conf. Exhib. Cer. Interconnect Cer. Microsyst. Technol. (CICMT)*, Denver, Colorado, 2009, pp. 227-231.

[67] Y. Y. Lim, Y. M. Goh, H. Tsuda, J. Akedo, M. Aoyagi, and C. Liu, "Adhesion of Aerosol Deposition Traces Targeted for Flexible Electronics Applications", in *Third Int. Conf. Adv. Manuf. Multifunct. Miniaturised Devices (ICAM3D)*, Tsukuba, Japan, 2014, 1 pp.

[68] T. Baras, Institut für Hochfrequenztechnik, Germany, Private Communication, 2011.

[69] K. Maekawa, M. Mita, K. Yamasaki, T. Niizeki, Y. Matsuba, N. Terada, and H. Saito, "Packaging of Electronic Modules through Completely Dry Process", in *58th Electon. Compon. and Technol. Conf. (ECTC)*, Florida, USA, 2008, pp. 950-955.

[70] M. Bonkohara, "Japan Activities in 1999, Electronic-System-Integration Technology", in *6th Ann. KGD Ind. Workshop*, California, USA, 1999.

[71] O. Azucena, J. Kubby, D. Scarbrough, and C. Goldsmith, "Inkjet Printing of Passive Microwave Circuitry", in *Microwave Symp. Digest (MTT-S)*, Atlanta, GA, 2008, pp. 1075-1078.

[72] G. Shaker, M. Tentzeri, and S. Safavi-Naeini, "Low-Cost Antenns for mm-Wave Sensing Applications Using Inkjet Printing of Silver Nano-particles on Liquid Crystal Polymers", in *IEEE Antennas Propag. Soc. Int. Symp. (APSURI)*, Toronto, ON, 2010, pp. 1-4.

[73] K. Takano, T. Kawabata, C.-F. Hsieh, K. Akiyama, F. Miyamaru, Y. Abe, Y. Tokuda, R.-P. Pan, C.-L. Pan, and M. Hangyo, "Fabrication of Terahertz Planar Metamaterials Using a Super-Fine Ink-Jet Printer", *Appl. Phys. Express*, vol. 3, no. 1, 2010.

[74] K. Murata, J. Matsumoto, A. Tezuka, Y. Matsuba, and H. Yokoyama, "Super-fine Ink-jet Printing: Toward the Minimal Manufacturing System", *Microsyst. Technol.*, vol. 12, no. 1-2, pp. 2-7, 2005.

[75] B. Shao, R. Weerasekera, L.-R. Zheng, R. Liu, W. Zapka, and P. Lindberg, "High Frequency Characterization of Inkjet Printed Coplanar Waveguides", in *12th IEEE Workshop Signal Propag. Interconnects*, Avignon, France, 2008, pp. 1-4.

[76] L. Xie, G. Yang, M. Mantysalo, L.-L. Xu, F. Jonsson, and L.-R. Zheng, "Heterogeneous Integration of Bio-Sensing System-on-Chip and Printed Electronics", *IEEE J. Emerging Sel. Topics Circuits Syst.*, vol. 2, no. 4, pp. 672-682, 2012.

[77] B. Karaguzel, H. Vahedi Tafreshi, and B. Pourdeyhimi, "Potentials and Challenges in Jetting Microdroplets on Nonwoven Fabrics", *J. Text. Inst.*, vol. 99, no. 6, pp. 581-589, 2008.

[78] E. Wilusz, *Military Textiles*, Woodhead Publishing Ltd, UK, 2008.

[79] W. Zhang, "How Silver Paste Can Improve Silicon Solar Cell Performance/Cost Ratio" [Online], Hereaus Materials Technology White Papers and Articles (accessed Dec 27, 2014).

[80] P. C. Duineveld, "The Stability of Ink-jet Printed Lines of Liquid with Zero Receding Contact Angle on a Homogeneous Substrate", *J. Fluid Mech.*, pp. 175-200, 2003.

[81] D.-Y. Shin, "Fabrication of an Inkjet-printed Seed Pattern with Silver Nanoparticulate Ink on a Textured Silicon Solar Cell Wafer", *J. Micromech. Microeng.*, pp. 125003 (10 pp.), 2010.

[82] Y. Li, R. Torah, S. Beeby, and J. Tudor, "An All-inkjet Printed Flexible Capacitor for Wearable Applications", in *Proc. Symp. on Design, Test, Integr. and Packag. of MEMS/MOEMS (DTIP)*, Cannes, France, 2012, pp. 192-195.

[83] A. Sridhar, J. Reiding, H. Adelaar, F. Achterhoek, D. J. van Dijk, and R. Akkerman, "Inkjet-printing- and Electroless-plating-based Fabrication of RF Circuit Structures on High-frequency Substrates", *J. Micromech. Microeng.*, vol. 19, no. 8, pp. 085020 (11 pp.), 2009.

[84] A. Sridhar, M. A. Perik, J. Reiding, D. J. van Dijk, and R. Akkerman, "Fabrication of RF Circuit Structures on a PCB Material using Inkjet Printing - Electroless Plating and the Substrate Preparation Therefor", *Trans. Jpn. Inst. Electron. Packag.*, vol. 2, no. 1, pp. 116-124, 2009.

[85] Y. Li, University of Southampton, UK, Private Communication, 2013.

[86] F300S and F300SQ Datasheet [Online]. Fusion UV Systems Inc. http://www.fusionuv.com/uploadedFiles/PDF_Library/SB623%20F300S.pdf (accessed Sept 27, 2013).

[87] A. Yakoub, M. Saadaouia, R. Cauchois, J. M. Li, and P. Benaben, "An Improved In-line Inkjet Printing Process for 3D Multilayer Passive Devices", *MRS Proc.* vol. 1401, pp. 20-25.

[88] A. Yakoub, Ecole Nationale Supérieure des Mines de Saint Etienne, France, Private Communication, 2013.

[89] Technical Information Leaflet - SunTronic Solsys EMD6415 UV Curing Jettable Insulator, Sun Chemical, 2011.

[90] Technical Information Leaflet - SunTronic Solsys Jettable Insulator EMD6200, Sun Chemical, 2011.

[91] H. Andersson, C. Lidenmark, T. Ohlund, J. Ortegren, A. Manuilskiv, S. Forsberg, and H.-E. Nilsson, "Evaluation of Coatings Applied to Flexible Substrates to Enhance Quality of Ink Jet Printed Silver Nano-Particle Structures", *IEEE Trans. Compon., Packag., Manuf. Technol.*, vol. 2, no. 2, pp. 342-348, 2012.

[92] InkAID Coatings [Online]. Inkaid. http://www.inkaid1.com/products/ (accessed May 12, 2012).

[93] J. Lin, P. Dahlsten, J. Pekkanen, M. Linden, M. Mantysalo, and R. Osterbacka, "Surface Energy Patterning for Inkjet Printing in Device Fabrication", in *Proc. SPIE Conf Org. Field Eff. Transistors*, San Diego, CA, 2009, pp. 1-8.

[94] J. R. Vig, "UV/Ozone Cleaning of Surfaces", *IEEE Trans. Parts, Hybrids, Packag.*, vol. PHP-12, no. 4, pp. 365-370, 1976.

[95] K. Y. Shin, S. H. Lee, and J. H. Oh, "Solvent and Substrate Effects on Inkjet-printed Dots and Lines of Silver Nanoparticle Colloids", *J. Micromech. Microeng.*, vol. 21, no. 4, pp. 11 pp., 2011.

[96] S. Luo, and C. P. Wong, "Effect of UV/Ozone Treatment on Surface Tension and Adhesion in Electronic Packaging", *IEEE Trans. Comp. and Packag. Tech.*, vol. 24, no. 1, pp. 43-49, 2001.

[97] D. E. King, "Oxidation of Gold by Ultraviolet Light and Ozone at 25 °C", *J. Vac. Sci. Technol. A* vol. 13, no. 3, pp. 1247-1253, 1995.

[98] K. Ma, J. Rivera, G. J. Hirasaki, and S. L. Biswal, "Wettability Control and Patterning of PDMS using UV–ozone and Water Immersion", *J. Colloid Interface Sci.*, vol. 363, no. 1, pp. 371-378, 2011.

[99] A. Olah, H. Hillborg, and G. J. Vancso, "Hydrophobic Recovery of UV/ozone Treated Poly(dimethylsiloxane): Adhesion Studies by Contact Mechanics and Mechanism of Surface Modification", *Appl. Surf. Sci.,* vol. 239, pp. 410-423, 2005.

[100] K. Efimenko, W. E. Wallace, and J. Genzer, "Surface Modification of Sylgard-184 Poly(dimethyl siloxane) Networks by Ultraviolet and Ultraviolet/Ozone Treatment", *J. Colloid Interface Sci.,* vol. 254, pp. 306-315, 2002.

[101] Q. Wei, *Surface Modification of Textiles*: Woodhead Publishing Ltd, 2009.

[102] C. W. M. Yuen, and C. W. Kan, "A Study of the Properties of Ink-jet Printed Cotton Fabric Following Low-Temperature Plasma Treatment", *Color. Technol.,* vol. 123, no. 2, pp. 96-100, 2007.

[103] N. Zander, D. Pappas, and B. Stein, *Oxidation of Polyethylene: A Comparison of Plasma and Ultraviolet Ozone Processing Techniques,*Technical Report for Army Research Laboratory, January 2009.

[104] J. J. Licari, and L. R. Enlow, *Hybrid Microcircuit Technology Handbook: Mateials, Processes, Design, Testing and Production*, Noyes Publications, 1998.

[105] E. C. Kinzel, H. H. Sigmarsson, X. Xu, and W. J. Chappell, "Laser Sintering of Thick-Film Conductors for Microelectronic Applications", *J. Appl. Phys.,* vol. 101, no. 6, pp. 1-9, 2007.

[106] P. Laakso, S. Ruotsalainen, E. Halonen, M. Mantysalo, and A. Kemppainen, "Sintering of Printed Nanoparticle Structures using Laser Treatment", in *Int. Congr. Appl. Lasers Electro-Optics (ICALEO)*, Florida,USA, 2009, pp. 1360-1366.

[107] T. Niizeki, K. Maekawa, M. Mita, K. Yamasaki, Y. Matsuba, N. Terada, and H. Saito, "Laser Sintering of Ag Nanopaste Film and Its Application to BondPad", in *Electron. Compon. Technol. Conf. (ECTC)*, Lake Buena Vista, USA, 2008, pp. 1745-1750.

[108] K. A. Schroder, S. McCool, D. Hamill, D. Wilson, W. Furlan, K. Walter, D. Willauer, and K. Martin, *Electrical, Plating and Catalytic Uses of Metal Nanomaterial Compositions*, W.O. Patent 2006071419 A2, July 2006.

[109] Advanced Curing for Printed Electronics [Online]. NovaCentrix.http://www.novacentrix.com (accessed Jan 30, 2012).

[110] J. Sears, M. Carter, and J. West, "Flash Lamp Curing of Nano-Particulates for Passive Device Fabrication", in *Pac. Int. Conf. Appl. Lasers Opt. (PICALO)*, Beijing, China, 2008, pp. 819-824.

[111] Y.-H. Chou, M.-J. Jeng, Y.-H. Lee, and Y.-G. Jan, "Measurement of RF PCB Dielectric Properties and Losses", *Prog. Electromagn. Res. Lett.,* vol. 4, pp. 139-148, 2008.

[112] L. Yang, A. Rida, R. Vyas, and M. M. Tentzeris, "RFID tag and RF Structures on a Paper Substrate using Inkjet-Printing Technology", *IEEE Trans. Microwave Theory Tech.,* vol. 55, no. 12, pp. 2894-2901, 2007.

[113] High Frequency Materials Product Selector Guide [Online], Rogers Corporation. http://www.rogerscorp.com/search/index.aspx? q=high%20 frequency (accessed Mar 15, 2012).

[114] J. Baker-Jarvis, M. D. Janezic, and D. C. DeGroot, "High-Frequency Dielectric Measurements", *IEEE Instrum. & Meas. Mag.,* vol. 13, no. 2, pp. 24-31, 2010.

[115] J. B. Jarvis, M. D. Janezic, B. F. Riddle, R. T. Johnk, P. Kabos, C. L. Holloway, and C. A. Grosvenor, *Measuring the Permittivity and Permeability of Lossy Materials: Solids, Liquids, Metals, Building Materials, and Negative-Index Materials*, NIST Technical note 1536, National Institute of Standards and Technology, 2004.

[116] M.-Q. Lee, and S. Nam, "An Accurate Broadband Measurement of Substrate Dielectric Constant", *IEEE Microwave and Guided Wave Lett.,* vol. 6, no. 4, pp. 168-170, 1996.

[117] S. Zhu, and R. Langley, "Dual-band Wearable Textile Antenna on an EBG Substrate", *IEEE Trans. Antennas Propag.,* vol. 57, no. 4, pp. 926-935, 2009.

[118] H. Lee, K. Naishadham, M. M. Tentzeris, and G. Shaker, "A Novel Highly-Sensitive Antenna-Based "Smart Skin" Gas Sensor Utilizing Carbon Nanotubes and Inkjet Printing", in *IEEE Antennas Propag. Soc. Int. Symp. (APSURI)*, Spokane, WA, 2011, pp. 1593-1596.

[119] T. F. Kennedy, P. W. Fink, A. W. Chu, and G. F. Studor, "Potential Space Applications for Body-Centric Wireless and E-Textile Antennas", in *IET Semin. Antennas Propag. Body Centric Wireless Comm*., London, UK, 2007, pp. 77-83.

[120] D. C. Thompson, O. Tantot, H. Jallageas, G. E. Ponchak, M. M. Tentzeris, and J. Papapolymerou, "Characterization of Liquid Crystal Polymer (LCP) Material and Transmission Lines on LCP Substrates from 30 to 110 GHz", *IEEE Trans. Microwave Theory Tech.,* vol. 52, no. 4, pp. 1343-1352, 2004.

[121] H. Sharifi, R. R. Lahiji, H.-C. Lin, P. D. Ye, L. P. B. Katehi, and S. Mohammadi, "Characterization of Parylene-N as Flexible Substrate and Passivation Layer for Microwave and Millimeter-Wave Integrated Circuits", *IEEE Trans. Adv. Packag.,* vol. 32, no. 1, pp. 84-92, 2009.

[122] K. C. Gupta, R. Garg, I. Bahl, and P. Bhartia, *Microstrip Lines and Slotlines*, Artech House, 1996, pp. 375-456.

[123] R. A. Pucel, D. J. Masse, and C. P. Hartwig, "Losses in Microstrip", *IEEE Trans. Microwave Theory Tech.,* vol. MTT-16, no. 6, pp. 342-350, 1968.

[124] V. Sanchez-Romaguera, M. A. Ziai, D. Oyeka, S. Barbosa, J. S. R. Wheeler, J. C. Batchelor, E. A. Parker, and S. G. Yeates, "Towards Inkjet-Printed Low Cost Passive UHF RFID Skin Mounted Tattoo Paper Tags based on Silver Nanoparticle Inks", *J. Mater. Chem. C*, vol. 1, pp. 6395-6402, 2013.

[125] E. Georgiou, A. Savva, M. Neophytou, F. Hermerschmidt, T. Demosthenous, and S. A. Choulis, "Evaporation-free Inverted Organic Photovoltaics using a Mixture of Silver Nanoparticle Ink Formulations for Solution-Processed Top Electrodes", *Appl. Phys. Lett.,* vol. 105, pp. 5 pp., 2014.

[126] D. K. Schroder, *Semiconductor Material and Device Characterization*, John Wiley & Sons Inc., NJ, 2006.

[127] C. L. Holloway, and E. F. Kuester, "A Quasi-Closed Form Expression for the Conductor Loss of CPW Lines, with an Investigation of Edge Shape Effects", *IEEE Trans. Microwave Theory Tech.,* vol. 43, no. 12, pp. 2695-2701, 1995.

[128] E. L. Barsotti, E. F. Kuester, and J. M. Dunn, "A Simple Method to Account for Edge Shape in the Conductor Loss in Microstrip", *IEEE Trans. Microwave Theory Tech.,* vol. 39, no. 1, pp. 98-106, 1991.

[129] B. Curran, I. Ndip, S. Guttowski, and H. Reichl, "A Methodology for Combined Modeling of Skin, Proximity, Edge, and Surface Roughness Effects", *IEEE Trans. Microwave Theory Tech.,* vol. 58, no. 9, pp. 2448-2455, 2010.

[130] Agilent Network Analyzer Basics [Online], Agilent Technologies, http://www.agilent.com (accessed Feb 15, 2015).

[131] B. Curran, *Loss Modeling in Non-Ideal Transmission Lines for Optimal Signal Integrity*, PhD Thesis, Technical University Berlin, 2012.

[132] S.-I. Oh, J.-W. Joung, and S.-N. Cho, *Method for Manufacturing Multi-layer Printed Circuit Board*, U.S. Patent 2008/0070011 A1, Mar 20, 2008.

[133] Y. S. Yang, I.-K. You, J. B. Koo, and Y.-Y. Noh, *Multi-layer Interconnection Structure Manufacturing Method Thereof*, E.U. Patent 2339624 A2, Jun 29, 2011.

[134] A. Sridhar, *An Inkjet Printing-Based Process Chain for Conductive Structures on Printed Circuit Board Materials*, PhD Thesis, University of Twente, 2010.

[135] E. O. Hammerstad, and Ø. Jensen, "Accurate Models for Microstrip Computer Aided Design", in *IEEE MTT-S Int. Microwave Symp. Dig.*, 1980, pp. 407-409.

[136] P. G. Huray, S. Hall, S. Pytel, F. Oluwafmi, R. Mellitz, D. Hua, and P. Ye, "Fundamentals of a 3-D "Snowball" Model for Surface Roughness Power Losses", in *11th IEEE Workshop on Signal Propag. Interconnects*, Italy, 2007, pp. 121-124.

[137] A. Koul, M. Y. Koledintseva, S. Hinga, and J. L. Drewniak, "Differential Extrapolation Method for Separating Dielectric and Rough Conductor Losses in Printed Circuit Boards", *IEEE Trans. Electromagn. Compat.,* vol. 54, no. 2, pp. 421-433, 2012.

[138] A. Sain and K. L. Melde, "Broadband Characterization of Coplanar Waveguide Interconnects with Rough Conductor Surfaces", *IEEE Trans. Compon. Packag. Manuf. Technol.,* vol. 3, no. 6, pp. 1038-1046, 2013.

[139] X. Chen, "EM Modeling of Microstrip Conductor Losses Including Surface Roughness Effect", *IEEE Microw. Wireless Compon. Lett.,* vol. 17, no. 2, pp. 94-96, 2007.

[140] B. Curran, Fraunhofer Institute for Reliability and Microintegration, Germany, Private Communication, 2014.

[141] T. Young, "An Essay on the Cohesion of Fluids", *Philos. Trans. R. Soc. London* vol. 95, pp. 65-87, 1805.

[142] D. K. Owens, and R. C. Wendt, "Estimation of the Surface Free Energy of Polymers", *J. Appl. Polym. Sci.*, pp. 1741-1747, 1969.

[143] P. Samyn, G. Schoukens, L. Vonck, D. Stanssens, and H. Van de Abbeele, "How Thermal Curing of an Organic Paper Coating Changes Topography, Chemistry, and Wettability", *Langmuir,* vol. 27, pp. 8509-8521, 2011.

[144] R. N. Wenzel, "Resistance of Solid Surfaces to Wetting by Water", *Ind. Eng. Chem.*, pp. 988-994, 1936.

[145] A. B. D. Cassie, and S. Baxter, "Wettability of Porous Surfaces", *Trans. Faraday Soc.,* vol. 40, pp. 546, 1944.

[146] D. G. Liu, B.Pfeiffer, U.Grzyb, J., Printed Millimeter Antennas – Multilayer Technologies, In *Advanced Millimeter-Wave Technologies: Antennas, Packaging and Circuits*, O. Lafond and M. Himdi, John Wiley & Sons Ltd, UK, 2009.

[147] H. Chahat, M. Zhadobov, and R. Sauleau, "60-GHz Textile Antenna Array for Body-centric Communications", *IEEE Trans. Antennas Propag.,* vol. 61, no. 4, pp. 1816 -1824 2013.

[148] Y. Y. Lim, M. D. Rotaru, A. Alphones, and A. P. Popov, "Improved and Fast Extraction of Dielectric Parameters of Thin Organic Packaging Materials using Open-Ended Coaxial Line Technique", in *6th Electron. Packag. Technol. Conf. (EPTC)*, Singapore, 2004, pp. 510-515.

[149] J. Krupka, R. N. Clarke, O. C. Rochard, and A. P. Gregory, "Split Post Dielectric Resonator Technique for Precise Measurement of Laminar Dielectric Specimens - Measurement Uncertainties", in *13th Int. Conf. Microwaves, Radar and Wireless Comm*., Wroclaw, 2000, pp. 305-308.

[150] S. Dill, M. Peichl, and H. Suess, "Determination of Dielectric Material Properties using Passive MMW Measurements for Security Applications", *Proc. SPIE,* vol. 6548, pp. 1-9, 2007.

[151] R. Alias, and S. Mohd Shapee, Rheological Behaviors and Their Correlation with Printing Performance of Silver Paste for LTCC Tape, In *Rheology* [Online], J. D. Vicente, Ed., InTech, 2012, Chapter 13, pp. 321-338.http://www.intechopen.com/books/rheology/rheological-behaviors-and-their-correlation-with-printing-performance-of-silver-paste-for-ltcc-tape

[152] W. R. Eisenstadt, and Y. Eo, "S-parameter-based IC Interconnect Transmission Line Characterization", *IEEE Trans. Compon., Hybrids, Manufact. Technol.*, vol. 15, no. 4, pp. 483-490, 1992.

[153] G. Ghione, and C. Naldi, "Parameters of Coplanar Waveguides with Lower Ground Plane", *Electron. Lett.,* vol. 19, no. 18, pp. 734-735, 1983.

[154] Dupont Tyvek Graphics Technical Handbook, Dupont, 2007.

[155] Silver Polymer Thick Film Conductor Ink S-020 Product Datasheet, Johnson Matthew Silver & Coatings Technologies.

[156] T. Vincent, *Transmission Line Features and their Influence on GHz Conductor Loss*, PhD Thesis, Worcester Polytechnic Institute, US, 2009.

[157] N. K. Das, S. M. Voda, and D. M. Pozar, "Two Method for the Measurement of Substrate Dielectric Constant", *IEEE Trans. Microwave Theory Tech.,* vol. MTT-35, no. 7, pp. 636-641, 1987.

[158] OLS4100 3D Measuring Laser Microscope Manual, Olympus Corporation, 2013.

[159] Right Angle Male-Female Adaptor Technical Data (R125.771.000 Series SMA) [Online], Radiall, http://www.datasheets360.com/part/detail/r125-771-000/9066780251830625087/ (accessed Jun 15, 2012).

[160] OSM Right Angle Plug to Jack Adapter Technical Datasheet [Online], AMP Incorporated, http://uk.farnell.com/te-connectivity-amp/1055065-1/adapter-sma-plug-sma-jack-right/dp/1831803 (accessed 15 Jun, 2012).

[161] ACP40-GSG-350 [Online], Cascade Microtech, http://www2.cmicro.com /product/acp40-gsg-350-0 (accessed 30 May, 2014).

[162] I. Locher, M. Klemm, T. Kirstein, and G. Troster, "Design and Characterization of Purely Textile Patch Antennas", *IEEE Trans. Adv. Packag.*, vol. 29, no. 4, pp. 777-788, 2006.

[163] J. Baker-Jarvis, M.D. Janezic, B.F. Riddle, R.T. Johnk, P. Kabos, C.L. Holloway, R.G. Geyer, C.A. Grosvenor, *Measuring the Permittivity and Permeability of Lossy Materials: Solids, Liquids, Metals, Building Materials, and Negative-Index Materials (NIST Technical Note 1536),*

National Institute of Standards and Technology, U.S. Government Printing Office: Washington, 2005.
[164] Agilent Basics of Measuring the Dielectric Properties of Materials [Online],Agilent Technologies, http://www.agilent.com (accessed Feb 20, 2012).
[165] S. P. Morgan, "Effect of Surface Roughness on Eddy Current Losses at Microwave Frequencies", *J. Appl. Phys.*, vol. 20, pp. 352-362, 1949.
[166] R. Faddoul, N. Reverdy-Bruas, and J. Bourel, "Silver Content Effect on Rheological and Electrical Properties of Silver Pastes", *J. Mater. Sci: Mater. Electron.*, vol. 23, pp. 1415-1426, 2012.
[167] Clear UV Dielectric Ink EMD 6200 Developmental Safety Data Sheet, Sun Chemical, 2012.
[168] Nano-silver Ink for Inkjet Printing [Online], Advanced Nano Products Co. Ltd, http://anapro.com/eng/product/silver_inkjet_ink.html (accessed Jan 15, 2012).
[169] Technical Information Leaflet - Solsys Jettable Silver EMD 5714 & EMD5603, Sun Chemical, 2011.
[170] 3M^{TM} Novec^{TM} 1700 Electronic Grade Coating, 3M, 2011.
[171] Norton Industrial Catalogue 2007, Norton, 2007, pp. 74-218.
[172] C. MacDonald, Rogers Corporation, Private Communication, 2012.
[173] ISO 4288-1996 Geometrical Product Specifications (GPS) — Surface Texture: Profile Method — Rules and Procedures for the Assessment of Surface Texture, The International Organization for Standardization, 1996.
[174] B. Xu, *Inkjet Printing of Silver for Direct Write Applications*, PhD Thesis, The University of Manchester, 2010.
[175] B. Derby, "Inkjet Printing Ceramics: From Drops to Solid", *J. Eur.Ceram. Soc.*, pp. 2543-2550, 2011.
[176] E. Tekin, P. J. Smith, and U. S. Schubert, "Inkjet Printing as a Deposition and Patterning Tool for Polymers and Inorganic Particles", *Soft Matter*, pp. 703-713, 2008.
[177] J. E. Fromm, "Numerical Calculation of the Fluid Dynamics of Drop-on-Demand Jets", *IBM J. Res. Dev.*, pp. 322-333, 1984.
[178] J. Perealer, Smith, P.J., van den Bosch, E., van Grootel, S.S.C., Ketelaars, P.H.J.M., Schubert, U.S., "The Spreading of Inkjet-Printed Droplets with Varying Polymer Molar Mass on a Dry Solid Substrate", *Macromol. Chem. Phys.*, pp. 495-502, 2009.
[179] N. Reis, Ainsley, C.,Derby, B., "Ink-jet Delivery of Particle Suspensions by Piezoelectric Droplet Ejectors", *J. Appl. Phys.*, pp. 094903., 2005.
[180] F. Gao, Sonin, A.A., "Precise Deposition of Molten Microdrops: The Physics of Digital Microfabrication", *Proc. R. Soc. London Ser. A*, pp. 533-554, 1994.
[181] S. Schiaffino, Sonin, A.A., "Formation and Stability of Liquid and Molten Beads on a Solid Surface", *J. Fluid Mech.*, pp. 95-110, 1997.
[182] R. Bhola, and S. Chandra, "Parameters Controlling Solidification of Molten Wax Droplets Falling on a Solid Surface", *J. Mater. Sci.*, vol. 34, pp. 4883-4894, 1999.
[183] M. Rebros, Fleming, P.D.,Joyce, M.K., "UV-inks, Substrates and Wetting", In *Proc. of TAPPI Coat. and Graphics Arts Conf.*, pp. 1-7, 2006.
[184] M. Pickrell, Sun Chemical, UK, Private Communication, 2013.

[185] E. Stathatos, Kanopoulos, N., Lianos, P., Katsagounos, Y., Makris, T., Scalable Production of Dye-sensitized Solar Cells using Inkjet Printing, U.S. Patent 2013/0139887 A1, 2013.

[186] R. D. Deegan, Bakajin, O., Dupont, T.F., Huber, G., Nagel, S.R., Witten, T.A., "Capillary Flow as the Cause of Ring Stains from Dried Liquid Drops," *Nat.*, pp. 827-829, 1997.

[187] T. Lamminmäki, Kettle, J., Rautkoski, H., Kokko, A., Gane, P., "Limitations of Current Formulations when Decreasing the Coating Layer Thickness of Papers for Inkjet Printing", *Ind. Eng. Chem. Res*, pp. 7251-7263, 2011.

[188] E. Svanholm, *Printability and Ink-Coating Interactions in Inkjet Printing*, PhD Thesis, Karlstad University, Sweden, 2007.

[189] G. R. Ström, Borg, J., Svanholm, E., "Short-Time Water Absorption by Model Coatings", in *Proc. 10th Adv. Coat. Fundam. Symp.*, Montreal, Canada, 2008, pp. 11-13.

[190] IPC-TM-650 Test Methods Manual (No. 2.6.2), IPC, Illinois, 1998.

[191] Summary of Properties for Kapton Polyimide Films [Online], Dupont, http://www2.dupont.com/Kapton/en_US/assets/downloads/pdf/summaryofprop.pdf (accessed May 15, 2013).

[192] DupontTM Teflon® PTFE TE-3885 Fluoropolymer Resin [Online],Dupont, http://www2.dupont.com/Teflon_Industrial/en_US/assets/downloads/k15764.pdf (accessed May 15, 2013).

[193] MatWeb Home Page. http://www.matweb.com/ (accessed May 15,2013).

[194] D. B. Soltman, *Understanding Inkjet Printed Pattern Generation*, PhD Thesis, University of California at Berkeley, US, 2011.

[195] J. Z. Wang, Z. H. Zheng, H. W. Li, W. T. S. Huck, and H. Sirringhaus, "Dewetting of Conducting Polymer Inkjet Droplets on Patterned Surface", *Nat. Mater.*, vol. 3, pp. 171-176, 2004.

[196] D. J. Lee, J. H. Oh, and H. S. Bae, "Crack Formation and Substrate Effects on Electrical Resistivity of Inkjet-printed Ag Lines", *Mater. Lett.*, vol. 64, no. 9, pp. 1069-1072, 2010.

[197] H. C. Jung, S.-H. Cho, J. W. Joung, and Y.-S. Oh, "Studies on Inkjet Printed Conducting Lines for Electronic Devices", *J. Electron. Mater.*, vol. 36, no. 9, pp. 1211-1218, 2007.

[198] Pressure Line UV Exposure Unit PLUVEX 1410 [Online], Mega Electronics, http://www.megauk.com/uv_exposure_units.php (accessed Aug 1, 2013).

[199] Blacklight (BL-350) datasheet, Sylvania, http://www.medrk.ru/ uploads/ doc/sylvania_bl350_ecat.pdf (accessed Aug 15, 2013).

[200] M. Pilkenton, J. Lewman, R. Chartoff, "Effect of Oxygen on the Crosslinking and Mechanical Properties of a Thermoset Formed by Free-Radical Photocuring", *J. Appl. Polym. Sci.*, vol. 119, no. 4, pp. 2359-2370, 2011.

[201] C. Decker, "Kinetic Study and New Applications of UV Radiation Curing", *Macromol. Rapid Commun.*, vol. 23, no. 18, pp. 1067-1093, 2003.

[202] D. G. Anderson, S. Levenberg, and R. Langer, "Nanoliter-scale Synthesis of Arrayed Biomaterials and Application to Human Embryonic Stem Cells", *Nature Biotech.*, vol. 22, pp. 863-866, 2004.

[203] J. Swenson, and V. Calder, UV Penetration and Plastic [Online], http:// www.newton.dep.anl.gov/askasci/eng99/eng99272.htm (accessed Sept 15 2013).

[204] S. H. Lee, L. W.G., B. G. Chung, J. H. Park, and A. Khademhosseini, "Rapid Formation of Acrylated Microstructures by Microwave-Induced Thermal Crosslinking", *Macromol. Rapid Commun.,* vol. 30, no. 16 pp. 1382-1386, 2009.

[205] Y. Lei, Q. Niu, H. Mi, Y. Wang, I. Nurulla, and W. Shi, "Carbazole-based Conjugated Polymer with Tethered Acetylene Groups: Synthesis and Characterization", *Dyes Pigm.,* vol. 96, no. 1, pp. 138-147, 2013.

[206] Y. Y. Lim, Y. M. Goh, and C. Liu, "Surface Treatments for Inkjet Printing onto a PTFE-Based Substrate for High Frequency Applications", *Ind. Eng. Chem. Res.,* vol. 52, no. 33, pp. 11564-11574, 2013.

[207] R. O. F. Verkuijlen, M. H. A. van Dongen, A. A. E. Stevens, J. van Geldrop, and J. P. C. Bernards, "Surface Modification of Polycarbonate and Polyethylene Naphtalate Foils by UV-ozone Treatment and mPlasma Printing", *Appl. Surf. Sci.,* vol. 290, pp. 381-387, 2014.

[208] A. Peyvandi, S. Ul Abideen, Y. Huang, I. Lee, P. Soroushian, and J. Lu, "Surface Treatment of Polymer Microfibrillar Structures for Improved Surface Wettability and Adhesion", *Appl. Surf. Sci.,* vol. 289, pp. 586-591, 2014.

[209] J. A. Jofre-Reche, and J. M. Martin-Martinez, "Selective Surface Modification of Ethylene-vinyl Acetate and Ethylene Polymer Blend by UV-ozone Treatment", *Int. J. Adhes. Adhes.,* vol. 43, pp. 42-53, 2013.

[210] PR-100 UV Ozone Photoreactor Operating Instruction Manual, UVP Inc., USA.

[211] Dimatix Materials Printer DMP-2800 Series User Manual,Fujifilm Dimatix Inc., 2007.

[212] B. Duncan, R. Mera, D. Leatherdale, M. Taylor, and R. Musgrove, Techniques for Characterising the Wetting, Coating and Spreading of Adhesives on Surfaces, National Physical Lab Report, March 2005.

[213] M. Blitshteyn, "Wetting Tension Measurements on Corona-Treated Polymer Films", *Tappi J.,* vol. 78, no. 3, pp. 189-195, 1995.

[214] K. Taki, and T. Nakamura, "Effects of Curing Conditions and Formulations on Residual Monomer Contents and Temperature Increase of a Model UV Gel Nail Formulation", *J. Cosmet., Dermatol. Sci. Appl.,* vol. 1, no. 4, pp. 111-118, 2011.

[215] C. P. Vazquez, R. Tayouo, C. Joly-Duhamel, and B. Boutevin, "UV-curable Bismaleimides Containing Poly(dimethylsiloxane): Use as Hydrophobic Agent", *J. Polym. Sci., Part A: Polym. Chem.,* vol. 48, pp. 2123-2134, 2012.

[216] J. R. Greer, and R. A. Street, "Mechanical Characterization of Solution-derived Nanoparticle Silver Ink Thin Films", *J. Appl. Phys.,* vol. 101, 103529 (5 pp.), 2007.

[217] R. C. Chiu, T. J. Garino, and M. J. Cima, "Drying of Granular Ceramic Films: I. Effect of Processing Variables on Cracking Behavior", *J. Am. Ceram. Soc.,* vol. 76, no. 9, pp. 2257-2264, 1993.

[218] R. C. Chiu, and M. J. Cima, "Drying of a Granular Ceramic Films: II. Drying Stress and Saturation Uniformity", *J. Am. Ceram. Soc.,* vol. 76, no. 11, pp. 2769-2777, 1993.

[219] Y. Chan, and Y. Mi, "A Study of the Versatile Micropatterns of Diblock Copolymer Micelles: The Effect of Copolymer Concentration, Substrate, Film Thickness and Micelles Morphology", *Polym.,* vol. 45, no. 10, pp. 3473-3480, 2004.

[220] A. Groisman, and E. Kaplan, "An Experimental Study of Cracking Induced by Desiccation", *Europhys. Lett.,* vol. 25, no. 6, pp. 415-420, 1994.

[221] E. A. Jagla, "Stable Propagation of An Ordered Array of Cracks During Directional Drying", *Phys. Rev. E,* vol. 65, 046147 (7 pp.), 2002.

[222] H. Lei, L. F. Francis, W. W. Gerberich, and L. E. Scriven, "Stress Development in Drying Coatings after Solidification", *AIChE J.,* vol. 48, no. 3, pp. 437-451, 2002.

[223] E. Santanach Carreras, F. Chabert, D. E. Dunstan, and G. V. Franks, "Avoiding "Mud" Cracks During Drying of Thin Films from Aqueous Colloidal Suspensions", *J. Colloid Interface Sci.,* vol. 313, no. 1, pp. 160-168, 2007.

[224] A. F. Routh, "Drying of Thin Colloidal Films", *Rep. Prog. Phys.,* vol. 76, 2013.

[225] K. Nakata, H. Kimura, M. Sakai, T. Ochiai, H. Sakai, T. Murakami, M. Abe, and A. Fujishima, "UV/Thermally Driven Rewritable Wettability Patterns on TiO2-PDMS Composite Films", *Appl. Mater. Interfaces,* vol. 2, no. 9, pp. 2485-2488, 2010.

[226] Silicone Surface-Active Agents [Online], Dow Corning Corporation, http://www.dowcorning.com/content/publishedlit/26-1365.pdf (accessed Jul 15, 2014).

[227] R. A. Ryntz, K. R. Kurple, Polysiloxane Graft Copolymers,Flexible Coating Compositions Comprising Same and Branched polysiloxane Macromers for Preparing Same, E.U. Patent 0284679 A1, 1988.

[228] Y.-I. Lee, Y.-S. Goo, K.-J. Lee, Y.-G. Hwang, Y. Byun, H. J. Park, D.-Y. Park, N. V. Myung, and Y.-H. Choa, "Effect of UV/Ozone Treatment on Interactions between Ink-jet Printed Cu Patterns and Polyimide Substrates", *Thin Solid Films,* vol. 519, pp. 6853-6857, 2011.

[229] L. Goehring, W. J. Clegg, and A. F. Routh, "Solidification and Ordering During Directional Drying of a Colloidal Cispersion", *Langmuir,* vol. 26, no. 12, pp. 9269-9275, 2010.

[230] S. H. Ko, H. Pan, C. P. Grigoropoulos, C. K. Luscombe, J. M. J. Frechet, and D. Poulikakos, "All Inkjet-printed Flexible Electronics Application on a Polymer Substrate by Low-temperature High-resolution Selective Laser Sintering of Metal Nanoparticles", *Nanotechnol.,* vol. 18, no. 34, 2007.

[231] H.-S. Kim, S. R. Dhage, D.-E. Shim, and H. T. Hahn, "Intense Pulsed Light Sintering of Copper Nanoink for Printed Electronics", *Appl. Phys. A,* vol. 97, pp. 791-798, 2009.

[232] D. Tobjörk, H. Aarnio, P. Pulkkinen, R. Bollström, A. Määttänen, P. Ihalainen, T. Mäkelä, J. Peltonen, M. Toivakka, H. Tenhu, and R. Österbacka, "IR-Sintering of Ink-jet Printed Metal-nanoparticle on Paper", *Thin Solid Films,* vol. 520, no. 7, pp. 2945-2955, 2012.

[233] P. Laakso, S. Ruotsalainen, E. Halonen, M. Mäntysalo, and A. Kemppainen, "Sintering of Printed Nanoparticle Strucures using Laser Treatment", in *Proc. Int. Conf. Appl. Lsers Electro-Opt. (ICALEO),* Orlando, Florida, 2009, pp. 1360-1366.

[234] S. Jang, Y. Seo, J. Choi, T. Kim, J. Cho, S. Kim, and D. Kim, "Sintering of Inkjet Printed Copper Nanoparticles for Flexible Electronics", *Scr. Mater.*, vol. 62, pp. 258-261, 2010.

[235] I. Kazani, C. Hertleer, G. De Mey, A. Schwarz, G. Guxho, and L. Van Langenhove, "Electrical Conductive Textiles Obtained by Screen Printing", *Fibres Text. East. Eur.*, vol. 20, no. 1, pp. 57-63, 2012.

[236] J. R. Larry, Method of Improving Line Resolution in Screen Printing, U.S. Patent 3672934 A, 1972.

[237] High Performance Microwave Probes Model 40A [Online], GGB Industries Inc., http://www.ggb.com/40a.html (accessed Dec 30, 2014).

[238] CST Computer Simulation Technology AG, CST Microwave Studio [computer software], http://www.cst.com

[239] Calibration Substrate CS-10, GGB Industries, 2012.

[240] T.E. Kolding, "A Four-Step Method for De-Embedding Gigahertz On-Wafer CMOS Measurements", *IEEE Trans. Electron. Devices*, vol. 47, no. 4, pp. 734-740, 2000.

[241] M. Aoki, K. Nakamura, T. Tachibana, I. Sumita, H. Hayashi, H. Asada, and Y. Ohshita, "30 μm Fine Line Printing for Solar Cells", in *39th IEEE Photovoltaic Specialists Conference (PVSC)*, Tampa Bay, Florida, 2013, pp. 2162-2166.

[242] D. Buzby, and A. Dobie, "Fine Line Screen Printing of Thick Film Pastes on Silicon Solar Cells", in I*nt. Microelectron. Assem. Packag. Soc. (IMAPS)*, Rhode Island, USA, 2008, pp. 1-5.

[243] U. Itoh, M. Yoshida, H. Tokuhisa, N. Ushifusa, I. Sumita, T. Fukunishi, M. Aoki, Y. Ohshita, and H. Kamata, "Screen Printed Finger Electrode with High Aspect Ratio by Single Printing for Crystal Si Solar Cell using Novel Screen Mask", in *38th IEEE Photovoltaic Specialists Conference (PVSC)*, Austin, TX, 2011, pp. 002167-002170.

[244] G. Zou, H. Gronqvist, J. P. Starski, J. Liu, and S. M. Johan Liu, *IEEE*, "Characterizaion of Liquid Crystal Polymer for High Frequency System-in-a-Package Applications", *IEEE Trans. Adv. Packag.*, vol. 25, no. 4, pp. 503-508, 2002.

[245] C. Griggs, and J. Sumerel, "Opportunities for Inkjet Printing in Industrial Applications", *Industrial + Specialty Printing*, no. May/June, pp. 4, 2010.

[246] H. L. Ritter, and L. C. Drake, "Pore-Size Distribution in Porous Materials - Pressure Porosimeter and Determination of Complete Macropore-size Distributions", *Ind. Eng. Chem., Anal. Ed.*, vol. 17, no. 12, pp. 782-786, 1945.

[247] ISO 15901-1: 2005, Pore Size Distribution and Porosity of Solid Materials by Mercury Porosimetry and Gas Adsorption-Part 1: Mercury Porosimetry, The International Organization for Standardization, 2005.

[248] Y. Y. Lim, Y. M. Goh, C. Liu, and D. Hutt, "Surface Modification of an Ambient UV-cured Dielectric to Realise Electrically Conducting Traces", *Surf. Coat. Technol.*, vol. 266, pp. 93-104, 2015.

[249] J. Akedo, J. Park, and H. Tsuda, "Fine Patterning of Ceramic Thick Layer on Aerosol Deposition by Lift-off Process using Photoresist", *J. Electroceram.*, vol. 22, no. 1-3, pp. 319-326, 2009.

[250] M. Momotani, N. Mori, S.-N. Nam, H. Kakemoto, S. Wada, T. Tsurumi, and J. Akedo, "Fabrication of Microstrip Band Pass Filters in GHz Region

by Aerosol Deposition Process", *Key Eng. Mater.*, vol. 301, pp. 117-120, 2006.
[251] Specialty Paper Brohure, Hexis UK Ltd, 2012.
[252] C. A. Schneider, W. S. Rasband, and K. W. Eliceiri, "NIH Image to ImageJ: 25 Years of Image Analysis," *Nat. Methods,* vol. 9, pp. 671-675, 2012.

Appendix A - Experimental Trial Results for Tyvek

This Appendix describes the methodology and the results obtained in inkjet printing onto Tyvek. This includes the surface profile characterisation of Tyvek (in terms of thickness and roughness measurements). Surface modification techniques were then performed to alleviate the surface roughness of Tyvek, and the results presented in this Appendix.

A.1 Surface Profile Characterisation

Characterising the thickness and surface roughness values of Tyvek was imperative as those values were not available from the supplier. In this case, a confocal gauge with a 3 mm measurement range (CLA-3mm, Talysurf CLI 2000, Taylor Hobson) was used to determine the thickness of Tyvek samples along with its surface roughness, as illustrated in Figure A-1. This involved using adhesive tape to attach the Tyvek sample along 3 of its sides to the measurement platform, leaving one side unattached for the gauge. The scan direction of the gauge is from east-west, with measurements obtained in 5 locations as shown in Figure A-1. The scan length was set to 7 mm, with a resolution of 0.5 µm at a measurement speed of 500 µm/s. A Gaussian filter of 2.5 µm cut-off length was used in the post-processing of the results, in accordance with the recommended cut-off in ISO 4288-1996.

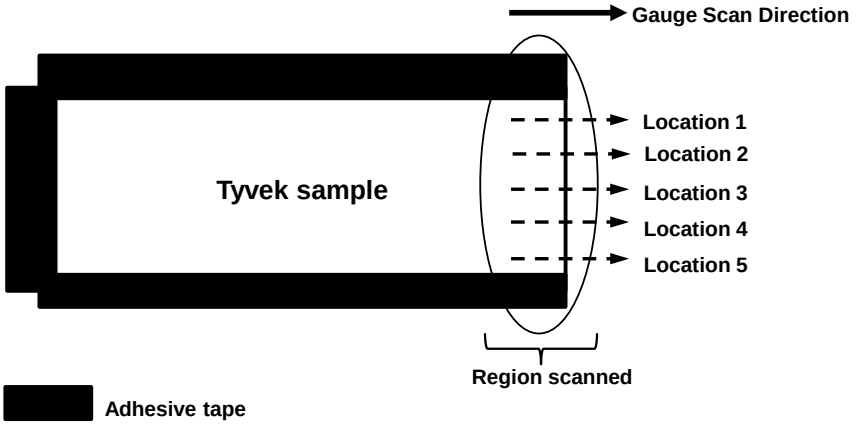

Figure A-1 Schematic showing surface profile measurement for Tyvek

Following the surface profile characterisation of Tyvek, the thickness of the measured Tyvek sample and the corresponding surface roughness are shown in Table A-1. From the table, the average thickness of Tyvek was around 333 µm

while the average (R_a**)** and root-mean-square (R_{rms}) surface roughness values are around 4.3 µm and 5.1 µm. Compared to the average surface roughness of around 1 µm on RO3006 substrate, the surface roughness of Tyvek is significantly higher by about 6-7 times.

Table A-1 Measured surface roughness of Tyvek

Measurement Location	Thickness (µm)	R_a (µm)	R_{rms} (µm)
1	350	4.09	4.84
2	329	4.04	4.72
3	326	4.83	5.69
4	329	4.22	4.99
5	330	4.25	5.06
Average	332.8	4.29	5.06

A.2 Sample Preparation of Tyvek for SEM Analysis

For the sample analysis using SEM imaging, the Tyvek samples were sliced with a sharp razor blade. The slicing motion was vertical, with care taken to avoid swaying the blade in the x-direction as that would result in an uneven edge. Next, the sample was sputtered with gold for 60 s and a conductive silver paint (Agar Scientific) was applied to the corners and sides of the sample to adhere it to the sample stub holder.

A.3 Maximum Temperature that Tyvek can Withstand

From the datasheet in Appendix B1, Tyvek begins to shrink at 118 °C and melts at 135 °C. On the other hand, the minimum sintering temperatures for the silver inks considered [168, 169] ranged from 120 °C to 150 °C, for durations of 30 min. As such, there is a need to determine the highest temperature which Tyvek can withstand, prior to the deposition of the silver inks using inkjet printing.

During testing, glass slides or small ceramic blocks were used to hold the Tyvek samples (2 x 1 cm) down. This is due to the small thickness of the Tyvek samples, which make them susceptible to being blown around the oven. The samples were tested in a reflow oven (JEM 310, Ok Industries), where the iron plate was covered with a wire gauze on which the samples were placed. A fluke thermocouple was used to gauge the temperature inside the reflow oven. The oven temperature was

initially set to be 100 °C and gradually increased to 110 °C, with different time settings.

- 100 °C for 15 min (Program #102): The set temperature was reached after 4 min. The maximum temperature observed was 110 °C at 15 min.
- 100 °C for 70 min (Program #103): Sample remained intact, ie not destroyed.
- 105 °C for 20 min (Program #104): Sample remained intact
- 110 °C for 20 min, followed by 40 min (Program #105,#106):
  Sample remained intact.

Prior to this, the Tyvek samples were tested in another oven (Gallenkamp FSL-400), where the temperature profile could be pre-set at 110 °C for 1 h (after ramping up). While the temperature was set at 110 °C, the values were observed to fluctuate when ramping up to that temperature. The temperature was observed to reach 117-118 °C after 45 min with the sample significantly crumpled, and a strong burning smell was detected.

The results obtained using the reflow oven indicated that a maximum temperature of 110 °C for 60 min is possible for Tyvek samples. While the maximum temperature is slightly lower than temperatures recommended for the silver inks, the corresponding time was increased significantly to 60 min to aid in the sintering process.

A.4 Surface Modifications on Tyvek

This section describes the surface modifications performed on Tyvek to alleviate its surface roughness. The modifications include the use of a hydrophobic coating, SU-8 coating and an UV-curable dielectric.

A.4.1 Hydrophobic Coating

The detailed specifications of the hydrophobic coating can be found in Section 5.2.3(a) of Chapter 5. The coating was applied to Tyvek via brushing, in order to minimise the contamination of the solution by the substrate.

After treating Tyvek with the hydrophobic coating, traces with designed line width/spacing (w/s) of 100/100 µm to 500/500 µm were inkjet printed onto the coated Tyvek using a silver ink (DGP 40LT-15C, Advanced Nano Products). The ink specifications and printing parameters used are described in Section 5.2.2 and Section 5.3.2 of Chapter 5 The results obtained are shown in Figure A-2 where the deposited silver traces on Tyvek were observed to be fibrous. This is because of the small thickness of a single printed layer, which resulted in the silver nanoparticles clinging onto the fibers as shown in Figure A-3.

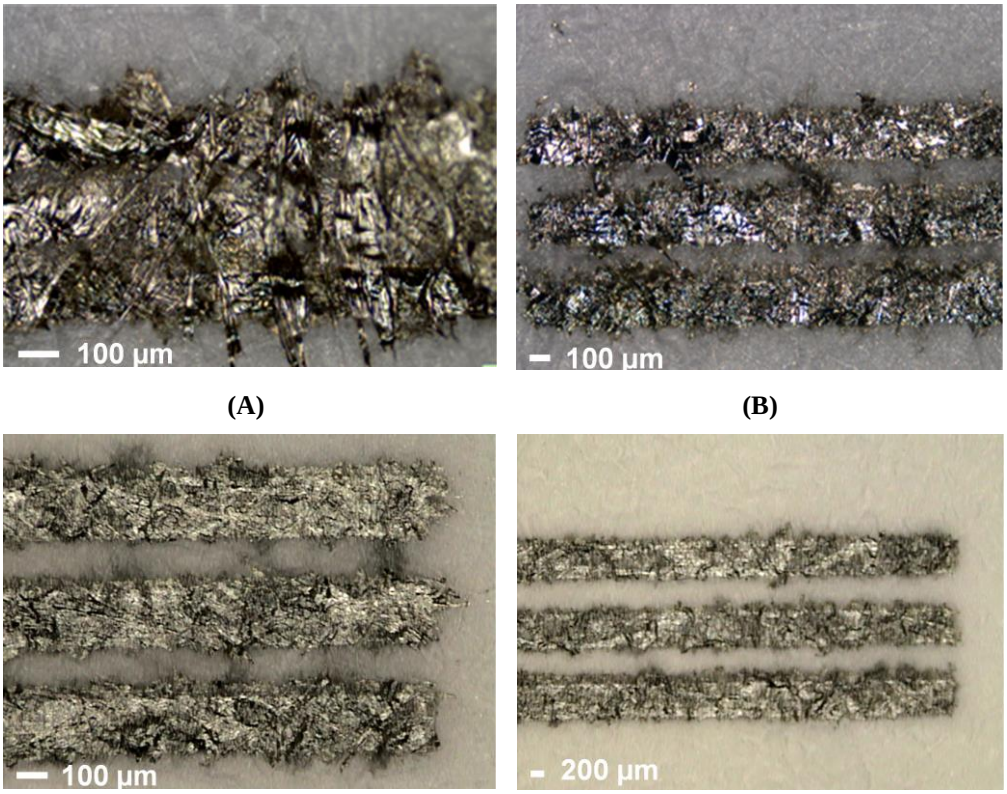

(A) **(B)**

(C) **(D)**

Figure A-2 Printed traces on Tyvek: (A) 100/100 µm (B) 200/200 µm (C) 300/300 µm (D) 400/400 µm traces

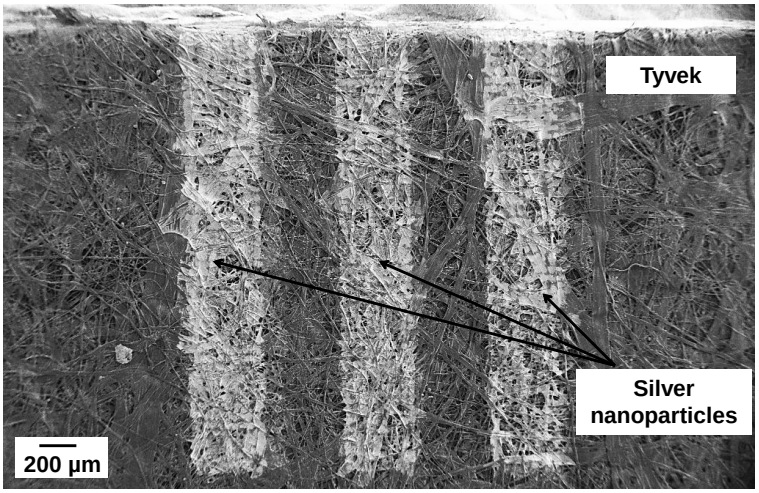

Figure A-3 SEM image of hydrophobic coated Tyvek (Top view)

From Figure A-2 (A), the 100 µm tracks were observed to have merged together. For the 200 µm tracks in Figure A-2 (B), parts of the tracks were bridged together across the gaps, while ink spread across adjacent traces was observed for the 300 µm tracks in Figure A-2 (C). The minimum width/spacing obtainable on the coated Tyvek without any bridging or ink spread is 400/400 µm, as shown in Figure A-2 (D).

Dimension measurements were made for the non-shorted printed traces. The measurements were obtained for at least 6 sections along the trace length and averaged, with the results shown in Table A-2. The notations used in Table A-2 are referenced from Figure A-4. From the results, a variation of within 10 % was observed for the 400/400 µm and 500/500 µm traces.

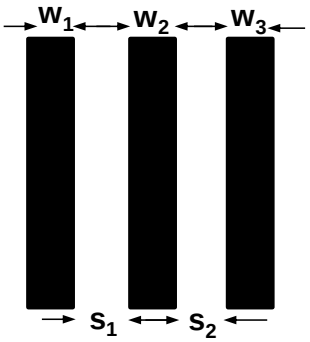

Figure A-4 Diagram of printed traces with the widths and spacings defined

Table A-2 Measured values (best fit) for varying pitches

Line width/ spacing (µm)	w/s	Target values (µm)	Measured values (µm)
400/400	w_1	400	396
	s_1	400	438
	w_2	400	370
	s_2	400	392
	w_3	400	412
500/500	w_1	500	482
	s_1	500	508
	w_2	500	511
	s_2	500	499
	w_3	500	462

Apart from depositing patterns with varying width/spacings, simple test patterns to characterise for the DC resistivity using two point probes were also inkjet printed. These test patterns had widths of 250 µm and lengths of 3.5 cm and 5 cm (Figure A-5).

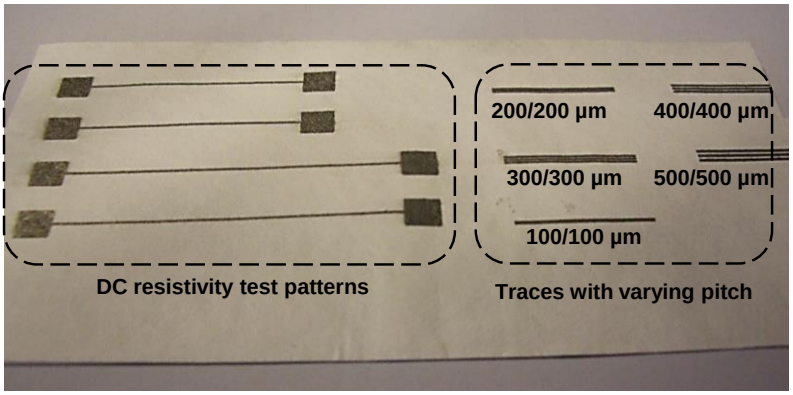

Figure A-5 Printed traces on coated Tyvek

After inkjet printing, the samples were thermally cured at 110 °C for 1 h. Two point probe resistance measurements were then performed after the thermal curing. However no values could be registered even with two rounds of thermal curing. Upon closer inspection, this could be attributed to a discontinuous trace as shown in Figure A-6, since the printed traces were observed to conform to the extremely discontinuous fibre morphology. From the white light images shown in Figure A-7, it can be observed that the printed tracks were not all connected on the same level, in contrast to a non-porous surface. Together with Figure A-3, the results suggest

that no continuous film was formed with the application of the hydrophobic coating, which could be due to the low solids content (2 %) present in the coating.

Due to the lack of a continuous film, while the bottom fibres appear to be deposited with silver nanoparticles from visual inspection, it is likely that the deposited nanoparticles within the fibre were not contacting, which results in a lack of electrical connection. This is further illustrated using a diagram in Figure A-8. The results may be improved with a thicker coat, which would require either several times of dip-coating (thicknesses of around 1 µm can be obtained), or using a hydrophobic coating with a higher solids content.

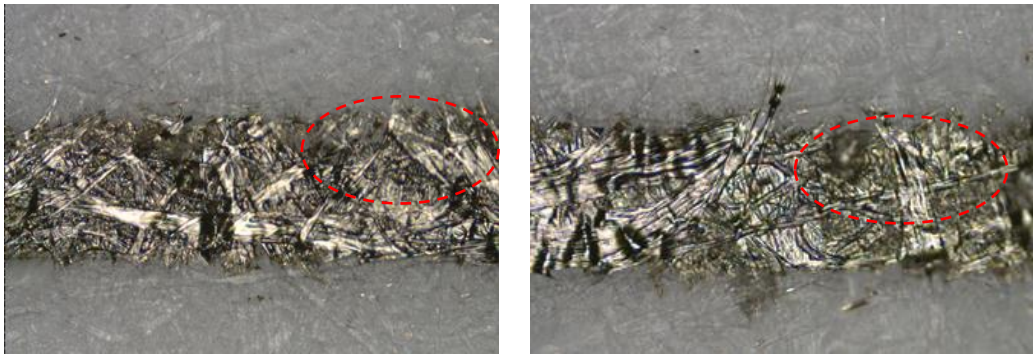

(A) **(B)**

Figure A-6 Gaps in the printed traces

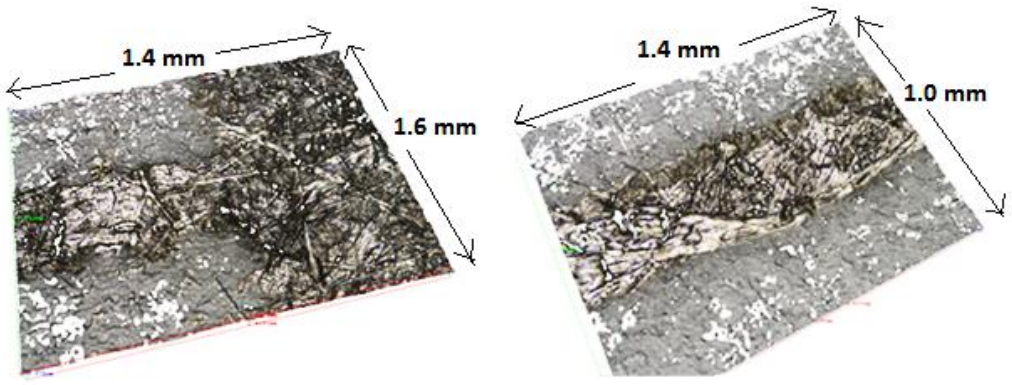

(A) **(B)**

Figure A-7 White light images of printed trace on Tyvek

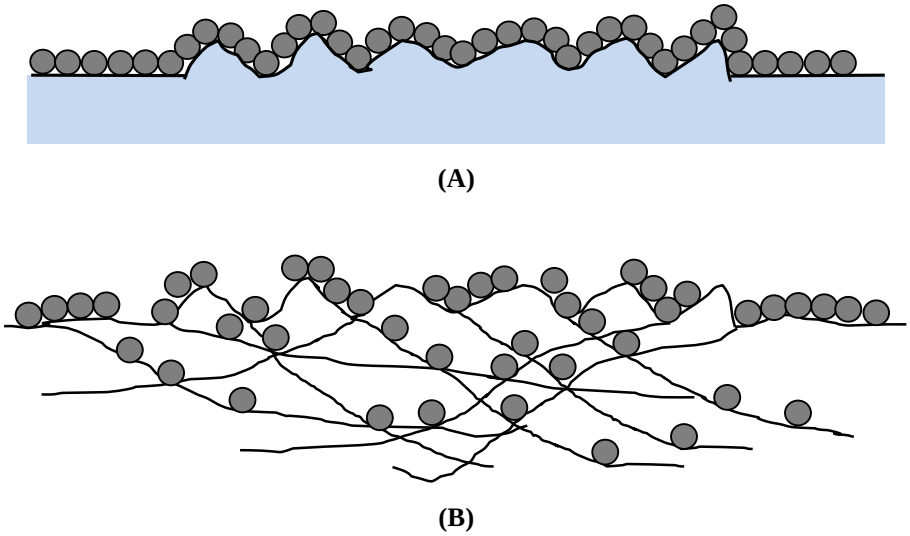

(A)

(B)

Figure A-8 Nanoparticle deposition: (A) A non-porous substrate with surface roughness (B) A porous substrate with surface roughness

A.4.2 SU-8 Coating

SU-8 (an epoxy based photo-resist, MicroChem Corp.) is a dielectric commonly used in silicon wafer processing to form passivation layers. In this case, SU-8 is applied to form a planarisation layer onto Tyvek, as illustrated in Figure A-9.

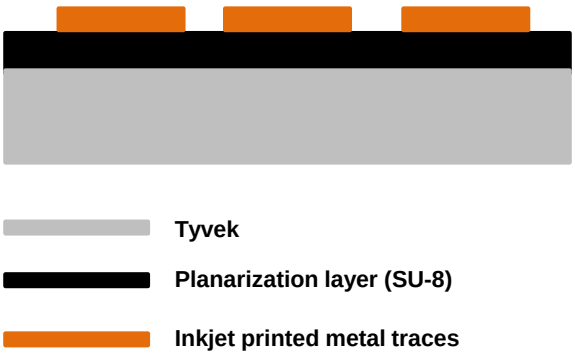

Figure A-9 Cross-section of surface modified Tyvek, with the planarisation layer

The application of the SU-8 dielectric is summarised in Figure A-10, with the parameters based on conventional silicon wafer processing. Firstly, 6 ml of the photo-resist was dispensed onto the substrate. The spin coating parameters were set at 500 rpm at 3000 rpm/sec (3 s) followed by 2500 rpm at 4000 rpm/sec (30 s). The coated substrate was then soft baked at 95 ºC for 1.5 min. Subsequently, the substrate was exposed with a dose setting of 250 mJ/cm ^{2} and post baked at two temperatures, namely 65 ºC for 1.5 min, and 95 ºC for 2 min. A final bake was

performed on the coated substrate at 115 ºC for 5 min. Overall, two coats of SU-8 were applied, as the first layer was found to be insufficient to coat over the surface when RO3006 was used as the reference substrate (Figure A-11).

The results obtained for Tyvek are shown in Figure A-12, which suggests that a double coat of SU-8 did not significantly planarise the surface of Tyvek, although it appeared to have filled some of the gaps present in the fibrous surface. This is further verified through the SEM image in Figure A-13, which revealed an uneven SU-8 coat. Further work would be needed to optimise the processing parameters for the Tyvek substrate, such that a homogeneous planarisation layer using SU-8 can be obtained.

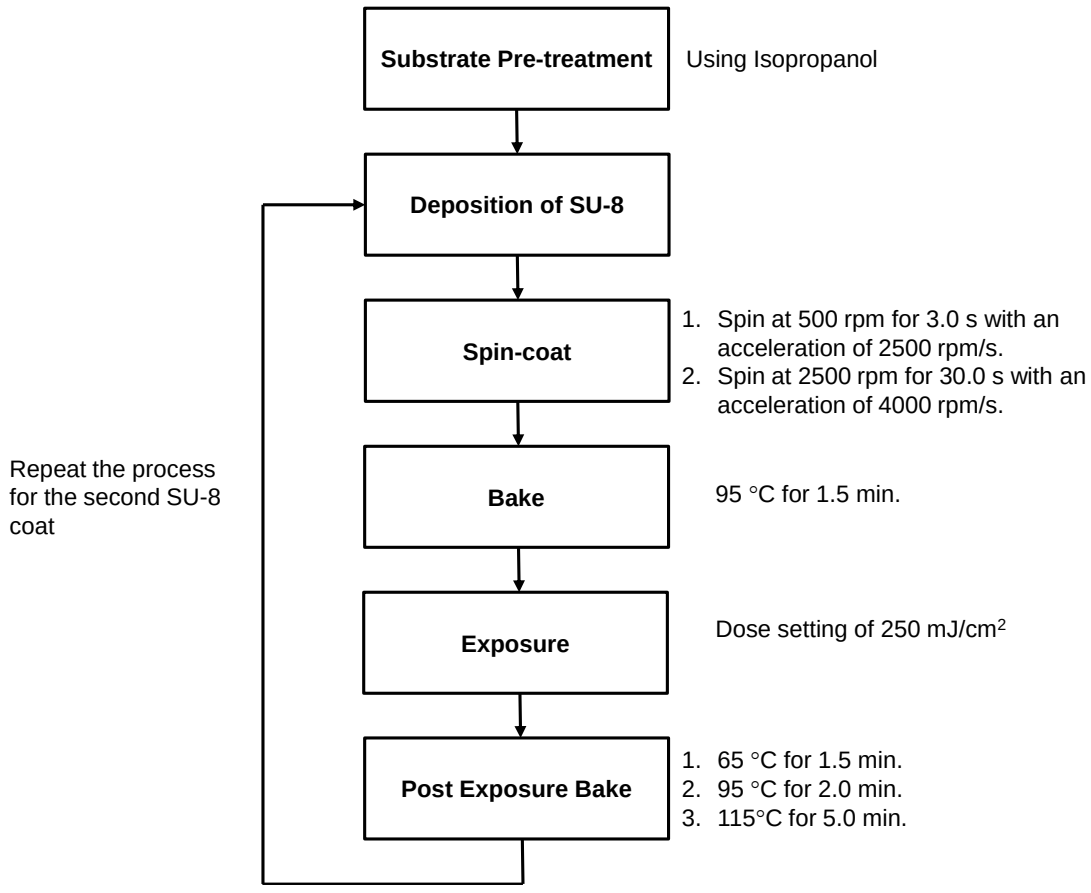

Figure A-10 Process flow for application of SU-8 onto Tyvek

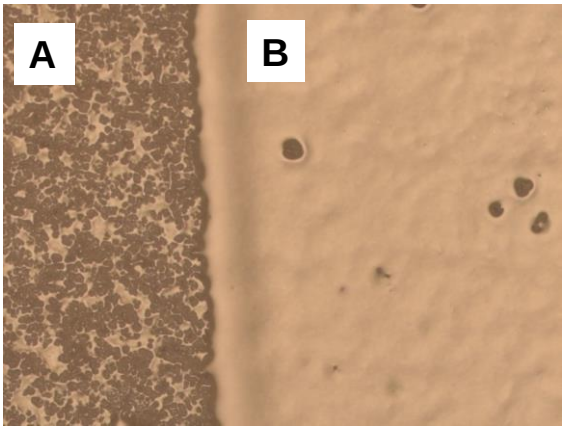

Figure A-11 Spin-coated SU-8 onto RO3006 substrate (A) After the first coat. (B) After the second coat.

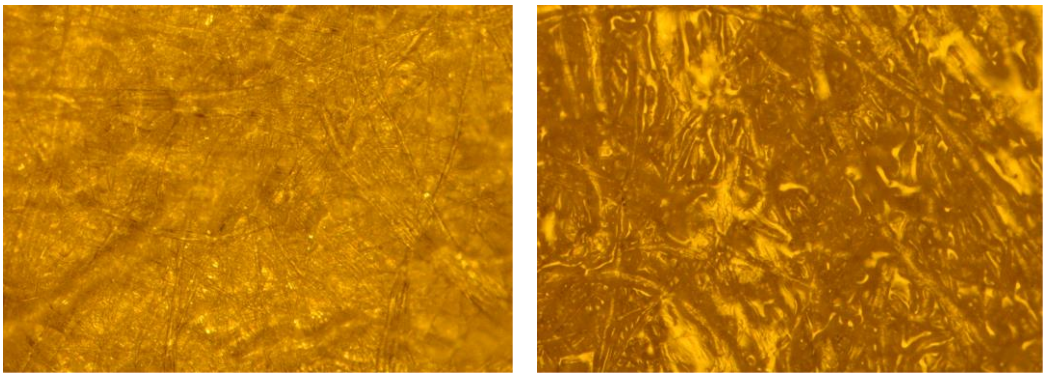

(A) **(B)**

Figure A-12 SU-8 coating on Tyvek (A) pre-coat (B) post-coat

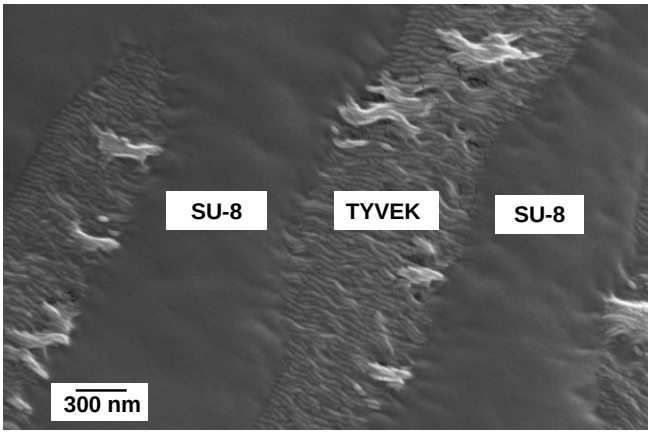

Figure A-13 SEM view of printed trace on SU-8 coated Tyvek (Top view)

A.4.3 UV Curable Insulator

The last surface modification involved the deposition of a UV-curable insulator onto Tyvek via inkjet printing to form a planarisation layer. A commercial UV curable dielectric (Solsys Jettable Insulator EMD 6415, Sun Chemicals) [89] was applied to the surface of Tyvek. The printing parameters used for the UV-curable insulator are detailed in Section 5.3.3 of Chapter 5. EMD 6415 has an ink viscosity of 11-13 mPa.s at 50°C and a surface tension of 35-37 mN/m. After the dielectric layer has been cured using a UV source, a silver ink (DGP 40LT-15C, Advanced Nano Products) was overprinted onto the layer using the printing parameters described in Section 5.3.2 of Chapter 5. The results obtained after thermal sintering are shown in Figure A-14.

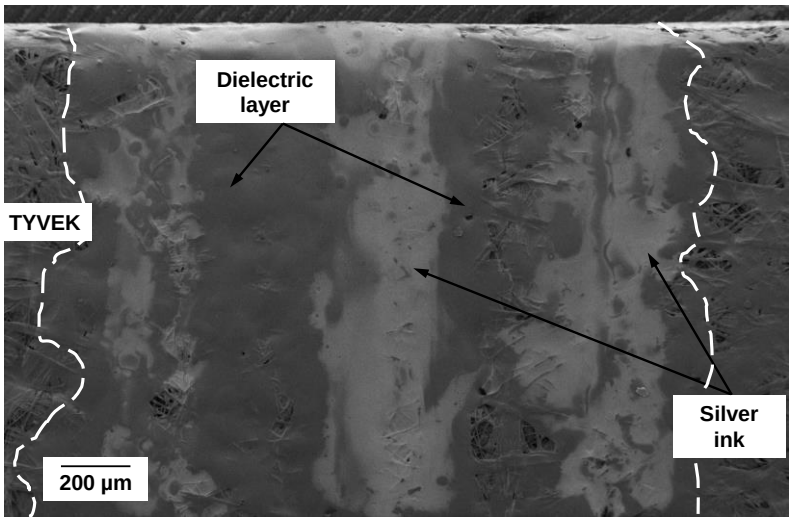

Figure A-14 SEM image of overprinted silver ink which de-wetted on the dielectric layer (Top view)

From Figure A-14, de-wetting was observed for the silver ink overprinted onto the dielectric layer, which indicates that the surface energies of the silver ink and the dielectric layer are not matched. This necessitates further work on understanding the processing parameters to eliminate the de-wetting phenomenon, towards the goal of realising of conductive traces on Tyvek. This work is further described in Chapter 6 of this thesis.

In conclusion, the porosity present in Tyvek posed challenges during surface modifications. In using hydrophobic coating, the low solids content did not yield a continuous coat on the porous substrate. In the deposition of SU-8 (via spin-

coating) and UV-curable dielectric (via inkjet printing), the liquids were observed to penetrate through the fibres during processing, resulting in non-uniform planarisation layers. In addition, de-wetting was encountered in overprinting the silver ink onto the planarisation layers. Consequently a need arises to simplify the analysis by considering a non-porous substrate to fulfil the objectives set out in the thesis.

Appendix B1 - Substrate Properties

This Appendix provides the detailed properties of Tyvek and RO3006 (high frequency substrate) used in this thesis. The properties for Tyvek are obtained from two sources. The general properties of Tyvek were obtained from the manufacturer (Dupont), and the specific Tyvek grade which is used in this thesis is obtained from the corresponding distributor (Hexis UK Ltd).

B1.1 RO3006 High Frequency Laminate [31]

Property	Typical value	Direction	Unit	Condition	Test Method
Dielectric constant, ε_r Process	6.15 ± 0.15	z	-	10 GHz, 23°C	IPC-TM-650 2.5.5.5 Clamped Stripline
Dielectric constant, ε_r Design	6.50	z	-	8-40 GHz	Differential Phase Length Method
Dissipation factor, tan δ	0.0020	z	-	10 GHz, 23°C	IPC-TM-650 2.5.5.5
Thermal coefficient of ε_r	-262	z	ppm/°C	10 GHz -50 to 150°C	IPC-TM-650 2.5.5.5
Dimensional stability	-0.30 -0.16	X Y	mm/m	COND A	ASTM D257
Moisture Absorption	0.02	-	%	D48/50	IPC-TM-650 2.6.2.1
Thermal Conductivity	0.79	-	W/m/K	80°C	ASTM C518
Coefficient of Thermal Expansion	17 17 24	X Y Z	ppm/°C	-55 to 288°C	ASTM D3386-94
Density	2.6		gm/cm3		

B1.2 Tyvek *(Hexis TYV500 Printable Tyvek Banner)*

White matt 125 gr/m^2 Tyvek banner [251] designed for solvent inkjet printing. TYV500 has a slightly textured effect and can be used for a variety of applications. These include hanging banners, advertisements, wallpaper, exhibition stands and decoration for theatres and studios. The material is available in rolls of 5 m and 50 m, with widths ranging from 1.37-2.22 m.

- **Dimensional stability [154]**

Tyvek remains dimensionally stable between 0 and 100 % relative humidity, where dimensions change less than 0.01 %.

- **Lightweight [154]**

The weight of Tyvek is less than half compared to materials of similar strength. The density of Tyvek is 0.38 g/cm^3.

- **Temperature range [154]**

Tyvek maintains its toughness and flexibility up to -75 °C. The material starts to shrink at 118 °C and melts at 135 °C.

- **Others [154]**

Tyvek has a smooth and a rough side, where the difference can be detected visually or using a low power magnifying glass. The material is printable on either side, but manufacturers recommend that the smooth side be used for printing. Tyvek has no grain direction.

Appendix B2 - Extracted DC Conductivity Values

The extracted DC conductivity values of traces which were screen printed on RO3006 and Tyvek are based on equation (4.16), where the trace edge profiles are assumed to be straight. L1 and L2 refer to the DC test structures shown in Figure 4.3(A) of Chapter 4, while R2a to R5b refer to the test structures with varying gaps from 200-500 μm (shown in Figure 4.4 of Chapter 4).

RO3006	**Width (μm)**	**Thickness (μm)**	**Length (cm)**	**Resistance (ohm)**	**Area (mm^2)**	**Area (cm^2)**	**Conductivity (S/m)**
L1	1000	13.0	10	2.9	0.0130	0.00013	2.65E+06
L2	1000	13.3	5	1.4	0.0133	0.000133	2.69E+06
R2a (Top)	200	15.0	4	4.8	0.0030	0.00003	2.78E+06
R2a (Bottom)	200	14.1	4	5.0	0.00282	0.0000282	2.84E+06
R2b (Top)	200	14.1	4	4.8	0.00282	0.0000282	2.96E+06
R2b (Bottom)	200	13.7	4	4.9	0.00274	0.0000274	2.98E+06
R3a (Top)	300	19.3	4	3.3	0.00579	0.0000579	2.09E+06
R3a (Bottom)	300	15.7	4	3.2	0.00471	0.0000471	2.65E+06
R3b (Top)	300	15.4	4	3.2	0.00462	0.0000462	2.71E+06
R3b (Bottom)	300	16.7	4	3.2	0.00501	0.0000501	2.50E+06
					Average Conductivity		**2.68E+06**

Tyvek (Panel 1)	**Width (μm)**	**Thickness (μm)**	**Length (cm)**	**Resistance (ohm)**	**Area (mm^2)**	**Area (cm^2)**	**Conductivity (S/m)**
L1	1000	24.2	10	4.8	0.0242	0.000242	8.61E+05
L2	1000	18.0	5	2.3	0.018	0.00018	1.21E+06
L3	1000	19.1	5	2.5	0.0191	0.000191	1.05E+06
R3a (Top)	300	28.1	4	4.8	0.00843	0.0000843	9.89E+05
R3a (Bottom)	300	31.7	4	5.3	0.00951	0.0000951	7.94E+05
R3b (Top)	300	24.5	4	5.0	0.00735	0.0000735	1.09E+06
R3b (Bottom)	300	31.2	4	5.4	0.00936	0.0000936	7.91E+05

R4a (Top)	400	25.7	4	4.1	0.01028	0.0001028	9.49E+05
R4a (Bottom)	400	21.6	4	4.1	0.00864	0.0000864	1.13E+06
R4b (Top)	400	19.8	4	4.2	0.00792	0.0000792	1.20E+06
R4b (Bottom)	400	23.1	4	4.1	0.00924	0.0000924	1.06E+06
R5a (Top)	500	19.4	4	3.5	0.0097	0.000097	1.18E+06
R5a (Bottom)	500	19.5	4	3.3	0.00975	0.0000975	1.24E+06
R5b (Top)	500	23.2	4	3.3	0.0116	0.000116	1.04E+06
R5b (Bottom)	500	24.1	4	3.3	0.01205	0.0001205	1.01E+06
					Average Conductivity		**1.04E+06**

Tyvek (Panel 2)	**Width (μm)**	**Thickness (μm)**	**Length (cm)**	**Resistance (ohm)**	**Area (mm^2)**	**Area (cm^2)**	**Conductivity (S/m)**
L1	1000	22.9	10	5.3	0.0229	0.000229	8.24E+05
L2	1000	23.8	5	2.6	0.0238	0.000238	1.62E+06
L3	1000	28.3	5	2.5	0.0283	0.000283	1.41E+06
R3a (Top)	300	24.7	4	5.2	0.00741	0.0000741	1.04E+06
R3a (Bottom)	300	22.2	4	5.3	0.00666	0.0000666	1.13E+06
R3b (Top)	300	20.7	4	5.7	0.00621	0.0000621	1.13E+06
R3b (Bottom)	300	23.3	4	5.8	0.00699	0.0000699	9.87E+05
R4a (Top)	400	26.4	4	4.4	0.01056	0.0001056	8.61E+05
R4a (Bottom)	400	25.8	4	4.4	0.01032	0.0001032	8.81E+05
R4b (Top)	400	16.8	4	4.1	0.00672	0.0000672	1.45E+06
R4b (Bottom)	400	19.1	4	4.1	0.00764	0.0000764	1.28E+06
R5a (Top)	500	26.3	4	3.6	0.01315	0.0001315	8.45E+05
R5a (Bottom)	500	30.6	4	4.0	0.0153	0.000153	6.54E+05
R5b (Top)	500	19.8	4	3.6	0.0099	0.000099	1.12E+06
R5b (Bottom)	500	18.9	4	3.7	0.00945	0.0000945	1.14E+06
					Average Conductivity		**9.69E+05**

Appendix B3 - *Matlab* Program (Dielectric Properties Extraction)

```
% ------------------------------------------------------------------
% Extraction for the dielectric properties of Tyvek up to mm-wave
% frequencies (30 GHz). S-parameters are from 3D simulation
results in CST.
% Equations considered are based on quasi-static analysis.
% ------------------------------------------------------------------

close all;
clear all;
clc;

% Eo's method requires only 1 transmission line length
L=3*10^-3; %L1=3mm
%L=2*10^-3;
c0=3*10^8; %speed of light
z0=50;%reference impedance
cond=9e6;%S/m
t=25e-6;%thickness for stencil-printed trace (from CST model)
u0=4*pi*10^-7;
ur=1;
rho=1/cond;

%Definition for Ghione's formulation
a=150*10^-6;%1/2 trace width
b=250*10^-6;%1/2(w+2s), where w=300um, s=100um
h=330*10^-6;%subst thickness
k = a/b;
k1=tanh((pi*a)/(2*h))/tanh((pi*b)/(2*h));
kprime=sqrt(1-k*k);
k1prime=sqrt(1-k1*k1);
K=ellipke(kprime)/ellipke(k);
K1=ellipke(k1)/ellipke(k1prime);

S=2*a;%CPW width
W=100*10^-6;%gap/spacing between signal and ground
Delta=(1.25*t/pi)*(1+log(4*pi*S/t));
ke=k+(1-k*k)*(Delta/(2*W));
keprime=sqrt(1-ke*ke);
c1=(1.25/pi)*log(4*pi*S/t)+1+((1.25*t)/(pi*S));
c2=2+(S/W)-((1.25*t)/(pi*W))*(1+log(4*pi*S/t));
c3=c2*c2;
kkprime=pi/(log(2*(1+sqrt(kprime))/(1-sqrt(kprime))));% for 0 <k
<0.707
Pprime=[k/((1-kprime)*(kprime^(3/2)))]*(kkprime*kkprime);

%simulation results - TYV
data1 = importdata('CPW_3mm_TYVEK_20GHz.txt'); %imported S-
parameter in .txt format

freq = data1(:,1).*(10^9);%freq expressed in Hz
s11_mag_sim = data1(:,2);
s11_dB_sim= mag2db(s11_mag_sim);
s11_ph_sim = data1(:,3);%in deg
```

```
s11_ph_d2r1=unwrap(s11_ph_sim/180*pi);
s12_mag_sim = data1(:,4);
s12_dB_sim= mag2db(s12_mag_sim);
s12_ph_sim = data1(:,5);%in deg
s12_ph_d2r1=unwrap(s12_ph_sim/180*pi);

s21_mag_sim = data1(:,6);
s21_dB_sim= mag2db(s21_mag_sim);
s21_ph_sim = data1(:,7);%in deg
s21_ph_d2r1=unwrap(s21_ph_sim/180*pi);

s22_mag_sim = data1(:,8);
s22_dB_sim = mag2db(s22_mag_sim);
s22_ph_sim = data1(:,9);%in deg
s22_ph_d2r1=unwrap(s22_ph_sim/180*pi);


for n=1:1001;

    %For L=3mm,Define a matrix of S-parameters
    %Simulation results
    s11n_sim(n) = s11_mag_sim(n)*exp(1i*s11_ph_d2r1(n));
    s12n_sim(n) = s12_mag_sim(n)*exp(1i*s12_ph_d2r1(n));
    s21n_sim(n) = s21_mag_sim(n)*exp(1i*s21_ph_d2r1(n));
    s22n_sim(n) = s22_mag_sim(n)*exp(1i*s22_ph_d2r1(n));

    %Finding K in Eo's paper
    k1n_sim(n) =(s11n_sim(n)*s11n_sim(n))-
(s21n_sim(n)*s21n_sim(n))+1;
    k2n_sim(n) = 2*s11n_sim(n);
    k3n_sim(n) = 2*s21n_sim(n);
    K_sim(n) = sqrt(((k1n_sim(n)*k1n_sim(n))-
(k2n_sim(n)*k2n_sim(n))./(k3n_sim(n)*k3n_sim(n)));

    %Finding propag. const
    a1_sim(n)=(1-
(s11n_sim(n)*s11n_sim(n))+(s21n_sim(n)*s21n_sim(n)))/(2*s21n_sim(n
))-K_sim(n);
    gamma_sim(n)=log(a1_sim(n))/(L);%gamma in rad/m

    %Extracting for the line impedance-Eo's paper
    Z2num(n)=(1+s11n_sim(n))*(1+s11n_sim(n))-
(s21n_sim(n)*s21n_sim(n));
    Z2den(n)=(1-s11n_sim(n))*(1-s11n_sim(n))-
(s21n_sim(n)*s21n_sim(n));
    Z2(n)=z0*z0*(Z2num(n)/Z2den(n));
    Z(n)=abs(sqrt(Z2(n))); %Z2 is complex; finding the magnitude
of the line

    %Extracting for the dielectric properties - standard equations
    %epseff=(gamma/beta)^2
    beta(n)=(2*pi)/(c0/freq(n));%phase constant in free space
    omega(n)=2*pi*freq(n);%in rad/s
    epseff(n)=(gamma_sim(n)/beta(n))*(gamma_sim(n)/beta(n));
    epseff_re(n)=abs(real(epseff(n)));

    %Extracting for epsr - Ghione's equation for a coplanar
waveguide with
    %a lower ground plane (ie. metal platen beneath substrate)
    epsr(n)=(epseff_re(n)*(1+K*K1)-1)/(K*K1);
```

```
   %Extracting loss tangent from total loss - Test if Wheeler's
and
   %If Ghione's quasi-static equations are valid to mm-wave
(Method 1)
   Rs(n)=sqrt(pi*u0*ur*freq(n)/cond);%skin resistance
   lambda(n)=c0/freq(n);

   %Extracting loss tangent without taking into account strip
thickness
   alpha_cond2(n)= 4.88*10^-
4*Rs(n)*epseff_t(n)*Zocp*(Pprime/(W*pi))*(1+(S/W))*(c1/c3)*(1/8.68
);%in Np/m; formula provided in dB/m
   alpha_diel2(n)=alpha_tot(n)-alpha_cond2(n);
   tand_sim2(n)=abs(alpha_diel2(n)*lambda(n))/(3.142)*((epsr(n)-
1)*(sqrt(epseff_t(n)))/(epsr(n)*(epseff_t(n)-1)))%in Neper/m

end

display(epseff_re);

subplot(2,1,1)
plot(freq/(10^9),epseff_re,freq/(10^9),epsr)
grid on;
xlabel('Freq(GHz)');
ylabel('Eff. & real dielectric constant');


subplot(2,1,2)
plot(freq/(10^9),tand_sim,freq/(10^9),tand_sim2);
grid on;
xlabel('Freq(GHz)');
ylabel('Loss tangent');
```

Appendix C1 - Process Characterisation of Inkjet Printing

To characterise the inkjet printing process using the Dimatix printer (DMP-2831), a printing trial was performed with the following objectives. The first objective is to evaluate the silver ink (EMD 5603) to be used, to ensure that the ink properties (adhesion, resistivity values) were consistent with the datasheet. From the technical datasheet [169], EMD 5603 was specified to adhere with various substrates such as Kapton (PI), FR4, glass and metals. The volume resistivity after thermal sintering was provided as 5-30 μΩ cm (at 150-300 °C). The second objective of the characterisation is to ascertain the repeatability of the printing process, through printing test patterns with varying widths (100 μm – 800 μm). The objectives are summarised in Table C1-1.

Table C1-1 Printing trial for process characterisation

Goals	Objectives	Tasks
• Silver ink works as expected.	• Silver ink can be printed on one of the substrates (PI) referred to in the datasheet.	Check that the ink remains intact (i.e. no de-wetting) after the printing and curing process.
	• Ascertain if sintering of silver nanoparticles has occurred.	Perform DC resistance measurements of the test patterns.
	• Adhesion of silver ink to a substrate (PI) mentioned in the datasheet.	Perform tape tests to ascertain the ink-substrate adhesion.
• Process characterisation of the printing process	• Repeatability of printed dimensions.	Print test patterns with different line widths.

C1.1 Materials

The substrate considered for the inkjet printing process characterisation is Polyimide (PI). PI is a smooth substrate commonly used in inkjet printing [22, 37-38, 91] and this substrate is used as the silver ink prints and adheres well to it as specified in the ink datasheet [169]. This makes PI suitable as a verification substrate to validate the properties of the silver ink specified in the ink datasheet.

The silver ink used in the process characterisation is EMD 5603, with the properties detailed in Section 5.2.2.

C1.2 Experimental Procedure

(i) Test Structures

The test structures considered for the process characterisation are shown in Figure C1-1 and Figure C1-2. The two point probe test structures in Figure C1-1 were imported via a bitmap file into DMP-2831, while those in Figure C1-2 were defined using the Pattern Editor function as described in Section 5.3.2. Following the definition of the test structures in Dimatix, the structures were printed onto PI.

For the test structures in Figure C1-1, the silver layer was printed with the platen at ambient temperature, following which the platen temperature was increased to 60 °C to aid in the drying process. All the samples were thermally sintered in the oven at 180 °C for 135 min.

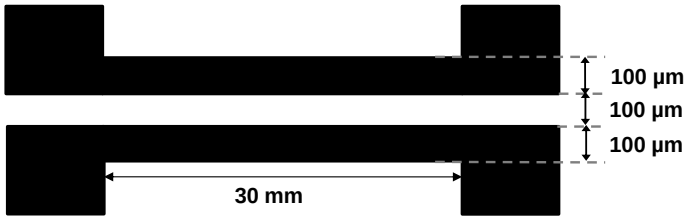

Figure C1-1 Test structures to measure for resistivity

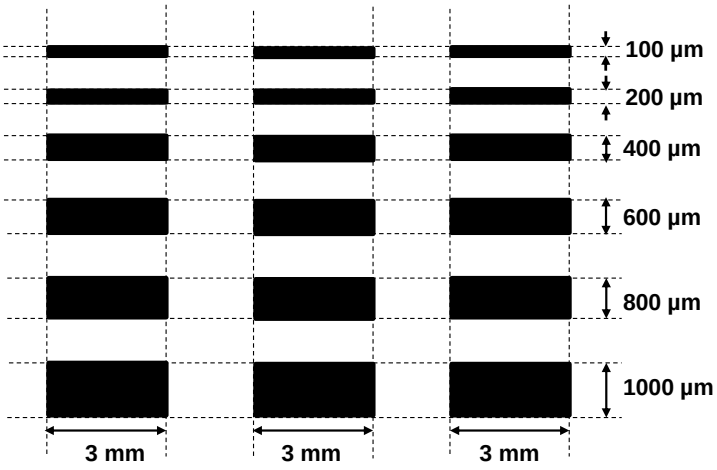

Figure C1-2 Test structures to determine repeatability of printed trace widths

(ii) Resistivity Measurements of Printed Traces

Using the same profile characterisation parameters described in Section 5.3.5 (Chapter 5), the printed trace thicknesses were measured. Three measurements were performed for each trace in an east-west direction along 3 different sections of the trace, as shown in Figure C1-3. Prior to the thickness measurements, the PI samples were placed onto the platform and taped along 2 sides. The measurement parameters used in the scan were 1.5 mm scan length, 0.5 μm spacing. From the measured resistance and thickness values, the DC resistivity could then be calculated using equation (C1-1):

$$\rho = \frac{R*w*t}{L} \qquad \text{(C1-1)}$$

where ρ is the extracted DC resistivity, R is the measured resistance, w is the trace width, t is the line thickness and L is the line length. For the extraction of ρ, a rectangular trace profile was assumed in computing for the cross-sectional area of the trace.

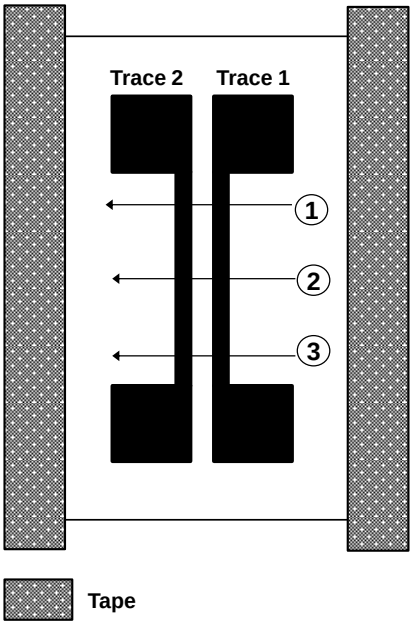

Figure C1-3 Measurement locations of trace thickness on PI

(iii) Adhesion Testing

A simple tape test is performed to determine if the adhesion of inkjet printed traces on PI is consistent with the ink datasheet [169]. The test was carried out using a pressure sensitive adhesive tape (P/N: 7305-2240, 3M). As the PI substrates were of a flexible nature, they were first adhered to a rigid PCB board. Prior to the tape test, the trace resistances were measured using a digital multi-meter (P/N: 72-7765, Tenma) to ensure that the electrical connection was still intact. Tape lengths of around 5 cm were cut and fixed to the central portion of the test structures as shown in Figure C1-4. The tape was then swiftly peeled off in one quick motion at an angle close to 180°.

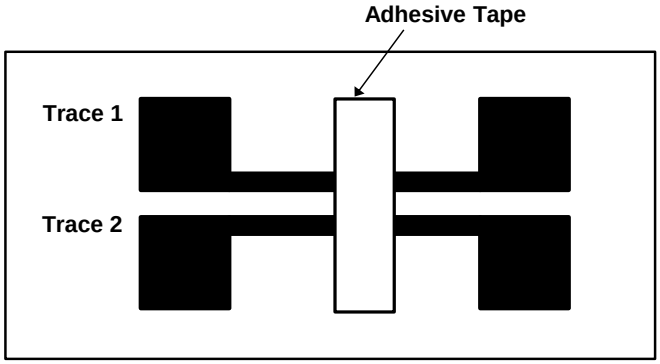

Figure C1-4 Schematic of tape test on PI samples

C1.3 Results and Discussion

(i) Repeatability of Printed Trace Widths

Figure C1-5 and Figure C1-6 show the test structures printed onto PI as described in Section (b) of this Appendix. The printed traces were captured using a high power microscope (Nikon Optiphot) with a x5 objective lens, and the trace widths were determined from the microscope images using *ImageJ* software [252]. At least 5 readings were made across each trace and averaged, with the results shown in Table C1-2.

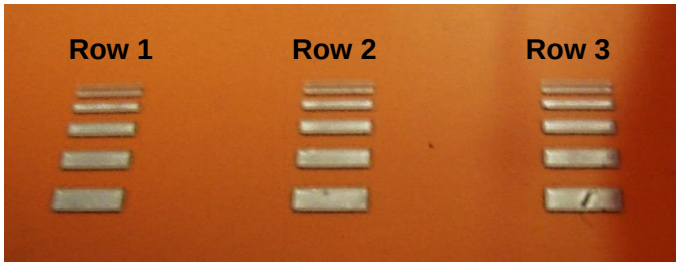

Figure C1-5 Printed test structures to ascertain repeatability

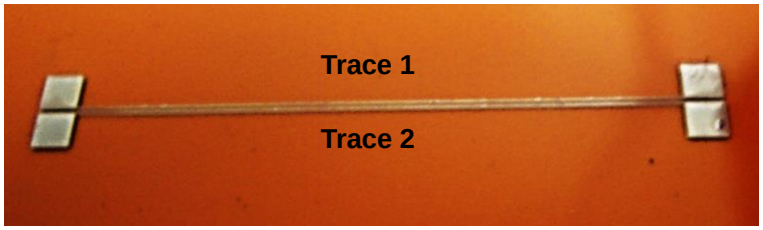

Figure C1-6 Printed test structures to measure for resistivity

Table C1-2 Measured dimensions for the test structures in Figure C1-5

Defined (µm)	Row 1	Row 2	Row 3
100	123.3 (23.2%)	122.0 (22.0%)	121.8 (21.8%)
200	221.7 (10.8%)	219.3 (9.7%)	219.5 (9.7%)
400	417.6 (4.4%)	416.5 (4.1%)	416.8 (4.2%)
600	597.1 (0.48%)	599.4 (0.1%)	597.1 (0.48%)
800	795.5 (0.6%)	796.6 (0.4%)	793.7 (0.79%)
1000	1012.7 (1.3%)	1012.93 (1.3%)	1010.13 (1.0%)

From the results in Table C1-2, a good repeatability of the dimensions can be observed across Rows 1 to 3. Furthermore it was observed that the trace variation is increased for smaller trace dimensions, with variations of 20 % obtained for 100 µm (designed) traces. This variation reduces to ≤ 10 % for trace widths of 200 µm and beyond. The larger variation observed for the 100 µm widths could be attributed to the wettability of the printed silver droplets onto the PI substrate. This could be better understood by considering the equation of Smith *et al.* [22] to estimate the minimum line width obtainable. Setting k = 1 in equation (5.5), and using an estimated contact angle of 11° from [22] for the EMD 5603 droplets on PI, a trace width of 124 µm is calculated, which agrees well with the measured trace width values of 122-123 µm in Table C1-2. In this case, the silver ink used on PI in [22] has a surface tension of 26.3 mN/m, which is close to that of EMD 5603 at

27-31 mN/m (i.e. similar wettability). The results indicate that the minimum trace width realisable on PI using EMD 5603 or a silver ink with similar surface tension is around 124 µm.

(ii) Calculated Resistivity for EMD 5603

The printed two point probe test structures are shown in Figure C1-6. The structures were printed using one jetting head (without satellite drops), and realised with 1 layer of overprinted silver. The trace widths were characterised using the process described in Section C1.2 (ii) of this Appendix. As the two point probe structures (Figure C1-6) are longer than those in Figure C1-5, 10 measurements of the trace width were made across the entire length and the values averaged.

The resistance values of the traces were measured using a digital multi-meter (P/N: 72-7765, Tenma) and averaged from 2 readings. These results are shown in Table C1-3, where the resistivity values are in the range of 12.7-15.9 µΩ-cm. This is within the resistivity range provided in the datasheet for EMD 5603, which is 5-30 µΩ-cm at 150-300 °C [169]. However the actual resistivity value is expected to be lower after taking into consideration the effect of the probe contacts during the resistance measurements.

Table C1-3 Extracted resistivity values for test structures

Trace[23]	Average resistance (Ω)	Average thickness (µm)	Resistivity (µΩ-cm)
1	63.9	0.45	12.7
2	55.1	0.65	15.9

[23]Trace notation is with reference to Figure C1-6.

(iii) Adhesion Test Results

Figure C1-7 shows the results after the tape test on the PI sample. From Figure C1-7 (B), a good adhesion was observed for the traces after the tape test, which agrees with the information provided in the datasheet [169]. The resistances of the traces after the tape test are shown in Table C1-4. Overall, the traces in the sample remained largely intact with a slight increase (≤ 2%) in the measured resistance.

Further images in Figure C1-8 reveal that some portions of the trace were removed during the tape test.

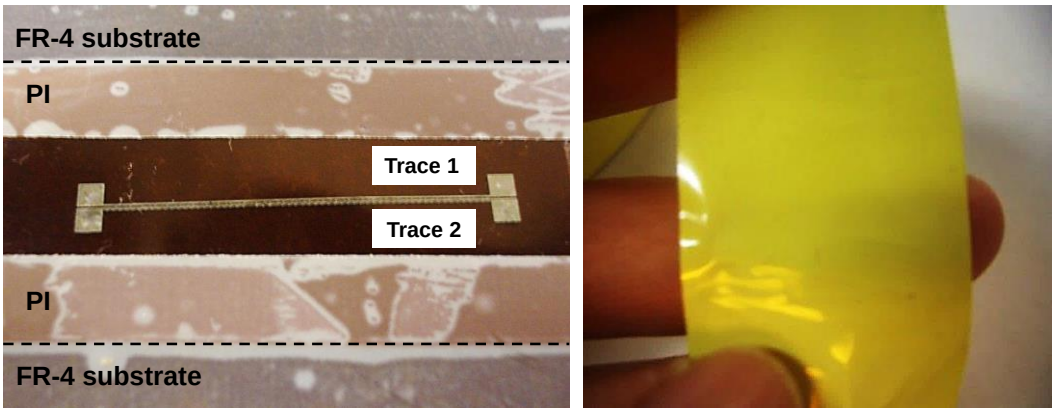

(A) **(B)**

Figure C1-7 Results of tape test on PI sample (A) View of test structure (B) View of adhesive tape after tape test

Table C1-4 Resistance values before and after tape test

No. of silver layers	Trace[24]	Average resistance (before tape, Ω)	Average resistance (after tape, Ω)
1	1	68.0	68.4
	2	58.0	59.1

[24]Trace notation is with reference to Figure C1-6.

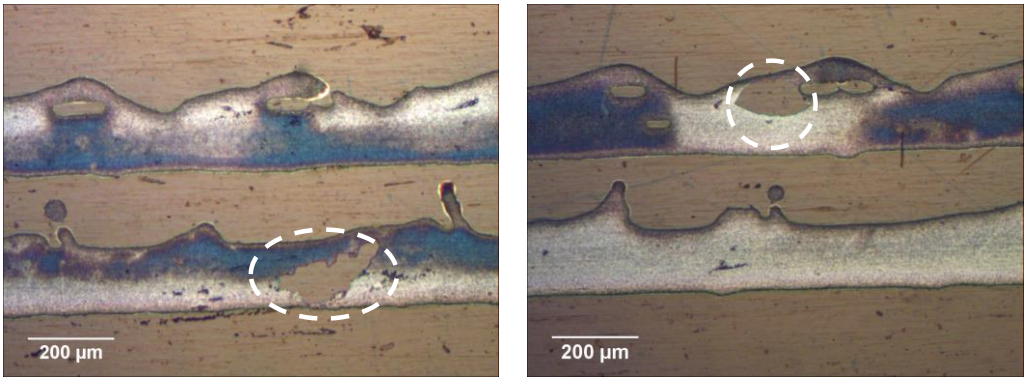

Figure C1-8 Microscope images showing portions of trace peeled off during the tape test

C1.4 Conclusions

A characterisation of the inkjet printing process on Dimatix printer (DMP-2831) was performed. From the results obtained, a good repeatability of the printed trace widths was obtained (≤ 2%). The minimum trace width obtainable on PI using EMD 5603 was around 124 µm. For trace widths of 200 µm and beyond, the

variation between the designed and printed trace widths was within 10 %. The extracted resistivity was within the range provided for EMD 5603 in the datasheet [169], and a simple tape test showed that there is a good adhesion between the printed trace and the PI substrate, with a resistance variation of 2 % before and after the tape test.

Appendix C2 - Values used for Error Bar Plot in Figure 5.11

Table C2-1 Measured mean and error limits from the surface morphology characterisation

R_a (µm)	Mean	Error (upper)	Error (Lower)
Untreated RO3006	0.76	0.22	0.11
Hydrophobic coating	0.93	0.08	0.15
EMD 6200 coating	0.44	0.16	0.11

Appendix D - Resistance Evaluation of Tyvek Samples

The objective of this Appendix is to determine whether measurable resistance values could be obtained on Tyvek samples coated with the UV-curable insulator. This is an extension of the results obtained in Chapter 6, where electrically conductive traces were demonstrated on coated glass samples exposed in both inert and ambient atmospheres.

The same experimental methods involving insulator ink drawdown (Section 6.3.1 of Chapter 6), UV exposure (Section 6.3.2 of Chapter 6) and UV-ozone post-treatment times (Section 6.3.3 of Chapter 6) were applied to the Tyvek samples. These parameters were used as an experimental trial to ascertain if measurable resistances could be obtained on the Tyvek samples. In this evaluation, only EMD 6415 [89] is considered as the ink has an increased cross-linking formulation. The increased cross-linking present in EMD 6415 is expected to alleviate the silver ink seepage (after overprinting) into the porous Tyvek substrate underneath, compared to the EMD 6200 [90] insulator used in Chapter 6.

The Tyvek samples were exposed under both inert and ambient atmospheres using a dosage of 600 mJ/cm^2. This is followed by UV-ozone post-treatments of 80 s (for samples exposed in inert atmosphere) and 3 min (for samples exposed in ambient atmosphere). Following that, silver ink was overprinted onto the samples using the printing parameters described in Section 6.3.4. Specifically, 25 mm long traces with defined widths of 100 µm, 500 µm and 1 mm were printed. The samples were then thermally sintered at 110 °C at 2 h intervals, up to a maximum of 10 h.

After the thermal sintering, no de-wetting was observed for the overprinted silver traces upon visual inspection, and clear linear traces were obtained as shown in Figure D-1. However the samples were observed to be warped from the prolonged thermal sintering period (Figure D-1). The resistance values were measured with a two point multi-metre after each interval. The results in Figure D-2 and Figure D-3 show the normalised resistance values for inert and ambient cured Tyvek samples. For each data point in Figures D-2 and D-3, the average resistance value was

obtained from three measurements and divided by the corresponding trace length over which the resistance was measured (in cm).

Figure D-1 EMD 6415 sample cured under an inert atmosphere with UV-ozone treatment (80 s). The silver ink traces (2 layers) are obtained after printing and sintering

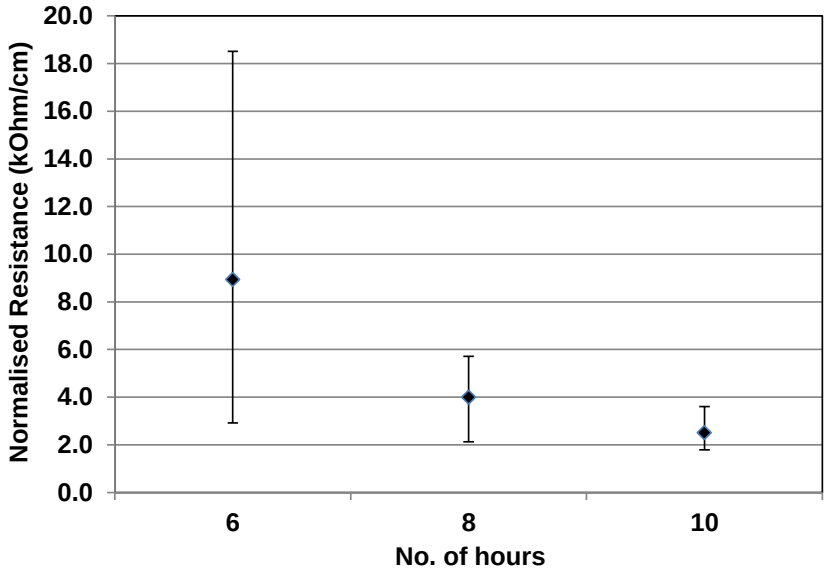

Figure D-2 Variation of the normalised resistance values for silver traces sintered for different periods of time at 110 °C. The results are for two layers of silver overprinted on inert cured EMD 6415 sample (with 20 s of UV-ozone post-treatment)

From Figure D-2, the resistance variation of the measured traces was observed to decrease with an increase in the sintering time. In particular, the resistance range narrowed significantly from 2.9-18.5 kΩ/cm (after 6 h of thermal sintering) to 1.8-3.6 kΩ/cm (after 10 h of thermal sintering).The large resistance range in kΩ/cm could possibly be due to the penetration of EMD 6415 into the porous Tyvek substrate during the ink drawdown. Consequently an uneven insulator layer could

have resulted, which affected the polymer cross-linking during UV exposure and the conduction path (i.e. resistance) of the overprinted silver nanoparticles.

Figure D-3 shows the normalised resistance values for measured traces overprinted on EMD 6415 exposed under ambient atmosphere with UV-ozone post-treatment. Compared to the results in Figure D-2, the normalised resistance values in Figure D-3 are significantly highly (3 times the order of magnitude) even after 10 h of thermal curing (Figure D-3). Since the samples were exposed under inert atmosphere in Figure D-2, the results in Figure D-3 imply significantly reduced cross-linking present in the samples UV cured in air, due to the oxygen inhibition effect. As discussed in Section 6.4.4, this could have affected the silver nanoparticle aggregation and hence the electrical path formed. Further investigation would be required to understand this phenomenon and improve the resistance range of the overprinted silver traces.

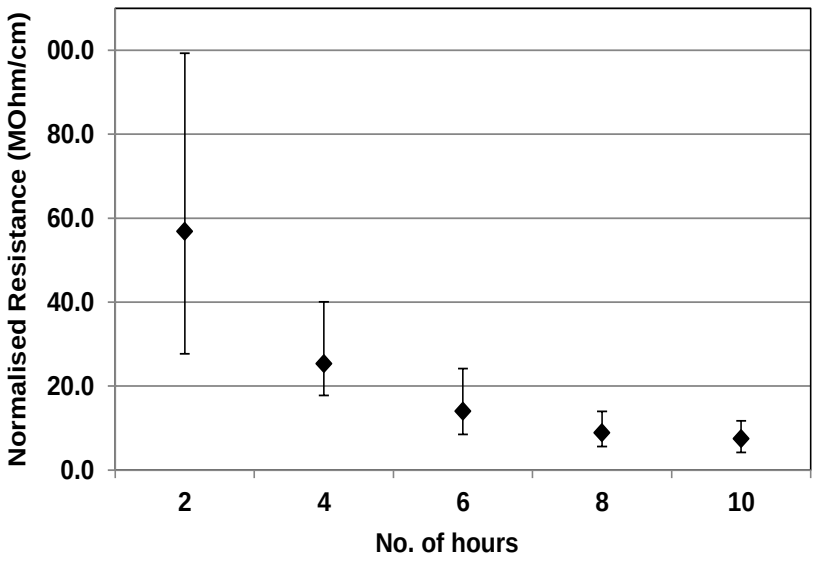

Figure D-3 Variation of the normalised resistance values for silver traces sintered for different periods of time at 110 °C. The results are for 2 layers of silver overprinted on ambient cured EMD 6415 samples (with 3 min of UV-ozone post-treatment)

Appendix E1 - Effect of Surface Roughness on CPW Line Loss

A motivation for obtaining an accurate simulation models is towards the aim of determining the influence of surface roughness on the RF performance of printed traces. Sain and Melde [138] have investigated the effect of surface roughness on interconnect losses using a 3D electromagnetic solver, which has the drawback of being computationally intensive. Curran [131] proposed an analytical approach which uses a variable *P* to account for the shape of the trace surface roughness. However this variable is characterised only for traces with a saw-tooth profile (i.e. chemically etched copper traces) and is unknown for other trace profiles.

With an accurate simulation model as that developed in this chapter, it is proposed that the surface roughness could be estimated using a correction factor *P*:

$$P = \frac{Resistance_{(rough)}}{Resistance_{(smooth)}} \tag{E1-1}$$

where $Resistance_{rough}$ in equation (E1-1) refers to the resistance of a trace with surface roughness which could be obtained from *S*-parameter measurements, while $Resistance_{smooth}$ refers to the resistance of an ideal trace (i.e. zero surface roughness) which is obtained from 3D simulation. From equation (E1-1), if the simulation model is accurate and the only variable is the surface roughness, the extra loss arising from the surface roughness can then be assessed.

The effect of surface roughness is investigated for a 15 mm CPW lines printed on two sets of quartz substrates. One set of quartz is polished to yield an average surface roughness of 1 µm while the other set has a smooth surface in the order of nanometres. The quartz substrates have thicknesses of 1 mm (Dielectric constant = 3.9, loss tangent < 0.001 at 500 MHz). With reference to Table 7.2 in Chapter 7, the CPW line is designed with a width of 350 µm and a gap of 50 µm. To realise these dimensions, the CPW lines were printed using paste 2 as this paste yields a lower spread after printing. The transmission lines were characterised for the RF performance using the parameters described in Section 7.3(e)(ii) of Chapter 7. The measured insertion loss results are shown in Figure E1-1.

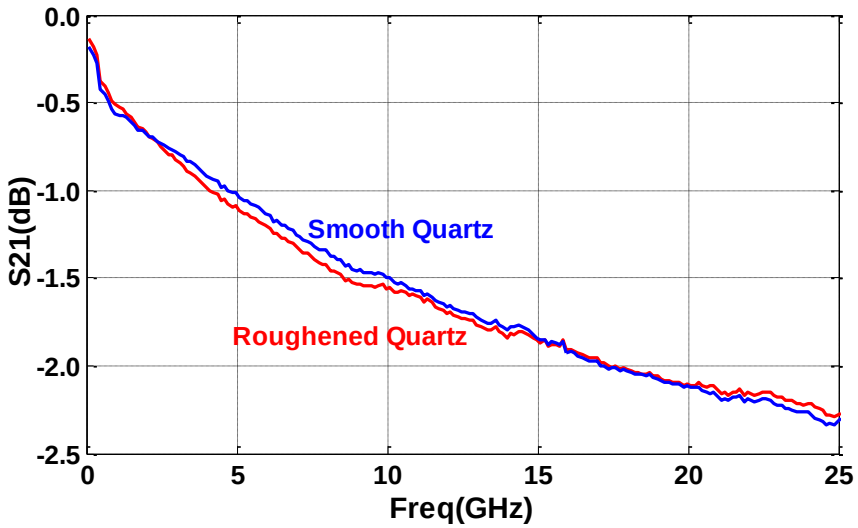

Figure E1-1 Measured insertion loss of 15 mm CPW line screen printed on smooth and roughened quartz

From Figure E1-1, a negligible difference is observed between the measured insertion losses of smooth and roughened quartz. This suggests that the transmission line length may not be sufficiently long to determine the influence of the trace edge roughness on the insertion loss of the transmission line. In addition, the gaps realisable using screen printing in this chapter may not be small enough for the effects of the trace edge roughness to be rendered significant.

Appendix E2 - Determination of Scan Speed (Non-contact Measurements)

This trial experiment seeks to determine a suitable scan speed (i.e. a compromise between time and speed) to be used for the imaging of the printed traces described in Chapter 7 using a 3D non-contact laser technique.

A x20 objective lens was used in the study and the results using the differential interference contrast (DIC) laser option were used as the reference value. The sample measured is a 2 mm CPW transmission line screen printed on RO3006 substrate. In the evaluation of the average surface roughness (R_a), the cutoff wavelength used was 80 µm for an evaluation length of 780 µm.

Table E2-1 Comparison of results using different scan configurations, with reference to Figure 7.10 (Chapter 7)

Scan Configuration	***w*** **(µm)**	g_1 **(µm)**	g_2 **(µm)**	***t*** [25] **(µm)**	R_a [26] **(µm)**	**Time taken (min)**
DIC Laser-Fine	146.1	78.4	75.0	8.5	0.5	42
DIC Laser-Fast	149.0	71.4	74.0	8.7	0.6	6
Fast	151.9	76.8	76.1	9.0	0.5	6
Ultrafast	159.2	65.6	65.6	8.6	0.5	4

[25] *t* represents the average conductor thickness for the signal and ground traces. [26] The measured R_a is for the signal trace of the CPW transmission line.

From the results in Table E2-1, a variation of 9 % is observed for *w*, in comparing the ultrafast measurement mode with the DIC laser-fine mode. The corresponding variation in the g_1 and g_2 values range from 13-17 %. In contrast a smaller variation of within 10 % is observed for the measured parameters using the DIC laser-fast mode, along with a significant reduction of the measurement time by 7 times. As such the DIC laser-fast mode was adopted for the characterisation of the trace profiles in Chapter 7.

Appendix E3- Values used for Standard Deviation Plot in Figure 7.17

Table E3-1 Measured mean and error limits from the surface morphology characterisation

Substrate Region[27]	Average DC Conductivity (S/m)		Standard Deviation	
	690µm width	150 µm width	690µm width	150 µm width
Region 1	1.05E+06	1.12E+06	5.46E+04	2.03E+04
Region 2	1.06E+06	1.10E+06	1.55E+04	3.35E+04
Region 3	1.07E+06	1.17E+06	6.13E+04	4.13E+04
Region 4	1.02E+06	1.10E+06	1.49E+04	3.93E+04

[27]Substrate Region is with reference to Figure 7.4

Appendix E4 - Adhesion of Inkjet Printed Traces

This experiment seeks to ascertain the adhesion of inkjet printed traces on glass substrates through an ISO tape test. The test is performed on an inkjet printed area of 20 x 20 mm on the substrate, using the procedure described below.

1. Cut a piece of ISO tape about 75 mm long.
2. Place the center of the tape over the trace. To ensure good contact with the film rub the tape firmly with the end of a pencil. The colour under the tape is an useful indication of whether good contact has been made.
3. Remove the tape by seizing the free end rapidly back upon itself.
4. Observe the grid area for removal of traces from the substrate using an optical microscope or a magnifying glass.

From Figure E4-1(B) it can be observed that most of the inkjet printed trace was removed after the tape test. This could be partly attributed to the silver ink formulation which is comprised of silver nanoparticles and solvents. After the solvents have evaporated following thermal sintering, only the silver trace is left, which is easily peeled off. The poor adhesion is also observed during the four point probe measurements of the inkjet printed test structures, where trace regions contacted by the probes were removed as shown in Figure E4-2.

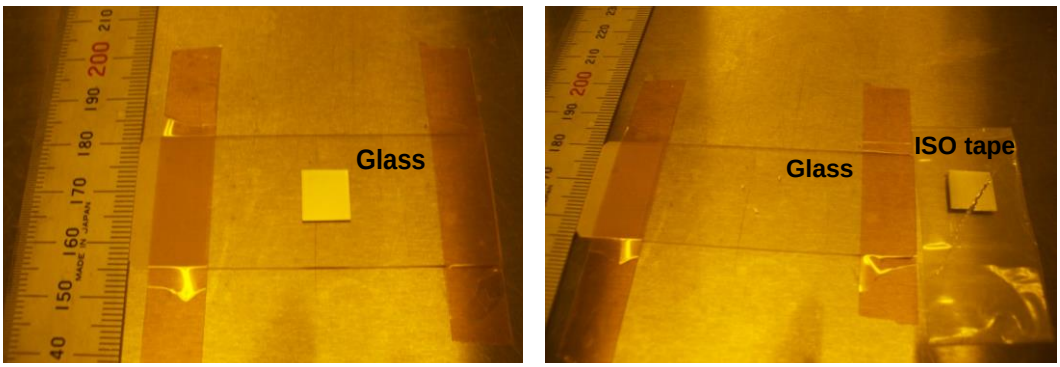

(A) **(B)**

Figure E4-1 Inkjet printed trace on glass substrate (A) Before tape test (B) After tape test

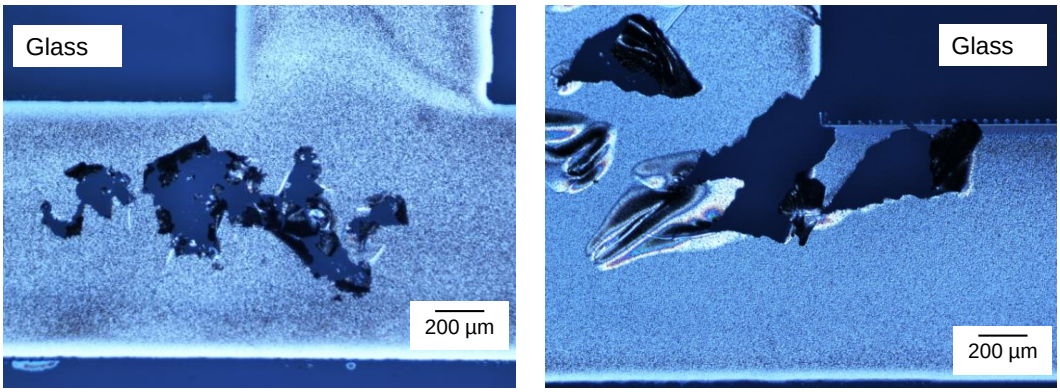

(A) **(B)**

Figure E4-2 Optical microscope images showing the removal of inkjet printed traces (1 layer) from a glass substrate during four point probe measurements